Using high-resolution modelling to improve the parameterisation of convection in a climate model

Leif Denby

Friday 17th March, 2017

Table of Contents

List of symbols

A	area	[m^2]
ρ	density	[kg/m^3]
D_v	diffusivity of water vapour	[m^2/s]
C_D	drag cofficient	[1]
μ	entrainment rate	[1/m]
z_{EL}	Equilibrium level	[m]
σ	fractional cross-sectional area	[m^2/m^2]
Γ	gamma-function	[1]
R	gas constant	[J/K]
R_d	gas constant for dry air	[J/K]
g	gravitational constant	[m/s^2]
Δx	grid-resolution	[m]
$c_{p,d}$	heat capacity at constant pressure for dry (atmospheric) air	[J/kg/K]
$c_{p,v}$	heat capacity at constant pressure for water vapour	[J/kg/K]
$c_{v,d}$	heat capacity at constant volume for dry (atmospheric) air	[J/kg/K]
$c_{v,v}$	heat capacity at constant volume for water vapour	[J/kg/K]
c_i	heat capacity for ice (frozen water)	[J/kg/K]
c_l	heat capacity for liquid water	[J/kg/K]
$đQ$	heat transfer into system	[J]
z	height	[m]
(i, j)	horizontal index	[1]
x, y	horizontal position	[m]
u, v	horizontal velocity components	[m/s]
U	internal energy	[J]
L_f	latent heat of freezing	[J/kg]
L_v	latent heat of vapourisation	[J/kg]
z_{LFC}	Level of Free Convection	[m]
z_{LCL}	Lifting Condensation Level	[m]
θ_l	liquid potential temperature	[K]
m	mass	[kg]
S	moist static energy	[J]
$N(r)dr$	number-density	[$1/m^3$]
ϵ	numerical error measure	[1]
θ	potential temperature	[K]
p	pressure	[Pa]
r	radius	[m]
RH	relative humidity	[%]
$p_{v,sat}$	saturation vapour pressure	[Pa]
e_{CAPE}	specific Convective Available Potential Energy	[J/kg]

e_{CIN}	specific Convective Inhibition energy	[J/kg]
q_l	specific mass of cloud liquid water	[kg/kg]
q_d	specific mass of dry air	[kg/kg]
q_r	specific mass of rain water	[kg/kg]
q_v	specific mass of water vapour	[kg/kg]
S_w	super-saturation	[1]
p_θ	surface reference pressure	[Pa]
T	temperature	[K]
K_a	thermal conductivity	[J/m/s/K]
t	time	[s]
$\hat{\mathbf{e}}$	unit-vector	[1]
k	vertical index	[1]
w	vertical velocity	[m/s]
V	volume	[m^3]
$đW$	work done on system	[J]

Chapter 1

Introduction

The contribution of clouds to climate sensitivity is the single-most uncertain component of the atmospheric system in the most recent IPCC report on climate predictions (*Stocker et al.* [2013]); in addition numerical weather prediction models show many systematic errors which have been attributed to poor representation of processes driven by and causing clouds (a detailed review will be given in Chapter 2). For these reasons there is an urgent need to better understand the physical processes that drive and influence the formation of clouds, and to study how the presence of clouds affects the immediate and large-scale environment. In this work, influences on and characteristics of convective clouds have been studied using high-resolution modelling with the aim to better understanding what influences the production of convective clouds and what are the characteristic properties of these clouds. These aspects of convective clouds have been studied with the aim to improve on the Convective Cloud Field Model (CCFM, *Wagner and Graf* [2010]).

To set this research in context, Chapter 2 contains a brief overview of the history of convective parameterisation, contemporary convection models, and the prevailing description of convection used in the literature. A more exhaustive description is given of CCFM and the accompanying cloud model including discussing some of the underlying assumptions of the model that may require re-evaluating, and how specifically these have been investigated in this work. The cloud model represents the dynamics of a single convective cloud and CCFM computes the grid-scale convective activity using this cloud model to represent multiple clouds interacting through the environment.

The detailed aim of this work is to:

a) make improvements on the single-cloud cloud-model used within CCFM by improving the representation of physical processes that have been observed in simulation and observations (such as the mixing of convective clouds with the environment, the representation of precipitation formation and the effect of windshear on convective plumes) and quantify the cloud-model's skill in predicting the properties of individual convective clouds

b) study and understand the assumptions of CCFM by quantifying its skill in predicting the properties of a large ($> 1000s$) number of mutually-interacting convective clouds and identify ways in which these assumptions may require altering to lead to a more physically sound formulation of the convection scheme.

In the aim to achieve the former, the historical development of the cloud-model equations has been reviewed and the equations re-derived from first-principles (so as to guarantee their physical consistency). In addition, the cloud-model has been re-implemented to allow for isolated testing and study. This work will be detailed in chapter 3. The predictive skill of the 1D cloud-model was assessed by performing numerical simulations of individual convective clouds using the Atmospheric Tracer High-resolution Atmospheric Model (ATHAM, [*Herzog et al.*, 1998]) and comparing extracted properties from these simulations to those predicted by the 1D cloud-model (Chapter 5). During this work it became necessary to give particular focus to the physical formulation and software implementation representing phase-transitions between water-species (the so-called *microphysics*); firstly to clarify exactly how and which processes are represented, and secondly to guarantee physical consistency between the representation of these processes in CCFM and ATHAM. This necessitated the development of a new microphysics framework (detailed in chapter 4) which is now used in both CCFM and ATHAM.

In the aim to achieve the latter goal, the spectrum of cloud sizes and the characteristic properties of these clouds were extracted from large-domain high-resolution simulations and used to investigate the assumptions in the formulation of CCFM, quantify the convection parameterisation's predictive skill, and through this suggest areas of potential improvement in further work. This work was undertaken at the Max Planck Institute of Meteorology, Hamburg and will be detailed in Chapter 6.

Finally in chapter 7 I will present my conclusions, and detail further work I see as naturally following on from this work.

Chapter 2

Background

Atmospheric moist convection describes how vertical transport in the Earth's atmosphere is affected through the buoyancy supplied through surface fluxes and produced by condensation of water vapour. Convection is the primary means of vertical transport of moisture, tracers, momentum and energy (in the form of both latent and sensible heat) in the atmosphere. On large scales, convection is coupled to the meridional Hadley and zonal Walker circulation, variations of which have been linked to the El Nino Southern Oscillation (*Oort and Yienger* [1996]). On smaller length and time scales, convection determines the production of thunderstorms, heavy precipitation and hurricanes (*Bechtold* [2014]). In addition, the formation of clouds is an important feedback mechanism with respect to climate change, because it modulates the Earth's overall albedo and known that clouds respond to climate change. In the most recent IPCC report (*Stocker et al.* [2013]) the feedback mechanism from cloud albedo (and its affect on out-going long-wave radiation) is the most uncertain contribution to the climate sensitivity (i.e. changes of Earth's temperature with e.g. doubling of CO_2 concentration). This is in line with numerous published reports on varying results with different convection models (eg *Senior and Mitchell* [1993]) and affirms the need for better convection parameterization.

The purpose of convection parameterization is to represent convective activity that takes place on length and time-scales not explicitly resolved in numerical simulations, i.e. features which are smaller in size or evolve more rapidly than than the resolution in space and time of a numerical simulation. Due physical limitations on the computing power available current numerical simulations in Global Circulation Models (GCMs) and in Numerical Weather Prediction (NWP) necessitates the need for convective parameterisation and will for decades to come. For example, the current Met Office (NWP) model has horizontal resolution of 17km for global and $1.5 - 4$km national forecasts (*MetOffice* [2014]), whereas individual convective clouds are generally on the scale of $\approx$ 500m for shallow convection and $\approx$ 2km for deep convection (*Rooy et al.* [2013]). The European Centre for Medium-range Weather Forecasts (ECMWF) expects to move to 5km resolution in 2020 (*ECMWF* [2013]) in their GCM, and it is projected that it will be decades before individual clouds will be

represented with high resolution in operational numerical models.

When the first parameterizations were developed roughly 40 years ago (*Manabe and Strickler* [1964], *Kuo* [1965]) the principal reason for needing convection parameterization was to provide a means of removing the conditional (saturated) instability produced in grid-resolved large-scale circulation. The dominant approach in operational Numerical Weather Prediction (NWP) models is to formulate a convection model, which, given the large-scale forcing provided by the global or regional model, calculates the convective activity in the vertical column of computational cells described by a single horizontal grid cell.

The following are required for a complete description of convection (*Arakawa* [2004]): a description of vertical mass transport, vertical distribution of moistening/drying and heating/cooling from convection, generation of water and ice phases (through condensation/evaporation and sublimation), interaction with Planetary Boundary Layer (PBL), interaction with radiation, mechanical interaction with mean flow and inclusion of stochastic effects. Today, there are numerous convective parameterization approaches published in the literature, and although these are all formulated as variations on a small set of basic concepts, there is not yet a single scheme which can accurately describe all the above aspects of convection, and thus they do not work consistently on all length-scales, time-scales and physical conditions. Studying single and multiple interacting convective clouds using high-resolution numerical simulation may shed light on some of these aspects, and will help improve the Convective Cloud Field Model (CCFM).

To put the research of this thesis into context it is necessary to be mindful of the plethora of issues over a range of time and length-scales that are common to many GCMs, and all linked to convection. In particular the diurnal cycle of precipitation is frequently predicted too early in the day (*Dai* [2006], *Dirmeyer et al.* [2012]), which is likely due to convection being triggered too readily. In addition, simulations often have a warm bias (*Kim et al.* [2013]) and moist bias (*Klingaman et al.* [2015]) in tropical conditions at and above the tropopause due to excess detrainment of saturated air, which causes an increased heating through subsidence. Thirdly, most models do not capture the intra-seasonal Madden-Julian Oscillation (MJO), which is a >100km region of organised convection that travels eastwards in the tropics on a time-scale of 30-90 days; (we still lack a theoretical basis for the MJO as it is not predicted by equatorial β-plane shallow equations, see *Matsuno* [1966] and *Wheeler and Kiladis* [1999]). And finally on longer time-scales the issue remains to constrain the impact of cloud feedback processes so that more confident climate predictions may be made. A principally important and poorly constrained process related to atmospheric convection is that of entrainment of atmospheric air into developing convective plumes. *Knight et al.* [2007] found a 30% variation in climate sensitivity across different global climate models, due to the variations in the entrainment coefficient used. In Section 2.2 a brief description of the previous studies on entrainment will be given and outline for this work aims to improve on the current understanding through high-resolution

numerical simulation.

In the following sections the conditions necessary for atmospheric convection to take place are firstly outlined, thereafter a brief overview of approaches to convective parameterisation is given with a detailed description of CCFM, and finally the importance of entrainment parameterisation is discussed.

2.1 Atmospheric conditions for moist convection

Vertical motion in the Earth's atmosphere is characterised by two key properties: the dry and the moist adiabatic lapse rate. Each of these describe how an air parcel cools as it ascends and expands, the former describing an air parcel which is below saturation of water vapour and the latter a parcel exactly at saturation. The difference in lapse rate in these two conditions stems from the extra heat produced as excess water vapour condenses when a parcel at saturation cools, causing the moist adiabatic lapse rate to be warmer, so that the parcel cools less rapidly during ascent. The rate of cooling is important because the temperature together with the pressure determines the density and so the buoyancy of a region of air relative to its environment.

Since pressure (p) generally decreases (due to pressure having to balance the force of gravity) a parcel of air undergoing vertical displacement will change temperature (T) and density even without exchanging heat with its environment. As temperature and pressure change the saturation of water vapour may also be reached which will cause a phase transition and associated heating/cooling from this. For this reason it is generally not very instructive to compare directly the state between two regions in terms of temperature and water vapour concentration. Instead it is convenient to formulate variables which are conserved (i.e. stay unchanged) during atmospheric motion and phase transitions so that two regions at different heights in the atmosphere may be directly compared and through this facilitate analysis of atmospheric convection.

One such variable is the "(dry) potential temperature" θ which is formulated to be constant during sub-saturated (dry) adiabatic ascent (no phase transitions or change in internal energy through heat exchange, radiation, mixing with the environment) and is formally defined as the temperature a parcel of air would have if its pressure p was changed adiabatically to some reference pressure p_θ:

$$\theta = T \left(\frac{p_\theta}{p} \right)^{\frac{R}{c_p}},$$

where R is the gas constant and c_p the heat capacity of the mixture respectively.

We may similarly define the liquid potential temperature (θ_l) which is unchanged under condensation of water vapour into liquid, assuming that this liquid does not precipitate

out (which of course in reality it would, and so with high rain-out this variable is only approximately conserved)

$$\theta_l = T \left(\frac{p_\theta}{p} \right)^{\frac{R_l}{c_l}} exp \left(-\frac{q_l L_v}{c_l T} \right),$$

where $R_l = q_d R_d + q_t R_v$ and $c_l = c_{p,d} q_d + c_{p,v} q_t$.

Given these definitions it is instructive to visualise convective processes by forming a thermodynamic diagram (such as the Tephigram in figure 2.1) with isolines of temperature, potential temperature, and liquied water potential temperature plotted against temperature (and thus altitude), as these lines describe the thermodynamic trajectories (in terms of temperature at a given pressure, i.e. height) that parcels would follow during dry (constant θ) and moist adiabatic (constant θ_l) ascent.

The diagram in addition contains lines describing the saturation water vapour specific mass at a given temperature and pressure. A specific vertical atmospheric profile may then be studied by plotting as a function of height (pressure) the temperature and moisture content and thus the proximity of the temperature (solid red) and moisture (solid green) lines provide a direct visualisation of the relative humidity. In figure 2.1 an idealised atmospheric profile prone to produce shallow convection has been plotted. This was created by forming a profile which contains two distinct regions characteristic of moist convection:

1. A well-mixed boundary layer near the surface, mixed through dry convection, within which the water vapour specific mass and potential temperature are thus approximately constant. This layer is formed through the heat and moisture fluxes from the Earth's surface and thus grows and decays over the diurnal cycle as insolation varies.

2. A conditionally stable layer above the boundary layer, thus only unstable to moist convection.

By considering individual parcels of air with slightly perturbed heat ($c_p \Delta T$) and moisture (Δq_v) content originating at the surface, and plotting the evolution of such a parcel in a Tephigram (an example is given as the grey line in figure 2.1), one may predict three key heights which are of interest to moist convection: the height at which condensation is likely to occur, the height at which convection is self-supporting and the height at which the convective cloud stops growing vertically. This can be estimated by "lifting" a parcel of air by reducing its temperature dry-adiabatically, reducing pressure until the saturation is reached. This height is typically denoted the Lifting Condensation Level (LCL) or Cumulus Condensation Level (CCL). As the parcel's pressure is further reduced, its temperature will fall with the moist adiabatic lapse rate due to the condensation of excess water vapour. Due to cooling the parcel is typically heavier than its environment

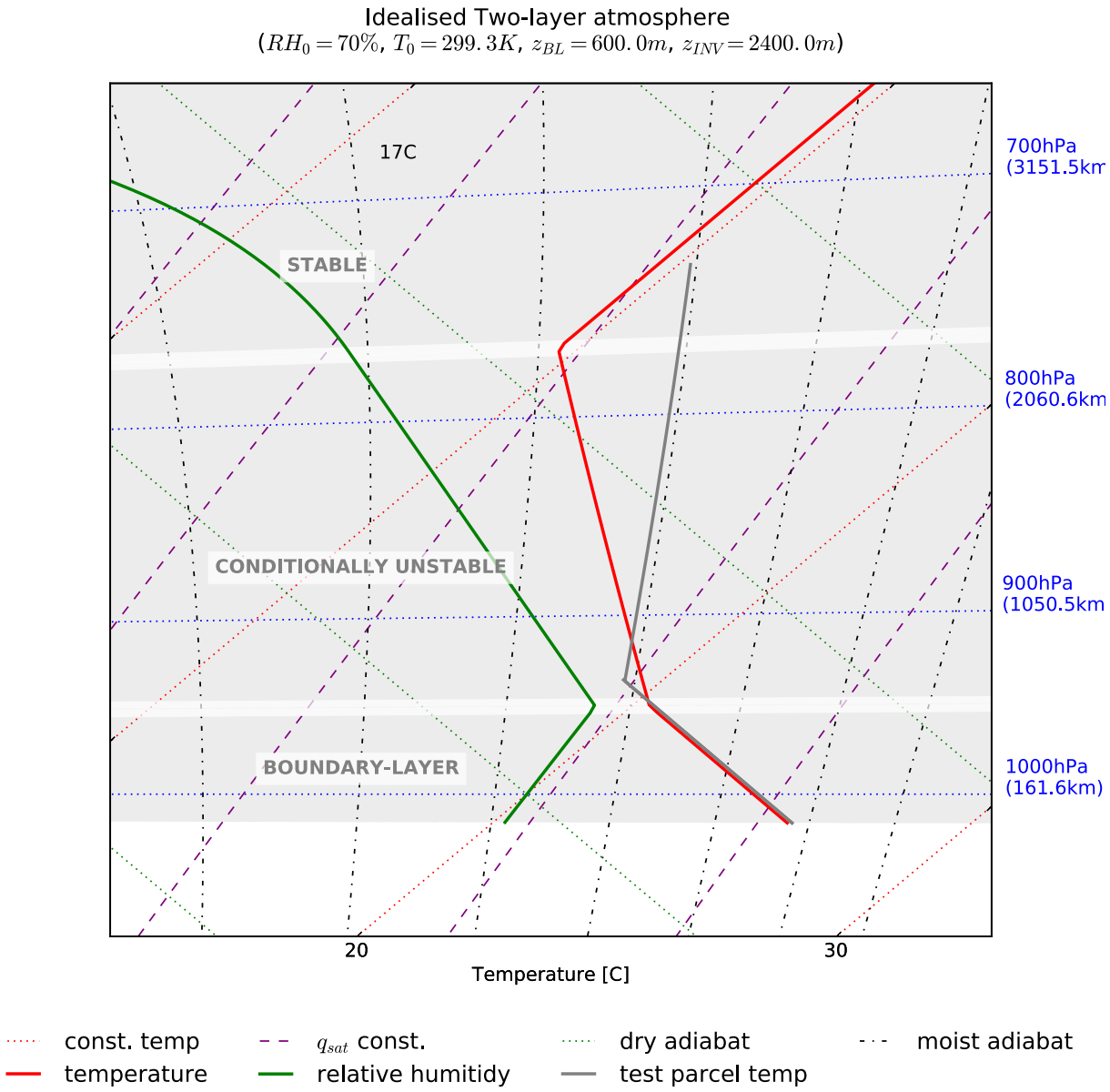

Figure 2.1: Tephigram of an idealised atmospheric profile characterisic of shallow moist convection, comprised of a well-mixed boundary-layer (constant moisture and dry-adiabatic lapse-rate), a layer with conditional instability (lapse-rate between dry and saturated) and a capping isothermal layer on the top. In grey is given the temperature evolution of a parcel of air with increased temperature and moisture originating at the surface.

when the LCL is reached, however above this height its temperature will cool more slowly than the environment and if the parcel has enough vertical momentum it will eventually reach the same density as the environment at the Level of Free Convection (LFC), above which at stays buoyant until it hits the stable layer above and its density once again equilibrates with the environment at the Equilibrium Level (EL) or sometimes called Level of Neutral Buoyancy (LNB).

The vertical distance below the LFC may be viewed a potential barrier that the parcel must overcome, its momentum working against the deceleration from gravity due to its heavier density than the environment. Similarly above the LFC the parcel will be accelerated by its postive buoyancy, gaining kinetic energy the further it rises. The amount of kinetic energy required below and supplied above the LFC are typically denoted the Convective Inhibition (CIN) and Convectively Available Potential Energy (CAPE) and may be quantified by vertically integrating the acceleration as given by Archimedes' principle, so that per unit mass they are respectively

$$e_{CIN} = \int_{z_{LCL}}^{z_{LFC}} \frac{\rho_e - \rho_c}{\rho_e} g \, dz, \quad e_{CAPE} = \int_{z_{LFC}}^{z_{EL}} \frac{\rho_e - \rho_c}{\rho_e} g \, dz.$$

Both e_{CIN} and e_{CAPE} may be related to the cloud's vertical velocity by considering the equivalent kinetic energy per unit mass. In this context convective inhibition (CIN) predicts a minimum vertical velocity that a parcel must have at the LCL to overcome the CIN, and convective available potential energy the vertical velocity attained once all CAPE has been consumed.

$$e_{CIN} = \frac{1}{2} w_{CIN}^2 \Rightarrow w_{CIN} = \sqrt{2 e_{CIN}}, \quad e_{CAPE} = \frac{1}{2} w_{CAPE}^2 \Rightarrow w_{CAPE} = \sqrt{2 e_{CAPE}}.$$

These estimates are purely based on the parcel's thermodynamic properties and do *not* take into account any dynamical processes (such as finite kinetic energy gained from rising a given distance to the LCL and loss of kinetic energy from mixing with environmental air), but may serve as a useful first-order measure of the relevant vertical velocities. By varying the perturbations in temperature and moisture (ΔT, Δq_v) and for each pair of values adiabatically lifting a parcel from the surface it is possible to calculate (from a purely thermodynamical point of view) what the CIN for a given parcel is, and so the minimum required vertical velocity required at the LCL. In Figure 2.2 this minimum vertical velocity has been plotted for different parcels lifted in a synthetic atmospheric profile characteristic of shallow convection (the details of how this profile was constructed will be given in 5.1.2), and thus represents the possible relative trade-off between vertical momentum, temperature and moisture content possible while still causing convection. This lifted-parcel approach to predicting the height at which convection takes place forms the basis for the first-order model of the necessary perturbations that should be introduced in LES simulations to initiate moist convection in a given environmental profile, and thus

is a valuable tool in restricting the parameter space (as will be discussed in Secion 5.1.3). In addition the figure appears to contain lines of constant w_{CIN} the slope of which would indicate the relative importance of moisture and potential temperature in overcoming CIN, which for the given profile is that $\frac{d\Delta q_v}{d\Delta T}\Big|^{parcel}_{w_{CIN}=const} \approx 1.8 g/kg/K$.

By varying the parcel's moisture and heat content the exact moist adiabat the parcel evolves along once saturation is reach will change and so the equilibrium height (EL, once the inversion/isothermal layer above is reached) will change. In the given example contours of constant height follow $\frac{\Delta q_v}{\Delta \theta} \approx 1.3 g/kg/K$.

$z_{bl} = 600.0m$, $RH_0 = 70\%$, $T_0 = 299.3K$, $p_0 = 101686.0Pa$, $w_0 = 1.68m/s$

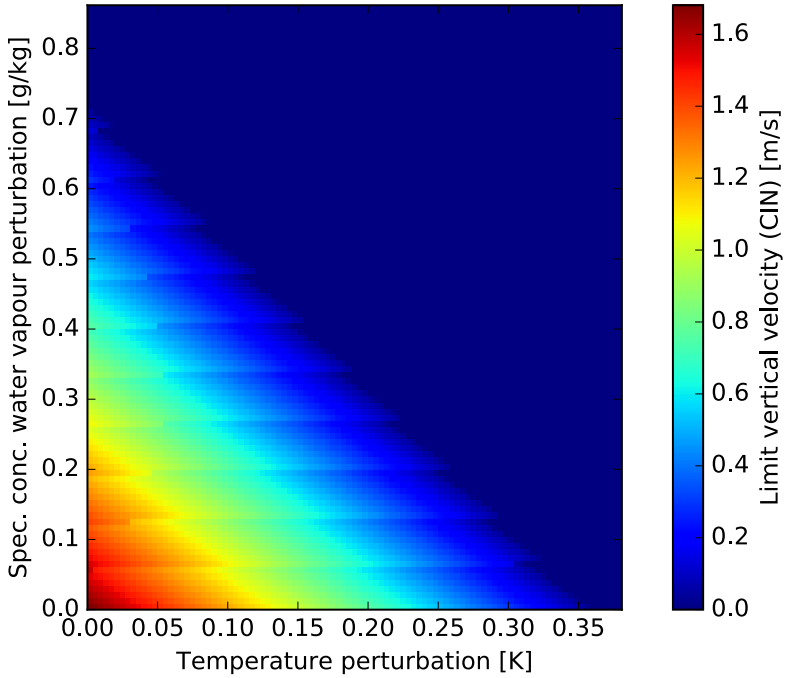

Figure 2.2: Heatmap plot showing the minimum necessary vertical velocity to overcome the potential barrier of the convective inhibition for different perturbations in moisture and temperature. The plot clearly shows the possible trade-off for creating convection between increasing heat, moisture or vertical momentum for a parcel of air. It is instructive to note that the limit values suggest that a bubble with either $\approx 0.7 g/kg$ extra moisture, $0.36K$ warmer or with a vertical velocity of $\approx 1.7 m/s$ would lead to convection. Note however that this model does *not* take into account any dynamical effects such as drag and entrainment, and so *actual* values are somewhat larger (as will be discussed below).

The primary limitation of this approach is that it firstly does not capture the dynamic behaviour of the air parcel, i.e. does not take into account the finite time and so finite acceleration that the parcel would undergo under ascent (reducing the effective CIN), and secondly it does not include any dilution (through entrainment) of the ambient air which would retard its vertical motion (increasing the effective CIN).

The process of determining when convection is likely to take place and at which height the clouds will form is called the *convective trigger*. This component is crucial in all convective parameterisations and is an active field of research in its own right. To simulate individual clouds with high-resolution simulations it was necessary to assert the main

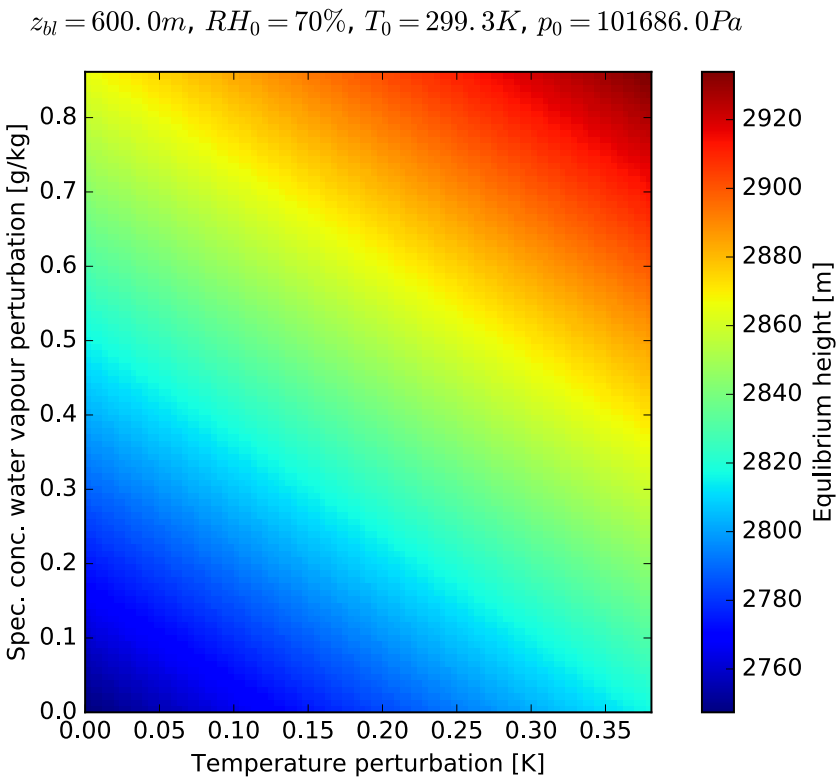

Figure 2.3: Heatmap plot showing height where lifted parcel reaches same density as environment (equilibrium level EL). The contours of constant height follows $\frac{\Delta q_v}{\Delta \theta} \approx 1.3 g/kg/K$.

principles of this as will be discussed in Section 5.1.3. Finally characteristic properties of the boundary-layer for shallow convection will be discussed in Section 6.3.7.

2.2 The importance of entrainment

Entrainment in the context of moist atmospheric convection describes the mixing of air from the environment into a convective cloud. This air dries the cloudy air (by virtue of having below-saturation relative humidity) and typically cools the cloud, too, by mixing in colder air. Both effects cause to retard the cloud's vertical growth by removing (potential) buoyancy produced by the latent heat of condensation.

The need for considering the entrainment of ambient air was first described by *Stommel* [1947], who observed that calculating the saturated ascent of a buoyant parcel alone (as was done in Section 2.1) leads to cloud top heights far in excess of observation. Considering a parcel of cloudy air of mass m, the only contribution to change the mass is through entrainment of ambient air[1]. The fractional change of total mass with height will be denoted as the entrainment rate μ[2] as

$$\mu = \frac{1}{m}\frac{dm}{dz}.$$

Drawing on water-tank laboratory experiments and accompanying similarity theory for buoyant plumes and jets (*Morton et al.* [1956], *Turner* [1962], *Turner* [1963]), *Simpson and Wiggert* [1969] prescribed the entrainment rate to have the following form:

$$\mu = \frac{\beta}{r},$$

where β is called the entrainment coefficient, and was determined experimentally (*Turner* [1962] estimated $\beta \approx 0.2$). This model will from herein be denoted the Morton-Turner model of entrainment. The Morton-Turner model is derived by assuming that the amount of entrainment, the mass flux across the cloud edge, is proportional to relative magnitude of the velocity between the interior of the buoyant plume and the surroundings. By assuming that the environment is stationary and so unperturbed by the rising cloud the entrainment is assumed to be proportional to the vertical velocity inside the rising cloud. That the entrainment rate has this form may be argued by geometrical means by noticing that the ratio of the plume circumference to the cross-section at a given height is inversely proportional to radius, and so the rate of dilution of the cloud will decrease as plume volume grows faster than the plume boundary with increasing radius.

In the context of convection parameterisation (see next section for a detailed review) the Morton-Turner model has been applied by using it for describing the entrainment into a single "bulk plume" which represents the collective convective transport of a whole

[1] In this work only *net* entrainment is considered, so that detrainment is considered as a negative contribution to entrainment

[2] The entrainment rate is here defined in terms of mass of the cloud parcel (m), but can equally be written in terms of the total mass-flux (M) through a plume cross-section, which can be seen from the detailed discussion in Appendix .1. Both formulations will be used where relevant in this work

ensemble of clouds in one grid cell. The principle challenge then becomes to define the entrainment rate for this *bulk plume* so that this single plume may represent the convective activity of the full cloud ensemble. The difficulty in attaining this is exemplified by *Knight et al.* [2007] who found a 30% variation in climate sensitivity across different global climate models due to the variations in the entrainment coefficient used.

Attempts have been made to extend or replace the Morton-Turner model, by parameterising entrainment as function of the ambient potential temperature (*Gregory* [2001]) and relative humidity (*Bechtold et al.* [2008], constituting the ECMWF operational model since 2010). However these entrainment models are largely bulk models, representing entrainment on the whole for a large number of convective clouds, and thus are optimized for use with bulk convection schemes (as will be described in the next section).

That more research into the nature of entrainment (both with respect to individual and ensembles of clouds) is needed is emphasised by a recent review (*Rooy et al.* [2013]), stating that "the nature of these mixing processes is still an active field of research and their parameterization is still in its infancy." The authors urge the use of high-resolution modelling to gain better understanding of cloud mixing processes.

In this work the aim is to study the extent to which the Morton-Turner model should be extended or modified when applied to individual moist convective clouds. This will be a continuation of work by *Arnold* [2010] (under the supervision of Dr. Herzog), which noted better agreement between CCFM's 1D cloud-model and LES simulations of individual clouds when the entrainment coefficient was made dependent on the vertical velocity at a given height, cloud-base radius and cloud-base vertical velocity. It is my primary aim to investigate these findings and to justify or amend this model using physical arguments.

2.3 Approaches to convective parameterisation

With the exception of the historic convection models based around moisture budgets (e.g. *Kuo* [1965]) and atmospheric adjustment to neutral stratification (*Manabe and Strickler* [1964]), most contemporary convection models are so-called "mass-flux" models (first put forward by *Arakawa and Schubert* [1974]). The principle assumptions are that:

1. Any convective instability produced by large-scale circulation and/or radiation is quickly (on the time-scale of the host model) consumed by convective activity. This means that the Convectively Available Potential Energy (CAPE) may be assumed to be near constant. This is the quasi-equilibrium assumption.
2. The convective vertical motion up is concentrated in clouds of small cross-section compared to the distance between individual clouds, and the large-scale subsidence of the environment is spread over a large area (so that the fractional cross-section of clouds $\sigma \ll 1$).

3. Convective clouds may be described as rising plumes of convective activity, all starting from the same cloud-base height (and are often represented by a single *mean* bulk cloud).

There are two principal types of mass-flux models: (1) bulk models (*Tiedtke* [1989], *Kain and Fritsch* [1990]), which represent the convection motion in a single grid-cell using a single cloud describing the mean cloud development, and (2) spectral models (*Arakawa and Schubert* [1974], *Donner* [1993], *Naveau and Moncrieff* [2003], *Wagner and Graf* [2010]) which resolve a spectrum of interacting (through modifications to their shared environment) clouds in a grid-cell. In this sense CCFM is a *spectral* model, representing different clouds over a range of sizes. An important component of the CCFM model is the cloud model, which represents the evolution of a single cloud in isolation, not taking into account interactions with other clouds. As my initial aim is to improve on this cloud model I will also give a detailed description of it below.

Although the scientific community has, through the established use of mass-flux based convection schemes, largely settled on a steady-state plume description of convective clouds, a recent review (*Yano* [2014]) indicates that this description may not fit all situations of convection. Of particular concern is the observation that shallow cumulus clouds have small height-to-width aspect ratios thus not resembling plumes, and even large cumulonimbus clouds have been observed (*Rooy et al.* [2013]) to be made up of collections of smaller, individual rising thermals, successively rising further, thereby contesting the assumption of a vertically uniform plume. In this regard the study of convective clouds using high-resolution numerical simulation may be viewed as a tool for investigating the transient and multi-scale composition of a convective cloud. This will be investigated by firstly quantifying the extent of the transient nature both when simulating individual convective clouds in Chapter 5 and analysing large-domain simulations of multiple interacting convective clouds in Chapter 6.

Finally no convection scheme to date takes into account the processes of windshear (which is likely to enhance entrainment) and mesoscale aggregation (promoting and suppressing convection locally), both of which have been observed (*Schumacher and Houze* [2006], *Bony et al.* [2015]) to greatly influence convective activity.

2.3.1 Convective Cloud Field Model (CCFM)

The Convective Cloud Field Model (CCFM) parameterizes the statistical effects of convection by representing the convective activity of an ensemble of interacting cumulus clouds. The model is based on the Arakawa & Schubert mass-flux model (*Arakawa and Schubert* [1974], denoted AS74 from here on), however it differs in the calculation of the mass-flux and in the closure assumption (defining the statistics of a system with large dimensions, e.g., many clouds). The AS74 convection scheme calculates a spectrum of mass-fluxes,

which leads to a lack of information about cloud dynamics and microphysics. CCFM instead calculates the distribution of clouds into different sizes (the cloud spectrum), each cloud being described by the same cloud model. Closure in AS74 is based on defining the cumulus strength by relating the cloud-base mass-flux to the large-scale forcing,

whereas CCFM calculates the convective activity by integrating the effect of the full ensemble of clouds predicted to exist. The cloud ensemble is predicted by solving a population-dynamics Lotka-Volterra system of equations, which describes a competitive system of interacting species (here clouds compete for atmospheric potential energy available for convection).

By simulating individual clouds, the vertical profiles of cloud radius (r), vertical velocity (w), density(ρ), temperature (T) and water species (q_l, q_v ...) are known for each cloud (instead of only the profile vertical mass-flux ($\pi r^2 w\rho$) for a single "mean" cloud), which enables:

- representation of microphysics with cloud-aerosol interaction
- representation of mixed-phase processes and precipitation as accurately as representation of the micro-physical processes (condensation, rain formation, etc) is possible
- a more physical treatment of entrainment/detrainment by considering its behaviour for individual clouds
- improved vertical transport of water vapour, energy and chemical tracers, by e.g. predicting detrainment at different heights for different cloud sizes (based on the cloud-top height) instead of single height (as would be predicted by a *bulk plume* model)
- improved cloud-cover estimates (usually, incorrectly, assumed to be zero in contemporary convection schemes), by taking the combined effect of all cloud-types present

CCFM consists of the following steps:

1. Calculate the vertical structure of each cloud type (denoted by radius at cloud base) using the cloud model (described in detail in the next section) and the ambient environment as given from the host model.
2. Calculate for each cloud type how the presence of this cloud will affect the environment temperature and moisture content.
3. Calculate cloud spectrum by solving a Lotka-Volterra system of interacting clouds. This is formulated by considering how the presence of one cloud type affects another, combined with how large-scale forcing will tend to produce a particular cloud type.
4. Having calculated the cloud spectrum, the changes to ambient state are fed back to the host model.

In Chapter 3 background on and improvements to the CCFM cloud-model will be discussed. The microphysics representation therein is described in Chapter 4, and high-resolution simulations and analysis to improve the cloud-model's representation of entrainment is presented in Chapter 5. Finally the cloud spectrum is studied through multi-cloud simulation and analysis in Chapter 6.

Chapter 3

1D Cloud-model

A principal component of the Convective Cloud Field Model (CCFM) is the cloud-model, which produces the vertical structure of individual convective clouds. There are three elements to the CCFM cloud model: the model equations, the boundary conditions for integrating these equations and the numerical algorithm implemented to integrate the model equations.

As part of this study the cloud-model equations were, firstly, re-derived based on first-principles and the conservation of mass, momentum and energy. The purpose of this was to:

- aide the analysis of the relative importance of different terms in the model equations, so that, for example, the entrainment term can be clearly distinguished from parameterised drag or "virtual mass" (as will be discussed below)
- create an energetically self-consistent formulation of the thermodynamic equation
- remove approximations often casually employed in meteorological formulations, such as the use of virtual temperature in the buoyancy formulation, casual substitution of specific concentrations with mixing ratios (mass fractions defined relative to the mixture or dry air mass respectively) and negligence of the effect of present water vapour when calculating the mixture heat capacity.

A detailed derivation and discussion of the model equations will be given in section 3.1.

The boundary conditions for integrating the cloud equations are provided in part by the environmental state within which the convective cloud develops, and partly by the properties at the base of the cloud (as the cloudy parcels are assumed to all originate from cloud-base). The environmental state is provided by the host model. In the current formulation the cloud-base conditions are estimated using the environmental state in the lower near-ground part of the atmosphere as will be detailed in Section 3.2.1.

Secondly, the existing numerical integration algorithm was replaced, as a number of shortcomings in the existing implementation for the model integration have been identified,

in particular with respect to its effect on the cloud hydrometeors (by assuming instantaneous formation of cloud-droplets from supersaturation). Here the aim was to:

- create a clear modular separation of the algorithm which implements the mathematical formulation of equation integration. This allows that different integration approaches (e.g. Forward/Backward-Euler, Runga-Kutta, etc.) may be introduced and their effect contrasted. In addition, the different integration algorithms may be tested in isolation and their numerical stability may be verified.
- remove any operator splitting (in effect the order of integration) so that each physical process (entrainment, microphysics, dynamics, etc.) is given the same priority and the final in-cloud state is not affected by the order of the individual parts in integration approach.

This work was undertaken in parallel to replacing the microphysics model in CCFM and ATHAM (which is discussed in Chapter 4), and the specific details relating to CCFM are described in Section 3.3 together with a detailed discussion of the shortcomings overcome. The final part of this work regarding the CCFM cloud-model has been to test the assumptions and predictions of CCFM, when applied to the case of shallow convection, by analysing high-resolution simulations of a large-area ($50km \times 50km$) domain within which there is a multitude of developing convective clouds. This work will be detailed in Chapter 6.

As a brief overview the components of the cloud-model equations are given in figure 3.1 which includes references for each component. Section 3.1 contains detailed derivations of each of the conservation equations including references to previous work where relevant. In Section 3.2 the boundary and initial conditions (i.e. the environment and cloud-base conditions, respectively) are introduced and their physical interpretation is discussed. Finally, in Section 3.4 the sensitivity to the input parameters (drag, entrainment, rain-out, etc) of the profiles predicted to the cloud-model is studied with the aim to study the physical limitations of the cloud-model and provide insight into the balance of physical influences which dominate the vertical structure of convective clouds under different conditions.

3.1 Cloud-model equations

This section gives a detailed derivation of the new formulation of the cloud-model equations for the cloud-model used in CCFM. For completeness, detailed differences between cloud-models ancestral to the CCFM cloud-model are included.

On the matter of notation, dry-air variables will be denoted by subscript d (e.g. specific concentration of dry air is q_d) and the three phases of water will be denoted by subscript

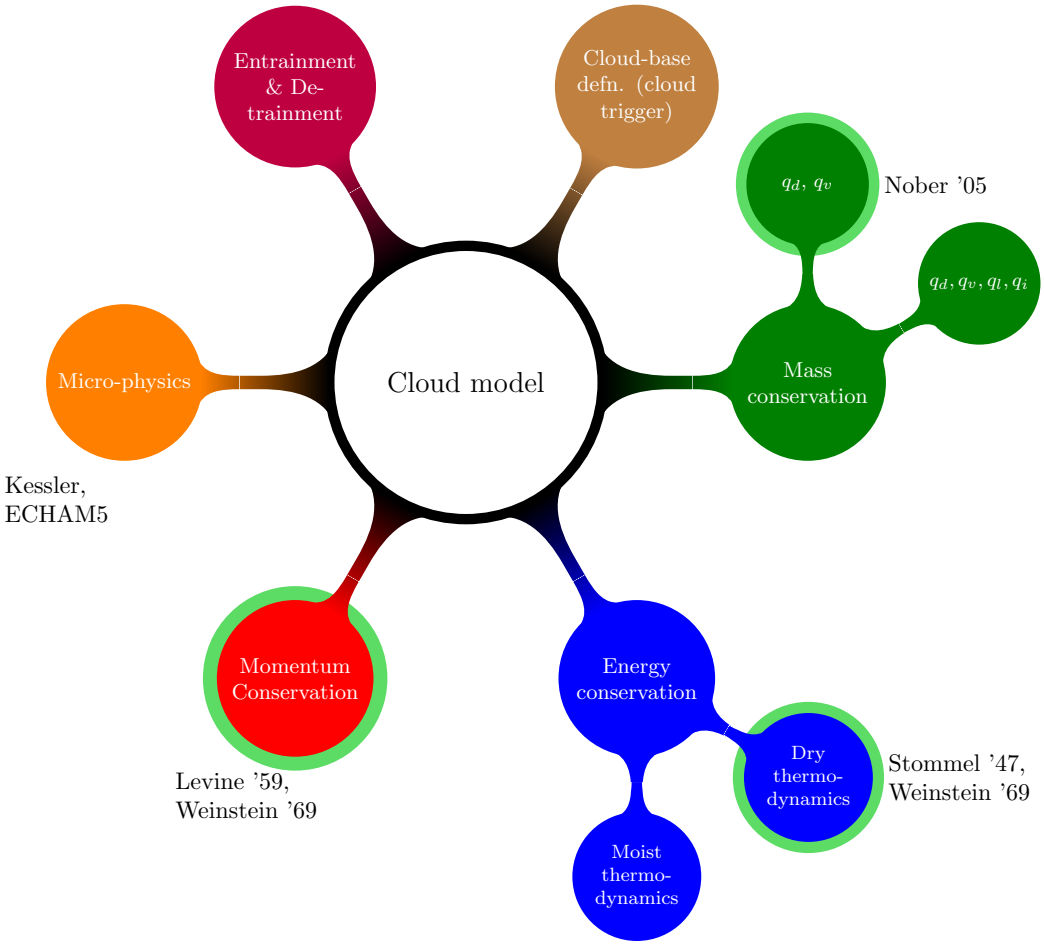

Figure 3.1: Overview of components of the 1D entraining parcel cloud-model including references to the literature

v for water vapour (q_v), l for liquid water (q_l) and i for ice (q_i). Depending on the microphysics implementation used (see Chapter 4) each of the water phases may be partitioned into different forms of hydrometeors (e.g. rain and cloud-water droplets for liquid water); for brevity these hydrometeor species will be grouped by water phase (as for example rain and cloud-droplets are assumed to behave identically thermodynamically and have the same density even though the former falls through the cloud as the latter will stay aloft, which is an effect of their relative size). To separate in-cloud and environment state variables, the in-cloud variables will be denoted by subscript c and the environment variables by subscript e, i.e. the in-cloud and environment temperatures are given as T_c and T_e respectively. Where subscripts are already used, e.g. to denote different phases of water when considering the specific concentration q, the in-cloud and environment are distinguished using subscript ",c" and ",e" respectively (e.g. for water vapour $q_{v,c}$ and $q_{v,e}$).

The cloud model within CCFM is used to represent each cumulus cloud that may develop within **the vertical column of single horizontal grid cell** of the host model. The model is based on work by *Simpson and Wiggert* [1969], and assumes that:

- The cloud does not change over the time-step of the host model (order of 10min for e.g. the ECHAM Global Circulation Model (*Rast et al.* [2013]). This allows for the formulation of steady-state equations (as mentioned in Section 2.3 this may not actually be an applicable assumption, however this will be discussed in later chapters)

- Clouds are horizontally homogeneous enough that they can be satisfactorily described by a single horizontal mean value at a given height for each cloud variable. This allows the set of model equations to only describe the cloud structure in the one-dimensional vertical direction.

- The cumulus cloud has the structure of a buoyant plume so that the buoyant updraft can be described as being diluted by the mixing (entrainment) of ambient air through the boundary of the cloud. This allows parallels to be drawn to previous work on buoyant plumes in other environments, so that the degree of entrainment can be parameterized. This will be discussed in detail below.

- The height at which a cumulus cloud develops in a given atmospheric environment may be described by the Lifting Condensation Level (LCL), the height at which a parcel from ground level lifted adiabatically reaches saturation. This is called the cloud base.

- The presence of the cumulus cloud does not substantially affect the environment, so the steady-state system can describe continuously rising parcels of saturated air from cloud base.

- Any precipitation produced in the cloud does not fall through the cloud and affect the composition, momentum and thermodynamic state below. This assumption is made so that the cloud equations may be developed by only considering mass-flux upwards and allow for integration of the equations in this direction. This assumption should be relaxed in future work as for example rain will in a real cloud fall through the cloud.

- The environment of the cloud is assumed to be at rest. The presence of down-drafts (as have been observed in LES by [*Heus and Jonker*, 2008]) would invalidate this assumption and the implications of this assumption should therefore be studied in further work.

The model consists of a system of Lagrangian one-dimensional equations describing the steady-state structure of a cumulus cloud, i.e. the vertical change with height of cloud radius, vertical velocity and temperature. These equations are developed from the conservation mass, momentum and energy and their derivation will be given in the following sections individually. In the following sections the conservation equations for each will be derived.

The original cloud-model of CCFM ([*Wagner*, 2009]) made a number of simplifying assumptions:

1. The rising parcel of cloudy air was assumed to be a at saturation (with respect to water or ice depending on the in-cloud temperature), thus fixing the parcel to the saturated moist lapse rate and thereby implying instantaneous condensation of water vapour in excess of saturation (and causing instantaneous heating) and therefore not allowing the presence of super- or sub-saturation.

2. Cloud droplets which transformed into rain were not removed, causing the mixture heat capacity and potential for re-evaporation of rain to be too high. Rain should instead be removed, making the parcel's thermodynamic evolution *pseudo-adiabatic* instead of *reversible*-adiabatic (i.e. irreversible because of the removal of rain)

These were in part addressed in recent work by *Cao* [2015], where in addition extensions for midlevel convection and the parameterisation of entrainment by windshear were attempted. Finally a different approach for defining the cloudbase conditions (which will be discussed in 3.2.1) was implemented.

3.1.1 Conservation of mass

Consider a fully-developed cumulus plume which has reached a steady-state, so that the cloud-radius (r) of the plume at a given height (z) does not change with time. The plume radius may however change with height as a parcel of the moist plume air rises

and interacts with the environment. Assuming a circualr horizontally homogeneous state through the cloud at a given height, we define the mass-flux per unit area (j) and total mass-flux (M) over the whole cross-section of the rising cloud plume as

$$j = \rho_c w, \tag{3.1}$$
$$M = \pi r^2 j = \pi r^2 \rho_c w, \tag{3.2}$$

where ρ_c is the in-cloud density and w the vertical velocity.

To find how the the cloud-radius changes with height, we isolate the cloud-radius and differentiate with respect to height

$$\begin{aligned} \frac{1}{r^2}\frac{d}{dz}\left(r^2\right) &= \frac{1}{r^2}\frac{d}{dz}\left(\frac{M}{\pi\rho_c w}\right), \\ \frac{2}{r}\frac{dr}{dz} &= \frac{1}{M}\frac{dM}{dz} - \frac{1}{w}\frac{dw}{dz} - \frac{1}{\rho_c}\frac{\rho_c}{dz}. \end{aligned} \tag{3.3}$$

It is clear from the above equation that the cloud radius is changed by three contributions, which are: vertical variation in total mass-flux, vertical velocity and in-cloud density.

Considering two consecutive cross-sections with a vertical spacing Δz conservation of mass requires that the total mass-flux can only be changed by mass-exchange with the environment over the distance Δz. The rate at which mass is contributed to the plume by the environment is called the *entrainment rate* μ, which is given as

$$\mu = \frac{1}{M}\frac{dM}{dz}.$$

To define the vertical variation in cloud-density, we assume that the in-cloud air is in pressure equilibrium with the environment $p_c = p_e$, both of which are assumed to be in hydrostatic equilibrium. Therefore,

$$\frac{dp}{dz} = -\rho_c g = -\rho_e g.$$

This effectively assumes that $\rho_c = \rho_e$, which is not generally true, but the difference in density is neglected when enforcing the pressure balance (and only included in the buoyancy-term of the momentum equation; in effect this is the commonly employed so-called *Boussinesq* approximation).

Finally we must choose an equation of state to close the system, so that we can relate the assumed vertical change in pressure and unknown density to the known in-cloud temperature.

In the original model by *Levine* [1965] (and the model employed by *Wagner* [2009]) only dry air is considered in the cloud thermodynamics, and so we use the ideal gas equation of state,

$$p = \rho_c R_d T_c = \rho_{d,c} R_d T_c,$$

where $\rho_{d,c}$ is the in-cloud dry-air concentration (i.e. $\rho_c = \rho_{d,c}$). Isolating the in-cloud density and taking the derivative with respect to height we have

$$\begin{aligned} \frac{1}{\rho_c}\frac{d\rho_c}{dz} &= \frac{1}{p}\frac{dp}{dz} - \frac{1}{T_c}\frac{dT_c}{dz} \\ &= -\frac{\rho_c g}{p} - \frac{1}{T_c}\frac{dT_c}{dz} \\ &= -\frac{g}{R_d T_c} - \frac{1}{T_c}\frac{dT_c}{dz}, \end{aligned} \tag{3.4}$$

and so the mass continuity equation (when only considering dry air) becomes:

$$\frac{2}{r}\frac{dr}{dz} = \left(\frac{g}{R_d T_c} + \frac{1}{T_c}\frac{dT_c}{dz}\right) - \frac{1}{w}\frac{dw}{dz} + \frac{1}{M}\frac{dM}{dz}$$

In recent work by *Cao* [2015] the water-content of the cloud-plume has been included in the model thermodynamics and so must also be included in the mass-continuity equation for consistency.

We wish to write an equation of state for the mixture within the cloud. To do this we assume that dry air and water phases (gasses) are uniformly distributed and occupy the volume $v_g = v_d + v_v$ together (where v_d and v_v are the volumes occupied by dry air and water respectively). The mixture equation of state is (subscript c has been dropped for brevity because all variables are in-cloud variables):

$$
\begin{aligned}
\rho^{-1} &= \sum_{n \in N_{phases}} \frac{q_n}{\rho_n} \\
&= \frac{q_d}{\rho_d} + \frac{q_v}{\rho_v} + \frac{q_l}{\rho_l} + \frac{q_i}{\rho_i} \\
&= \frac{m_d/m}{m_d/v_d} + \frac{m_v/m}{m_v/v_v} + \frac{q_l}{\rho_l} + \frac{q_i}{\rho_i} \\
&= \frac{\cancel{m_d}/m}{\cancel{m_d}/v_d} + \frac{\cancel{m_v}/m}{\cancel{m_v}/v_v} + \frac{q_l}{\rho_l} + \frac{q_i}{\rho_i} \\
&= \frac{v_d}{m} + \frac{v_v}{m} + \frac{q_l}{\rho_l} + \frac{q_i}{\rho_i} \\
&= \frac{v_g}{m} \frac{q_d R_d + q_v R_v}{q_d R_d + q_v R_v} + \frac{q_l}{\rho_l} + \frac{q_i}{\rho_i} \\
&= \frac{q_d R_d + q_v R_v}{\frac{\cancel{m}}{v_g}\frac{m_d}{\cancel{m}} R_d + \frac{\cancel{m}}{v_g}\frac{m_v}{\cancel{m}} R_v} + \frac{q_l}{\rho_l} + \frac{q_i}{\rho_i} \\
&= \frac{q_d R_d + q_v R_v}{\frac{m_d}{v_g} R_d + \frac{m_v}{v_g} R_v} + \frac{q_l}{\rho_l} + \frac{q_i}{\rho_i}
\end{aligned}
$$

Assuming that the dry air and water vapour occupy the volume v_g together and treating each as an ideal gas, we may write each the equation of state as

$$
p_d = \frac{m_d}{v_g} R_d T, \quad p_v = \frac{m_v}{v_g} R_v T.
$$

Note that the density here is calculated relative to the volume occupied by the gasses (and not the total mixture), and so the finite volume of the condensates has been taking into account.

With the above expressions the mixture equation of state becomes:

$$
\begin{aligned}
\rho^{-1} &= \frac{q_d R_d + q_v R_v}{\frac{m_d}{v_g} R_d + \frac{m_v}{v_g} R_v} + \frac{q_l}{\rho_l} + \frac{q_i}{\rho_i} \\
&= \frac{q_d R_d + q_v R_v}{\frac{p_d}{T} + \frac{p_v}{T}} + \frac{q_l}{\rho_l} + \frac{q_i}{\rho_i} \\
&= (q_d R_d + q_v R_v) \frac{T}{p_d + p_v} + \frac{q_l}{\rho_l} + \frac{q_i}{\rho_i} \\
&= (q_d R_d + q_v R_v) \frac{T}{p} + \frac{q_l}{\rho_l} + \frac{q_i}{\rho_i},
\end{aligned} \tag{3.5}
$$

where in the last step we have employed Dalton's law of partial pressures, assuming that the condensate phases do not contribute to the pressure (i.e. are incompressible so that $p = p_d + p_v$).

It is instructive to re-order this equation to isolate the pressure term:

$$
\begin{aligned}
\Rightarrow \frac{T}{p} &= \left[\frac{1}{\rho} - \frac{q_l}{\rho_l} - \frac{q_i}{\rho_i}\right] \frac{1}{R_v q_v + R_d q_d} \\
&= \left[\frac{q_d}{\rho_d} + \frac{q_v}{\rho_v}\right] \frac{1}{R_v q_v + R_d q_d} \\
&= \left[\frac{\cancel{m_d}/m}{\cancel{m_d}/v_d} + \frac{\cancel{m_v}/m}{\cancel{m_v}/v_v}\right] \frac{1}{R_v q_v + R_d q_d} \\
&= \frac{v_d + v_v}{m} \frac{1}{R_v q_v + R_d q_d} \\
&= \frac{v_d + v_v}{m_d + m_v} \frac{m_d + m_v}{m} \frac{1}{R_v q_v + R_d q_d} \\
&= \frac{v_d + v_v}{m_d + m_v} \frac{q_v + q_d}{R_v q_v + R_d q_d} \\
\Rightarrow p &= \frac{m_d + m_v}{v_d + v_v} \frac{R_v q_v + R_d q_d}{q_v + q_d} T \\
p &= \rho_g R^* T, \qquad (3.6)
\end{aligned}
$$

where $R^* = \frac{R_v q_v + R_d q_d}{q_v + q_d}$ may be viewed as the effective gas constant for the mixture and **note** that the gas density $\rho_g = \frac{m_d + m_v}{v_d + v_v}$ is defined relative to the volume of the gasses, not the volume of the mixture. From the above form of the mixture equation of state it is clear that it can be thought of as a modified ideal gas equation of state, considering only the gaseous components in the volume they occupy and with a mass-weighted gas-constant.

As a simplification of the above equation of state, we may follow Cao and further assume that the specific concentrations of the condensed water phases are negligible ($q_l \approx 0$, $q_i \approx 0$ $\Rightarrow q_d + q_v \approx 1$), and so the equation of state becomes:

$$
\begin{aligned}
\rho_c^{-1} &= (q_{c,d} R_d + q_{c,v} R_v) \frac{T_c}{p} \\
\Rightarrow p &= \rho_c T_c (q_{v,c} R_v + q_{d,c} R_d) \\
&= \rho_c T_c (q_{v,c} R_v + (1 - q_{v,c}) R_d) \\
&= \rho_c T_c R_d (1 + \frac{R_v - R_d}{R_d} q_{v,c}) \\
p &= \rho_c R_d T_{v,c}, \qquad (3.7)
\end{aligned}
$$

where we have defined the virtual temperature T_v:

$$
T_v = T(1 + \frac{R_v - R_d}{R_d} q_v),
$$

which is the temperature a dry parcel of air would need so as to have the same density and pressure as a moist parcel of air, not including the condensed water phases.

Using eqn 3.7 together with the assumption of hydrostatic equilibrium, we find an expression for the vertical change in in-cloud density (now introducing subscript c for in-cloud variables for clarity) with height:

$$\begin{aligned}
\frac{1}{\rho_c}\frac{d\rho_c}{dz} &= \frac{1}{\rho_c}\frac{d}{dz}\left(\frac{p}{R_d T_{v,c}}\right), \\
&= \frac{1}{\rho_c}\left(\frac{dp}{dz}\frac{1}{R_d T_{v,c}} + \frac{p}{R_d}\frac{-1}{T_{v,c}^2}\frac{dT_{v,c}}{dz}\right) \\
&= \frac{1}{\cancel{\rho_c}}\frac{-\cancel{\rho_c} g}{R_d T_{v,c}} + \frac{1}{\cancel{\rho_c}\cancel{R_d}}\frac{\cancel{p}\,\cancel{-1}}{T_{v,c}^{\cancel{2}}}\frac{d}{dz}\left(T_c(1+\frac{R_v-R_d}{R_d}q_{v,c})\right) \\
&= \frac{-g}{R_d T_{v,c}} - \frac{1}{T_{v,c}}\frac{d}{dz}\left(T_c(1+\frac{R_v-R_d}{R_d}q_{v,c})\right) \\
&= \frac{-g}{R_d T_{v,c}} - \frac{\cancel{(1+\frac{R_v-R_d}{R_d}q_{v,c})}}{T_c\cancel{(1+\frac{R_v-R_d}{R_d}q_{v,c})}}\frac{dT_c}{dz} + \frac{\cancel{T_c}}{\cancel{T_c}(1+\frac{R_v-R_d}{R_d}q_{v,c})}\frac{R_v-R_d}{R_d}\frac{dq_{v,c}}{dz} \\
&= \frac{-g}{R_d T_{v,c}} - \frac{1}{T_c}\frac{dT_c}{dz} + \frac{1}{(1+\frac{R_v-R_d}{R_d}q_{v,c})}\frac{R_v-R_d}{R_d}\frac{dq_{v,c}}{dz},
\end{aligned} \tag{3.8}$$

If, instead of neglecting the finite specific concentration and volume of the condensates, we use the full equation of state (eqn. 3.5), and furthermore use the in-cloud temperature instead of virtual temperature, the vertical gradient of the in-cloud density becomes:

$$\begin{aligned}
-\rho_c^{-2}\frac{d\rho}{dz} &= \left(\frac{dq_{v,c}}{dz}R_v + \frac{dq_{d,c}}{dz}R_d\right)\frac{T_c}{p} + (q_{v,c}R_v + q_{d,c}R_d)\left[\frac{1}{p}\frac{dT_c}{dz} - \frac{T_c}{p^2}\frac{dp}{dz}\right] + \frac{1}{\rho_i}\frac{dq_{i,c}}{dz} + \frac{1}{\rho_l}\frac{dq_{l,c}}{dz} \\
\Rightarrow \rho_c^{-1}\frac{d\rho}{dz} &= -\rho_c\left(\frac{dq_{v,c}}{dz}R_v + \frac{dq_{d,c}}{dz}R_d\right)\frac{\cancel{T_c}}{\rho_{g,c}R^*\cancel{T_c}} - \frac{\rho}{\rho_i}\frac{dq_{i,c}}{dz} - \frac{\rho}{\rho_l}\frac{dq_{l,c}}{dz} \\
&\quad - \rho_c\left(q_{v,c}R_v + q_{d,c}R_d\right)\left[\frac{1}{\rho_{g,c}R^*T_c}\frac{dT_c}{dz} + \frac{\cancel{T_c}}{\rho_{g,c}^2 R^{*2}T_c^{\cancel{2}}}\rho_c g\right] \\
&= -\frac{\rho_c}{\rho_{g,c}R^*}\left(\frac{dq_{v,c}}{dz}R_v + \frac{dq_{d,c}}{dz}R_d\right) - \frac{\rho_c}{\rho_i}\frac{dq_{i,c}}{dz} - \frac{\rho_c}{\rho_l}\frac{dq_{l,c}}{dz} \\
&\quad - \frac{q_{v,c}+q_{d,c}}{\cancel{q_{v,c}R_v + q_{d,c}R_d}}\cancel{(q_{v,c}R_v + q_{d,c}R_d)}\left[\frac{\rho_c}{\rho_{g,c}T_c}\frac{dT_c}{dz} + \frac{\rho_c^2}{\rho_{g,c}^2}\frac{g}{R^*T_c}\right] \\
&= -\frac{q_{g,c}\rho_c}{\rho_{g,c}}\frac{\rho_c}{\rho_{g,c}}\frac{g}{R^*T_c} - \frac{q_{g,c}\rho_c}{\rho_{g,c}}\frac{1}{T_c}\frac{dT_c}{dz} - \frac{\rho_c}{\rho_{g,c}R^*}\left(\frac{dq_{v,c}}{dz}R_v + \frac{dq_{d,c}}{dz}R_d\right) - \frac{\rho_c}{\rho_{i,c}}\frac{dq_{i,c}}{dz} - \frac{\rho_c}{\rho_{l,c}}\frac{dq_{l,c}}{dz}.
\end{aligned} \tag{3.9}$$

There is again a lapse-rate term, a temperature gradient term and, in addition, each hydrometeor is represented by a gradient term. Note that $\frac{\rho_c q_{c,g}}{\rho_g} = \frac{v_g}{v}$, so that if the condensate phases are neglected this term is unity.

With this definition for the vertical gradient of in-cloud density the continuity equation

becomes

$$\frac{2}{r}\frac{dr}{dz} = \underbrace{\frac{q_{g,c}\rho_c}{\rho_{g,c}}\frac{\rho_c}{\rho_{g,c}}\frac{g}{R^*T_c} + \frac{q_{g,c}\rho_c}{\rho_{g,c}}\frac{1}{T_c}\frac{dT_c}{dz}}_{\text{adibatic expansion}}$$
$$+ \underbrace{\frac{\rho_c}{\rho_{g,c}R^*}\left(\frac{dq_{v,c}}{dz}R_v + \frac{dq_{d,c}}{dz}R_d\right) + \frac{\rho_c}{\rho_{i,c}}\frac{dq_{i,c}}{dz} + \frac{\rho_c}{\rho_{l,c}}\frac{dq_{l,c}}{dz}}_{\text{microphysics}} + \underbrace{\frac{1}{M}\frac{dM}{dz}}_{\text{entrainment}} - \underbrace{\frac{1}{w}\frac{dw}{dz}}_{\text{accelleration}} \tag{3.10}$$

Note that ρ_e does not figure in these equations. This is because the density of the environment is only relevant when considering mass-exchange with environment, which is described by the $\frac{1}{M}\frac{dM}{dz}$ term.

3.1.2 Conservation of momentum

We consider here the vertical momentum wm_c for a parcel of cloud air with mass m_c and vertical velocity w (subscript c omitted because environment is assumed to be at rest). The total derivative of momentum is

$$d(wm_c) = wdm_c + m_c dw \tag{3.11}$$

And so we may write

$$F_t = \frac{d(wm_c)}{dt} = w\frac{dm_c}{dt} + m_c\frac{dw}{dt}, \tag{3.12}$$

Where F_t is the force acting to change the parcel momentum. This force is comprised of contributions from buoyancy (F_b) and drag (F_d) from motion through the surrounding air

$$F_t = F_b + F_d. \tag{3.13}$$

Using the vertical velocity we may replace the time derivatives with vertical derivatives; (this will allow for the formulation of steady-state solutions by assuming that all variables are only a function of height)

$$\frac{dw}{dt} = \frac{dw}{dz}\frac{dz}{dt} = \frac{dw}{dz}w, \tag{3.14}$$

$$\frac{dm_c}{dt} = \frac{dm_c}{dz}\frac{dz}{dt} = \frac{dm_c}{dz}w. \tag{3.15}$$

And so (combining Equations 3.12, 3.13, 3.14 and 3.15) we have

$$F_b + F_d = w^2\frac{dm_c}{dz} + wm_c\frac{dw}{dz}. \tag{3.16}$$

Isolating the vertical change in velocity with height, we arrive at

$$\begin{aligned} w\frac{dw}{dz} &= \frac{1}{m_c}F_b - w^2\frac{1}{m_c}\frac{dm_c}{dz} - \frac{1}{m_c}F_d \\ w\frac{dw}{dz} &= \frac{1}{m_c}F_b - \mu w^2 - \frac{1}{m_c}F_d, \end{aligned} \tag{3.17}$$

where we have identified the term describing fractional vertical entrainment (μ).

By Newton's second law the force on a body is given as a product of the body's mass m and its acceleration a.

$$F = ma$$

The different cloud-model equations vary significantly in how the buoyancy force F_b is defined, both in regards to the mass of the air parcel and regards to the acceleration it experiences.

Below the assumptions in the original cloud-model by *Levine* [1965] will be outlined as well as the assumptions used by other models which are inspired by Levine's work.

The original model derivation by *Levine* [1965] introduces the concept of *apparent mass* (or *virtual mass*), where the body is described as having a larger *apparent mass* than its actual mass, so as to reduce the effective acceleration. This concept derives from solid body mechanics and is introduced to describe the force necessary to accelerate the surrounding fluid previously at rest. Assuming that the cloud can be described as a solid sphere rising in a stationary ambient atmosphere, Levine defines the accelerated cloud mass as $m_c = (1+\gamma)m$, where γ is the *virtual mass coefficient* ($\gamma = 0.5$ for a solid sphere, see *Falkovich* [2011] for details). This is different to the *drag force* that some models include, as the drag force is dependent on the relative velocity and not relative acceleration of the rising fluid and the surroundings.

As for the acceleration force, this is derived by using Archimedes' principle, where the force experienced by a submerged body is equal and opposite to the force experienced by the displaced fluid, so that

$$a = \frac{\rho_e - \rho_c}{\rho_e} g,$$

where ρ_c is the mean cloud density, ρ_e the environmental air density and g the gravitational acceleration constant. Therefore,

$$F_b = \frac{1}{1+\gamma} m_c \frac{\rho_e - \rho_c}{\rho_e} g.$$

The conservation of vertical momentum (Equation 3.17) then becomes

$$\begin{aligned} w\frac{dw}{dz} &= \frac{1}{\cancel{m_c} w}\frac{1}{1+\gamma}\cancel{m_c}\frac{\rho_e - \rho_c}{\rho_e} g - \mu w^2, \\ w\frac{dw}{dz} &= \frac{1}{w}\frac{1}{1+\gamma}\frac{\rho_e - \rho_c}{\rho_e} g - \mu w^2 - \frac{1}{m_c} F_d. \end{aligned} \tag{3.18}$$

A typical further assumption employed is to assume that the cloud and environmental air can be treated as an ideal gas, so that the ideal gas equation of state may be used and changes in density can be translated to variations in temperature. In addition temperature

is often replaced with virtual temperature (the temperature that a dry parcel of air needs to have to have the same density as a moist parcel of air at a given pressure), so as to include moisture effects. These simplications were typically made for historical reasons to make field measurements tractable, but the simplications are not neccssary when doing numerical simulation as they introduce additional errors.

Considering now the drag force, the physical justification for the drag formulation is consideration of so-called *form-drag* where a moving body must displace the fluid through which it moves, thereby giving the displaced fluid kinetic energy, and so the rate of energy deposition is given by the cross-sectional area (A) times the kinetic energy ($\propto u^2$), so that the drag force is given by

$$F_d = \frac{1}{2}\rho_e u^2 A C_D$$

where ρ_e is density of the fluid and the scaling factor C_D (the *drag*-coefficient) is dependent on the geometry of the moving body and the extent to which the flow is laminar (high viscosity fluid, low Reynolds number) or turbulent (low viscosity fluid, high Reynolds number). For a convective cloud (given characteristic values for the cloud-radius r, density ρ, velocity w and dynamic viscosity of air μ) the typical Reynolds number (Re) is

$$Re = \frac{u\rho r}{\mu} \approx \frac{2\text{m/s} \times 1\text{kg/m}^3 \times 500m}{2 \times 10^{-}5\text{kg/m/s}} \approx 5 \times 10^7,$$

which puts the flow in the high Reynolds number regime. The drag coefficient has been measured in experiments (*Faber* [1995], *Hoerner* [1965]) to be order of $C_{D,sphere} \approx 0.5$ for a solid sphere moving a through low-viscosity fluid (i.e. at high Reynolds number). Similarly the drag-coefficient for a cylinder is $C_{D,cylinder} \approx 1$ at high Reynolds numbers (*Hoerner* [1965]).

Considering the drag-force as applied to a sphere of radius r and mass m_c moving with velocity w through a fluid at rest with similar density ρ to the sphere, the drag force becomes

$$\begin{aligned} F_d &= \frac{1}{2}\rho_e w^2 A C_D \\ &= \frac{1}{2}\frac{m_c}{\frac{4}{3}\pi r^3}\pi r^2 w^2 C_D \\ &= \frac{3}{8} m_c \frac{w^2}{r} C_D \\ \Rightarrow \frac{1}{m_c}F_d &= \frac{3}{8} C_D \frac{w^2}{r}. \end{aligned} \tag{3.19}$$

Assuming the Morton-Turner model for the entrainment rate ($\mu \propto \frac{1}{r}$) the drag term

will be of similar form to the entrainment term. For this reason many models which employ the Morton-Turner parameterisation of entrainment, absorb the drag term into the entrainment term by using a larger entrainment coefficient β. For completeness this assumption will not be made here, as it is the intention to study the validity of describing entrainment using this relation. The impact of altering the entrainment term to include the effect of drag will however briefly be discussed in Section 3.4.2, by considering how entrainment affects not only momentum, but also mass and energy conservation, and the impact this has on a cloud's evolution.

The equation describing the conservation of momentum for a buoyant plume is thus

$$w\frac{dw}{dz} = \frac{g}{1+\gamma}B - \mu w^2 - \frac{3}{8}C_D\frac{w^2}{r}. \tag{3.20}$$

To ease comparison between different models the *buoyancy variable* B has been introduced to represent how the relative density of the cloud plume and environment are calculated when calculating the plume buoyancy. The form of the drag term has been kept so that the drag coefficient has the traditional interpretation found in the literature. The different definitions for *virtual mass* coefficient (γ), buoyancy coefficient (B) and drag coefficient (C_D) are given in the table below.

In this work the values for the virtual mass coefficient and drag coefficient have been chosen to be representative of values found in the literature ($\gamma = 0.5$, $C_D = 0.5$). The effect of varying these constants will be studied in Section 3.4 and the appropriate values of use for shallow convection will be constrained through high-resolution modelling in Chapter 5 and Chapter 6.

Table 3.1: Buoyancy-force for different cloud-model equations. $T_{v,c}$ and $T_{v,e}$ are the in-cloud and environmental virtual temperature respectively, q_l is the specific mass of cloud liquid water, $r_{n,c}$ the mixing ratio of in-cloud condensates, $r_{l,c}$ and $r_{l,e}$ are the liquid water mixing ratio in-cloud and in the environment.

Model	B	γ	C_D
Levine [1959]	$\frac{\theta_c - \theta_e}{\theta_e}$	0	0.506
Levine [1965]	$\frac{\theta_c - \theta_e}{\theta_e} - (r_{l,c} - r_{l,e})$	0.5	0
Simpson and Wiggert [1969]	$\frac{T_{v,c} - T_{v,e} - T_{v,c} q_{l,c}}{T_{v,e}}$	0.0	0.506
Simpson and Wiggert [1969]	$\frac{T_{v,c} - T_{v,e} - T_{v,c} q_{cn}}{T_{v,e}}$	0.5	0
Levine [1959]	$\frac{T_{v,c} - T_{v,e}}{T_{v,e}}$	0.5	$\frac{3}{8}0.506$
Wagner [2009][1]	$\frac{T_{v,c} - T_{v,e}}{T_{v,e}} - (1+\gamma) g (r_{l,c} - r_{r,c} - r_{i,c} - r_{s,c})$	0.5	0
Arnold (unpublished)	$\frac{T_{v,c} - T_{v,e}}{T_{v,e}} - (1+\gamma) g (r_{l,c} + r_{r,c} + r_{i,c} + r_{s,c})$	0.4	0
Cao (*Cao* [2015])	$\frac{T_{v,c}}{T_{v,e}}(1 - r_{n,c}) - 1$	0.5	0
Density-based	$\frac{\rho_c - \rho_e}{\rho_e}$	0.5	0.5

[1]Note that the mass of the hydrometeors aren't scaled by the virtual mass coefficient

3.1.3 Conservation of energy

In this section the energy conservation equation is derived. In contrast to previous formulations of CCFM's cloud-model (*Wagner* [2009], *Wagner and Graf* [2010] and *Cao* [2015]) here specific concentrations (i.e. specific mass relative to the mixture's total mass) instead of mixing ratio (relative to dry air mass) is used. This greatly simplifies the final equation, makes the equation exact and facilitates direct analysis of the individual terms. Other variation with respect to previous versions will be given in the derivation below.

To formulate an energy-conservation equation we must find a description of energy that is conserved during moist ascent. From the second law of thermodynamics we have that

$$dU = đQ + đW,$$

where $dU, đQ$ and $đW$ are changes in internal energy, the heat transferred from (or to) the system and the work done by (or to) the system on (or by) its environment ($đ$ denoting that these are inexact differentials, i.e. path dependent). For a rising parcel of air the work is expansion against the pressure of the environment, and so $đW = -pdV$, where p and V are the pressure and volume, respectively. As we are considering a volume of rising air it is more convient to introduce the enthalpy, as we may know how the pressure changes with height in the environment:

$$H = U + pV, \tag{3.21}$$

$$\begin{aligned} dH &= dU + pdV + Vdp, \\ &= đQ - \cancel{pdV} + \cancel{pdV} + Vdp, \\ &= đQ + Vdp. \end{aligned} \tag{3.22}$$

On the timescale of convection it is reasonable to assume that no heat transfer through conductivity occurs and we assume that loss/gain through radiation is small too (so that $đQ = 0$). In addition we assume that the parcel does not affect the environment so that the parcel is rising in an environment at static equilibrium:

$$\begin{aligned} \frac{dp}{dz} &= -\rho g, \\ \Rightarrow Vdp = \frac{m}{\rho}dp &= -mgdz \end{aligned} \tag{3.23}$$

Isolating the heat transfer term ($đQ$) in eqn. 3.22 and substituting in eqn. 3.23, we define the *moist static energy* (S), which is conserved under vertical motion for a (non-precipitating and non-interacting with radiation) moist parcel,

$$(đQ =)\ dS = dH - mgdz = 0.$$

By integrating and dividing by the cloud mass m, we define the specific moist static energy as

$$s = h - gz. \tag{3.24}$$

A moist parcel of air is made up of dry air and water in different phases, and the distribution depends on the parcel temperature. Enthalpy is typically related to the temperature of a body, by considering how the addition of heat to a body raises the temperature. This can be seen by considering a parcel at rest, at constant pressure ($dp = 0$). We integrate 3.22 to find the enthalpy stored in each of the constituent parts of the moist parcel

$$\begin{aligned} đQ &= dH + \cancel{V dp}, \\ \Rightarrow \left.\frac{dH}{dT}\right|_p &= \left.\frac{đQ}{dT}\right|_p = C_p, \end{aligned} \tag{3.25}$$

where we have defined C_p, the heat capacity at contant pressure. Integrating with temperature and assuming that C_p is independent of temperature[2] we have that

$$\begin{aligned} H &= C_p T, \\ h &= c_p T, \end{aligned} \tag{3.26}$$

where again lowercase h and c_p denote the specific enthalpy and heat capacity at constant pressure respectively.

The total specific enthalpy for the mixture is then given as

$$\begin{aligned} h &= \frac{H}{m}, \\ &= \frac{1}{m}\left(H_d + H_v + H_l + H_i\right), \\ &= \frac{1}{m}\left(m_d h_d + m_v h_v + m_l h_l + m_i h_i\right), \end{aligned} \tag{3.27}$$

[2] this is not strictly true, but the error is small. The variation being for example $\approx 1\%$ for the heat capacity of liquid water between $T = 273$K and $T = 330$K (*Angell et al.* [1982])

To rewrite the enthalpies in terms of known variables we introduce the latent heat of vaporisation (L_v) and fusion (L_f) which are the difference in enthalpy between liquid water and, respectively, water vapour and ice water:

$$L_v = h_v - h_l,\ L_f = h_l - h_i, \tag{3.28}$$

$$\Rightarrow h_v = h_l + L_v,\ h_i = h_l - L_f \tag{3.29}$$

The specific enthalpy of the mixture becomes

$$\begin{aligned}
&= \frac{1}{m}\left(m_d h_d + m_v(h_l + L_v) + m_l h_l + m_i(h_l - L_f)\right), \\
&= q_d h_d + q_v(h_l + L_v) + q_l h_l + q_i(h_l - L_f), \\
&= q_d h_d + (q_v + q_l + q_i)h_l + q_v L_v - q_i L_f, \\
&= q_d c_{p,d} T + q_t c_l T + q_v L_v - q_i L_f, \\
&= \bar{c_l} T + q_v L_v - q_i L_f.
\end{aligned} \tag{3.30}$$

where $\bar{c_l} = q_d c_{p,d} + (q_v + q_l + q_i)c_l$ is the heat capacity of the mixture in the reference state where all moisture is in the liquid phase.

And so the specific static energy (expressed per unit of mixed moist air) becomes

$$s = \bar{c_l} T + q_v L_v - q_i L_f + gz, \tag{3.31}$$

which in this form (the reference state being only dry air and liquid water) is called the *moist static energy* (as apposed to the *liquid static energy* where the reference state is dry air and water vapour which can be found by substituting with the heat of sublimation L_s above instead of L_f).

We now wish to consider how the moist static energy changes with height. By definition, moist static energy it is conserved following an adiabatically rising moist parcel, and so can only change due to entrainment of ambient air or detrainment (loss to the environment) of the mixed cloud air. We write the change in cloud mass as Δm_c and split this into contributions from entrainment ($\Delta^+ m$) and detrainment ($\Delta^- m$), so that $\Delta m_c = \Delta^+ m + \Delta^- m$. By balancing the moist static energy inside the cloud (s_c) before and after exchange with the environment (moist static energy s_e) we have (to first order):

$$
\begin{aligned}
(s_c + \Delta s_c)(m_c + \Delta m_c) &= s_c m_c + s_e \Delta^+ m - s_c \Delta^- m, \\
\cancel{s_c m_c} + \Delta s_c m_c + s_c \Delta m_c + \cancel{\Delta s_c \Delta m_c}^{\approx 0} &= \cancel{s_c m_c} + s_e \Delta^+ m - s_c \Delta^- m, \\
\Delta s_c m_c &= s_e \Delta^+ m - s_c \Delta^- m - s_c \Delta m_c, \\
\Delta s_c m_c &= (s_e - s_c)\Delta^+ m - 2 s_c \Delta^- m, \\
\Delta s_c &= (s_e - s_c)\frac{1}{m_c}\Delta^+ m - 2 s_c \frac{1}{m_c}\Delta^- m, \\
\frac{\Delta s_c}{\Delta z} &= (s_e - s_c)\frac{1}{m_c}\frac{\Delta^+ m}{\Delta z} - 2 s_c \frac{1}{m_c}\frac{\Delta^- m}{\Delta z}, \\
\Rightarrow \frac{ds_c}{dz} &= (s_e - s_c)\frac{1}{m_c}\left.\frac{dm}{dz}\right|^+ - 2 s_c \frac{1}{m_c}\left.\frac{dm}{dz}\right|^- \quad as\ \Delta z \to 0.
\end{aligned}
\tag{3.32}
$$

Taking the detrainment to be zero ($\left.\frac{dm}{dz}\right|^- = 0$) and writing the entrainment term in its typical form $\mu = \frac{1}{m_c}\left.\frac{dm}{dz}\right|^+$, we have that

$$
\frac{ds_c}{dz} = \mu(s_e - s_c).
$$

We now differentiate the in-cloud moist static energy (eqn 3.31 with in-cloud variables) with height

$$
\begin{aligned}
\frac{ds_c}{dz} &= \frac{d}{dz}\left[\bar{c}_l T_c + q_{v,c} L_v - q_{i,c} L_f + gz\right] \\
&= T_c \frac{d\bar{c}_l}{dz} + \bar{c}_{l,c}\frac{T_c}{dz} + L_v \frac{dq_{v,c}}{dz} + q_{v,c}\frac{dL_v}{dz} - L_f \frac{dq_{i,c}}{dz} - q_{i,c}\frac{dL_f}{dz} + g,
\end{aligned}
\tag{3.33}
$$

here we must take into account that the latent heat of freezing (L_f) and evaporation (L_v) are not constants (as commonly assumed in many models) but instead functions of temperature and so will vary with z. In particular the latent heats may be defined relative to the reference values at absolute zero ($T_{00} = -273.15$K) as (*Bechtold* [2014])

$$
\begin{aligned}
L_v &= h_v - h_l = h_v(T_{00}) + c_{p,v} \times (T_{00} + T) - h_l(T_{00}) - c_l \times (T_{00} + T), \\
&= L_v(T_{00}) + (c_{p,v} - c_l)(T_{00} + T), \\
L_f &= h_l - h_i = h_l(T_{00}) + c_l \times (T_{00} + T) - h_i(T_{00}) - c_i \times (T_{00} + T), \\
&= L_f(T_{00}) + (c_l - c_i)(T_{00} + T), ,
\end{aligned}
$$

so that

$$\frac{dL_v}{dz} = (c_{p,v} - c_l)\frac{dT}{dz}, \;\; \frac{dL_f}{dz} = (c_l - c_i)\frac{dT}{dz}$$

With this the vertical derivative of in-cloud moist static energy (Eq 3.33) becomes

$$\begin{aligned}
\frac{ds_c}{dz} &= T_c\frac{d\bar{c}_l}{dz} + \bar{c}_{l,c}\frac{T_c}{dz} + L_v\frac{dq_{v,c}}{dz} + q_{v,c}(c_{p,v} - c_l)\frac{dT_c}{dz} - L_f\frac{dq_{i,c}}{dz} - q_{i,c}(c_l - c_i)\frac{dT_c}{dz} + g \\
&= T_c\frac{d\bar{c}_l}{dz} + (q_{d,c}c_{p,d} + c_l(\cancel{q_{v,c}} + q_{l,c} + \cancel{q_{i,c}}))\frac{dT_c}{dz} + L_v\frac{dq_{v,c}}{dz} + q_{v,c}(c_{p,v} - \cancel{c_l})\frac{dT_c}{dz} \\
&\quad - L_f\frac{dq_{i,c}}{dz} - q_{i,c}(\cancel{c_l} - c_i)\frac{dT_c}{dz} + g \\
&= (q_{d,c}c_{p,d} + c_l q_{l,c} + q_{v,c}c_{p,v} + q_{i,c}c_i)\frac{dT_c}{dz} + T_c\frac{d\bar{c}_l}{dz} + L_v\frac{dq_{v,c}}{dz} - L_f\frac{dq_{i,c}}{dz} + g \\
&= c_m\frac{T_c}{dz} + T_c\left[c_{p,d}\frac{dq_{d,c}}{dz} + c_l\left(\frac{dq_{v,c}}{dz} + \frac{dq_{l,c}}{dz} + \frac{dq_{i,c}}{dz}\right)\right] + L_v\frac{dq_{v,c}}{dz} - L_f\frac{dq_{i,c}}{dz} + g \\
&= c_m\frac{T_c}{dz} + T_c c_{p,d}\frac{dq_{d,c}}{dz} + (T_c c_l + L_v)\frac{dq_{v,c}}{dz} + T_c c_l\frac{dq_{l,c}}{dz} + (T_c c_i - L_f)\frac{dq_{i,c}}{dz} + g \qquad (3.34)
\end{aligned}$$

where $c_m = q_{p,c}c_{p,d} + q_{v,c}c_{p,v} + q_{l,c}c_l + q_{i,c}c_i$ is the *actual* heat capacity of the mixture.

We now isolate the temperature change with height to arrive at an equation describing the steady-state temperature profile inside a rising moist column of air:

$$\begin{aligned}
\frac{dT_c}{dz} &= \frac{1}{c_m}\left(\frac{ds_c}{dz} - g - \left[T_c c_{p,d}\frac{dq_{d,c}}{dz} + (T_c c_l + L_v)\frac{dq_{v,c}}{dz} + T_c c_l\frac{dq_{l,c}}{dz} + (T_c c_l - L_f)\frac{dq_{i,c}}{dz}\right]\right) \\
&= -\frac{g}{c_m} + \frac{\mu}{c_m}(s_c - s_e) - \frac{1}{c_m}\left[T_c c_{p,d}\frac{dq_{d,c}}{dz} + (T_c c_l + L_v)\frac{dq_{v,c}}{dz} + T_c c_l\frac{dq_{l,c}}{dz} + (T_c c_i - L_f)\frac{dq_{i,c}}{dz}\right] \\
\frac{dT_c}{dz} &= \underbrace{-\frac{g}{c_m}}_{\substack{\text{adiabatic} \\ \text{lapse rate}}} + \underbrace{\frac{\mu}{c_m}\left[\bar{c}_{l,e}T_e - \bar{c}_{l,c}T_c + (q_{v,e} - q_{v,c})L_v - (q_{i,e} - q_{i,c})L_f\right]}_{\text{entrainment of moist static energy}} \\
&\quad \underbrace{-\frac{1}{c_m}\left[T_c c_{p,d}\frac{dq_{d,c}}{dz} + (T_c c_l + L_v)\frac{dq_{v,c}}{dz} + T_c c_l\frac{dq_{l,c}}{dz} + (T_c c_i - L_f)\frac{dq_{i,c}}{dz}\right]}_{\text{species change through microphysics and entrainment}}, \qquad (3.35)
\end{aligned}$$

Note the self-consistency of the above equations in that all heating terms are scaled by the mixture heat-capacity to produce a change in temperature.

3.1.4 Tracer equations

Every incompressible hydrometeor q_n (here considering each hydrometeor species represented by the microphysics, so that n is for cloud water, rain, ice) may be changed through

entrainment, phase transitions captured by the microphysics (Chapter 4) and loss through precipitation, and so each will have a evolution equation of the form

$$\frac{dq_{n,c}}{dz} = \mu(q_{n,e} - q_{n,c}) + \frac{1}{w}\left.\frac{dq_{n,e}}{dt}\right|_{\text{microphysics}} + \phi_n$$

Here ϕ_n denotes an additional source/loss term which is used for rain droplet concentration and is necessary to allow for rain-out of rain droplets from the ascending parcel so that rain does not build up (and through this non-physically increase the parcel's density and heat capacity). Note (as mentioned previously) that in the current formulation the cloud model does not represent rain into a parcel from above. From geometrical arguments this term can be postulated to depend on the relative magnitude of the parcel's vertical velocity w and the rain-droplet fall velocity w_r, but must in addition contain a vertical length-scale l_{pr} to be dimensionally consistent, so that $\phi_r = \frac{w_r}{w}\frac{1}{l_{pr}}$. There is currently no clear understanding of the physical interpretation of this length-scale. For this reason the impact of varying this parameter will be investigated in Section 3.4.4.

The inclusion of these tracer equations may appear as an afterthought given their position as the last section on the cloud-model equation in this chapter; however this should not be taken as a sign of their importance. In fact, as will be seen in Section 3.4, in particular the entrainment of water vapour plays a dominant role in the cloud-profiles predicted by the cloud-model, due to the fact this has a direct affect on how quickly a cloud is dried out by mixing with the environment.

3.1.5 Summary of cloud-model equations

In summary the equations describing the conservation of momentum, hydrometeor mass, energy and mixture mass in the 1D entraining parcel-model are:

$$w\frac{dw}{dz} = \frac{g}{1+\gamma}\frac{\rho_c - \rho_e}{\rho_e} - \mu w^2 - D\frac{w^2}{r} \tag{3.36}$$

$$\frac{dq_{n,c}}{dz} = \mu(q_{n,e} - q_{n,c}) + \frac{1}{w}\left.\frac{dq_{n,e}}{dt}\right|_{\text{microphysics}} + \phi_n \tag{3.37}$$

$$\begin{aligned}\frac{dT_c}{dz} = &- \underbrace{\frac{g}{c_m}}_{\substack{\text{adiabatic}\\ \text{lapse rate}}} + \underbrace{\frac{\mu}{c_m}\left[\bar{c}_{l,e}T_e - \bar{c}_{l,c}T_c + (q_{v,e} - q_{v,c})L_v - (q_{i,e} - q_{i,c})L_f\right]}_{\text{entrainment of moist static energy}} \\ &- \underbrace{\frac{1}{c_m}\left[T_c c_{p,d}\frac{dq_{d,c}}{dz} + (T_c c_l + L_v)\frac{dq_{v,c}}{dz} + T_c c_l \frac{dq_{l,c}}{dz} + (T_c c_i - L_f)\frac{dq_{i,c}}{dz}\right]}_{\text{species change through microphysics and entrainment}},\end{aligned} \tag{3.38}$$

$$\begin{aligned}\frac{2}{r}\frac{dr}{dz} = &\underbrace{\frac{q_{g,c}\rho_c}{\rho_{g,c}}\frac{\rho_c}{\rho_{g,c}}\frac{g}{R_c^* T_c} + \frac{q_{g,c}\rho_c}{\rho_{g,c}}\frac{1}{T_c}\frac{dT_c}{dz}}_{\text{adibatic expansion}} \\ &+ \underbrace{\frac{\rho_c}{\rho_{g,c}R_c^*}\left(\frac{dq_{v,c}}{dz}R_v + \frac{dq_{d,c}}{dz}R_d\right) + \frac{\rho_c}{\rho_{i,c}}\frac{dq_{i,c}}{dz} + \frac{\rho_c}{\rho_{l,c}}\frac{dq_{l,c}}{dz}}_{\text{microphysics}} + \underbrace{\frac{1}{M}\frac{dM}{dz}}_{\text{entrainment}} - \underbrace{\frac{1}{w}\frac{dw}{dz}}_{\text{accelleration}},\end{aligned} \tag{3.39}$$

where

$$\begin{aligned}\bar{c}_{l,c} &= q_{d,c}c_{p,d} + (q_{v,c} + q_{l,c} + q_{i,c})c_l, \\ \bar{c}_{l,e} &= q_{d,e}c_{p,d} + (q_{v,e} + q_{l,e} + q_{i,e})c_l, \\ c_m &= q_{p,c}c_{p,d} + q_{v,c}c_{p,v} + q_{l,c}c_l + q_{i,c}c_i, \\ R_c^* &= \frac{R_v q_{v,c} + R_d q_{d,c}}{q_{v,c} + q_{d,c}}.\end{aligned}$$

The above order reflects the order of numerical evaluation, so that the vertical derivative of e.g. temperature evaluated at a given height may be used in the radius equation.

3.2 Boundary and initial conditions

3.2.1 Cloud-base conditions

In CCFM (as of *Wagner* [2009], *Wagner and Graf* [2010]) the cloud-base absolute temperature and specific mass of water-vapour are predicted by adiabatically lifting a parcel with the temperature and moisture content in the first model level to the height at which this parcel first condenses (the LCL). From here the parcel is lifted along a moist adiabat (assuming saturation adjustment) until the the level of free convection is reached (LFC)

requiring that that the parcel's density temperature is throughout $T_\rho > 0.5K + T_{\rho,e}$ which effectively means that the below-cloud parcel is 0.5K warmer than the environment and thereby allows for a non-zero amount of convective inhibition (CIN) larger than would be directly implied by the environment profile. The vertical velocity at cloud-base is parameterised through turbulent kinetic energy at the condensation height ($e_{tke,base}$) as:

$$w_{base} = min(1.5\sqrt{e_{tke,base}} + 0.8\text{m/s}, 3\text{m/s}),$$

which constrains the cloud-base vertical velocity to be between 0.8m/s and 3m/s. The applicability of these values will be discussed in Section 6.3.7 where the cloud-base vertical velocity will be extracted from a large distribution of clouds from a LES simulation of shallow convection. The sensitivity of cloud-growth to the cloud-base conditions is briefly studied, which together with the analysis of large-domain convective systems in Chapter 6 shows how even small variations in moisture and heat content (on the order of 0.1g/kg and 0.1K), respectively, can decide whether a cloud breaks through the CIN. The impact of the trigger mechanism on the predictions of the cloud-model will also briefly be investigated in Section 3.4.5

Additional trigger mechanisms for CCFM have been proposed, one of which was recently implemented by *Cao* [2015], and although they are not the focus of this thesis they are mentioned here for completeness, and their possible merits given the results of high-resolution modelling will be discussed. In summary, the three trigger mechanisms of increasing complexity are:

1. cloud-base height defined as single height (determined from an adiabatically lifted parcel) and cloud-base radii prescribed as uniform distribution between the surface ($z = 0$m) and the boundary-layer depth z_{pbl} (as provided by the host-model).

2. Use entraining parcel of prescribed radius from ground to predict a single cloud-base height. At this height define the cloud-types by picking different cloud-base radii.

3. Entraining parcel model with different initial radii at ground giving rise to multiple cloud-base heights, with cloud-base radius at each height given by entraining parcel model.

Given well-mixed nature of the boundary layer it is likely that the entraining parcel model is not needed for prediction of plumes in the boundary layer, but instead the boundary layer profiles could be described by a parametric function and the cloud-base properties and radius defined analytically. This will be investigated in future work by further studying the properties of the boundary layer.

3.3 Model integration algorithm

This section outlines the algorithm applied to integrating a single cloud profile, the steps of this algorithm are as follows:

1. Cloud-base conditions are determined through "cloud trigger" method, either:
    a. Calculating the Lifting Condensation Level
    b. Integrating the cloud-model equations in the *sub-cloud* layer (see *Cao* [2015] for details)
2. Given state the cloud base state $Q(r, w, T, q..)$ integrate the governing equations:
    a. Calculate derivative of vertical velocity using momentum equation
        - dependent on in-cloud temperature through buoyancy term (which may be calculated using the EoS or traditionally using virtual temperature).
        - requires that vertical velocity is non-zero
    b. Calculate time-derivatives of water species using microphysics model (see Chapter 4 for details)
    c. Calculate total change of hydrometeors
        - includes microphysics, entrainment and extra sources/sinks (i.e. fall-out of rain)
        - time-derivative of microphysics transformed to vertical derivative through vertical velocity (which must therefore be non-zero and known)
    d. Calculate derivative of temperature $\frac{dT}{dz}$ using energy equation
        - only dependent on in-cloud temperature T and vertical derivatives of hydrometeors
    e. Calculate derivative of cloud radius.
        - needs estimate for change in cloud temperature and vertical velocity, so must be done last

The integration is continued until the vertical velocity drops to zero or equivalently the radius becomes excessively large (due to deceleration).

The above ordering allows that all derivatives may be evaluated at the given height and integrated identically. The integration is numerically done using an adaptive-step numerical method which will be described in detail in Chapter 4. This integration algorithm avoids the numerically enforced sub-saturation which existed in previous cloud-models of *Wagner* [2009], *Wagner and Graf* [2010] and *Cao* [2015], which due to integrating the effect of entrainment after the microphysics processes would leave the air parcel sub-saturated even

if the dynamical processes would drive the air parcel to saturation. As well be seen in the results of Section 3.4 all integrated cloud profiles do in fact produce super-saturation which may be important to properly capture aerosol activation (*Slawinska et al.* [2012]) and should be investigated in future work.

When applying this integration algorithm to integrating the vertical distance of the cloud-profiles (in contrast to the time-evolution of the microphysics in a single control volume, as in Chapter 4) the maximum integration length-scale was set to $\Delta z = 5m$. In addition the step-size was adapted to achieve a maximum error in the cloud-hydrometeor specific concentrations of $0.1mg/kg$. These values were found by experimentation and are necessary as the numerical algorithm does not guarantee stability and may go through a non-physical evolution if inappropriate target errors are used. These limit values bear a strong impact on the computational cost of applying the integration algorithm and thus on the computational cost of running the CCFM convection scheme. The search for an optimal integration algorithm and appropriate limit values for integration should therefore be the focus of further work.

3.4 Properties of convective clouds inferred from entraining-parcel model

The purpose of this section is to study the sensitivity of the cloud model to different values of the input parameters, and identify characteristics of the integrated cloud-profiles which are robust to variations in these parameters. This will firstly make it possible to identify possible limitations of the cloud-model and further develop qualitative insight into what physical parameters control the vertical structure of convective clouds, insight which will be further developed and scrutinised in the later chapters of this thesis where high-resolution numerical modelling is used to study the development of convective clouds.

There are four key parameters of the entraining parcel model which are currently poorly constrained: the entrainment rate (β, or indeed the form of the entrainment term μ), the drag coefficient (D), the precipitation rain-out rate (f_{pr}, this work defined through the rain-out length-scale l_{pr}) and the virtual mass-coefficient (γ). In the following sections each of these will be varied and their effects studied together and in isolation so that their effects can be identified. Finally with these variabilities of the cloud-model in mind, the convection producing perturbation-analysis of the parcel-model (see Section 2.1) is repeated so that the qualitative effects on ability to overcome convective inhibition (CIN) and the eventual cloud-top height can be re-examined when the dynamical effects of cloud-development are taking into account.

All cloud-profile integrations are carried out in an ambient atmosphere with an idealised vertical profile consisting of a well-mixed boundary layer, above which a conditionally

unstable layer is topped by an inversion layer (the detailed functional form for the state variables are given in Section 5.1.2). The cloud-base height, temperature and moisture content are defined using the lifting-condensation level cloud-trigger described in Section 3.2.1 unless otherwise noted. In all cloud-model integrations the Morton-Turner model has been used for the entrainment parameterisation, improving on this model will be the focus of Chapter 5.

3.4.1 Effect of drag on cloud-evolution

Setting the entrainment rate to zero ($\mu = 0$) and varying the drag coefficient (D), the effect of drag may be studied in isolation. From figure 3.2 it is clear (as expected) that the principal effect of drag is the retardation of the cloud's vertical growth, in that higher drag causes the cloud to slow and further expand horizontally. As the drag coefficient is increased the vertical velocity decreases, the result of which is a reduced overshoot into the inversion region where the cloud is negatively buoyant. For all integrations with a non-zero drag coefficient the vertical velocity is so small that nearly no overshoot is observed and instead the maximum cloud-top height is dominated by the buoyancy term, so that these clouds all equilibrate at $z \approx 3km$ where the cloud's density is close to that of the environment.

Interestingly, the thermodynamic behaviour is almost unchanged as the drag coefficient is increased, so that the only change is a small increase in super-saturation for the cases with least drag, caused by the finite condensation time leading to less condensation with a faster moving cloud. In summary, drag in itself appears to be insufficient to halt the cloud's vertical development and has little impact on the cloud's thermodynamics so that the buoyancy produced through condensation is near-constant.

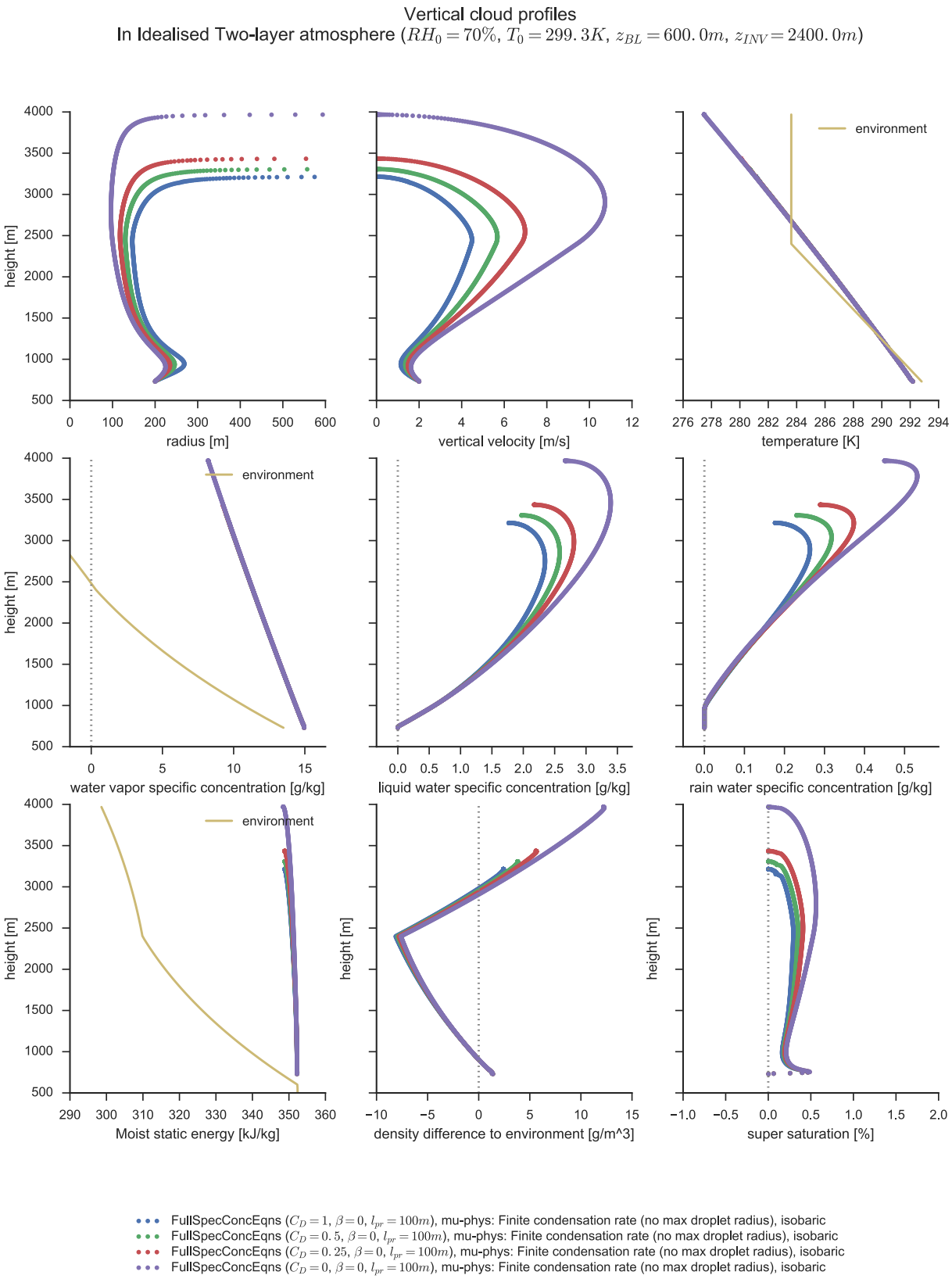

Figure 3.2: Four cloud-profiles integrated with cloud-model with varying drag coefficient, representing the full range of drag coefficients in the literature. Note all integrations with non-zero drag-coefficient result in a cloud-top height at $z \approx 3km$, suggesting that drag in itself has little impact on a cloud's eventual maximum height. Each cloud was integrated from LCL as predicted by CCFM's cloud-trigger

3.4.2 Entrainment vs drag

Assuming the Morton-Turner model to parameterise the entrainment rate ($\mu = \frac{\beta}{r}$), the entrainment term and drag term in the momentum equation (Eq 3.20) have the same form, both having dependency on the velocity (w^2), and so if the dynamical behaviour of a convective cloud dominates the cloud's evolution, drag and entrainment will exert a similar influence; if instead mass conservation and thermodynamics (which are not effected by drag) play a dominate role, the relative influence of drag and entrainment will be different. The purpose of this section is to theoretically investigate the differences observed when changing entrainment and drag, and thereby qualitatively describe the effects of these forcings. This is done by varying the entrainment coefficient β and drag coefficient C_D to keep the sum of the entrainment and drag terms in the momentum equation constant, and thereby study how the physical processes of drag (affecting only momentum) and entrainment (affecting also mass and energy conservation) affect a cloud's evolution. This will make it possible to assert the impact of assuming that drag may simply be included in the cloud-model by increasing the entrainment rate.

In Figure 3.3 integration of the cloud-model has been carried out for two cloud-base radii ($r = [200, 300]$m) and the drag and entrainment rate have been varied together through three discrete values ($C_D = [0.3, 0.5, 0.7]$ and $\beta = [0.125, 0.2, 0.275]$) so as to keep the combined contribution to the momentum equation of the drag and entrainment term constant. These values are representative of the variation in drag and entrainment coefficients found in the literature (although for smaller range than Figure 3.2 as the aim was to keep both drag and entrainment non-zero). By noticing that for a discrete cloud-base radius, the cloud profiles produced differ greatly in cloud-top height depending on whether entrainment was increased or decreased, it is clear that the contribution of entrainment to the other conservation equations is significant, as the vertical profiles would have otherwise been largely unchanged. This agrees with the effect of drag (or equally, entrainment) through the momentum equation, as discussed in the previous section, indicating that drag in itself has little impact on the eventual cloud-profile, but the variation in cloud-profiles must instead come about through the effects of entrainment on the other conservation equations; (this will be discussed in detail in the next sections).

Ultimately the above analysis suggests that the effect of drag should not be included by simply increasing the entrainment term. Instead the entrainment should be optimized first by achieving the correct thermodynamic structure of the final plume (this will be the focus of the high-resolution simulations in Chapter 5) and the effect of drag included to account for variations in cloud-radius not captured when entrainment has been constrained.

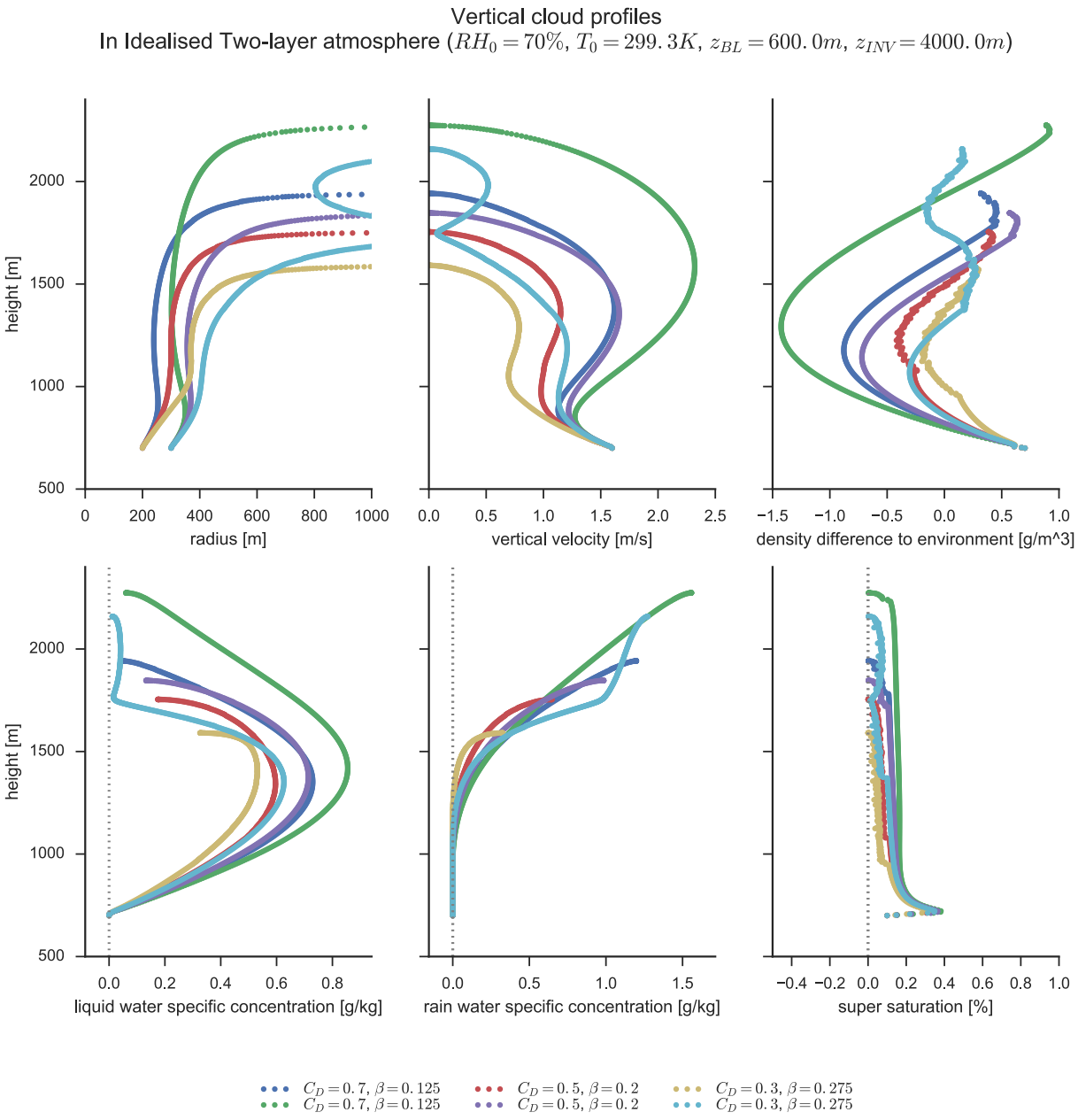

Figure 3.3: Cloud-profiles for integrations of the cloud-model from two initial cloud-base radii where for each the drag and entrainment terms have been varied through three steps will keeping the contribution to the momentum equation constant. It is clear that although the impact of the momentum equation is unchanged changing the entrainment rate has a significant impact on the mass and energy equations, leading to wide variations in cloud-top height. Note that the rain-out length-scale has been set to infinity ($\mathrm{l}_{pr} = \infty$) so that no rainout takes place. This was done because (as will be noted in Section 3.4.4) the loss of rain water in some instances causes an otherwise decaying cloud to become positively buoyant, causing multiple growth phases and thereby obscuring to some extent the analysis here. Note also that the inversion height was lifted to $z_{INV} = 4000m$ to avoid any of the integrated clouds hitting the inversion and having their developed profile affected by the inversion.

3.4.3 Effect of entrainment on cloud-evolution

As mentioned in 2, the principal motivation for introducing entrainment into models of convective clouds is to cause the clouds to halt their vertical development before they hit an inversion at high altitude, a characteristic not predicted by simple parcel theory but frequently observed in nature. This effect can be seen in Figure 3.4 where the entrainment rate has been varied between zero and the Morton-Turner estimate ($\beta = 0.2$). It is clearly seen that withouth entrainment the cloud grows until the isotherm above is hit whereas with increasing entrainment the cloud halts its vertical velopment further below the height of the isotherm. It is clear that the exact value of the entrainment rate has a profound effect on the cloud's vertical profile, solidifying the need to study and understand the nature of entrainment better.

As one of the principal aims of this study is to investigate the extent and effect of entrainment into convective plumes, it is sensible to first assert how entrainment (given how it is currently parameterised) contributes to the integrated cloud profiles. Each of the mass (radius), momentum (vertical velocity) and energy (temperature) conservation equations contain an entrainment term, as do the equations describing the change of hydrometeors, however entrainment may be more or less relevant to either of these equations depending on the relative values of other terms in these conservation equations.

To study the extent to which entrainment of only mass and momentum is adequate to cause this retardation of the cloud's growth, the cloud-model was integrated without entrainment of moist static energy or hydrometeors (by setting the entrainment rate to zero in these equations) so that temperature change is only affected through the dry-adiabatic lapse rate and heating from condensation of excess water vapour, and the in-cloud density is not affected by dilution of the cloud through entrainment of dry air. This effectively amounts to assuming that in-cloud and environment moist static energy are the same, which although untrue is an instructive assumption as it allows us to study how entrainment of only momentum and mass is important. In Figure 3.5 where the cloud-model has been integrated with increasing values of the entrainment coefficient (β), it is clear that even with an absurdly high entrainment-rate ($\beta = 10$) the cloud-top height is unchanged. This indicates that only entraining mass and momentum is not enough in causing the convective clouds to stop their vertical development below the inversion height. and suggests (as expected) that together the cooling through entrainment of moist static energy and the dilution from entrainment of dry air are the principle physical processes necessary in correctly capturing the cloud's vertical development.

Finally, the relative importance of the entrainment of dry air and heat (through the moist static energy) can be seen by varying the relative humidity of the environment in which the convective cloud develops, not in the boundary layer, but above the level of free convection, as increasing the amount of moisture in the environment will reduce the drying from entrainment and to a much lesser extent reduce the entrainment of heat. To study this

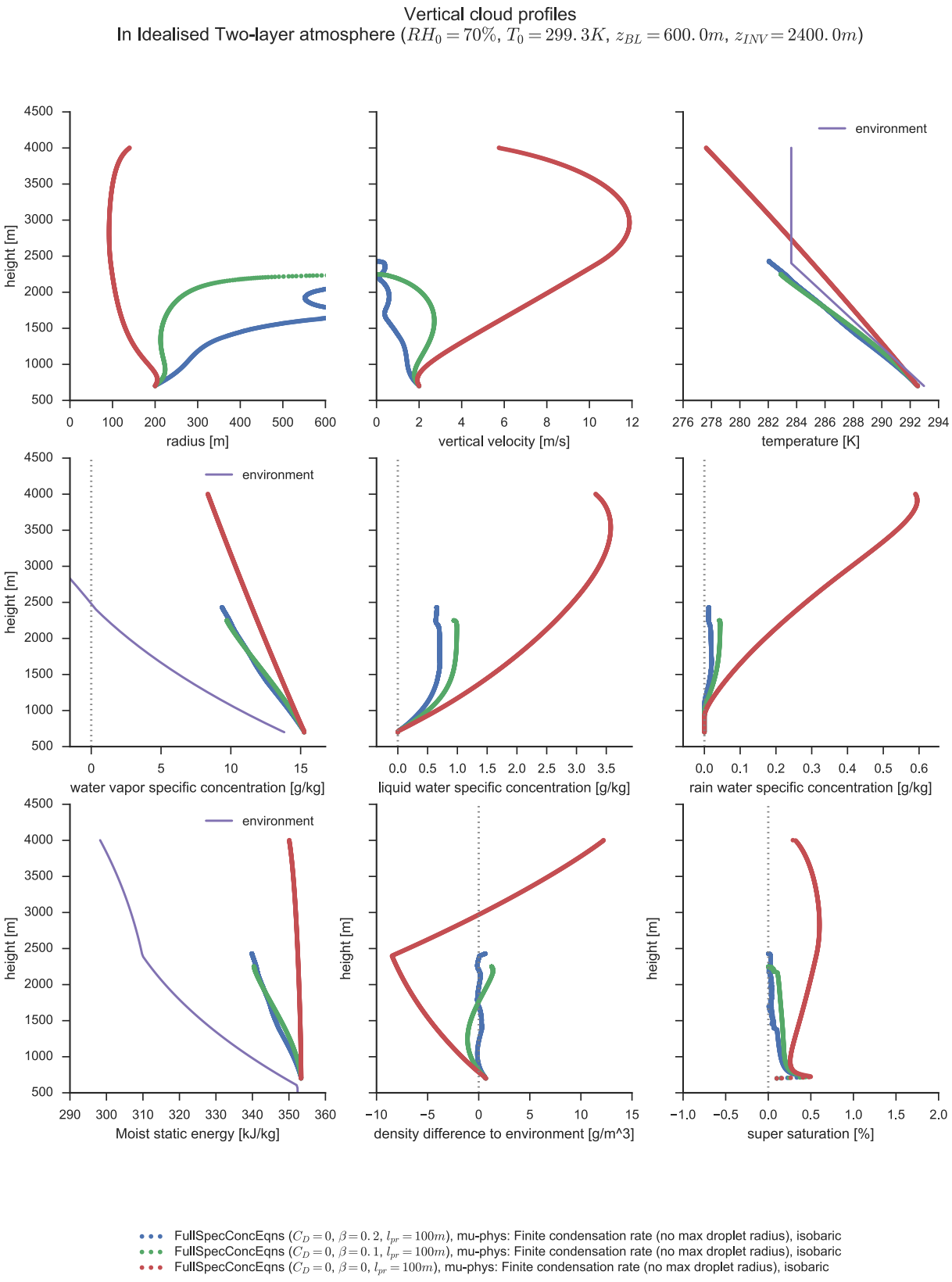

Figure 3.4: Predicted cloud-profiles while varying the entrainment rate. Note that only with non-zero entrainment does the cloud-evolution stop so that cloud-top height is significantly below the isotherm (as expected), and that doubling the entrainment rate strongly affects the cloud-top height.

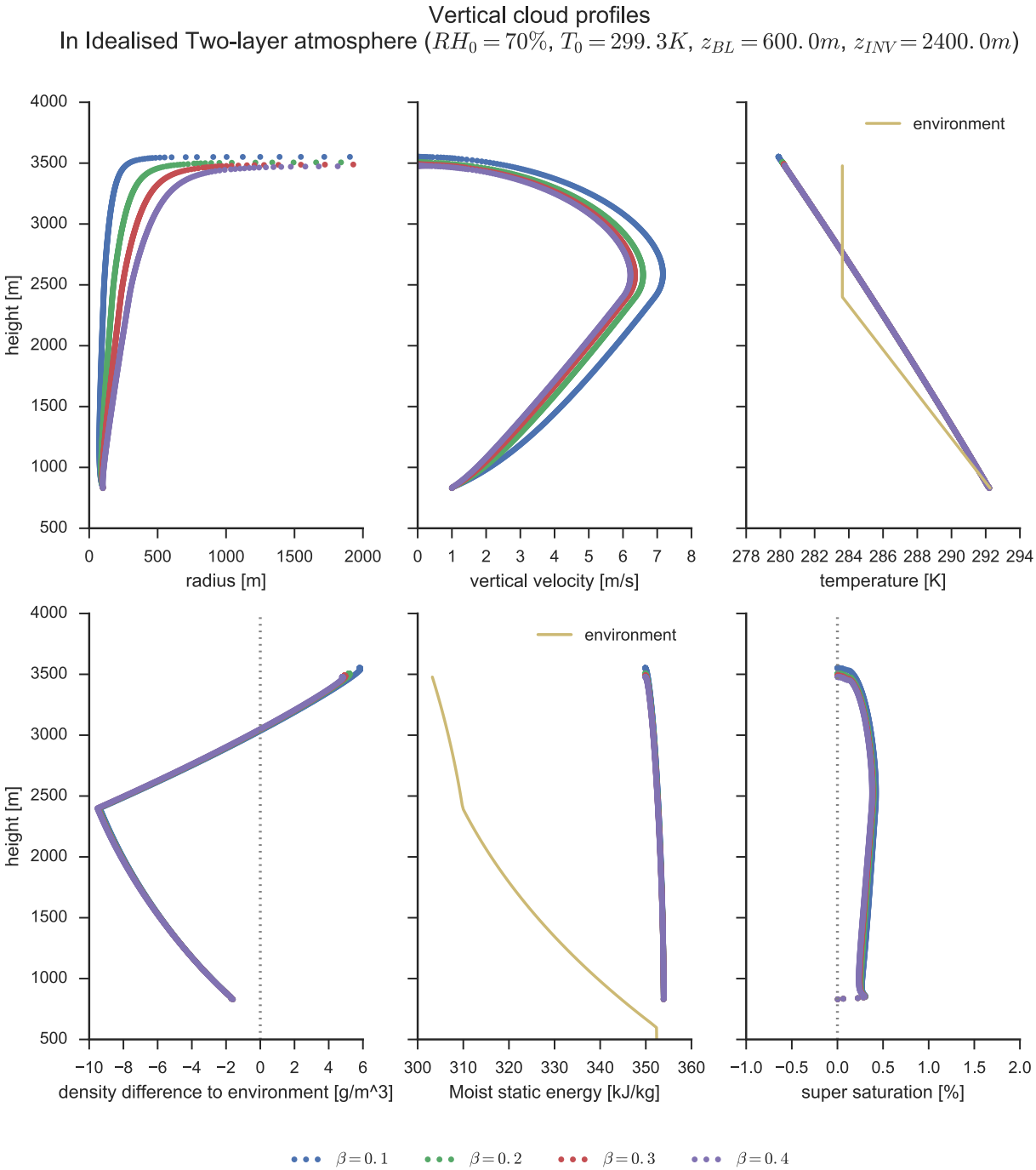

Figure 3.5: Predicted cloud-profiles without entrainment of moist static energy and dry air, with increasing entrainment rate. As the entrainment rate is increased the vertical-velocity profile tends to a limiting vertical structure, but the final cloud-top height is unchanged $z_{top} \approx 3300\text{m}$, suggesting that entrainment of mass and momentum on its own is insufficient to halt a cloud's vertical growth below the inversion layer.

effect the cloud-model was integrated in three ambient profiles where only the rate of decrease in ambient relative humidity above the level of convection (LFC) was changed. The profiles were constructed with a very small convective inhibition so that the effect of CIN has little impact on the vertical growth of each cloud. As seen in Figure 3.6 purely altering the ambient relative humidity can decide whether a cloud will stop developing vertically significantly below the inversion layer so that the cloud which developed in the atmosphere with highest ambient moisture reaches the highest cloud-top height. The observed behaviour where drier environments contribute to causing the cloudtop heights to decrease suggests that the entrainment of moist-static energy plays an deciding role in restricting the vertical extent of the convective cloud. It is interesting to note here that the cloud formed in the most moist of the three ambient profiles has the highest density difference to the environment, even though the ambient is lighter through loading of water vapour (the gas constant of water vapour is $\approx 50\%$ higher than that of dry air leading to a lower density at same pressure and temperature), and so the change in density of the environment through higher moisture content does not appear to significantly cause the cloud to reduce its buoyancy.

The large variation seen above from purely varying the ambient moisture content highlights the importance in accurately representing the environment in which a cloud grows, and in particular the moisture content in the environment. At high values of ambient relative humidity ($> 90\%$) the cloud-profiles produced were observed through numerical experimentation to be nearly insensitive to other variations in the cloud-model parameters and cloud-trigger formulation. This corroborates the notion that entrainment of dry air and heat are the main driving forces in determining a cloud's vertical profile, so that if the environment is very moist and of similar temperature, there is nothing affecting the cloud's development.

This suggests that the relative humidity of the environment has a *very* important impact on a cloud's development; however it is not necessarily the case that it is the difference in moisture content between the cloud and environment which *drives* entrainment (as implied by *Bechtold et al.* [2008] parameterisation of entrainment in the ECMWF operational convection scheme), but instead this difference in moisture content is very important for the eventual *effect of* entrainment. This will be investigated through high-resolution modelling of individual clouds in Chapter 5.

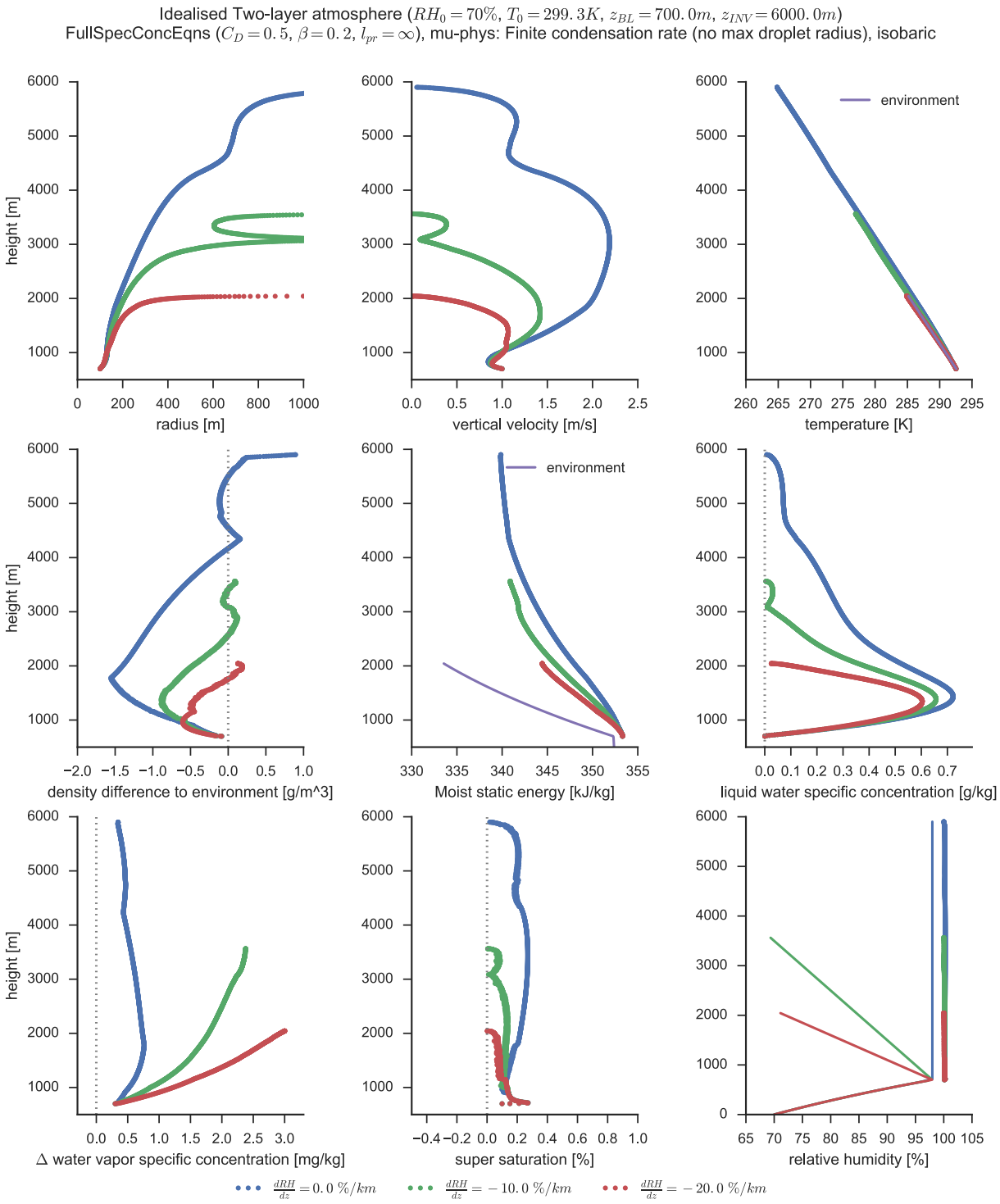

Figure 3.6: Predicted cloud-profiles with entrainment of moist static energy and varying ambient profiles of relative humidity. Drier environments cause the cloudtop heights to decrease suggesting that entrainment of moist-static energy plays an deciding role in the vertical extent of the cloud. Note that boundary-layer depth was increased to $z_B L = 700\mathrm{m}$ to decrease the convective inhibition and the rain-out of water has been disabled ($l_p r = \infty$) as the rain-out can cause a slowing cloud to increase in buoyancy due loss of mass (see next section)

3.4.4 Sensitivity of cloud-profiles to rain-out rate

As mentioned above, the entraining-parcel model relies on a vertical scale-height to characterise the length-scale at which precipitable rain-droplets leave the cloudy parcel. There is currently no clear physically motivated way of defining this scale height and therefore this section will study the extent to which variations in this parameter effect the predicted vertical cloud-profiles. The principal way in which rain-out affects the model-equations is through the increase in the specific concentrations of other hydrometeor species and dry air, which in turn: 1) directly decreases the density (liquid water being heavier than the cloud mixture) and decreases the heat capacity (the heat capacity of liquid water being larger than both that of dry air and water vapour), and 2) through this alters the rate of condensation/evaporation of water vapour and formation of more rain by altering the effective droplet size.

In Figure 3.7 the rain-out rate length-scale has been varied by four orders of magnitude, causing at one extreme hardly any rain-out, and at the other extreme all rain-droplets are rapidly removed from the entraining parcel.

In either extremes the in-cloud specific concentration of rain is either seen to build up through the cloud's vertical evolution (when $l_{pr} = \infty$, and so no rain-out takes place), or is near-instantaneously removed as soon as it is produced (for small l_{pr}, e.g. $l_{pr} = 10\text{m}$) as expected. The rapid removal of rain-droplets also affects the in-cloud concentration of cloud-droplets as these are no longer removed by accretion by the larger, faster-falling rain-droplets; and so the in-cloud concentration of liquid water increases the more rapidly rain-droplets are removed.

A further characteristic of the cloud-profiles with finite rain-out length-scale is the frequent presence of growth and acceleration phases in the cloud's vertical structure, so that although a cloud is entraining and thus generally losing buoyancy with altitude, the loss of rain-droplets may decrease the cloud's density, causing it again to accelerate and gain buoyancy through latent heat release. The extent to which this is a physical effect is currently unclear and should be investigated in further work. This effect does however have a detrimental effect on the numerical integration scheme, as the frequent changes in whether a cloud is buoyant or not poses a challenge for the integration scheme. It may be that a more physically motivated formulation of the rain-out rate would avoid this issue. In particular, the current formulation does not take into account the amount of rain at a given height which has fallen from the cloud above (as the integration is done from the cloud-base and up). This could be addressed in future work by assuming an in-cloud precipitation profile and adjusting this in an iterative manner consistent with the conservation equations, thereby allowing for rain falling from cloud-top to be present at cloud-base (and further below). To constrain the current rain-out rate parameter, high-resolution simulations may give insight into the appropriate rain-out rate, but it ultimately will be necessary to develop a more physically-consistent formulation in future

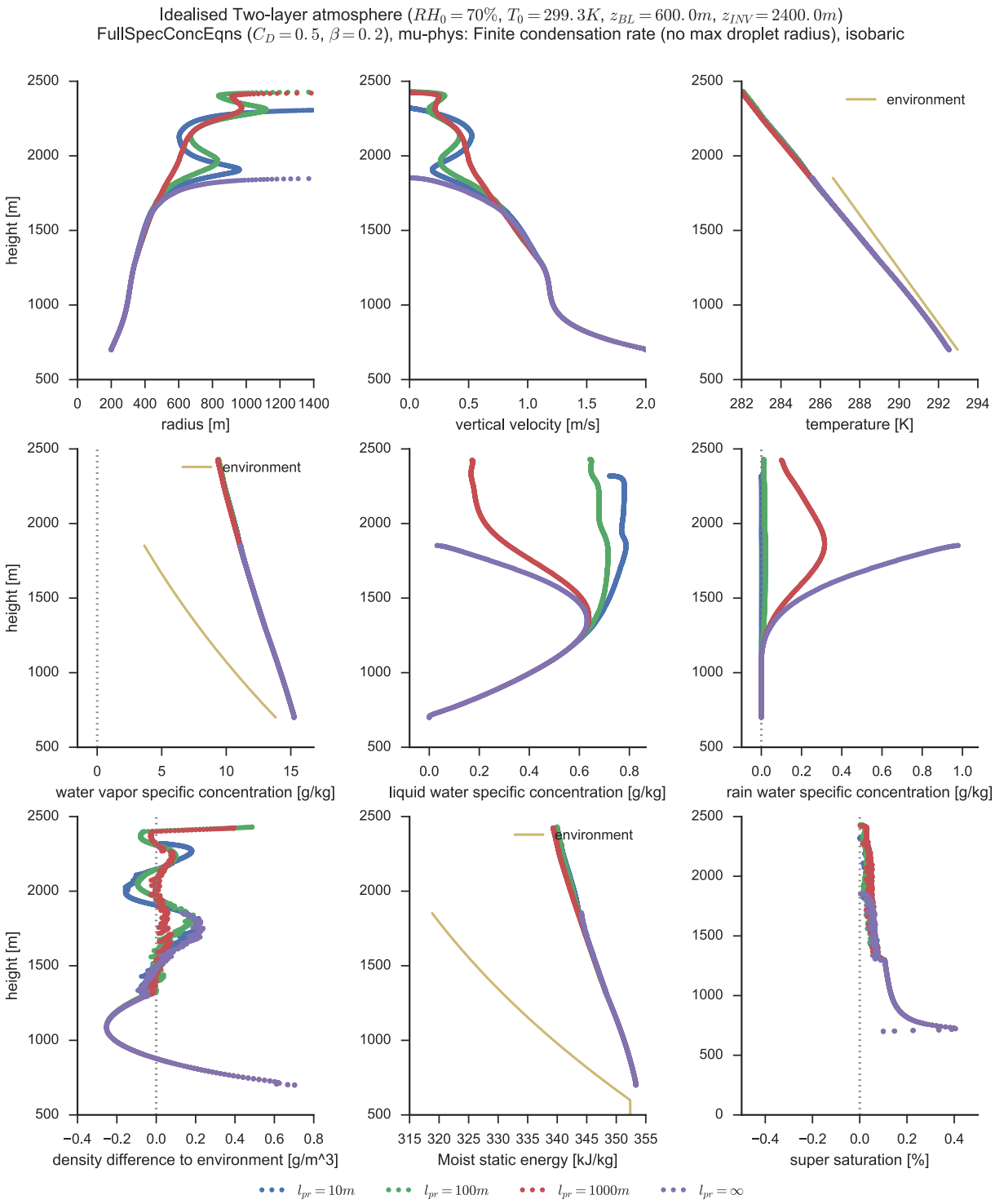

Figure 3.7: Predicted cloud-profiles as produced when varying the rain-out length-scale (l_{pr}). This length-scale determines the rate at which formed rain droplets leave the cloud-parcel. By increasing the rain-out length-scale the rate at which rain is removed from the cloud is seen to decrease as expected. This further affects the in-cloud cloud-water concentration as cloud-droplets are to a lesser extent removed through aggregation by falling rain-droplets (as these have been removed). A notable sensitivity of the cloud-model (and possible non-physical effect) is the return to buoyancy of clouds otherwise decelerating which occurs due to a cloud losing density from loss of rain-droplet mass. This short length-scale change in buoyant/non-buoyant behaviour also has a notable affect on the numerical stability of the integration scheme, which can be seen by the large variation in in-cloud super-saturation and density excess.

work.

3.4.5 Boundary-layer perturbations and predicted cloud-profiles

In this section multiple values for the cloud-producing perturbation are used in the cloud trigger, and with this the cloud-profile integrated for each perturbation in the same atmospheric profile. This is done with the aim to examine the variation of the cloud-profiles with the variability of dry perturbations formed present in the boundary layer. The perturbations applied are defined in terms of the specific concentration of water vapour using values ($\Delta q_v = [0., 0.2, 0.4]g/kg$) characteristic of results from the analysis large-domain multi-cloud simulation of shallow-convection in Chapter 6; each perturbation used to trigger a cloud at two different cloud-base radii ($r_{base} = [100, 200]$m). The cloud-base height is defined using the lifting condensation level, and so increasing the water vapour specific concentration of the cloud-producing perturbation leads to a reduction in the cloud-base height, which can be seen in the top-left of Figure 3.8. Examining the profiles of cloud-radius, it is clear that the clouds with smaller radius ($r_{base} = 100$m) feel a stronger entrainment and are not able to overcome the convective inhibition. This suggests that through the process of entrainment the effective CIN experienced by a developing cloud is larger than would be predicted from an adiabatically lifted non-entraining parcel, as the buoyancy inherent and produced in the cloud is diluted through entrainment, and the entraining parcel cools more rapidly than the saturated moist lapse rate. Assuming that the amount of entrainment is inversely proportional to the cloud radius (as in the Morton-Turner model) this suggests that there is a cloud-base radius dependent effective CIN, which as the cloud-base radius is decreased causes a particular cloud's level of free to convection to become ever higher. Taking this into account may form better predictions of the production of shallow cumulus, which should be considered in future work.

Considering now the clouds which do reach the level of free convection, it is interesting to note that the cloud developed from the largest perturbation in water vapour concentration leads to the highest eventual cloud-top height, even though the condensation level is the lowest and so the cloud has risen significantly farther than the cloud produced from the smallest perturbation. This variation in total cloud-height is a manifestation of the fact that increasing the water vapour concentration in the cloud-producing perturbation places the developing cloud at a higher moist adiabat (higher θ_l) which will reach its equilibrium level at a higher altitude.

In general the largest variation in cloud-top height was seen through experimentation to stem from variations in cloud-base radius, so that the variations in cloud-producing perturbation produce a spread about the height characteristic of a given-cloud base radius. This sensitivity comes about from the strong dependency of entrainment on the cloud radius, compared to the small variation in moist-adiabat when keeping the cloud-base radius

constant. This analysis will be further extended in Section 6.5.1 where the variations in cloud-top height, cloud-base radius and cloud-producing perturbation have been extracted from large-domain simulations of large number (1000s) of convective clouds, and will be compared to predictions by the cloud-model.

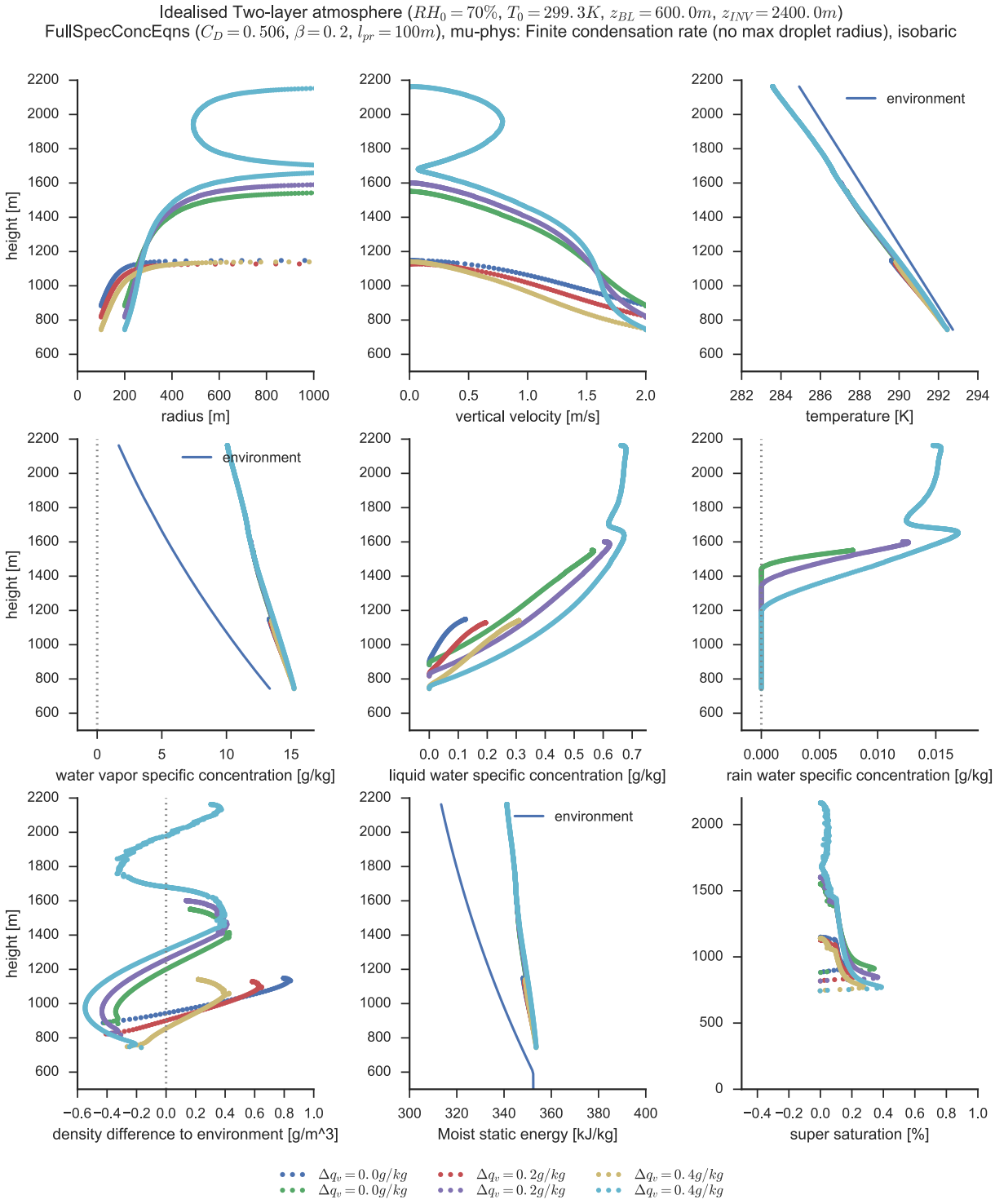

Figure 3.8: Vertical cloud-profiles produced by varying the cloud-producing perturbation (in terms of water vapour) at two values of cloud-base radius. The variations in perturbation-size are representative of those for large-domain simulation of shallow convection (Chapter 6). Note how at the smaller cloud-base radius all three clouds entrain so strongly so as to be stopped by the convective inhibition. At larger cloud-base radius the largest perturbation causes the cloud to travel along a higher moist adiabat, leading to a greater cloud-top height (even compensating for the reduction in cloud-base height).

Chapter 4

Cloud microphysics

In this chapter the processes involved in phase-transitions of water and in producing precipitation which are relevant to convective cloud development will be described. These processes are together called *microphysics* as their characteristic length-scales are on the order of micro-meters. This chapter will also detail new microphysics software routines developed to replace the microphysics routines in ATHAM and CCFM which were previously implemented separately and based on different model formulations. This new piece of software was developed as an isolated framework with a general interface for operating within any atmospheric flow application, and so the microphysics processes are viewed as a separate module which allows for isolated testing and consistency between different models due to code-reuse. It is implemented in Fortran 90 to be compatible with ATHAM and CCFM, with a Python wrapper and tests written in Python. The use of Python allows for tests written in a high-level representation, which facilitated isolated testing of each component part of the microphysics framework.

The role of the microphysics module is to predict how the concentrations of hydrometeors change in time, so that if the dynamics force the system into a non-equilbrium state (e.g. supersaturation of water vapour) the microphysics will predict how the system will respond (e.g. by condensing excess water vapour into liquid water). In addition the cloud-microphysics also predict the rate at which precipitation (rain water) is formed, so that the dynamics can remove excess moisture from a cloudy region at the physically correct rate.

The field of microphysics is a research field of its own (with many aspects still poorly understood) and this chapter will not be an exhaustive review of our current understanding but instead serve as a minimum working-model which was used in this study. The importance of cloud-microphysics when considering convective clouds is exemplified by the fact that the dominant source of buoyancy for a convective cloud is produced by the latent heat release from the condensation of water vapour. Of equal importance to the processes considered is the numerical implementation of the cloud-microphysics module, specifically how the time-integration method of these processes is implemented.

The new microphysics framework was specifically implemented to address the following:

1. To guarantee model consistency between CCFM and ATHAM, and through this to facilitate the comparison of predictions of bulk-properties of convective clouds (e.g. cloud-top height and total precipitation) and compare predictions of entrainment rates as calculated from LES simulations using ATHAM and estimated through the cloud-equations in CCFM; (this will be the focus of Chapter 5).

2. The existing microphysics scheme in ATHAM had a number of unnecessary assumptions, errors and inconsistencies (as will be discussed below), and limitations due to how the microphysical process time-derivatives where numerically and algorithmically integrated. In addition a clearer separation of the different processes was sought.

As well as developing a unified framework which is now used within both ATHAM and CCFM my focus has been on developing an adaptive-step integration method for use with microphysical processes (section 4.2.1) and a new method for droplet formation (section 4.1.1) which can be used with this adaptive-step integration method.

The scientific question studied through this work is to what extent a simple conceptual model which allows for cloud-droplets to form at a finite rate would produce physically realistic results while being employed within the framework of adaptive time-step numerical integration scheme. In addition the existence of a simple, testable, isolated and modular microphysics framework makes it possible to study the effects of different cloud-microphysical processes on convective cloud-formation in current and future work.

4.1 Microphysics processes

This section describes the processes of phase-changes and dynamic evolution of water's many forms captured in the new microphysics framework. For each process the relevant the physical laws will be briefly introduced and the mathematical formulation given. The processes currently represented are that of formation of cloud-droplets (Section 4.1.1) and of rain-droplets (Section 4.1.2). As a description of droplet fall-speed is necessary for the formation of rain-droplets the fall-speed of droplets will be discussed in Section 4.1.3.

Since the microphysics module captures only the behaviour within a single volume it does not take into account any relative motion of the hydrometeors that would lead to loss out of (or influx into) this volume. This dynamical behaviour must instead by captured by the host-model in which the microphysics scheme is being used. This becomes significant when predicting for instance the fall-out of rain from this volume, which will be discussed in section 4.1.3.

The microphysics scheme implemented thus far does not capture the ice phase of water and thus is only applicable to shallow convection (as ice-formation is required to drive

the development of deep convective anvil clouds). This limitation was chosen both to limit the scope of the project (and focus on shallow moist convection) and due the fact that ice-microphysics is still an area of active research with many aspects of it poorly understood and frequently developed by assuming similar behaviour to warm (liquid) processes. It is the intention that in future work the recent P3 (*Morrison and Milbrandt* [2015]) ice-microphysics scheme will be implemented.

4.1.1 Droplet formation and growth model

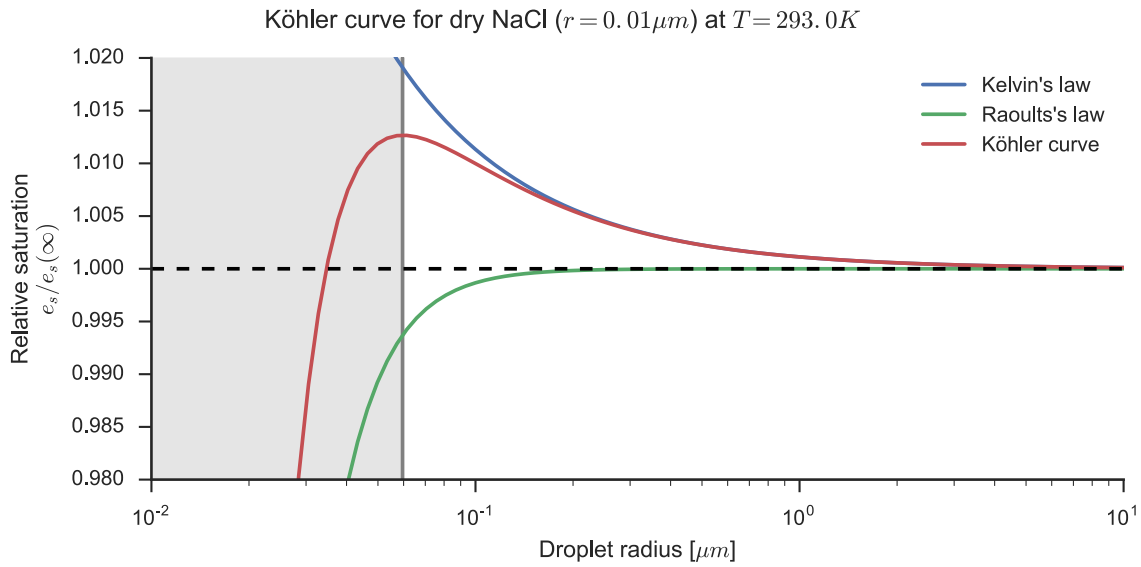

Figure 4.1: Köhler curve with contributing Kelvin effect and Raoult's law. The stable non-activated cloud-droplet region is shaded on the left. Once a cloud droplet-reaches the critical radius r^* at the peak of the Köhler curve the droplet may grow while consuming the environmental moisture.

Due to the curvature of water droplets, the saturation vapour pressure (the vapour pressure required to keep a droplet in equilibrium with the environment and not grow/shrink) is larger than it is over a flat surface. This effect is called Kelvin's effect and indicates that unless high values of super-saturation are attained ($\approx 350\%$ at $T = 290K$, [*Rogers and Yau*, 1989]) cloud-droplets cannot form from only water vapour (homogenous nucleation), as any molecules colliding to form a droplet would quickly break away and the droplet immediately evaporate. In fact observed supersaturation levels in clouds are simply too low for homogeneous nucleation to take place (*Rogers and Yau* [1989]).

A competing effect to Kelvin's effect is the attractive forces produced by hydroscopic particles (for example sea-salt or sulphates), which cause lowering of the saturation vapour pressure for solution droplets, their effect increasing with increasing solute concentration. This effect is called Raoult's law, and because of their effect these particles are called cloud-condensation nuclei (CCNs) and are crucial to cloud formation by enabling the production of small droplets which may then grow.

Combining these two effects one can plot a so-called Köhler curve (Figure 4.1) which describes the equilibrium saturation vapour pressure of a droplet as a function of radius. There are two distinct stages in the growth of a cloud droplet, separated by the max in the Köhler curve, the so-called critical radius. Before this peak the necessary ambient water vapour concentration for equilibrium increases with radius, however since increasing the radius requires taking water vapour from the environment, the further droplet's growth is inhibited. Once a droplet is larger than the critical radius (which can be achieved by increasing the ambient relative humidity) the droplet can grow unhindered (these droplets are typically termed *activated*), consuming water vapour from the environment.

In the existing microphysics formulations used in both ATHAM and CCMF, both separately produced cloud-droplets by, in a single timestep, quenching all excess water vapour (relative to the saturation water vapour at the given pressure and temperature) and turning this into cloud droplets, and thus did not capture the finite time it takes for cloud droplets to grow. Removing all excess water vapour instantaneously has two undesired effects: 1) the adaptive-step integration algorithm (as described later in this chapter) which relies on an error estimate to adapt the timestep size will only be influenced by the droplet-formation process in the first sub-cycling timestep causing the numerical error to be insensitive to the step size, and thus instantenous condensation makes calculation of step-adaptation (based on the numerical error) in the overall numerical algorithm intractable, 2) the mutual and non-linear interactions between the different microphysics processes will not be correctly captured as the other processes will evolve in a time-dependent manner. To avoid these issues it was necessary to implement a cloud-droplet activation process that captures the finite time required for droplet formation.

The conceptual model developed was based on assuming the initial presence of $N_0 = 200 \times 10^6/m^3$ already *activated* "droplets" of $r_0 = 0.1\mu m$, onto which water vapour can then condense at a finite rate. This formulation does not take into account the curvature and solute effects mentioned above to determine when droplets are activated, but instead these were used to estimate a physically reasonable value for the initial radius of the *activated* droplets. In future work, if coupled to a host-model which predicts the aerosol concentration, the microphysics framework may be extended to include the effects of droplet *activation*.

By assuming thermodynamic equilibrium with the environment the rate at which water droplets grow/shrink (called the condensation/evaporation rate) is given by (*Rogers and Yau* [1989]):

$$\left.\frac{dq_c}{dt}\right|_{cond/evap} = \frac{4\pi}{\rho} N_c r_c \frac{S_w - 1}{F_k + F_d},$$
$$F_k = \left(\frac{L_v}{R_v T} - 1\right) \frac{L_v}{K_a T},$$
$$F_d = \frac{R_v T}{p_{v,sat} D_v},$$

where F_k and F_d describe the effects of heat transfer by conductivity and diffusion respectively, and thermal conductivity (K_a) and water vapour diffusivity (D_v) is empirically (*Rogers and Yau* [1989]) defined as

$$K_a = a_K(T - T_0) + b_K, \; D_v = a_D \left(\frac{T}{T_0}\right)^{b_D \frac{p_0}{p}},$$

with $a_K = 8 \times 10^{-5}$, $b_K = 2.4\times^{-2}$, $a_D = 2.2 \times 10^{-5}$ and $b_D = 1.92$.

By allowing for a finite condensation time it is possible that super-saturation may exist in the cloudy updrafts (it may even increase with height in strong updrafts). This capability is an extension of the UCLALES model (used in chapter 6) which condenses excess water-vapour by moist adjustment (*Seifert and Beheng* [2006]). The extent to which *actual* convective clouds have regions of super-saturation is poorly understood, however it may be important for aersol-activation (i.e. the number of sites available for cloud-droplet formation) (*Slawinska et al.* [2012]), which should be considered in further work. Values of super-saturation observed in both the CCFM cloud-model and ATHAM are on the order of $< 2\%$, and so within the range of predictions by *Rogers and Yau* [1989].

4.1.2 Formation and re-evaporation of rain

Inside a cloud exist water-droplets with a large range of sizes; only the largest of these are large enough to attain a fall-speed to fall out of the cloud and to not evaporate immediately once leaving the super-saturated environment of the cloud. If these large droplets reach the ground these are what we experience as *rain*. In the context of formation of rain the concepts of *autoconversion* and *accretion* are a way of looking at how the empirically observed initially unimodal distribution of water droplet radii evolves into a bimodal distribution with small (non-precipitating) and larger (precipitating) droplets. These are often denoted as two different categories of condensed water "cloud liquid water" (q_c) and rain (q_r) (so that the total liquid water is $q_l = q_c + q_r$). Having prescribed the number of activated cloud-droplets (N_0) the cloud-droplet radius is fixed through the total density of cloud-droplets ($q_r \rho$). Instead of prescribing a fixed number of rain-droplets (as was done above with cloud-droplets) the emperically derived rain size distribution of *Marshall and Palmer* [1948] will be used:

$$N_r(r)dr = N_{r,0}e^{-\lambda_r r}dr,$$

where $N_{r,0} = 10^7 m^{-4}$ (experimentally determined) and λ relates to the mass of rain-water per unit air through:

$$\lambda_r = \left(\frac{8\rho_w \pi N_0}{q_r \rho}\right)^{1/4},$$

where ρ_w is the density of liquid water. Through this the total number of rain-droplets is $N_r = \frac{N_0}{\lambda_r}$.

The formation of rain first requires the condensation of water vapour into cloud droplets (q_c) some of which will grow large enough to precipitate out. Due to their small sizes and similar fall-velocity cloud droplets will infrequently and so at a slow rate collide and combine with other cloud droplets; this is the so-called *autoconversion* process of converting cloud droplets to rain. In the *Kessler* [1969] model of autoconversion the rate is given as

$$\left.\frac{dq_r}{dt}\right|_{autoc} = max\left[k_c\left(q_c - \frac{q_g}{\rho_g}a_c\right), 0\right]$$

where q_g is the specific concentration of all gasses in the mixture, $k_c = 10^{-3}s^{-1}$, $a_c = 5 \times 10^{-4} kg\ m^{-3}$. The max operation ensures that rain-droplets are only created through this process, not destroyed. This in turn implies that there is a critical cloud-water specific mass below which auto-conversion does not take place.

Once rain droplets have formed these may then further grow through collision with cloud droplets, which come into contact due to their different (mass-dependent) fall velocities. By integrating the rain-droplet size distribution with the "sticking probability" E_{rc} and droplet fall velocity (see Section 4.1.3), the rate of formation of rain-droplets through accretion is given by

$$\begin{aligned}\left.\frac{dq_r}{dt}\right|_{accr} &= \int_0^\infty E_{rc} q_c \pi r^2 w_r(r) N_r(r) dr, \\ &= \frac{\pi}{4} N_{0,r} a_r \sqrt{\frac{\rho_0}{\rho}} \Gamma(3.5) \lambda_r^{-3.5} q_c,\end{aligned}$$

This process is call accretion and is a much faster process, but it only takes place once the first rain droplets have been created by autoconversion.

Finally once-formed rain-droplets may grow/shrink through condensation/evaporation of water vapour in the same manner as cloud-droplets. As these droplets are moving relative to the cloud it is common to include a so-called *ventilation coefficient* (f_r, *Rogers and*

Yau [1989]) to represent an in increase in the condensation/evaporation due to changing environment of the cloud

$$f_r = \begin{cases} 1.00 + 0.09Re, & 0 \leq Re \leq 2.5 \\ 0.78 + 0.28Re^{1/2}, & Re > 2.5 \end{cases},$$

where Re is the Reynolds number, denoting the relative importance of viscosity and inertia in influencing the droplet's dynamic evolution, and thus given by

$$Re = \frac{2\rho r u}{\mu},$$

where r is the droplet radius, μ the dynamic viscosity, ρ fluid (surrounding air) density and u the droplet fall-speed (relative velocity to fluid).

Given typical rain-droplet velocities (see Section 4.1.3) the flow is generally characterised by high Reynolds numbers ($Re \gg 2.5$) so that the condensation/evaporation of rain-droplets becomes

$$\begin{aligned} \left.\frac{dq_r}{dt}\right|_{cond/evap} &= \int_0^\infty 4\pi\rho_w \frac{S-1}{F_k + F_d} N_r(r) f_r dr \\ &= 4\pi \frac{\rho_w}{\rho} \frac{S-1}{F_k + F_d} N_{0,r} \left[\lambda_r^{-2} + 0.22 \left(\frac{2a_r}{\nu}\right)^{1/2} \left(\frac{\rho_0}{\rho}\right)^{1/4} \Gamma(2.75) \lambda_r^{-2.75} \right] \end{aligned}$$

4.1.3 Fall-speed of rain

Once formed (through autoconversion and accretion) raindrops may due to their large mass fall through the cloud and recipitate as rain. Properly capturing this behaviour is important for two reasons: firstly it alters the thermodynamical properties of a given volume of cloudy air as the loss of water reduces the mixture's heat-capacity and removes the ability to reversibly re-evaporate the liquid water, and so a descending air-parcel will heat at the warmer dry-adiabatic lapse rate, and secondly location, amount and intensity of rain determines the diabatic heating of the atmosphere and has a strong impact at the Earth's surface, determining biological processes and cooling the surface through evaporative cooling which may in turn affect further cloud development.

Since the droplet size (on the order of millimeters) is orders of magnitude smaller than the simulation resolution, we cannot resolve the dynamics of individual droplets falling under gravity, and must instead employ parameterisations. We assume that a falling droplet quickly (i.e. over a short distance compared to the grid resolution) obtains its terminal fall-speed, i.e. the force of acceleration by gravity balances that of drag from falling through the ambient air.

Assuming a spherical droplet, its terminal velocity has a different parametric form depending on the relative importance of the droplets inertia and the surrounding air's viscosity, which is captured by the Reynold's number (Re), given rise to three flow regimes:

$$w_r = \begin{cases} r^2 \ \frac{2}{9}\frac{\rho_w g}{\mu}\left[1 + \frac{L}{r}(0.864 + 0.29e^{-1.25r/L})\right] & for \quad r < 35\mu m & \text{laminar} \\ r \ k_2 \rho_w \frac{\rho_0}{\rho} & for \quad 50\mu m < r < 500\mu m & \text{intermediate} \\ r^{1/2} \ \sqrt{\frac{8}{3}\frac{\rho_w g}{C_D \rho}} & for \quad r > 500\mu m & \text{turbulent} \end{cases}$$

where L is the droplet's mean free path length, C_D the drag coefficient and $k_2 = 2.2 \times 10^3 \text{cm}^{1/2}/s$. The dynamic viscosity is parameterised according to *Rogers and Yau* [1989] and is only dependent on temperature:

$$\mu(T) = 1.72 \times 10^{-5} \left(\frac{393K}{T + 120K}\right)\left(\frac{T}{273}\right)^{3/2}.$$

Given Earth atmosphere's low viscosity and the characteristic length-scale (millimeters) of rain-droplets, the dynamical behaviour is typically in the regime of high Reynolds-number flow, so that the fall-speed may be parameterised using the $w_r \propto r^{1/2}$ expression.

As will be detailed in Section 5.1.1 ATHAM is able to capture the relative motion of different tracer fields falling under gravity, making it possible to explicitly capture the fall-out of rain. Due to formulation of the cloud-model in CCFM (see chapter 3) the fall-out of rain cannot be accurately represented in CCFM when predicting the vertical cloud profiles. The importance of this will be studied in chapter 5 when the predictions of the CCFM cloud-model will be compared to those of high-resolution simulations with ATHAM.

4.2 Unified microphysics module

In this section the details about the microphysics framework's implementation will be discussed: firstly related to the code's structure, and secondly with emphasis on the integration scheme. In addition to resolving the issues outlined in the introduction of this chapter, the microphysics framework was also developed with the aim to allow for easy extensibility in future, both in terms of adding new parameterisations, more hydrometeor-relevant scalar fields and studying the effects of changing the integration scheme. This was achieved by defining a clear separation between the routines that calculate the time-derivatives of physical field variables and the numerical algorithm that performs the adaptive step-size integration. The modular structure allows that a new model of the microphysics processes as a whole (here denoted as a *microphysics model*) may be simply created by: 1) defining the number of hydrometeors it required (and the

number of moments of each) and 2) writing a single `Fortran90` function which returns the temporal evolution of each component of the microphysical state.

The microphysics framework is split into a number of components: a) a central microphysics model registration interface, b) modules describing each available integration algorithm operating on vectors of a fixed-length and c) modules describing the physical processes represented (the *microphysics model*). Based on the microphysical processes described in the previous section, currently two microphysics models are implemented: 1) cloud-water only model (i.e. no formation of rain) and 2) warm-processes including rain formation. Having both models available enables the study of impact of rain on the evolution of convective clouds.

The remainder of this section is devoted to describing the current microphysics integration algorithm, firstly from a mathematical perspective in Section 4.2.1 and later discussing special considerations when applying this algorithm to integrating the time derivatives of the physical processes in Section 4.2.2.

4.2.1 Time integration

Given that different processes in cloud-microphysics evolve at different time-scales and given that the timestep of the host model is often orders of magnitude larger that these characteristics timescales (minutes rather than seconds), it is important to implement a numerical integration scheme which accurately and with stability is able to integrate the microphysics processes in time. The ideal integration scheme would be able to take small time-steps at times where microphysics processes are evolving rapidly (e.g. at super/sub-saturation) to guarantee stability and take large time-steps where little is changing (e.g. at saturation) to minimize the number of integration steps, while guaranteeing a overall accuracy over the entire integration duration. For this reason, a numerical integration scheme with adaptive timestep was implemented. The integration scheme will then perform a number of *sub-steps* at a variable step-size until full integration distance requested by the host-model has been covered.

A fundamental component of an adaptive integration scheme is the method by which the timestep is adapted. A common method is to compare the relative error produced by two different integration schemes of different numerical order, adjusting the integration step-size to approach the desired accuracy. This error-based integration step adaptation method necessitates that all represented processes occur at a finite rate, so that the error will change monotonically as the integration step-length is modified. This is necessary because any state change which is instantaneous (i.e. has no time-dependency) would occur in full magnitude independent of the integration timestep, and so the error would not be modified by changing the timestep length. In addition, the evolution of the system would be sensitive to the timestep length if some processes occur on a finite timescale and

others instantaneously, as the state evolution is dependent on the interaction of different processes. The exact algorithmic steps taken in the integration scheme will be detailed below.

The Fehlberg 4-5 method (*Fehlberg* [1970]) uses the difference between a fourth and fifth Runge-Kutta integration to estimate the error in a single integration step. Using this error estimate it is possible to estimate how the timestep should be scaled to achieve a target error. The insight of Fehlberg (the so-called "Fehlberg trick") was to realise that the number of machine operations could be reduced by constructing the 4th and 5th-order Runge-Kutta substeps so that the coefficients calculated can be reused.

A Runge-Kutta method is comprised of a multiple of substeps so that the new estimate is given by:

$$y_{n+1} = y_n + h \sum_{i=1}^{s} b_i k_i, \tag{4.1}$$

where k_i are the values of the intermediate steps given by

$$\begin{aligned} k_1 &= f(t_n, y_n), \\ k_2 &= f(t_n + c_2 h, y_n + a_{21} k_1), \\ &\vdots \\ k_s &= f(t_n + c_s h, y_n + \sum_{j=1}^{s-1} a_{sj} k_j). \end{aligned} \tag{4.2}$$

The constants c_i, a_{ij} and b_i define the Runge-Kutta method, and may be condensely written in a so-called Butcher Tableau as below

0					
c_2	a_{21}				
c_3	a_{31}	a_{32}			
$\vdots$	$\vdots$	$\vdots$	$\ddots$		
c_s	a_{s1}	a_{s2}	$\cdots$	$a_{s,s-1}$	
	b_1	b_2	$\cdots$	b_{s-1}	b_s

Table 4.1: The Butcher tableau for the explicit Runge–Kutta method.

By writing the fourth and fifth-order Runge-Kutta estimates of the Runge-Kutta-Fehlberg in a Butcher Tableau the re-use of the constants becomes clear:

Using the Butcher tableau the integration method applied to integration of a single

0						
1/4	1/4					
3/8	3/32					
12/13	1932/2197	−7200/2197	7296/2197			
1	439/216	−8	3680/513	−845/4104		
1/2	−8/27	2	−3544/2565	1859/4104	−11/40	
	16/135	0	6656/12825	28561/56430	−9/50	2/55
	25/216	0	1408/2565	2197/4104	−1/5	0

Table 4.2: The Butcher tableau for the fourth and fifth-order explicit Runga-Kutta methods used by Fehlberg (1970), the coefficients of the two methods are in the second to last and last row respectively.

ODE ($\frac{dy}{dx} = f(x, y)$) will be detailed, extending this to integrating a vector of quantities (i.e. describing the full microphysical state) will be discussed in Section 4.2.2.

$$
\begin{aligned}
k_1 &= f(x, y^n), \\
k_2 &= f(x + a_2\Delta_x, y^n + \Delta_x b_{21} k_1), \\
k_3 &= f(x + a_3\Delta_x, y^n + \Delta_x (b_{31} k_1 + b_{32} k_2)), \\
k_4 &= f(x + a_4\Delta_x, y^n + \Delta_x (b_{41} k_1 + b_{42} k_2 + b_{43} k_3)), \\
k_5 &= f(x + a_5\Delta_x, y^n + \Delta_x (b_{51} k_1 + b_{52} k_2 + b_{53} k_3 + b_{54} k_4)),
\end{aligned}
$$

$$
\begin{aligned}
y_{IV}^{n+1} &= y^n + \Delta x (c_{1,1} k_1 + c_{2,1} k_2 + c_{3,1} k_3 + c_{4,1} k_4 + c_{5,1} k_5), \\
y_{V}^{n+1} &= y^n + \Delta x (c_{1,2} k_1 + c_{2,2} k_2 + c_{3,2} k_3 + c_{4,2} k_4 + c_{5,2} k_5),
\end{aligned}
$$

where y_{IV}^{n+1} and y_{V}^{n+1} are the fourth and fifth-order estimates at $x^{n+1} = x^n + \Delta x$.

$$
\epsilon_{abs} = |y_V^{n+1} - y_{IV}^{n+1}|, \;\; \epsilon_{rel} = \epsilon_{abs} / y_V^{n+1}
$$

Defining target absolute ($\hat{\epsilon}_{abs}$) and relative error ($\hat{\epsilon}_{rel}$) the maximum total error may be defined ($\hat{\epsilon}_{tot} = \hat{\epsilon}_{abs} + y_V^{n+1} \hat{\epsilon}_{rel}$) and through this the optimal integration-step adjustment may be shown to be

$$
s = 0.84 \left(\frac{\hat{\epsilon}_{tot}}{y_V^{n+1} - y_{IV}^{n+1}} \right)^{1/4},
$$

when integrating the microphysical processes the state will be represented by a vector of scalar values (temperature, condensate concentrations, etc) and thus the error estimation and step-adaptation must be extended to be applied to a vector of quantities. This extension and other considerations when integrating the processes relevant to microphysics will be discussed in the next section.

4.2.2 Adaptive integration for moist-processes

For numerical stability it is also necessary to guarantee positive definiteness for variables that may not become negative (e.g. specific concentrations, pressure, temperature) and so a stable sub-cycling timestep length must be defined. The Fehlberg method does not inherently guarantee this as each sub-step is effectively a Euler-forward method that may produce a non-physical state if the integration step is too large. To circumvent this issue the following two approaches were investigated:

1. When any variable that should stay positive becomes negative , its value is set to zero. When this occours for a variable describing specific mass all specific mass variables were rescaled to sum to unity. This approach may therefore lead to loss of hydrometeor mass which is undesirable. In addition is not clear how the other state variables should be rescaled which would be necessary to avoid reaching a non-physical state. For these reasons this method although simpler than that below was replaced.

2. Scaling the timestep if *any* state variable becomes non-physical in *any* Runge-Kutta step. This was done by checking for *nans* (not a number, occuring when e.g. taking the square-root of a negative number, indicating that a physical variable that should not become negative has become negative) at the end of each sub-step and reducing the current stepsize if any nans were present. This method was used as it was found to be the most stable and guaranteed to be conservative. Its the steps will be detailed below and a detailed flow-chart of the integration algorithm can be seen in Fig 4.2.

Instead of using the host-model timestep as the initial integration timestep, the initial size of the sub-cycling timestep (Δt_s) was defined by estimating the maximum timestep allowed if a single Euler-forward integration step was performed given the current microphysical state. The flow of the final algorithm is given in Figure 4.2. In detail we wish to numerically solve a set of non-linear equations describing the time-evolution of a moist-parcel of atmospheric air, written as:

$$\frac{d\underline{y}}{dt} = f(t, \underline{y}),$$

with the state given as $\underline{y} = [y_0, y_1, y_2, ..., y_N]$ with N components, e.g. $\underline{y} = [T, w, q_v, q_c, q_r, q_i, q_{gr}]$, where T is the temperature, w the vertical velocity, $q_v, q_c, q_r, q_i, q_{gr}$ and the phases of water (water vapour, cloud water, rain, cloud ice and graupel).

The constraint on the numerical solution is that some variables are required to be positive definite (e.g. temperature and specific concentrations) and the maximum tolerated absolute error is different for different state variables (e.g. we are less sensitive to $0.5K$ change in

temperature compared to a $0.5kg/kg$ change in water vapour specific concentration). In addition, the total specific concentration of water must be conserved.

Define a vector of maximum tolerated absolute error $\underline{y}^{err} = [T^{err}, w^{err}, q_v^{err}, q_c^{err}, ...]$, a vector indicating the conserved mass variables $\underline{c} = [0, 0, 1, 1, 1, 1, 1]$ and the variables that must stay positive definite $\underline{p} = [1, 0, 1, 1, 1, 1, 1]$. In terms of notation we will denote $\underline{y}^n$ to be the initial state at t^n, and the derivative at t^n by:

$$\frac{d\underline{y}^n}{dt} = f(t^n, \underline{y}^n)$$

We can estimate the maximum timestep for each scalar in the state by dividing every state variable component with its derivative at t_n to produce a vector of time-increments:

$$\Delta \underline{t}^n_{max} = \frac{\underline{y}^n}{\frac{d\underline{y}^n}{dt}},$$

The largest permissible time-increment (Δt_{max}) to guarantee positive definiteness will be given by the smallest non-zero element of $\Delta \underline{t}^n_{max}$ for the variables which are required to be positive definate, so that

$$\Delta t^n_{max} = \min_{i \in N_p}(t^n_{max,i}) \text{ where } N_p = \{j \mid p_j \neq 0 \text{ and } t^n_{max,j} \neq 0, j \in N\}.$$

Given t^n_{max} we compute sub-cycling timestep length (Δt_s) by ensuring that the timestep is not larger than request by the host model (Δt^{host}_{max})

$$\Delta t_s = \min(\{\Delta t^n_{max}, \Delta t^{host}_{max}\}).$$

Once the initial sub-cycling timestep (Δt_s) has been defined one substep is integrated with the RKF method described in the previous section, producing the fourth ($\underline{y}^n_{IV}$) and fifth-order ($\underline{y}^n_V$) estimate for the state after Δt_s has elapsed. These states each checked for `NaN`s (as these indicate devide by zero or square-root of negative numbers) and if found the timestep scale factor is set to reduce the timestep by an order of magnitude ($s = 0.1$). If no `NaN`s are found the timestep scale factor is calculated so as to minimize the number of integration steps while keeping the solution to the desired order of accuracy (see the previous section for details). The lower-order estimate (y^n_{IV}) is taken as the new solution and the total elapsed time incremented by the subcycling timestep length. Further Runge-Kutta steps are then performed until the total elapsed time equals that requested by the host-model.

It is important to note that in each integration sub-step it is necessary to update the temperature, which amounts to relating heating developed from phase transitions to changes in temperature. This requires the definition of a heat capacity for the mixture, which in

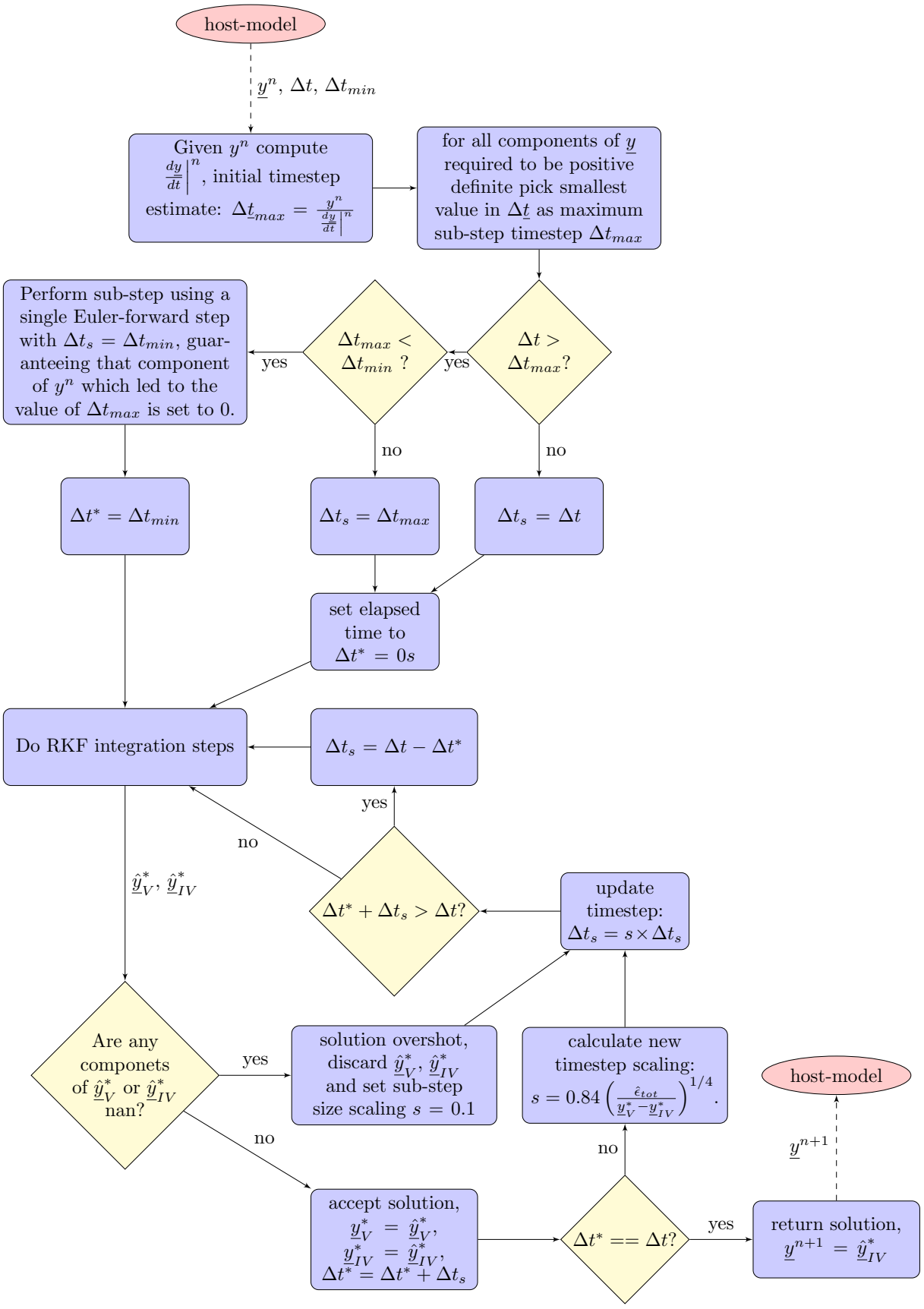

Figure 4.2: Flow-chart of microphysics integration scheme showing how the adaptive timestep during sub-stepping is implemented.

turn depends on whether the microphysics processes are assumed to evolve isobarically (constant pressure) or isometrically (constant volume). Because ATHAM operates at constant volume whereas CCFM's cloud-model integration is carried out a constant pressure (allowing the cloud-parcel to expand) both integration constraints were implemented in the microphysics framework. These were implemented as "integration helpers" which are separated from the numerical algorithm carrying out the actual numerical integration, and separated from the individual microphysics models so that the individual microphysics model may be formulated without considering the integration constraint. When initiating the microphysics framework the host model indicates whether integration is to be performed isobarically or isometrically.

4.3 Simulation results

In this section two examples of non-equilibrium initial states are integrated in time with the microphysics framework to show its physical correctness and numerical capability. This section confirms (together with the use of the microphysics framework in the CCFM cloud-model in Chapter 3 and in ATHAM in Chapter 5) the correct working operation of the new microphysics framework.

In the first example only water vapour is present in the initial condition and this above the level of saturation. This water vapour condenses onto the initial "droplets" (representing activated cloud condensation nuclei), releasing latent heat in the process and thereby heating the mixture until an equilibrium is reached. As soon as cloud-water droplets are formed these begin to form into rain-droplets once the cloud-water droplets reach a critical size. This process of cloud-water droplet growth over a finite time is one of the new components of the implemented microphysics, and is shown here to predict the formation on cloud-droplets on the timescale of seconds, similar to values in the literature (*Rogers and Yau* [1989]).

In Figure 4.3 the evolution of specific concentrations, temperature and pressure over time are plotted, as predicted with the old ATHAM "Kessler" microphysics, the new framework presented here and equilibrium state as calculated by moist adjustment. As a point of reference moist-adjustment has been used to calculate the equilibrium state by doing three iterations of moist adjustment. By comparing the predictions of the old ATHAM microphysics with the equilibrium state as predicted from moist adjustment it is clear that the old microphysics overshoots the change in water vapour concentration, bringing the state from super to sub-saturation before converging to a solution slightly away from saturation. This convergence to a state away from convergence points to an issue with the calculation of the saturation vapour pressure in the old ATHAM microphysics. In addition, the old microphysics non-physically predicts a decrease in pressure instead of an increase. As this increase comes about from the heating at finite volume caused by latent heat release, it is possible that the latent heating is not taken properly into account, and therefore the pressure increase (occurring due the integration constraint being isometric) is not correctly estimated.

Examining now the evolution with the new microphysics framework the evolution is seen to converge monotonically to the concentrations, temperature and pressure as predicted by moist-adjustment, but in contrast to moist adjustment the finite time condensation time of cloud-droplets is represented. As the old ATHAM microphysics internally uses a form of moist adjustment, by after integrating all other microphysics processes converting all excess water vapour into cloud-liquid water (effectively doing a one-step moist-adjustment in each host-model timestep), the time of cloud-condensate formation in the old ATHAM microphysics is dependent on the host-model timestep. Due to the rapid creation of cloud-condensate the creation of rain-droplets also takes place earlier which may explain

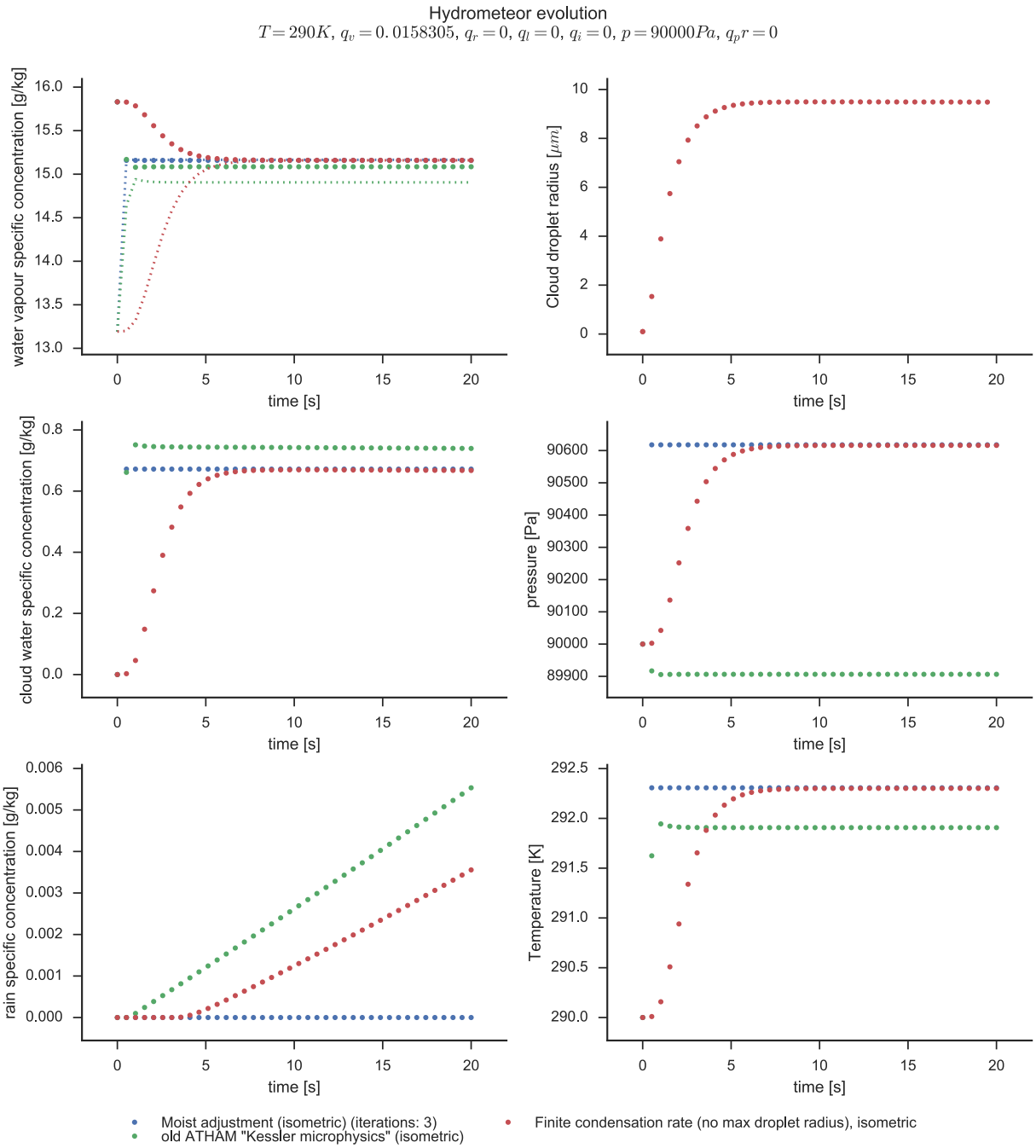

Figure 4.3: Time-evolution (isometric) plot of the hydrometeor state using three different microphysics representations for cloud droplet and growth: moist adjustment, original ATHAM microphysics and new droplet-growth model. The moist-adjustment scheme may be viewed as the reference for the correct final state, but importantly it doesn't capture the state evolution. The ATHAM microphysics internally uses moist adjustment to produce cloud-droplets; this may be observed by the overshoot in ATHAM following condensation non-physically taking the state from super to sub-saturation (sign by the dotted saturation line in the water vapour plot). Also note the smooth temperature evolution of the finite condensation rate model even as it switches from increasing the droplet radius to increasing the number of cloud droplets. In addition, the rapid droplet creation in ATHAM causes earlier onset of rain production.

the excess precipitation which has previously been observed in simulations with ATHAM.

The second example (see Figure 4.4) exhibits the numerical stability of the adaptive-step integration scheme implemented in the new microphysics framework. Here the initial condition is again at super-saturation, but the pressure and temperature reduced to represent typical in-cloud values of pressure at the height where clouds may typically form. The timestep of the host-model is then varied from quite small ($\Delta t = 2$s) to an order of magnitude larger ($\Delta t = 30$s) representative of timescales permissible by the CFL-condition at $\Delta x = 100$m grid resolution if sound-waves or advective transport respectively is restricting the maximum timestep.

Note firstly that with the large host-model timestep the old ATHAM microphysics does not converge during the 120s simulation time, this is due to its internal use of effectively one-step moist adjustment. With a finer time-resolution of the host-model the solution does converge (although to the incorrect state, again predicting a pressure decrease instead of increase). It is therefore clear that the rate of convergence of the old ATHAM microphysics is dependent on the size of the host-model timestep.

Comparing now to the evolution of the state using the new microphysics framework both evolutions are seen to evolve monotonically and convergence to the equilibrium state (the rate of condensation) is now unchanged as the host-model timestep changes. This is due to the internal sub-cycling and use of an adaptive timestep within the new microphysics framework, predicting the same rate of condensation while guaranteeing numerical stability independent of the size of the host-model timestep.

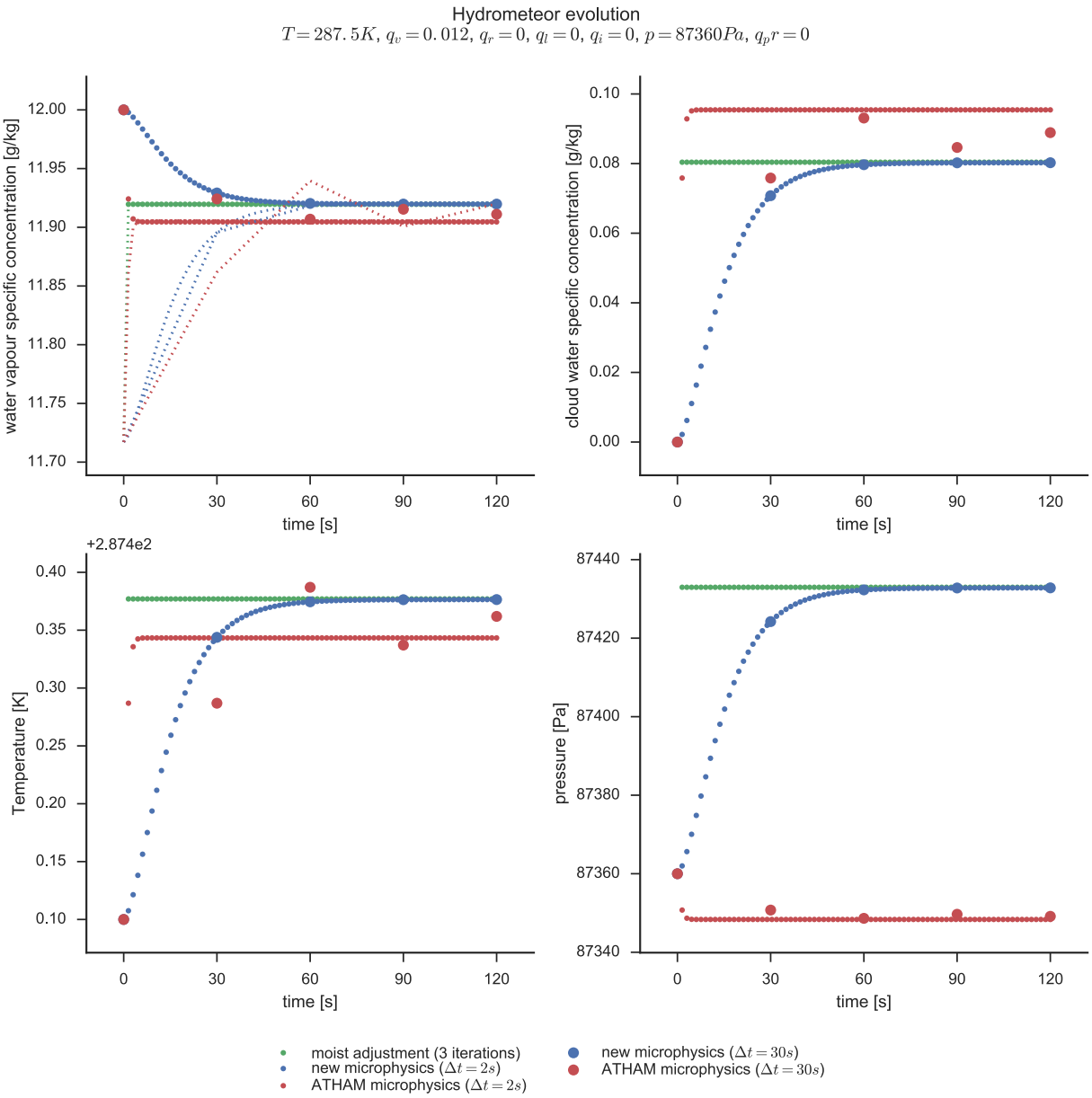

Figure 4.4: Plot of microphysical evolution (isometric) with old ATHAM and new microphysics with both short ($2s$) and long ($30s$) integration time-scale in the host model. Note how the old ATHAM microphysics overshoots and creates oscillations in hydrometeor concentration, temperature, etc., whereas predictions of the new microphysics model is unchanged as the host-model timestep is changed (due to the adaptive-timestep sub-cycling within the new microphysics scheme). Also note that the old ATHAM microphysics incorrectly predicts a reduction in pressure in the isometric integration.

Chapter 5

Single-cloud studies

In this chapter the methods, analysis and results regarding studying the behaviour of individual convective clouds using high-resolution modelling are presented. The aim of this chapter is to gain insight into the dominant characteristics of the development of convective clouds, firstly, to assert what parameters of the environment and the cloud-producing localised perturbation are important for the cloud's eventual vertical structure, and secondly, to study how these parameters interact with the entrainment of ambient air. Having a more complete understanding of the relative importance and interplay between the different factors contributing to the cloud's development will serve as insight that will be used to discuss the assumptions and formulation of the existing CCFM convection scheme, and will secondly serve to indicate under which conditions the traditional Morton-Turner entrainment parameterisation for individual clouds may require modification, so that the 1D cloud-model used within CCFM may be improved.

The use of numerical modelling allows that the cloud may evolve freely once the initial and boundary conditions have been defined, so that the exact evolution of the cloud is driven only by the spatial and temporal variation in mass, momentum and energy and the physical laws of conservation that govern these (the Navier-Stokes equations). To facilitate the production of a convective cloud in a numerical simulation, the initial condition, the ambient atmospheric profile, must contain a vertical region within which the atmosphere is conditionally unstable (i.e. unstable under vertical displacement of saturated air parcels), and an isolated region in this atmosphere must be perturbed so as to become positively buoyant. The approach to defining the atmospheric profile will be covered in Section 5.1.2 and the cloud-producing perturbation will be discussed in 5.1.3.

There are two elements to the numerical simulations in this chapter that could lead to non-physical cloud evolutions, both of which will be addressed in individual sections. Firstly, due to numerical discretisation necessary when solving the governing equations on a computer, extra diffusion (in this context called *numerical diffusion*) may occur and, if the grid-resolution is too poor (i.e. the minimum length-scale represented is large), may dominate the evolution of the convective cloud. This issue will be investigated through

examining the change of a cloud's evolution with changing resolution in Section 5.1.4. Secondly, the method by which a localised region is made buoyant to produce a convective cloud may force the system into a non-physical state, if for example the perturbation is large enough to alter the ambient environment, or the perturbation itself may become the driving influence of the cloud's later evolution by providing buoyancy far in excess of what the cloud will attain through the condensation of water vapour. With the aim to study these issues and formulate a physically motivated approach for inducing the formation of a convective cloud, the effect of varying which variables are perturbed as well as the shape, magnitude and duration the perturbation will be discussed in Section 5.1.3.

With the possible pitfalls of numerical simulation in mind it is important to point out the vast flexibility available by fully controlling the initial (ambient) conditions and the cloud-producing perturbation. Firstly, by being able to exactly define the atmospheric profile and the perturbation that produces a convective cloud, the physical parameter space can be studied in a systematic manner instead of relying on variations developing organically in simulation (as will be studied in Chapter 6). To limit the numerical simulations to physically representative conditions, the parameter space has been restricted firstly by formulating a generalised atmospheric profile (Section 5.1.2) based on the horizontal mean profiles from large-domain simulations in Chapter 6; secondly, by using predictions of the lifted-parcel model of convective initiation and, thirdly, by extracting characteristic distributions of cloud-base perturbations from large-scale high-resolution simulations (Chapter 6). In addition to enabling systematic study of the parameter space the use of numerical simulation also allows that a so-called *passive tracer* may be added to the flow, a variable that is simply advected by the flow but without affecting the flow, and so may be used to indicate the extent to which different regions have mixed. Using a number of passive tracers it is thereby possible to numerically estimate the extent of entrainment into a cloud, the details of which will be given in Section 5.1.5.

The research questions in this chapter concern, firstly, defining the requirements when performing numerical simulation of convective clouds, and, secondly, how different processes affect a cloud's development. Specifically the aim is to understand:

- to what extent are axisymmetric simulations adequate in capturing the dynamic behaviour of a convective cloud? Are the predictions of total precipitation and cloud-top height robust?
- to what extent does the lifted-parcel model produce correct estimates of the perturbations necessary to overcome the convective inhibition?
- how does entrainment vary through the vertical structure of a convective plume, and during its development? Does entrainment change when going from 2D axisymmetric to 3D simulations? Does the presence of precipitation alter the entrainment characteristics?

- what is the predictive skill of the 1D cloud-model equations when comparing to profiles extracted from LES, in particular with respect to predictions of cloud-top height and total precipitation?
- how does precipitation effect the development of a convective cloud? This will be studied through enabling/disabling the rain-formation in the cloud-microphysics, and through this, asses the importance of rain formation and seek to constrain the poorly defined *rain-out rate* formulation currently in CCFM.
- what factors control whether a transient thermal or steady-state plume will be developed? Are these the same in 3D and 2D axisymmetric simulations?
- how does windshear affect the development of a convective plume? Specifically how are cloud-top height and precipitation affected?

Before being able to answer these questions, the physical validity of the modelling setup had to be verified (as mentioned above, these are in Section 5.1), and thereafter a number of procedures for analysis had to be created which will briefly be discussed here.

To compare against the 1D cloud-model (and in the context of volcanic plumes against the traditional 1D models) it is necessary to reduce the four (or three) dimensional dataset describing evolution of the whole simulated 3D (or 2D axisymmetric) domain in time, and through this to produce a one-dimensional profile of plume variables.

The way in which this reduction in dimensionality is done depends fundamentally on whether we assume the convective cloud to be in a steady-state or not. As mentioned above a convective cloud may under some circumstances appear to bear the characteristics of a steady-state plume and under others may appear more like a bubble. In the former regime only a single timestep (once steady state is reached) is analysed and the vertical coordinate represents the vertical height in-cloud, in the latter regime each timestep represents the entraining parcel having reached a given height and so successive timesteps are analysed to produce a vertical profile describing the state in an entraining parcel at a given height. Both of these regimes may be represented by the entraining-parcel model (Chapter 3) as its formulation does not in itself assume steady-state, the only term changing between either regime is the drag-coefficient which depends on the cloud's topology.

Finally the plume envelope (edge) must be defined so that the in-cloud region can be separated from the environment and in-cloud values can be calculated. Many choices can be made in terms of how this plume envelope is defined, both in terms of which scalar fields are used and the cut-off value is used. Bearing this in mind it was important to establish the extent to which these in-cloud estimates would be affected by how the cloud edge is defined as this would make any analysis of a cloud dependent on exactly how the edge was defined. This has been carried out below in both the view of steady-state and temporal analysis.

These analysis methods were developed so as to facilitate the analysis of any 2D axisymmetric or 3D plume simulation, and were during this study applied in two recent publications as part of a volcanic plume simulation inter-comparison study (*Suzuki et al.* [2016] and *Costa et al.* [2016]) to simulations performed with ATHAM.

5.1 Simulation setup

In this section the tools, setup and considerations necessary when carrying out numerical modelling of individual convective clouds will be detailed. Firstly, the numerical model used (the Active Tracer High-resolution Atmospheric transport Model, ATHAM) will be described in detail, including issues identified and fixed through its use (Section 5.1.1). Secondly, the initial condition in terms of vertical atmospheric profile necessary for producing convective clouds in simulation will be reviewed. Thereafter the methods developed for locally perturbing the atmospheric structure to induce condensation will be discussed, with emphasis on the shape, time-dependency and magnitude of the perturbation and what physical variables may perturbed to minimize non-physical simulations. Finally, the necessary resolution and the extent to which 2D axisymmetric simulations are adequate will be studied.

5.1.1 ATHAM

All simulations in this chapter were performed with the Active Tracer High-resolution Atmospheric transport Model (ATHAM, *Oberhuber et al.* [1998], *Herzog et al.* [1998]). ATHAM is a non-hydrostatic finite-difference numerical model which is solved in on a Arakawa C-type grid (i.e. the velocity components are staggered relative to the cell-centers, being defined on the volume faces) using a semi-implicit solver, where the advective and source terms are first integrated explicitly, after which a pressure field is found implicitly, which removes any divergence in the velocity field; (this is the common predictor-corrector type approach which is typically employed when solving this type of equation: see the references above for details).

ATHAM assumes that exchange of momentum and heat between the fluid's constituents is in equilibrium, so that a single equation for volume mean momentum and heat content is used. However, ATHAM does allow for the relative movement of a fluid's constituents explicitly using the fall-velocity of rain to predict precipitation rate.

5.1.1.1 Fixes to and peculiarities in ATHAM

During the research carried out in this work a number of aspects of ATHAM were improved. In particular the following issues were addressed:

- previously ATHAM contained an incorrect formulation of mass conservation equation so that addition of water vapour led to an increase in mixture density.

- a new microphysics representation was implemented (as discussed in Chapter 4). The main limitations of the old microphysics scheme were the saturation adjustment-based creation of cloud-condensate and the time-split integration scheme making the microphysical state sensitive to the integration order of the different processes. The new microphysics implementation explicitly resolves the finite condensation time of cloud droplets and integrates all microphysical processes in parallel.

- previously ATHAM assumed a reference surface pressure which, due to how atmospheric profiles were represented in the simulation configurations, caused the atmospheric profile in the initial condition to be miss-represented. This in turn lead to the LCL and LFC being at incorrect heights when attempting to reproduce the environmental conditions of the RICO shallow convection study (see Chapter 6 for details about RICO), making comparison with the analysis of Chapter 6 impossible.

Finally some issues were encountered which should be addressed in further work:

- for numerical stability ATHAM uses an artificial diffusion which removes interpolation overshoots. Unfortunately this diffusion has the exact same effect as the process of entrainment (the effect of mixing) and so to study the process of entrainment (the focus of this study) it is necessary to use a high enough resolution so that the majority of mixing is done by resolved eddies and not by the numerical diffusion. The artificial diffusion is applied with an integration timescale so that any feature with a characteristic time-scale smaller than this time-scale is filtered out. The time-scale must currently be manually set, but it is difficult to predict what an appropriate time-scale should be. Through experimentation using the warm bubble test case of *Bryan and Fritsch* [2002] it was noted that the necessary time-scale decreases as the resolution is increased, so that less artificial diffusion is needed. At $\Delta x = 10m$ resolution a diffusion time-scale of $\tau = 120s$ appears adequate. In future work it would be beneficial to either remove the need for the artificial diffusion (by implementing a different advection scheme) or to formulate the diffusion term in a manner so that it is no longer necessary to manually identify an appropriate value for a particular grid-resolution, but instead make this diffusion term scale in a predictable manner as the grid-resolution changes.

- when performing 2D axisymmetric simulations of convective clouds the rising cloud would frequently form a kink at the bubble front. This indent would deepen over time eventually causing the cloud to non-physically split. As the bubble front is the most buoyant and contains the largest amount of cloud condensate this splitting and is non-physical. It appears that this issue arises from the odd-even ordering of the

relaxation method used to solve the elliptic problem of the pressure equation, so that the on-axis pressure in some instances was predicted too high. This would cause evaporation which would further reduce the buoyancy, leading to a positive feedback of eventual splitting at the bubble front. The issue may also be an artifact of the fact that the cylindrically symmetric fluxes are computed through area-weighting instead of as a source-term as in *Toro* [2009]. This indentation is not observed when performing 3D simulations and should be investigated in future work.

5.1.2 Environmental (ambient) conditions

All simulations carried out in this chapter were performed using an idealised atmospheric profile (see Figure 5.1) which contains the characteristic properties of an atmosphere in which shallow convection may take place. These profiles are characterised by two distinct layers: 1) the surface boundary-layer and 2) the moist convection permitting-layer, above which a temperature inversion caps the profile and inhibits vertical growth of convection. Assuming the boundary-layer to be well-mixed the potential temperature and moisture content (water vapour specific mass) is assumed to be near-constant in the boundary layer. Defining the surface pressure as $p_0 = 101325Pa$, the idealised profiles are characterised by six variables, the first three define the boundary-layer properties and condensation level relative humidity: the boundary-layer depth (z_{BL}), surface relative humidity (RH_0) and the surface potential temperature (θ_0), and the remaining three defining the convection-permitting layer: the inversion-layer height (z_{INV}), the lapse-rate $\Gamma_{II} = \frac{dT}{dz}$ (required to be $\Gamma_{dry} > \Gamma_{II} > \Gamma_{moist}$ for conditional instability) and the relative-humidity gradient ($\frac{dRH}{dz}$).

In this work this profile is applied to simulating shallow convection, with characteristic values for the above parameters extracted from the large-domain shallow convection simulation in Chapter 6. This profile can also be used for studying deep convection by simply increasing the inversion layer height (z_{INV}) to the tropopause height and reducing the magnitude of the lapse rate and relative humidity gradient.

In future work observational studies of atmospheric profiles and precipitation rate, for example observational datasets from the ARM IOPs (Intensive Operational Period), will be used to test the improvements made in CCFM as a whole (including the spectrum calculation which is not studied in this work). This was not done in this study because the measured atmospheric profiles in observational datasets frequently contain numerous variations in lapse-rate, moisture gradient, etc which when used in simulation all contribute to the eventual structure and general properties of developed convective clouds. By using idealised profiles the number of features can be carefully controlled and the influences on characteristic features of developed convective clouds can be more clearly attributed to the structure of the atmospheric profile. In Section 5.3.6 the wind-profile of Chapter 6 is in addition used so that the effect of windshear on convective cloud development may be investigated.

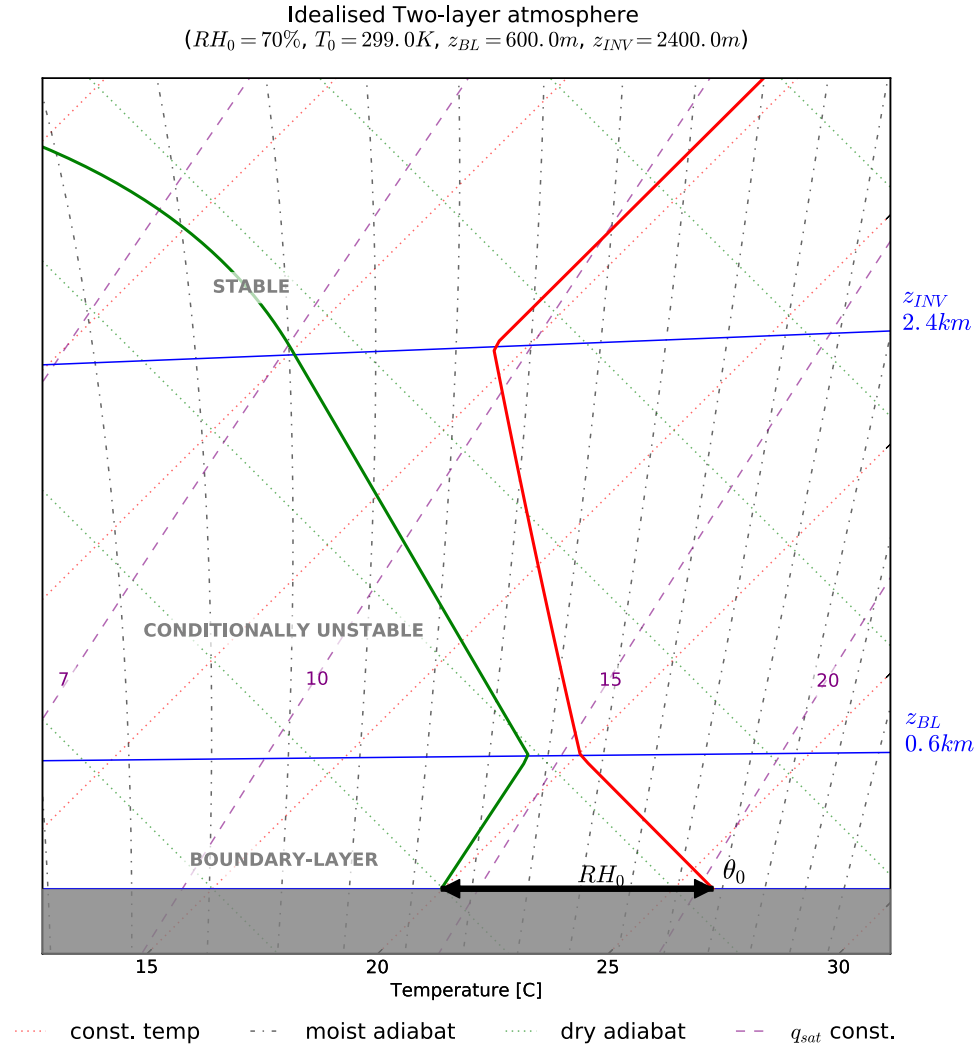

Figure 5.1: Tephigram of idealised profile used for shallow convection simulations. Note the well-mixed boundary layer up to z_{BL} above which is a conditionally stable layer, capped by an inversion (at z_{INV}). By varying the surface relative humidity (RH_0), potential temperature (θ_0) and boundary-layer depth, as well as the lapse rate and vertical gradient of relative humidity above, this profile can be used to systematically study how moist convection takes places under different conditions, varying the convective inhibition, level of free convection and saturated adiabat at free convection.

5.1.3 Cloud forcing

To form a convective cloud in simulation two ingredients are necessary: firstly an atmospheric profile with a layer of conditional instability, and secondly a perturbation which causes localised condensate to form and thus triggers the positive feedback of further condensation through convectively buoyant air. The former can be achieved by using an idealised atmospheric profile (as in figure 5.1) as the initial condition and the latter by introducing an appropriate perturbation in a localised region in the simulation domain. The purpose of this section is to discuss the approach used for finding these cloud-producing perturbations.

In Section 2.1 the lifted-parcel model approach to finding the minimum vertical velocity (w_{CIN}) required to overcome the convective inhibition (CIN) was introduced. This first-order model was used to constrain the parameter space of physically relevant perturbations in numerical simulations performed, to test the applicability of this parcel model to predict the actual CIN when considering all dynamical effects, and examine the extent to which the combination of moisture and temperature perturbation may be used to predict the cloud-top height.

In simulation output the transition from inhibited to free convection can be observed as a rapid increase in maximum cloud altitude as the moisture or temperature perturbation is increased, so a small change in perturbation causes a large change in the eventual maximum cloud altitude. This can be seen in figure 5.2. By picking the points of rapid transition the relative importance of water vapour and temperature in overcoming CIN can be determined so that $\frac{d\Delta q_v}{d\Delta T}\Big|^{simulation}_{e_{CIN}=const} \approx 1.4 g/kg/K$ which is very close to the lifted-parcel model predictions of 2.1 suggesting that for these simulations the transition to free convection can well described by considering purely the thermodynamics. There is however one important caveat here which points to a numerical artifact in ATHAM mentioned in the previous chapter. At larger perturbations in temperature the front of the cloud was observed to "split", as a small indentation in plume front on the centreline would be exacerbated and causes the cloud to split into two. This observation means that 2D axisymmetric simulations with high ($\Delta\theta > 0.6K$) temperature perturbations in this work are to a lesser degree physically capturing the evolution which would be expected.

It is important to point out here that the *actual* perturbation present at the time of condensation at cloud-base is not the same in magnitude and shape/size as was introduced below cloud-base. This is due to the fact that the rising (non-saturated) bubble which is created through the localised perturbation mixes with the environment, both drying it out and causing it to cool. The amount of mixing was seen to be heavily dependent on the grid-resolution used, so that at higher resolution the amount of mixing was drastically reduced. It is therefore clear that a large amount of the mixing that does take place is due to numerical diffusion. Nevertheless, the general agreement above in prediction of the relative importance of heat and moisture in leading to convective cloud formation

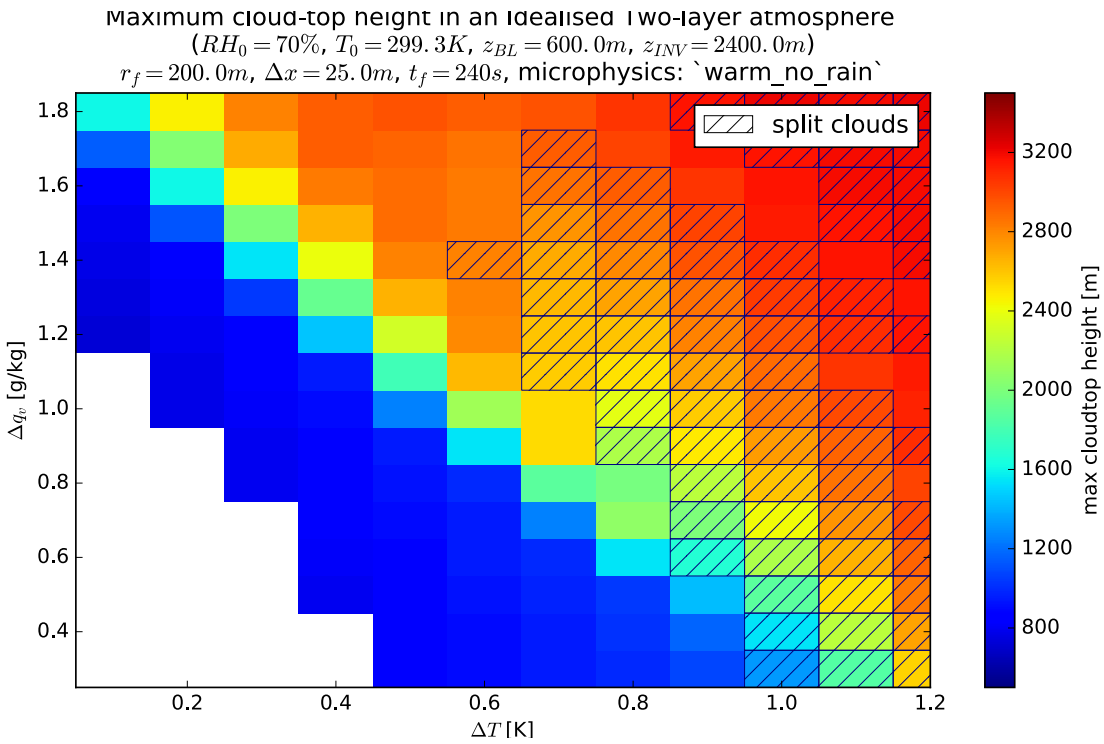

Figure 5.2: Maximum cloud-top height for *axisymmetric* cloud-simulations in ATHAM ($\Delta x = 25m$) with varying magnitude of potential temperature and moisture perturbation of radius $r_f = 200m$. The transition to free convection is clearly visible as the discontinous change in cloud-top height (from $z \approx 800m$ below the CIN layer, and rapidly increasing above) as the water vapour perturbation is increased for different values of temperature perturbation. Due to an issue in the ATHAM numerics some clouds split along the centreline, as these go through a different dynamical evolution these have been identified in the plot. Note that a large number of clouds were observed to non-physically "split", which likely alters the entrainment characterisics and thus cloud-top height.

indicates that at a given resolution non-saturated bubbles at a fixed grid-resolution mix similarly with the environment, and so the fractional change in moisture and heat content could be predicted based on the amount of numerical diffusion. As an indication of the correlation between cloud-producing perturbation and cloud-base conditions Figure 5.3 shows the magnitude of both, indicating that at for example $\Delta x = 25m$ the perturbation is on the order of 1/3 of the perturbation which was introduced.

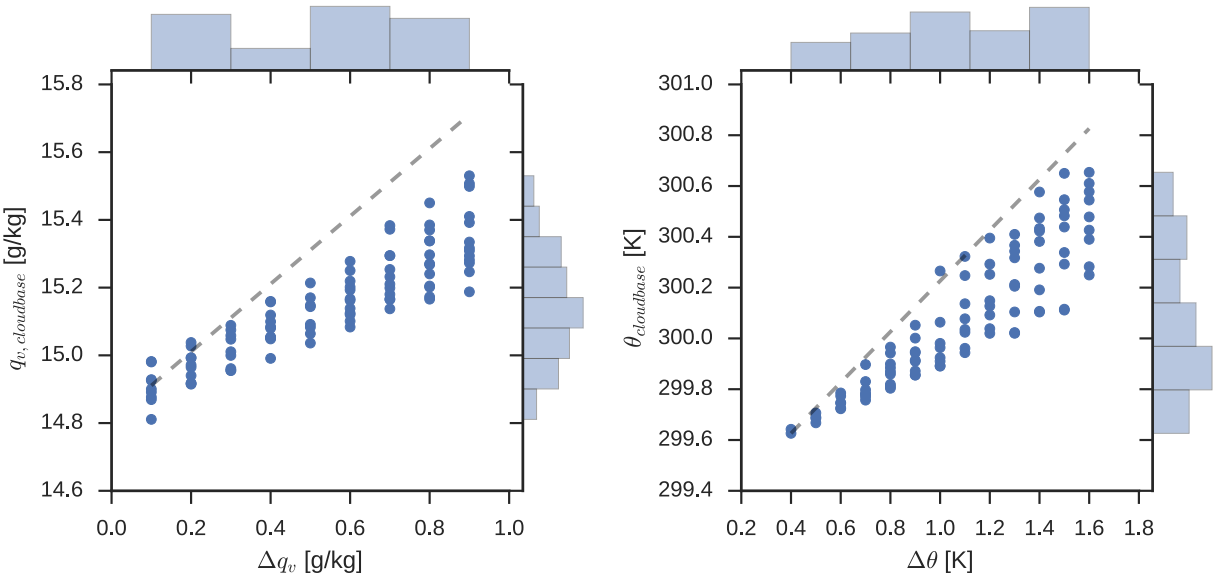

Figure 5.3: Perturbation extracted at cloud-base vs locally introduced perturbation which triggered convective cloud formation from LES. Note that the perturbation at cloud-base is significantly less than was introduced in the below-cloud perturbation, if the cloud-base perturbation was the same value all points would fall on the dashed unit line.

5.1.4 Resolution and domain symmetry

In this section the aim is firstly to assess to what extent resolution is important in numerically simulating individual convective clouds, and secondly to assess the extent to which 2D axisymmetric simulations are able to capture the dynamics of convective clouds. These are important considerations because increasing the spatial resolution leads to a rapid increase in the computational cost, so that for example doubling the resolution in 3D typically causes at least a $2^4 = 16$-fold increase in simulation time (8-fold from doubling resolution in each dimension, and additional 2-fold due the fact that because of the CFL-criterion, the maximum timestep size is inversely proportional to the grid resolution, doubling the number of timesteps required). Similarly the use of 2D axisymmetric simulations allows a drastic reduction in simulation time. In this context a number of simulations have been performed of individual clouds simulated in both a 3D and with 2D axisymmetric setup, with varying resolution and with varying perturbation size (in terms of water vapour). From each simulation the cloud-top height (defined as the highest point with $q_l > 0.1g/kg$) during a cloud's evolution was extracted and plotted in Figure 5.4. Using the cloud-top height as a characteristic property of

a cloud's evolution facilitates the analysis of the effects of varying grid-resolution on a cloud's development using just a single variable, which although not capturing *why* changes to a cloud's evolution take place the cloud-top height does indicate *how* a cloud's evolution changes. As the ultimate aim of this chapter is to understand the full dynamical characteristics of convective clouds, the spatial and temporal evolution of other in-cloud variables will be considered in later sections.

The first characteristic property for all resolutions, perturbations and for both 2D axisymmetric and 3D simulations is that the initial condensation height is $\approx 750m$, very close to the height predicted through adiabatically lifting a parcel (Section 2.1) and in agreement with near-constant cloud-base height across multiple clouds predicted in the large-domain simulations analysed later in this thesis (Chapter 6).

Across all resolutions it is clear that as the magnitude of the cloud-forcing perturbation is increased the ability of the produced cloud to overcome the convective inhibition is increased and the cloud achieves a higher maximum altitude. However the critical value of perturbation magnitude determining whether a cloud will overcome the CIN and reach the level of free convection (LFC) is strongly resolution dependent, so that at the finest resolution ($\Delta x = 12m$) a water vapour perturbation of $\Delta q_v = 1.0g/kg$ produces a freely convecting cloud, whereas at the two coarser resolutions ($\Delta x = 50m$ and $\Delta x = 25m$) the same perturbation does not lead to a freely convecting cloud. This is likely due to higher mixing with the environment at the coarser resolutions due to the increased numerical diffusion at coarser resolution, causing dilution of the cloud and thereby loss of buoyancy.

The increased mixing at coarser resolution can also be observed by noting that the predicted cloud-top height generally increases with increasing resolution, so that higher resolution leads to less mixing with the environment, thereby less dilution of the cloud-core, making the cloud more buoyant and thus a higher final altitude. Similarly at higher resolution the resulting cloud's larger buoyancy causes the cloud to rise more rapidly.

Another noticeable trend is that the change in cloud-top height with change in perturbation size is dependent on the grid resolution, so that at the highest resolution ($\Delta x = 12m$) there is little change in the maximum cloud-top height with change in perturbation magnitude compared to the change in cloud-top height at lower resolution ($\Delta x = 50m$ in particular). This may due to entrainment playing a stronger role than numerical diffusion at higher resolution, as entrainment is dependent on the cloud-radius (circumference scaling as r vs cross-sectional area scales as r^2) whereas the amount of numerical diffusion happens at each time step, so that slower rising clouds experience more numerical diffusion.

It is interesting to note that the 2D axisymmetric simulations generally agree well with the 3D simulations during most of the cloud's vertical growth phase, even at the relatively coarse resolution of $\Delta x = 25m$ where convergence clearly has not been reached. For the highest resolution simulations the 2D axisymmetric clouds generally overshoot as compared to the 3D simulations, which may suggest that the 2D axisymmetric clouds to a

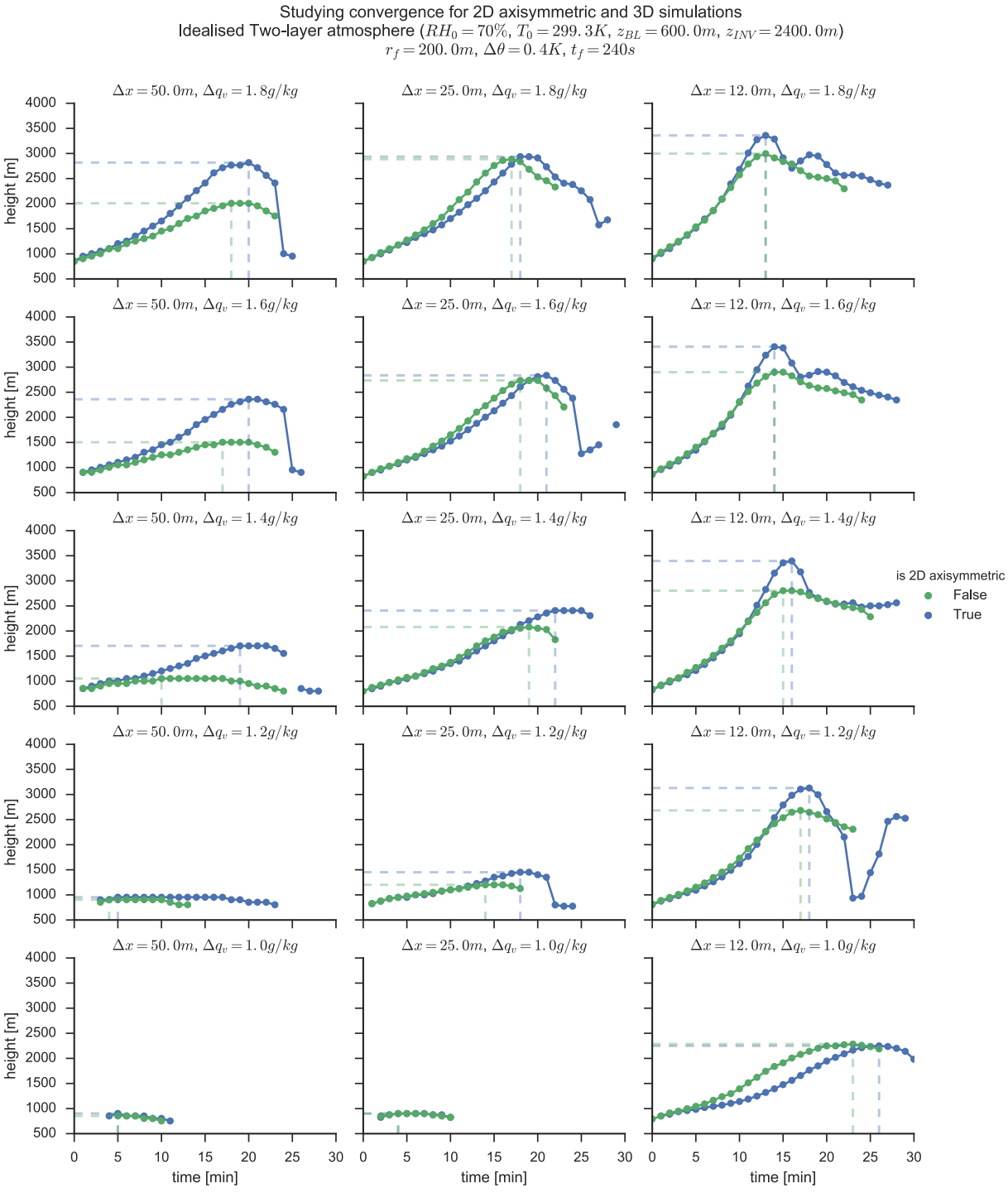

Figure 5.4: Evolution of cloudtop height for 3D and 2D axisymmetric simulations in ATHAM with varying resolution (Δx) and varying cloud-triggering perturbation (Δq_v), with increasing resolution to the right and highest perturbation at the top. Cloud-top is defined as maximum altitude where $q_l > 0.1g/kg$. The stippled lines indicate the time and height when the maximum altitude was reached.

lesser degree mix in ambient air during the deceleration experienced once the inversion at $z_{INV} = 2400m$ is reached, so that the 3D clouds experience a more rapid deceleration due to higher entrainment of ambient air. This could be due to the entrainment eddies in 2D axisymmetric simulations being constrained to the radial and azimuthal directions, thereby restricting the form mixing that can take place.

In addition, generally the 2D axisymmetric simulations reach their maximum cloud-top height later than the 3D simulations; this is largely due to the axisymmetric clouds staying buoyant for longer and reaching a higher altitude.

Given the above analysis it appears that at least $\Delta x = 12$m resolution is required to capture the dominant dynamical effects that affect the growth of convective clouds, although further simulations shold be performed at higher resolution to ensure convergence is achieved. In addition 2D axisymmetric simulations do not appear to capture the full development and decay of a convective plume, but may possibly be of relevance to the growth phase of a convective plume and could also be used to form qualitative arguments about the influences on cloud-top height.

5.1.5 Discrete estimate of entrainment rate

In this section the different methods by which the entrainment rate is estimated are detailed. All methods discussed below require that the cloud edge (or envelope) has been defined (which will be discussed in Sections 5.2 and 5.3 for steady-state and transient analysis respectively) and that an "axis of evolution" (either time or a distance coordinate) be defined (as will also be discussed in the later sections). Once these are known so that the region into which entrainment takes place is known as well as the direction along which entrainment changes, we may consider how to formulation the calculation of entrainment rate. In this section three methods will be detailed.

Firstly, using the definition of the entrainment rate it may be calculated from the vertical derivative in the total mass-flux at a given height:

$$\mu = \frac{1}{M}\frac{dM}{dz}$$

In Chapter 3 it was shown that this may equivalently be formulated by considering the mass of a parcel of m into which mass is being entrained. Using this formulation the entrainment rate can be estimated considering the entire cloud as an entraining parcel:

$$\mu = \frac{1}{m}\frac{dm}{dz} = \frac{1}{m}\frac{1}{w}\frac{dm}{dt},$$

where in the final form the vertical velocity has been used so that the entrainment may be evaluated when considering the transient evolution of the cloud.

The second method for estimating the entrainment rate uses a so-called passive tracer to track the source of mass which is present inside the plume envelope. This passive tracer is a scalar field which is simply advected with the flow but doesn't affect the flow, in so in effect a passive tracer simply "colours" the fluid (exactly as it was done in water-tank experiments in the 1960s).

The implementation in this work uses a passive tracer ϕ_0 which is initialised to be $\phi_0 = 1$ above the cloud-base condensation height (determined using the lifted-parcel approach in Section 2.1 and another tracer set to $\phi_0 = 0$ below the cloud-base height. As the simulation evolves the tracer is reset to $\phi_0 = 0$ below cloud-base height so that any fluid fed up through the base of the cloud is guaranteed to have $\phi_0 = 0$. The density of entrained mass anywhere inside the plume is thus $\rho\phi_0$ which may then be integrated over the entire plume or through a plume cross-section to compute the change in entrained air with height (the entrainment rate).

The third and final method for estimating the entrainment rate uses the cloud-model equations (Chapter 3) by isolating the entrainment rate and numerically evaluating (from LES simulations) the other terms in the cloud-model equations. Through the cloud-model integration studies in Section 3.4 it appears that the thermodynamic profile of a convective cloud shows the most impact of entrainment, and to a lesser extent the momentum and radius equations. For this reason the temperature equation would be the most appropriate to use.

5.2 Instantaneous (steady-state) plume analysis

In the section the instantaneous profile of individual clouds have been extracted from simulation. Through this the entrainment rate was calculated and compared to predictions by the Morton-Turner model. To perform this analysis is it is firstly necessary to identify the time at which the convective plume has reached at steady-state, its entire vertical structure being un-changed in time. As discussed in the introduction to this chapter, and as may be seen by the analysis of cloud-top height in Section 5.1.4, the shallow convective clouds studied in this work cannot generally be considered as attaining a steady-state, instead the cloud-base has generally disappeared by the time maximum cloud-top height is attained. However, as the cloud-model used in CCFM assumes steady-state (and for completeness), the convective cloud analysis will in this section be carried out as-if the cloud is in a steady-state. The timesteps used for analysis were picked to capture a point in a convective cloud's development where a well-defined cloud-base was still present while the cloud's vertical extent is significant.

To begin analysis of the quantities inside the plume it is necessary to define the plume boundary or envelope. The influence that the choice of cloud envelope has on the extracted cloud profile will be examined in Section 5.2.2. In *Turner* [1962] the difficulty of defining

the plume envelope is also discussed, in the context of defining the plume envelope in water tank experiments. There a passive tracer (a dye) was used, and the plume perimeter was chosen to be where the concentration of the tracer dropped to 1% of the initial value.

In regards to reducing the spatial dimensions of the data inside the plume, it was important to use a procedure which closely mimics the assumptions used in the 1D cloud-model. As the 1D model describes the mean plume behaviour as a function of height and assumes cylindrical symmetry it seems intuitive to compute average values of the scalars of interest in planes perpendicular to this central line of symmetry. The full 3D simulations are however by their very nature not cylindrically symmetric, and so although the concept of a plume centreline is still intuitive, defining it numerically is a significant challenge. A number of methods were developed to estimate this symmetry line, each of which will be detailed in Section 5.2.1.

Once the centreline is known and plume envelope is defined, the plume profile can be constructed as the mean over cross-sections perpendicular to the plume centreline. Section 5.2.3 briefly discusses the characteristics of such an instantaneous profile, motivating the need for consindering the time-dependent nature of convective clouds.

5.2.1 Finding the centreline

Common to all centreline methods is that once a starting position has been defined ($\mathbf{x}^0$, typically in the centre of the plume base) the local direction of centreline $\hat{\mathbf{e}}(\mathbf{x})$ must be continually approximated and integrated at chosen distance (Δx_c) to develop the full 3D structure of the centreline.

$$\mathbf{x}^n = \mathbf{x}^{n-1} + \Delta x_c \hat{\mathbf{e}}^n$$

A number of methods for approximating $\hat{e}^c$ were developed which will be detailed below and their relative merits outlined.

5.2.1.1 Plume-base released scalar gradient method

This method employs the use of a passive scalar which must be released at the plume base. It was developed in the context of volcanic plumes where the passive tracer described the SO_2 concentration, which is released at the volcano vent.

Following the intuition that in any given cross-section the centreline should pass through the point of largest concentration of SO_2, and the largest concentration of SO_2 in the whole domain will be present at the vent, it seems obvious that the centreline should be everywhere in the direction of the gradient of the scalar SO_2 field, so that

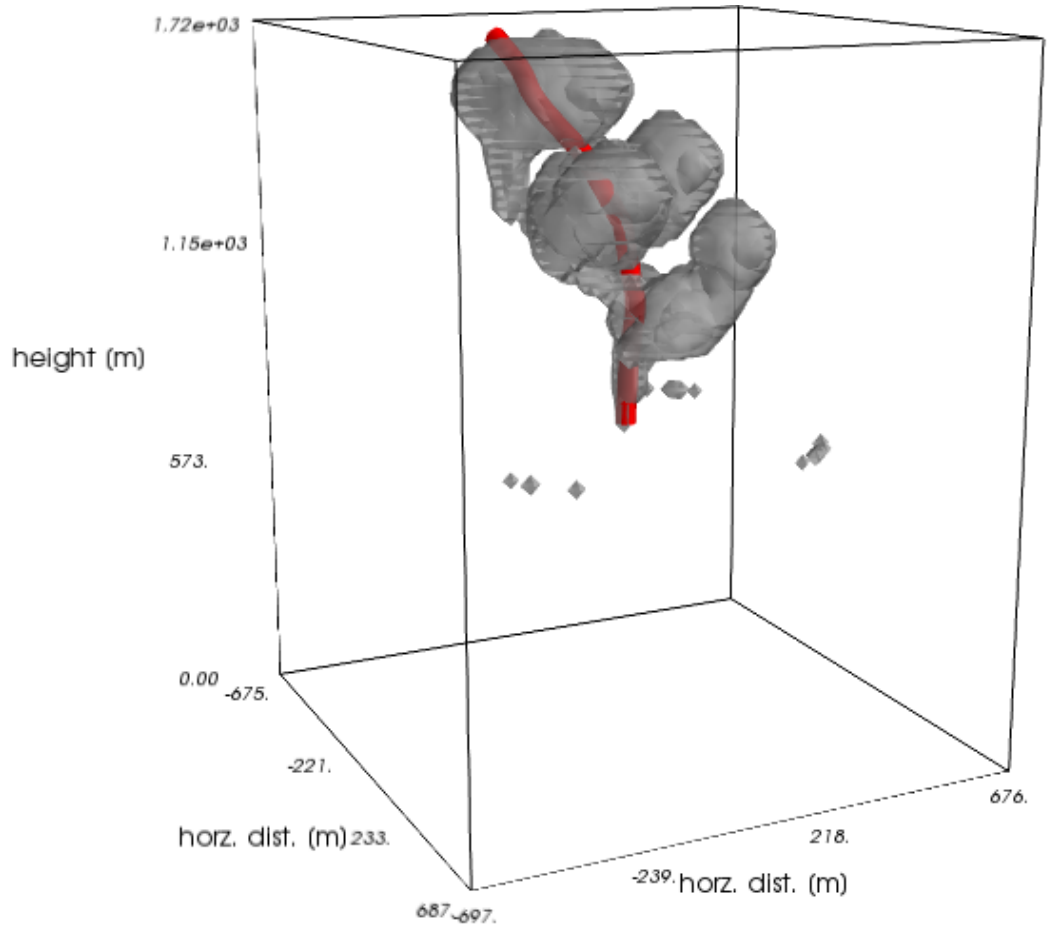

Figure 5.5: Plume envelope (defined by isosurface of liquid water specific mass $q_l = 0.1g/kg$) and centreline (in red) visualised from 3D LES with windshear. Note that the small amount of condensate near the LCL is likely from gravity waves triggered by rising thermal

$$\hat{\mathbf{e}} \propto \nabla q^n$$

This method is highly sensitive to local variations in the scalar concentration, and therefore the path integration was performed from low concentration, as the vent is likely to be in the direction of maximum increase of SO_2. This is similar to how there is a clear shortest direction to the top of a mountain (if there is a single, well-defined top) once a starting position (below) has been defined, however there are numerous ways to come off a mountain. The centreline direction is in decrease in SO_2 concentration away from the source, however the SO_2 concentration decreases in all directions away from the source. The important choice in this method is the choice of "plume top" position, which may be taken as the point farthest from source which is inside the plume envelope.

To avoid stagnating in local maxima of SO_2 concentration the direction for a particular integration step is formed as a linear combination of the direction in the previous step and the gradient at the current position

$$\hat{\mathbf{e}}^n = \alpha \frac{\nabla q}{|\nabla q|} + (1-\alpha)\hat{\mathbf{e}}^{n-1},$$

a value of $\alpha = 0.25$ was used, the greater the value the more the local gradient is used instead of previous gradient calculations. The optimal value for α can be found by starting at $\alpha = 1.0$, and then integrating from the starting point. If the end of the integrated curve does not lie near the volcanic vent then the curve-finding method has ended in a local maxima of SO_2 concentration. The value of α is then decreased, the curve integration repeated from the starting point ($\mathbf{x}^0$). This process is repeated until a curve joining the starting point and the plume vent has been found. By using the highest possible value of α the most information about the plume curvature is retained.

The local gradient (∇q) was calculated using the traditional 7-point second-order centered-difference stencil, from values interpolated from the full 3D solution defined on a stretched grid.

5.2.1.2 Principal rotation-axis method

The guiding idea here is the observation that the plume dynamics will cause a distribution of a plume scalar (e.g. mass) in a preferential direction along the plume's length. The local direction of the centreline was estimated by first calculating the local moment of inertia tensor and then numerically calculating the eigen-vectors and eigen-values. The eigen-vector with the largest eigen-value describes the mass distribution's preferential axis of rotation, and thus the local asymmetry in the mass distribution. This method has the benefit compared to the gradient method that the internal plume structure within a

defined volume is considered instead of simply the gradients in this volume. The method also does not require a passive scalar or the definition of the "end" of the centreline.

5.2.1.3 Shell-volume mass-distribution method

As a starting point this method needs a point at the plume base, the first direction is taken to be vertical. Using this starting point as the centre, a radially uniform distribution of points on a shell of an initial radius ($r_i = \Delta x_c$, where Δx_c is the target centreline point separation) is created.

Given r_{sphere} and Δx_c:

$$\begin{aligned}
\theta_i &= \frac{i\pi}{N^{lon}}, i \in 0...N^{lon}, \text{where } N^{lon} = int\left(\frac{\pi r_{sphere}}{\Delta x_c}\right), \\
\phi_{i,j} &= \frac{j2\pi}{N_i^{lat}}, j \in 0...N_i^{lat}, \text{where } N_i^{lat} = int\left(\frac{2\pi r_{sphere} cos(\theta_i)}{\Delta x_c}\right), \\
\mathbf{x}_{i,j}^s &= r_{sphere}\left[cos(\theta_i)cos(\phi_{i,j}), cos(\theta_i)sin(\phi_{i,j}), sin(\phi_{i,j})\right]
\end{aligned} \tag{5.1}$$

The envelope tracer is then interpolated at these points and the number of points inside vs outside the plume is determined. If all points are inside the plume, then the sphere radius is increased until the fraction of points inside relative to outside equals a certain fraction (through experimentation). To avoid infinite loops in the iteration the rate of the radius change is adaptive, decreasing in size as the number of radius changes is increased.

Having established the number of points on this interpolation sphere which are inside the plume these now provide an indication of the direction of the plume. Computing the average azimuthal and polar angle is however inadequate as can be seen by considering that the average angle of two opposite points in for instance the azimuthal plane, say at $\phi = 0$ and $\phi = \pi$ is $\pi/2$. There is therefore a degeneracy in the angle of the points on the sphere. To collapse this degeneracy the previous normal direction is used by reflecting the points that point in the opposite direction to the normal in the plane of the normal. Finally the azimuthal and polar angles are averaged and used to calculate a new guess $\mathbf{e}_{guess}$ for the normal. This normal is weighted together with the old guess, based on how similar the two are to avoid too rapid change in the centreline direction.

$$\begin{aligned}
\alpha &= \hat{\mathbf{e}} \cdot \hat{\mathbf{e}}_{guess}, \\
\hat{\mathbf{e}}^{n+1} &= (1-\alpha)\hat{\mathbf{e}}^n + \alpha\hat{\mathbf{e}}_{guess}
\end{aligned} \tag{5.2}$$

This method is constrained by the envelope geometry and does therefore not take into account the internal structure of the plume. It is possible that the angle degeneracy would

better removed by using the local principle rotation axis (extracted as described above). This will be investigated in further work.

5.2.2 Defining plume envelope

This section briefly outlines the considerations necessary in defining the plume edge when carrying out analysis of the entire convective plume as if in a steady-state. This discussion overlaps to a large extent with that in Section 5.3.1 and will be carried out in detail there.

As a first-order estimate of the sensitivity of in-cloud estimates to the definition of the plume envelope we may consider how the total volume of the cloud changes as the envelope criterion is changed. If the volume of a cloud is an intrinsic property of a cloud and less a function of the exact scalar value used to define the edge of the cloud, it would be expected that the cloud volume be largely unchanged as the envelope definition is changed. In Figure 5.6 the change in total volume of the cloud can be seen with changing envelope cut-off value, here using the cloud condensate to indicate the cloud interior. In this figure three regimes may be identified. Firstly with too high a cut-off value large parts of the cloud's interior are excluded and the cloud volume rapidly decreases as the envelope cut-off value is increased. In the other extreme with very small cut-off value parts of the domain which contain condensate due to the finite accuracy of the numerical model cause the cloud volume to change rapidly as the envelope value is changed. Note that the region for too low cut-off value is far below what would be assumed if machine precision was assumed (10^{-16} for double precision). In the third and intermediate range the cloud volume changes very little with change in envelope cut-off value. The presence of this region provides encouraging evidence that the volume of a cloud (and other state variables of a cloud as will be discussed later) is a characteristic property of a cloud and so may be defined in a way which is largely independent of how the edge if the cloud is defined.

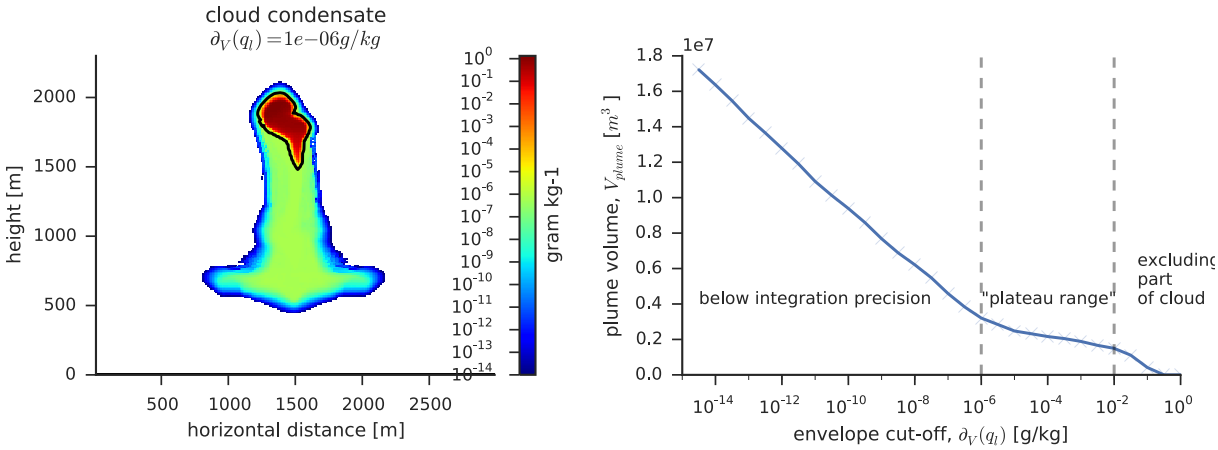

Figure 5.6: Left is vertical outline of cloud shown as max-value of cloud-condensate in one horizontal direction. The plume envelope at $\partial V(q_l) = 10^{-6} g/kg$ is shown in black. Right the value of the total cloud volume is plotted as a function of the envelope definition. The presence of an intermediate range where the cloud volume changes very little as the envelope is changed over several orders of magnitude suggests that the cloud volume may be thought of as an intrinsic property of the cloud. This simulation was carried out in 3D at $\Delta x = 12m$, with forcing charactericstic of shallow convection.

5.2.3 Cloud profiles

In Figure 5.7 the vertical instananeous profile of a convective plume simulated in 3D has been extracted. The radius was calculated as the radius of a circle with the equivalent area of a cross-section at a given height.

It is firstly noted that the convective plume is not in steady-state. This can be seen by the vertical velocity profile which should be positive throughout the vertical profile so as to provide transport from the cloud-base and through the plume to the cloud-top. In addition the radius profiles indicate that the cloud has multiple "lobes" each of which is evolving in time. This lobed structure is absent in 2D axisymmetric simulations showing the need for 3D simulations to capture the full dynamic behaviour of convective plumes.

Because of the transient nature of the plume it is also difficult to calculate the entrainment rate in a manner which would allow for predictions with the 1D cloud-model. The entrainment rate varies widely in many parts of the vertical profile becoming negative. It should be noted however that in parts of the vertical profile the LES estimated entrainment rate *does* agree very well with the Morton-Turner entrainment rate model, suggesting that through the cloud's evolution some regions do entrain exactly as would be predicted by the Morton-Turner model.

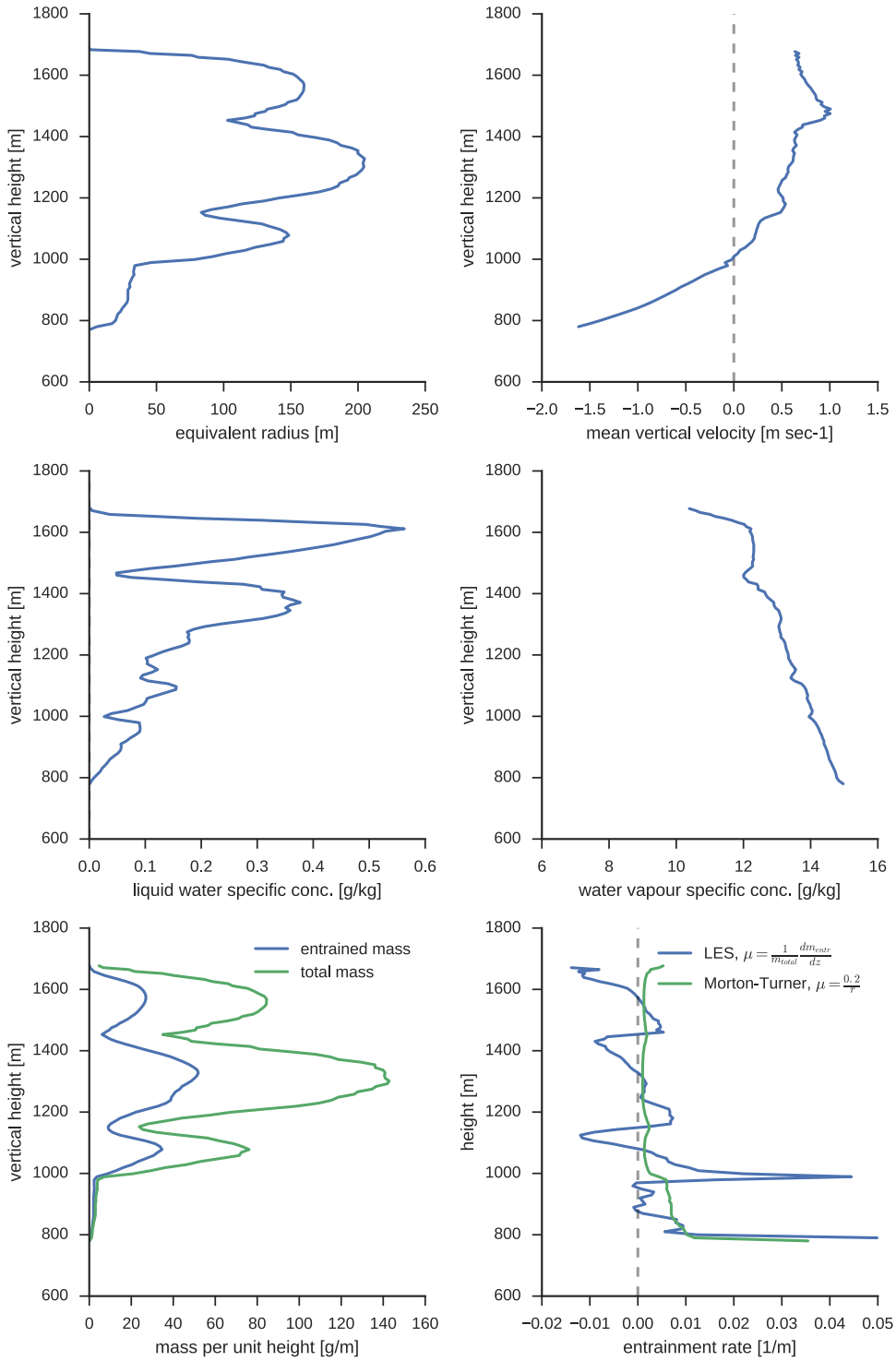

Figure 5.7: Vertical plume profile extracting a single timestep. The lobed structure and negative vertical velocity below $z \approx 1000m$ clearly shows that this cloud is not in steady-state. In addition the amount of total and entrained mass varies with the vertical lobes so that the entrainment rate estimate shows large variation with several regions of negative entrainment rate.

5.3 Transient (time-dependent) plume analysis

In this section the convective cloud's evolution in time is considered and the cloud's vertical profile constructed by considering the entire cloud as an entraining parcel. As well as requiring that the cloud's edge be defined (as with the steady-state analysis of the previous section) the transient analysis necessitates that one characteristic height, radius, temperature, vertical velocity and moisture content be predicted at every timestep in a cloud's evolution. The choice of how these characteristic values are calculated has implications for how comparisons to the cloud-model predictions can be made, and so should be calculated in a way that is consistent with the assumptions of the cloud-model (to the extent this is possible). This will be discussed in detail in the following sections.

Having asserted the appropriate methods for defining the plume envelope and calculating the cloud variables the section investigates the extent to which the entrainment rate diagnosed from simulation is in agreement with predictions of the Morton-Turner model. And finally the effect of rain formation and windshear on convective cloud development is briefly investigated.

5.3.1 Defining the plume envelope

In this section the method for defining the edge ("envelope") of the cloud is considered and its implications for the in-cloud estimates of temperature, moisture and vertical velocity are discussed. This is important because the comparison with the cloud-model assumes that the cloud *does* have a characteristic temperature, moisture content and vertical velocity at a given time and so these values should not change substantially if the envelope criterion is changed, otherwise the in-cloud values become a function of how the cloud edge is defined and not an intrinsic property of the cloud itself.

As the cloud-model predicts the change of these state variables as a function of height it will in addition be necessary to define the "height" of a cloud during its evolution, but since there is no unique measure of a height for a rising convective cloud this analysis will be studied in the next section. To avoid the complications arising from defining a cloud's height at a given time the sensitivity of the in-cloud variables to the envelope definition will here be studied as a function of time instead of height.

There are a number of variables which could be considered to enable the definition of a cloud's edge. Firstly the condensate itself (which defines what visually a cloud *is*) could be used. Secondly vertical velocity could be considered as the cloud is through its evolution rising. And finally a passive tracer might be advected with the flow to mark the interior and exterior of a cloud. As one of the principal aims of a convection model is to predict the vertical transport of moisture it would seem natural to use the condensate itself to indicate where a cloud is present. Through analysis of 2D axisymmetric and 3D simulations it

was noted that gravity waves produced from convection and compensating circulation outside the region of condensate lead to variations in vertical velocity which make it less robust as a method of defining the cloud edge. In addition when analysing convective clouds produced in an environment of wind-shear (Section 5.3.6) the direction of motion in and around the convective plume is no longer strictly vertical and so the use of velocity becomes challenging.

In Figure 5.8 the evolution of in-cloud potential temperature, moisture content and vertical velocity has been plotted for three clouds produced with increasing perturbation size and with three different cut-off values of cloud liquid water for the cloud envelope. Potential temperature and moisture content was calculated as a plume average whereas vertical velocity was calculated as the mass-averaged vertical velocity (i.e. by considering the vertical momentum of the entire plume). It was also investigated the extent to which the vertical velocity of the cloud's centre of mass could be used as a measure of the vertical velocity, however this variable (as will be seen in Section 5.3.3 when examining the entrainment rate) did not produce an entrainment rate which caused agreement with the predictions of the cloud-model. It is interesting that this measure of the vertical velocity produced estimates different from the mass-averaged vertical velocity and the origin of this will be considered of future work.

Firstly it should be noted that (as expected) that the cloud produced from the largest perturbation has higher potential temperature and liquid water content (because this cloud attains a higher altitude) and vertical velocity (due to larger CAPE).

Secondly the variation in each variable is only a few percent even when varying the plume envelope cut-off value of several orders of magnitude. This suggests that the convective cloud *does* have an intrinsic temperature, moisture content and vertical velocity as these estimates are relatively insensitive to the envelope definition. It should be noted here (as was mentioned in the instantaneous analysis in Section 5.2.2) that there is a limit to the range over which the envelope cut-off variable can be varied, in the extreme of too large a large part of the condensate region will be excluded and in the other extreme regions which will be included that only contain contensate due to the finite accuracy of the integration algorithm in the LES model.

It is interesting to note here that the vertical velocity in all clouds contains a variability on a charactericstic time-scale which through frequency analysis was seen to be at exactly the Brunt-Vaisala buoyancy frequency ($N = \sqrt{\frac{g}{\theta}\frac{d\theta}{dz}}$) at the height of plume growth, being gravity-waves triggered by the rising convection. To consider the longer time-scale vertical ascent of the cloud this frequency component was removed when examining the entrainment rate in Section 5.3.3 using a low-pass temporal filter.

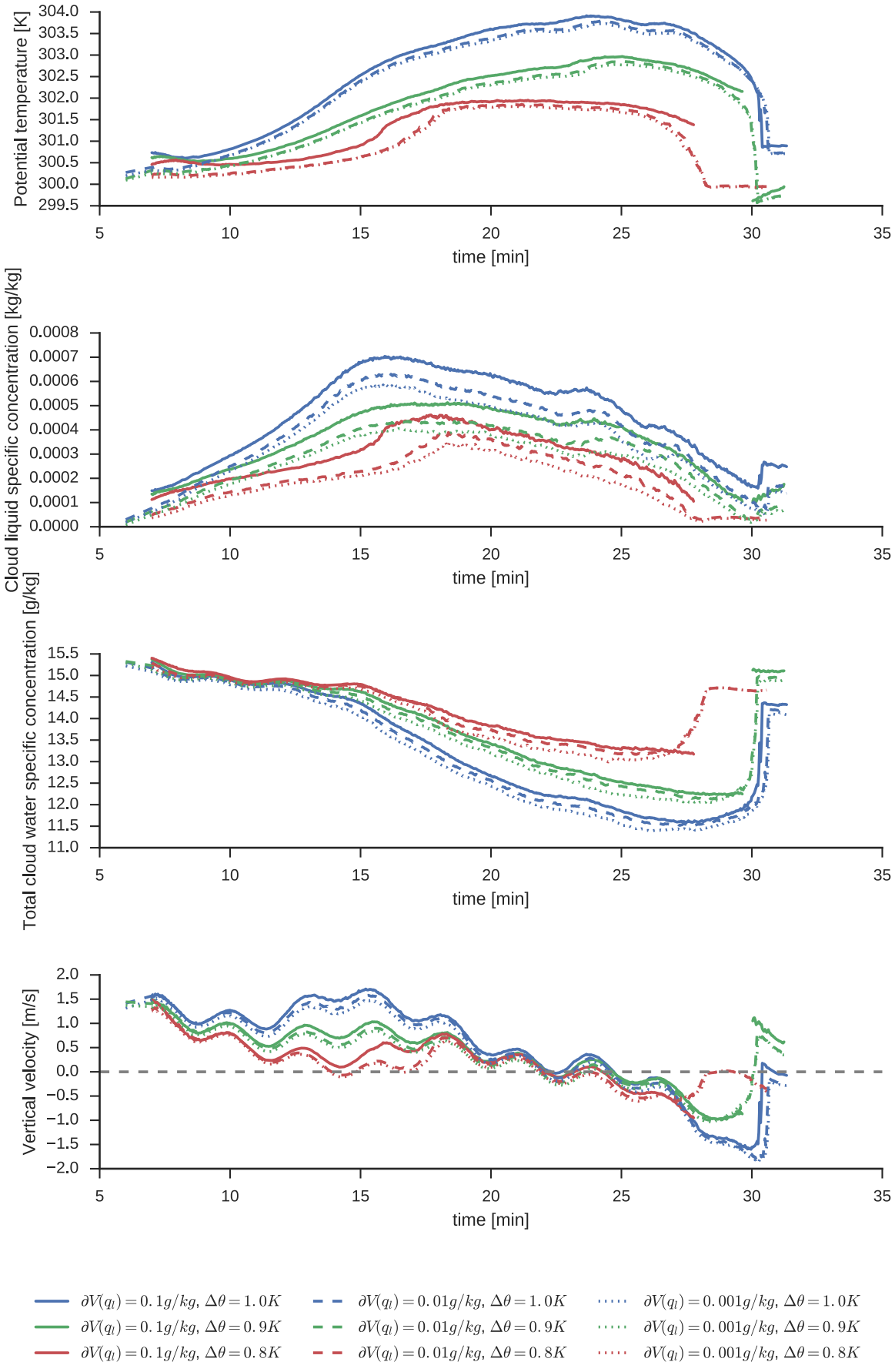

Figure 5.8: Temporal evolution of plume-averaged scalar values for three different initial conditions (with increasing temperature of the cloud-producing perturbation) in blue, red and green calculated with three different values for the plume envelope cut-off value ($\partial V(q_l) = [0.1, 0.01, 0.001]g/kg$) with different line-styles. Simulations were carried out with 2D axisymmetry at $\Delta x = 12m$. The closeness of lowermost envelope values indicates that smaller values are more appropriate for defining a plume "edge".

5.3.2 Plume radius and height

When comparing the evolution of a single convective cloud to the vertical profile predicted by the 1D cloud-model (Chapter 3) it is necessary to at every timestep represent the cloud's characteristic radius and altitude in addition to the in-cloud variables such as temperature, moisture content, vertical velocity which can be estimated by averaging over the plume envelope (as was described in the previous section). If the cloud did in fact rise in the shape of a perfect sphere (or even cylinder) it would be simple to estimate these variables as the center of this geometry and its radius. However, the shape of clouds evolves as a cloud rises and so defining these variables becomes non-obvious. One way of approaching this issue is to consider what impact each variable has on the predictive capability of the cloud-model as the ultimate aim is to produce the best-possible agreement between the cloud-properties extracted from the LES simulations and the predictions of the cloud-model.

The principal effect of the cloud-radius in the cloud-model is through the entrainment rate as defined using the Morton-Turner model, so that smaller clouds have greater entrainment. Two estimates of cloud-radius were considered (see Figure 5.9), firstly the radius at height of the maximum cross-sectional area (r_{max}, calculated as the radius of a circle with the equivalent area to a cross-section) and secondly a spherical radius (r_{sphere}), calculated as the radius of a sphere with same volume as the entire plume. By comparing these two measures as a function of height it is interesting to note that above $z \approx 1000$m the shape of the cloud is well approximated by a sphere, whereas below this height (in the initial condensation phase, before the LFC is reached) the cloud shape is more elongated and r_{max} is significantly larger. When comparing integrations of the 1D cloud-model to profiles extracted from LES (Section 5.3.4) there was no better agreement between the measured and predicted entrainment rate when either the of these estimates were used, and as r_{sphere} averages over the entire cloud envelope whereas r_{max} only uses the cloud cross-section at a single height the former is significantly less noisy than the latter, the former was used in further comparisons.

The principal effect of the exact "height" of a cloud is to determine exactly which environmental state is present at a given point in its evolution when integrating the cloud-model, and so defines the relative moisture and heat content that can be entrained and the buoyancy of the cloud at this point in time. Given the relatively large variations in the environmental state over short vertical distances the definition of a cloud's height becomes critical to getting any form of agreement between the cloud-model and the LES estimates. Four definitions of cloud-height were considered by integrating the cloud-model, which were: cloud-top height, maximum radius height and center-of-mass height. Using cloud-top height caused the environment to be too cold and dry, leading to far too buoyant clouds. Using the height of maximum radius was also discarded too to the high amount of numerical noise because of the few points being averaged over (as mentioned above

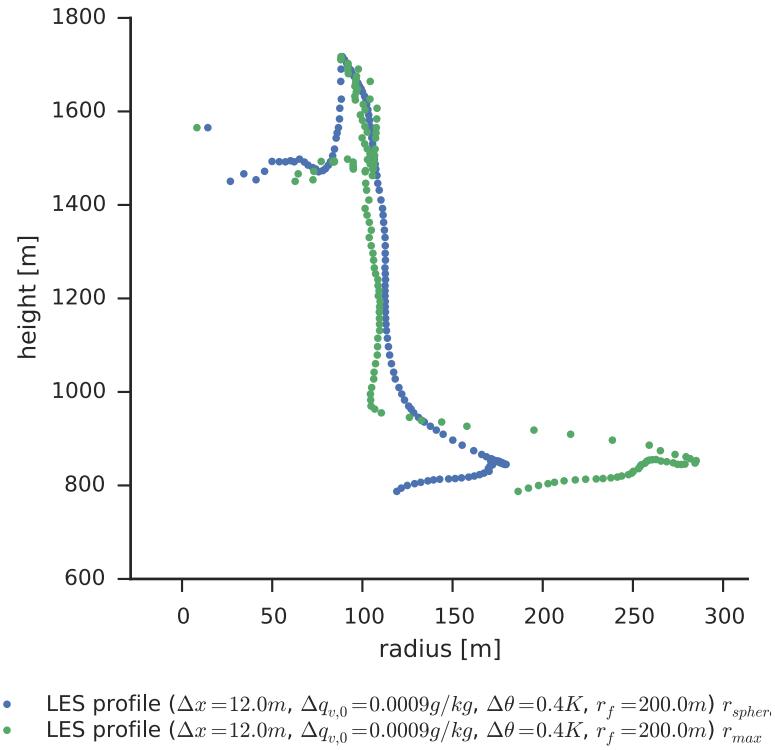

Figure 5.9: Vertical profile of cloud radius of a single convective cloud extracted from LES simulations using two different methods of radius estimation (equivalent spherical radius and maximum cross-sectional radius). Here mass-averaged height is used as the height coordinate

the maximum radius itself shows a large amount of numerical noise). It appears that an integral value such as centre-of-mass height is more robust as it considers the cloud as a whole, however it is significantly weighted towards the bottom of the cloud as density decreases with height.

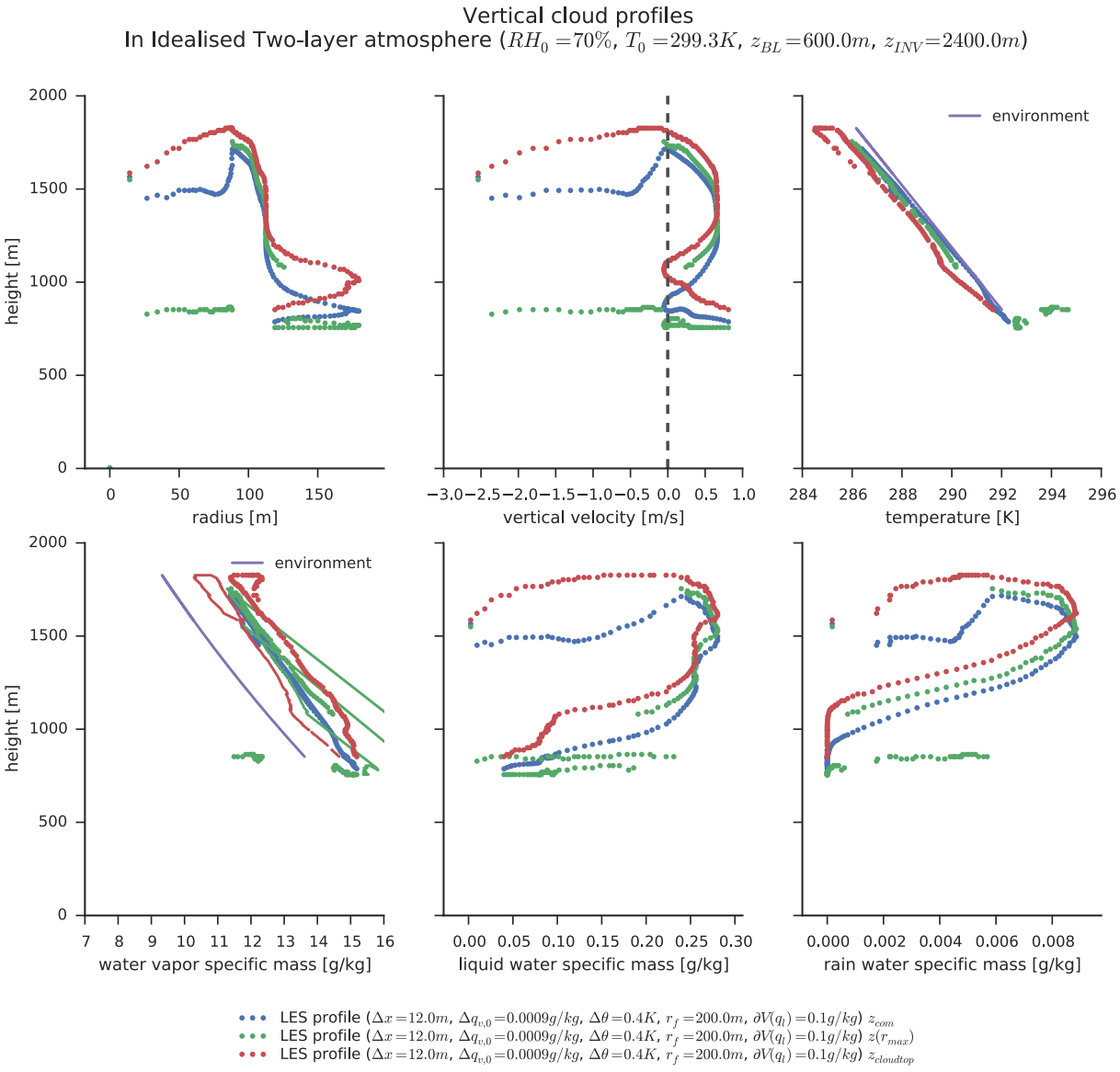

Figure 5.10: In-cloud profiles plotted using three different methods of cloud height calculation; cloud-top height (red), centre-of-mass height (blue) and maximum radius height (green). Note that maximum radius height lacks robustness seen from the discontinous jumps in radius whereas both centre-of-mass and cloud-top height are continous. Cloud-top height is too high to be representative of the height at which the cloud experiences the environment. Note that the vertical velocity was filtered with a low-pass filter to remove the gravity-wave component.

5.3.3 Cloud profiles

In this section the vertical profiles for simulations carried out with a 2D axisymmetric domain and in 3D with varying cloud-producing perturbations will be discussed.

It will be evident that: a) the vertical structure of the convective clouds is significantly different between 2D axisymmetric simulations and b) that the cloud-producing perturbation has a strong impact on the cloud evolution beyond simply influencing the maximum cloud-top height (as would be assumed if only considered the equilibrium height for a parcel with a given moist static energy).

In Figure 5.11 vertical profiles for identical ambient and cloud-forcing conditions simulated in a 2D axisymmetric domain and 3D with the same resolution ($\Delta x = 12m$) are shown. The 3D simulation has larger cloud condensate amount and larger vertical velocity, which may explain the increased amount of entrained mass (Figure 5.12). In addition, the cloud radius also appears larger in the 3D simulation, which however should cause less entrainment. This discrepancy may be a factor in the poor agreement between the cloud-model predictions and the 3D LES profiles which will be discussed in the next section.

The importance of the cloud-producing perturbation is shown by the drastic change in characteristic structure of the convective cloud profiles in Figure 5.13 when changing the potential temperature perturbation from $\theta = 0.4k$ to $\theta = 0.1K$. In the former of which initially produces a large flat cloud which looses total and entrained mass until reaching the height $z \approx 1100m$, suggesting a negative entrainment rate, whereas the latter entrains throughout its evolution. Given the negative entrainment rate of the former the 1D cloud-model is through its formulation unable to predict the profile of a cloud with this characteristic structure, the extent to which this is a short-coming of the cloud-model or simply indicates that clouds of this structure cannot be formed by naturally occurring rising thermals in the boundary layer will be investigated in future work.

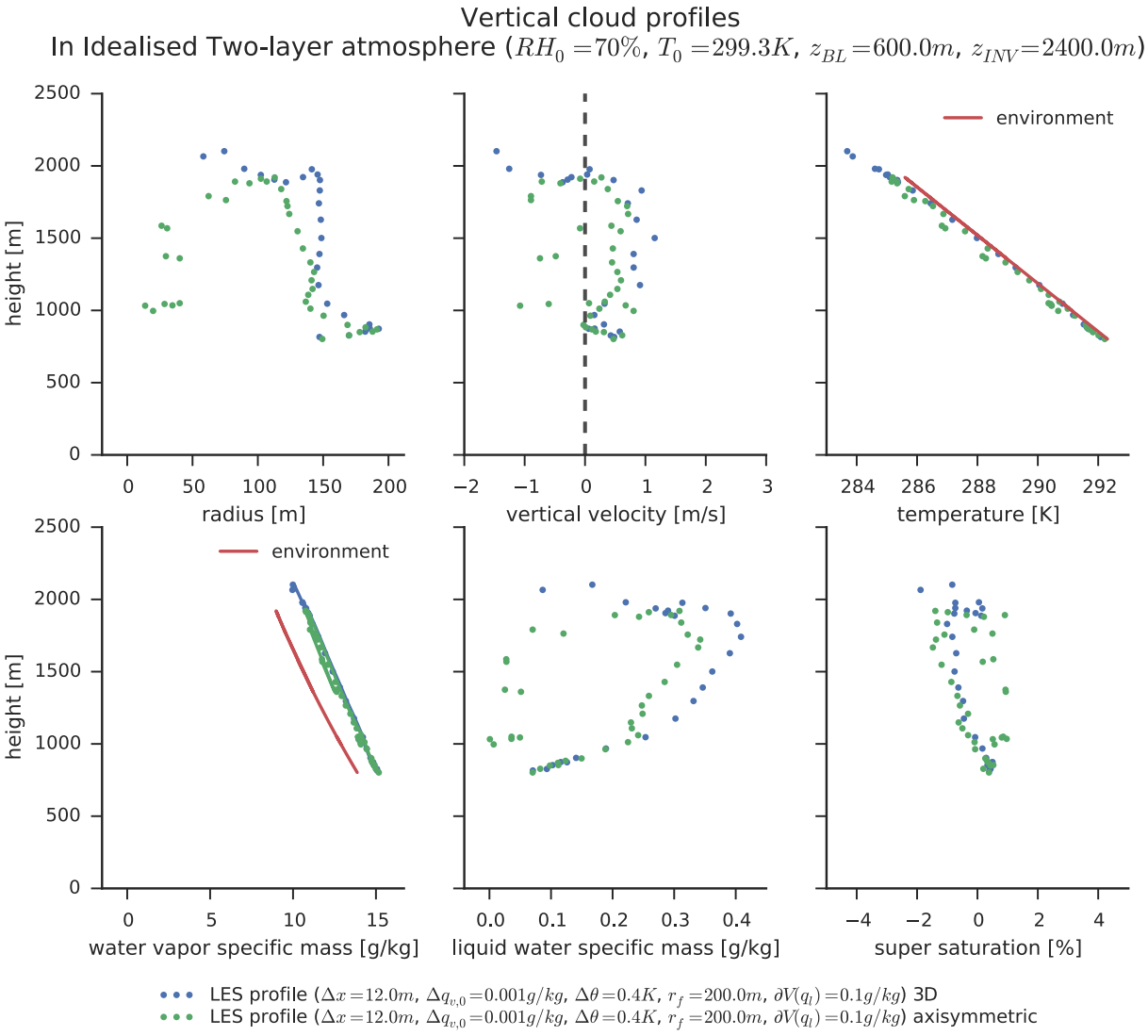

Figure 5.11: Vertical profiles of 2D axisymmetric and 3D simulations with identical resolution, ambient conditions and cloud-forcing perturbation. Note before the level of free convection ($z \approx 900m$) is reached the 2D and 3D simulations show close agreement, once the cloud starts rising and developing above these 2D axisymmetric cloud grows wider and with higher vertical velocity. Note that the vertical velocity was filtered with a low-pass filter to remove the gravity-wave component.

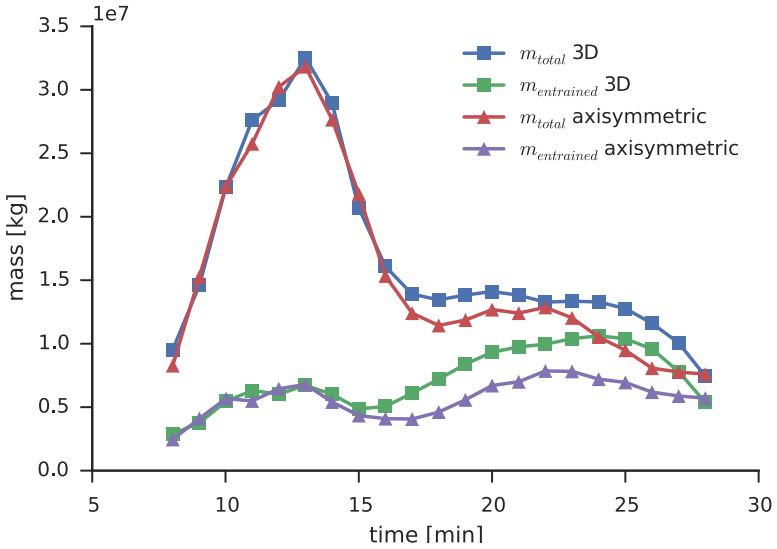

Figure 5.12: Total and entrained mass in 2D axisymmetric and 3D simulations. The 3D simulations shows significantly more entrainment, suggesting that the full dynamical structure of entrainment can only be captured with 3D simulation.

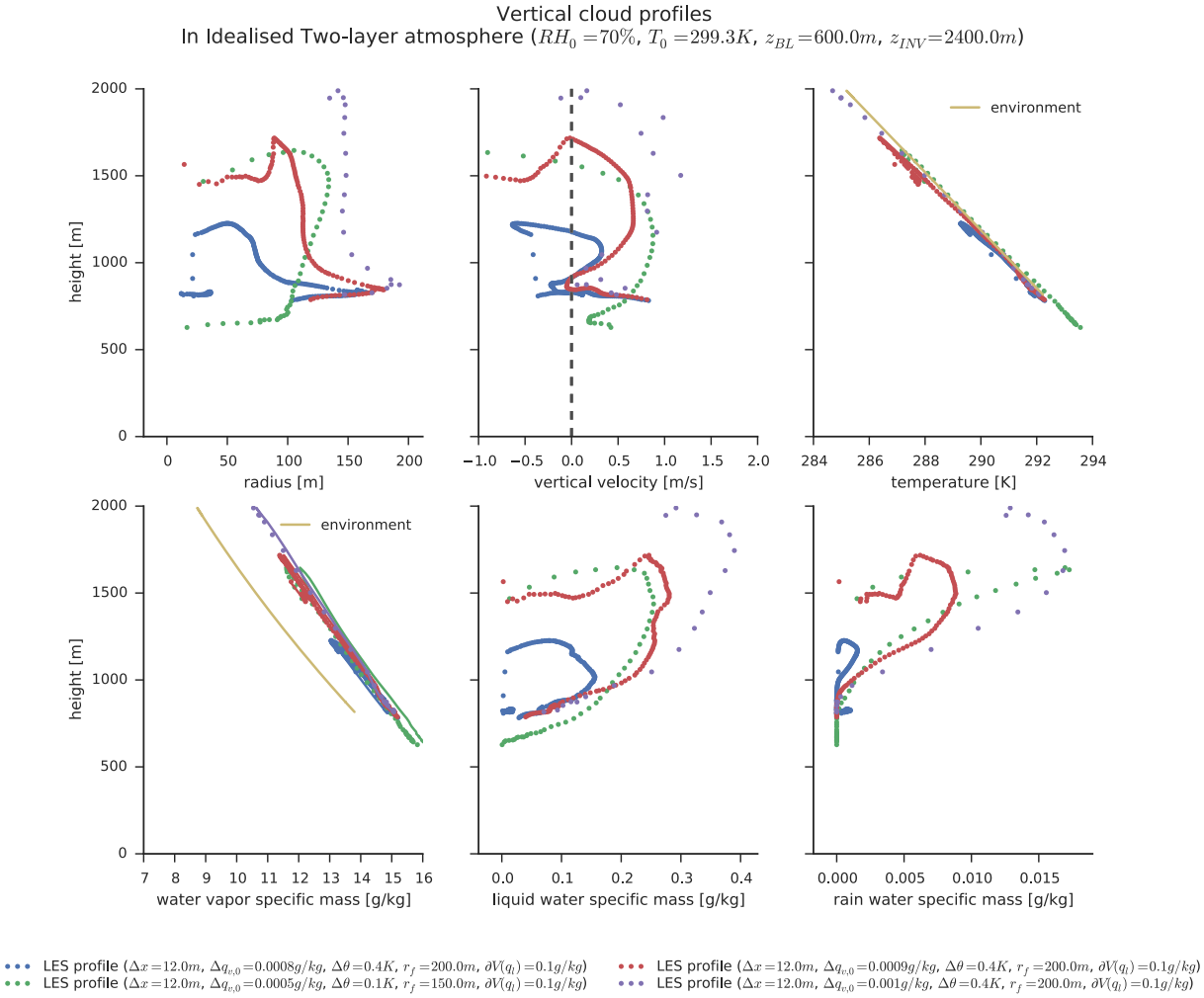

Figure 5.13: Vertical profiles of from 3D simulations with identical resolution and ambient conditions, but with varying cloud-forcing perturbation and cloud-base radius. Note how a small change in cloud-forcing perturbation greatly changes the cloud's evolution. The vertical velocity was filtered with a low-pass filter to remove the gravity-wave component.

5.3.4 Comparison with cloud-model

In this section the cloud-model of Chapter 3 is integrated and the predictions compared to the profiles extracted from the LES simulations. The cloud-model is integrated both using the Morton-Turner model for entrainment rate and using the entrainment rate as estimated from the LES simulations. As the previous section highlights the characteristic behaviour of a cloud in terms of when in its evolution entrainment takes place is heavily influenced by the perturbation that produced a cloud and whether the simulations as carried out in 2D axisymmetry or in 3D.

The first observation made while carrying out this work is that the predictions of the cloud-model are heavily influenced by the integration starting point. Theoretically the cloud-model should predict the *entire* evolution of a convective cloud and so any point in the LES extracted profile should give rise to the same cloud-profile, however this was not generally true. Instead widely different profiles were produced when different points in the LES profiles were used to initiate the cloud-model. In future work this should be exploited by identifying the largest points of departure from the LES-extracted cloud profiles, thereby identifying situations under which the cloud-model's current formulation is inadequate or where the process by which the cloud-profiles are created should be altered. In this section the cloud-model was in each instance initiated with integration with the lowest height extracted from the LES simulations.

The second observation made was that the best prediction of the cloud-model so far was with profiles extracted from 2D axisymmetric cloud-simulations where the convective cloud did in fact "split" (as mentioned previously this splitting should not take place, and is not observed in 3D). This agreement was obtained when the entrainment rate as estimated from the LES simulation was used in place of the Morton-Turner model, without any modification to this entrainment rate. Figure 5.14 shows the profile extracted from LES simulation compared to the cloud-model integration with the Morton-Turner entrainment rate and using the LES-extracted entrainment rate. Note the near-perfect prediction of in-cloud condensate and vertical velocity.

In Figure 5.15 the cloud-model has similarly been integrated and here compared with a 3D LES simulation. Both with the Morton-Turner model for entrainment rate and with the entrainment-rate as extracted from the LES-simulations the agreement is poor. This may suggest that the effect and formulation of the entrainment rate must be altered to account for the mixing processes that take place when fully 3D dynamics is captured.

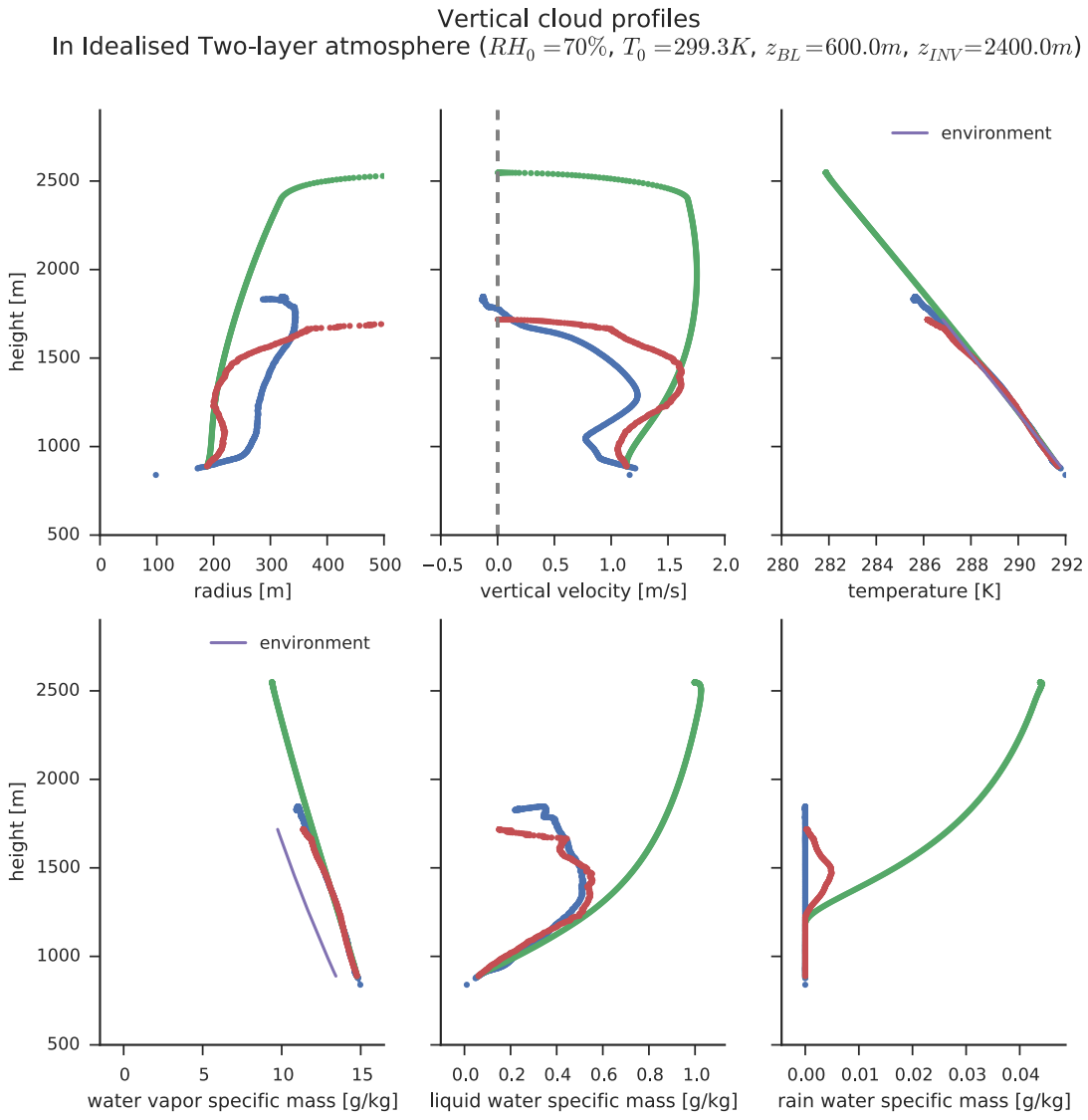

Figure 5.14: Vertical cloud profiles from 2D axisymmetric LES simulation and as predicted with the 1D cloud-model, using the Morton-Turner model for entrainment rate and entrainment rate as estimated from the LES simulation. Note the improved agreement of the cloud-model when using the LES-based entrainment rate. Note that the vertical velocity was filtered with a low-pass filter to remove the gravity-wave component.

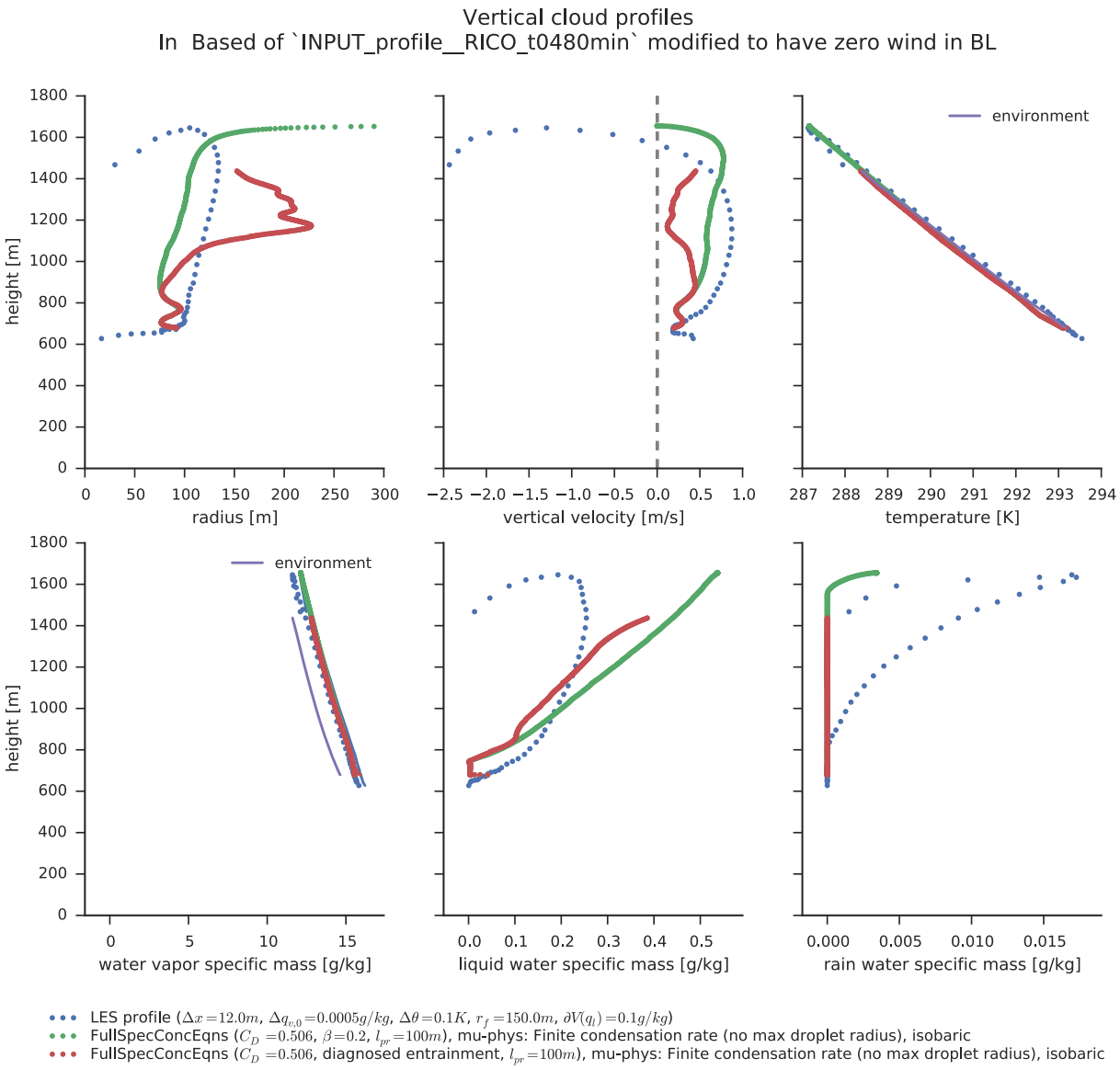

Figure 5.15: Cloud-model predictions (with Morton-Turner and LES-based entrainment rate) compared to LES-extracted cloud profiles. The cloud-model predicts fundamentally different behaviour than what was observed in the LES simulations, suggesting that the in-cloud state should calculated differently. Note that the vertical velocity was filtered with a low-pass filter to remove the gravity-wave component.

5.3.5 Studying the impact of rain formation

In this section the impact of rain on the evolution of a convective cloud is investigated by performing simulations with and without the rain process in the microphysics module enabled. In Figure 5.16 the cloud profiles for both simulations are shown, where the specific concentration of rain represents the amount of precipitation found inside the plume envelope at any given time, and so does not include any rain that has fallen out of the cloud as precipitation.

Based on the final cloud-height and liquid water profile it is clear that allowing for the formation of rain has only a small effect on the cloud's profile, marginally reducing the amount of cloud-water through conversion into rain. Both clouds attain similar heights, although this may be due their vertical extent being determined by the inversion layer. Based on the rate at which rain is formed compared to the amount of in-cloud condensate and on the investigations into the implications of the rain-out rate in Section 3.4.4 it appears that the rain-out length-scale in the cloud-model should not be larger than $l_{pr} = 100m$. This should be further investigated in future work once a better understanding (and representation) of the entrainment rate has been found. In terms of the effect of precipitation formation on the entrainment rate it appears from Figure 5.17 that allowing for the formation of rain has little to no effect on the amount of mass entrained as there is no discernible change in in-cloud total and entrained mass with or without rain formation. This suggests that a better representation of entrainment may be sought after in future work without the need for representing the rain-formation process. In future work the total amount of precipitation as extracted from the LES simulations should be investigated, so that this may be used to formulate physically consistent precipitation formation rate in the 1D cloud-model.

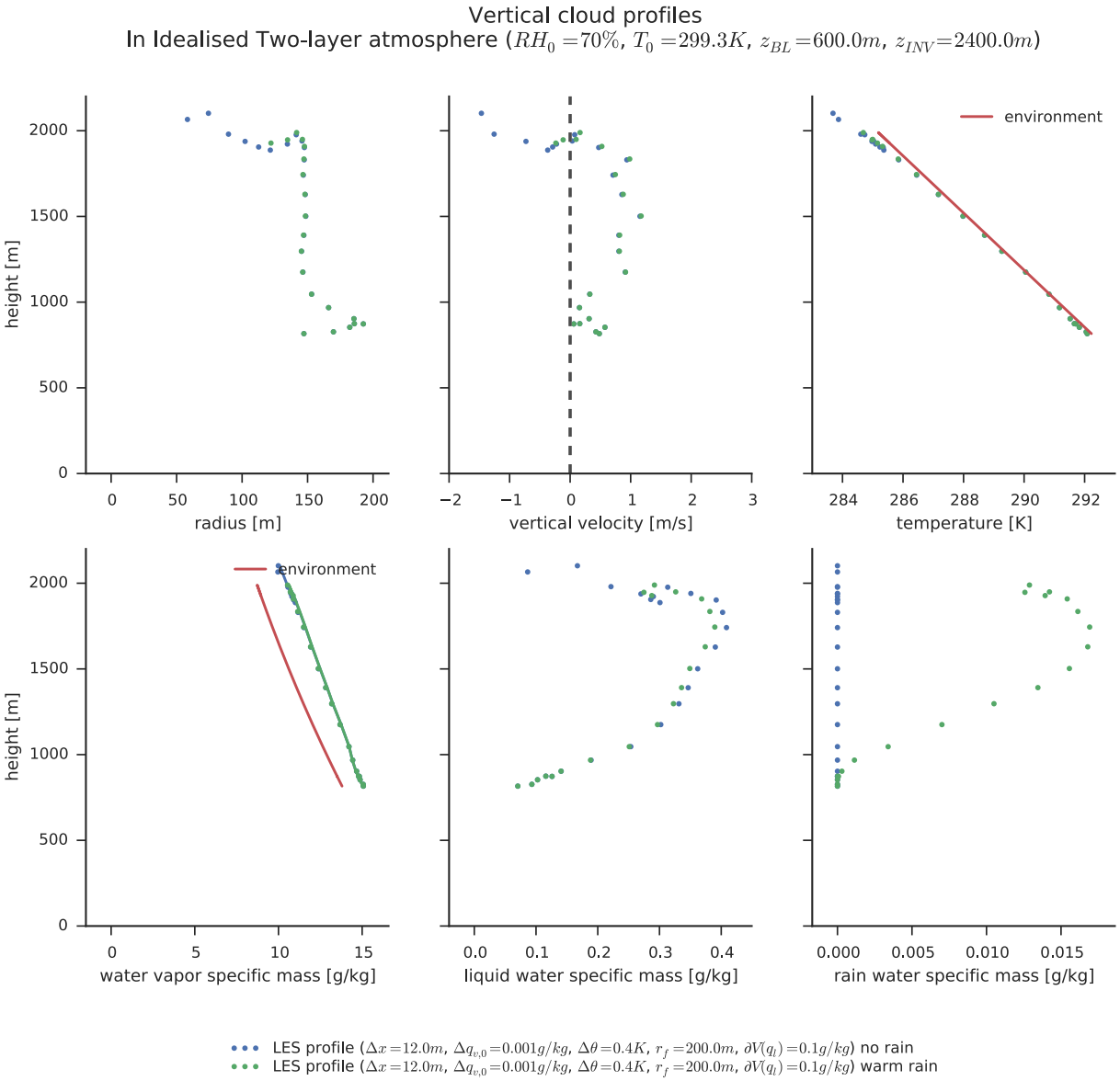

Figure 5.16: Vertical profiles for two clouds with identical forcing and environmental conditions with and without the formation of rain enabled in the microphysics module. Note the small change in in-cloud cloud-water and the otherwise unchanged vertical profile.

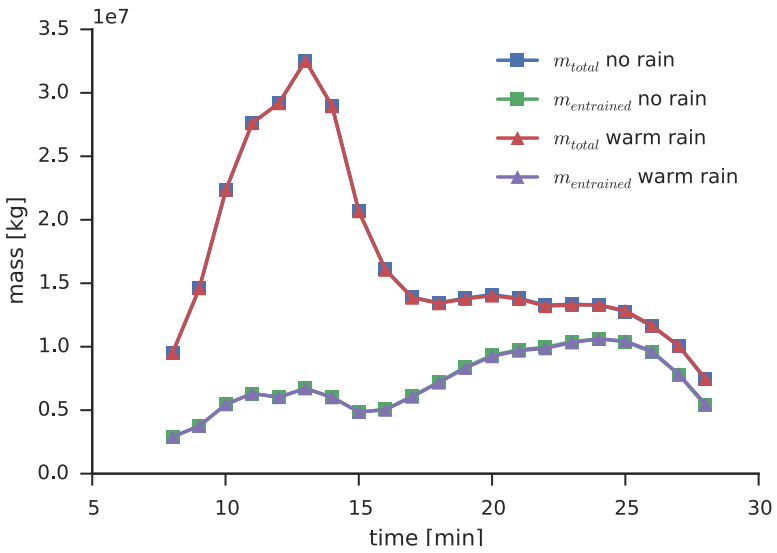

Figure 5.17: Plots of total and entrained mass as function of time in simulations with and without the formation of rain, which suggest that the formation of rain has neglible effect on the entrainment rate.

5.3.6 Windshear effect on clouds

In this section the effect of windshear on convective cloud development is briefly investigated. The ambient profile used is that of the RICO test case of Chapter 6, and the cloud-forcing perturbation is characteristic of what was extracted from the LES simulations of that chapter.

In Figure 5.18 cloud profiles for simulations with and without windshear are plotted, showing very little change in the cloud's structure, the principal difference being a small reduction in cloud-water for the cloud developing in a windy environment. Condering the temperature profile it appears that the convective cloud under both conditions reached the inversion layer above and so neither was stopped by entrainment. Based on the neglible change in entrained mass when introducing windshear (Figure 5.19) it appears that entrainment is not increased to the degree expected. This may be due to the cloud being too buoyant, so that entrainment contributes very little to the maximum cloud-top height compared to the height of the inversion layer. This should be investigated further by carrying out further simulations with smaller cloud-producing perturbation.

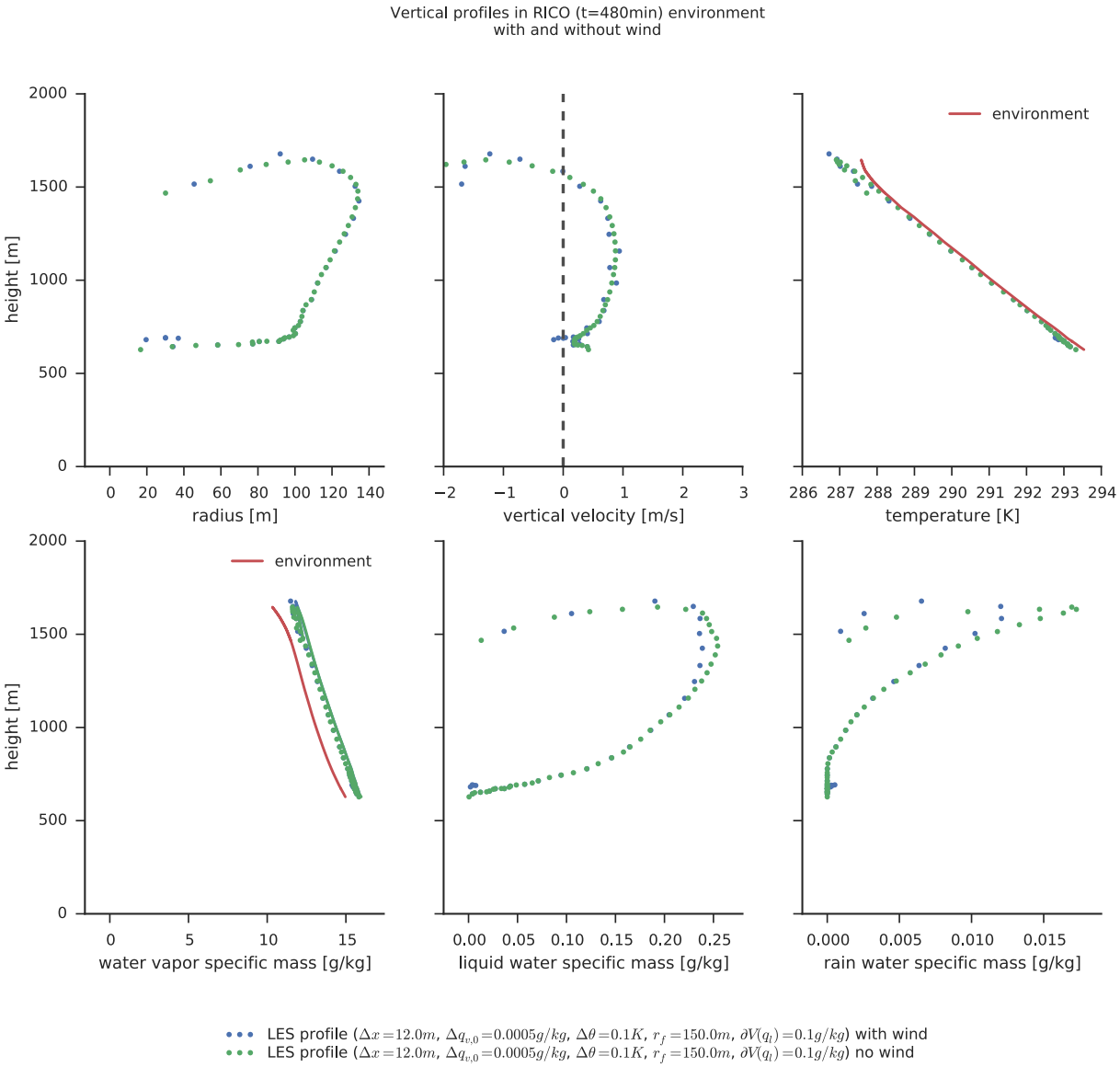

Figure 5.18: Vertical profiles for two clouds with identical forcing and environmental conditions with and without the windshear, which reduces the amount if in-cloud water by a neglible amount.

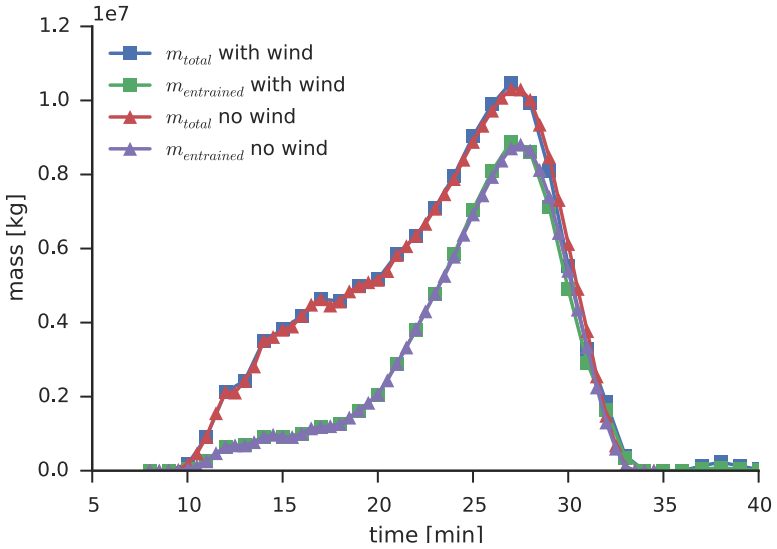

Figure 5.19: Plots of total and entrained mass as function of time in simulations with and without windshear, suggesting that for this setup windshear has neglible effect on the entrainment rate.

Chapter 6

Multi-cloud analysis

This chapter details work carried out while visiting the Max Planck Institute of Meteorology, Hamburg. To complement the work of chapter 5 on studying the characteristics of convective clouds through simulations of individual isolated clouds, this chapter uses simulations over a large horizontal domain in which multiple interacting clouds grow and decay.

In contrast to the single-cloud studies, the clouds in these simulations were not triggered explicitly by introducing a localised bubble-shaped perturbation, but instead develop randomly through the wide-range of length-scales of motion which develop in the below-cloud boundary layer through large-scale and surface horizontally homogeneous forcing of water vapour, momentum and heat content. This setup where convection and cooling through radiation balances forcing is called Radiative Convective Equilibrium (RCE) and has become a ubiquitous research tool in recent years. Only applying forcing and allowing the system to equilibrate through convection allows that clouds which have not been artificially "triggered" may be studied, and thus makes it possible to study what triggers the clouds and influences their development without risking that the convective clouds are artificially forced to grow in a particular manner. In addition it is possible to study how clouds interact and modify their environment. However, due to the random nature of the length and time-scales in this approach, the complexity of analysis is drastically increased in a number of ways.

Firstly, the presence of multiple clouds necessitates that the individual clouds are identified and tracked in time (see section 6.2). Secondly, due to the random triggering of clouds those that are present at a given point in time will be in different stages of their development, trigger, growth and decay (identifying when individual clouds are fully developed will be discussed in section 6.3.2). Thirdly, the clouds in these simulations are frequently comprised of multiple buoyant cores (as is often observed in nature), originating from horizontally displaced regions within the same cloud (i.e. region of condensed water vapour), and so display behaviour which is currently very poorly understood and will require development of new conceptual models which is beyond the scope of this study.

Finally, these simulations display behaviour called *aggregation* in which convective activity over time tends to concentrate in horizontally isolated regions, skewing the distribution of cloud size towards larger and deeper clouds. This is an area of very active research (one of the four crucial questions in future climate research put forward by *Bony et al.* [2015]), suggesting that clouds modify their environment through the creation of *cold-pools* in the boundary layer, modifying the boundary layer's structure over time and locally inhibiting convection, so that convection tends to cluster. This clustering of convection makes it further difficult to analyse individual convective plumes. Currently no existing convection scheme takes into account the effect of aggregation on convection.

As the current cloud-model in CCFM contains only a description of isolated convective plumes, the analysis in this chapter will focus primarily on the characteristics of individual convective plumes (i.e. they have a single buoyant core) to facilitate comparison with predictions of CCFM. The analysis will however be set in context by discussing the implications of the simplifications made when neglecting to represent all convective behaviour (i.e. multi-core clouds, passive plumes, aggregation, etc).

Although these additional complexities of convective cloud-development will not be analysed in depth, this should not be taken as an indication of their importance (or lack of it). It is likely that to accurately predict convective cloud activity the CCFM convection scheme will have to be extended to include all these effects. As well as to study the assumptions of the single-plume cloud-model used in CCFM and the way in which the spectrum is quantised, this chapter will also serve to provide suggestions for extensions to CCFM which may be valuable to consider in future work, and avenues for advancement of convection parameterisation in general.

In that context, the purpose of the work presented in this chapter is twofold:

1. to assess the validity of the assumptions made in performing the spectrum calculation in CCFM

2. to study and constrain the ambient and cloud-base conditions that lead to development of convective clouds, and study the effects these conditions have on the convective cloud development.

In particular the aim is to answer the following questions each of which will be revisited in the following sections:

1. Do all clouds have a well-defined base (as assumed by CCFM), i.e. is it reasonable to speak of a "cloud base" region over which the underside of the cloud is at a near-constant height?

2. Do all clouds develop from the same height? This is assumed in the original version of CCFM (*Wagner* [2009]), but in recent work by *Cao* [2015] a new sub-cloud treatment

which allows for variation in cloud-base height was implemented. To what extent is it important to consider multiple cloud-base heights? And is there a relationship between cloud-base radius and cloud-base height?

3. Do clouds with the same cloud-base radius reach the same cloud-top height? This is assumed in CCFM so that a *cloudtype* is singularly defined by its cloud-base radius, and a single vertical integration is performed per discrete cloud-base radius chosen.

4. What is the shape, magnitude and duration of the perturbation (relative to the ambient atmosphere) at cloud-base which leads to the convective cloud initiation?

5. How does the cloud-base velocity change over time?

6. What is the spatial and temporal variation of cloud-base velocity over a single cloud?

7. How is the immediate environment of an individual cloud characterised? Does it differ from the horizontal mean of the environment?

These questions will be studied by analysing simulation data from LES simulations performed with the UCLA-LES model (*Stevens et al.* [2005]) by *Heus and Seifert* [2013] at the Max Planck Institute of Meteorology, Hamburg. The ambient and initial conditions used were from the RICO (*Rauber et al.* [2007]) study, which are idealised conditions for shallow convection synthesized from a measuring compaign campaign at Antigua and Barbuda in November 2004 - January 2005. A more detailed description of the RICO setup and UCLALES model will be given in section 6.1.

Through studying these questions a more fundamental assumption of CCFM will also be considered which has implications for how the analysis is performed and how the questions are interpreted. The question here is to what extent the assumption that convective clouds are in a "steady-state" is valid, i.e. to what extent a convective cloud is a plume or a thermal. Fundamentally this dichotomy in the principal description of convection has existed for decades (see for example review by *Yano* [2014]) and it is not the aim of this thesis to resolve this issue for convection in general, but study its relevance for the current setup. The analysis will be performed in such a manner as to highlight the differences between the two descriptions, and identify within which regimes it may be necessary to alter the current description in CCFM.

To extract statistical properties across multiple clouds which evolve in a given 3D simulation, it is necessary to firstly develop a method to identify in which regions of the domain individual clouds are and to track these as they evolve, and secondly it is necessary to pick a time (or times) for each cloud at which to extract these properties. The method employed for tracking individual clouds will be discussed in section 6.2 and importance of choosing the time of analysis will be discussed when different cloud properties are extracted will be discussed in Section 6.3.2.

6.1 Modelling setup and evolution characteristics

The modelling setup used was Radiative Convective Equilibrium (RCE) where the forcing of moisture and heat (representing the effect of large-scale advection and radiation) is balanced by spontaneously forming convection. The boundary and initial conditions used are from the RICO campaign (*Rauber et al.* [2007]) and describe shallow convection over ocean in the tropics. The principal effects of the forcing are to add heat and moisture near the surface (representing evaporation from the sea-surface, and heating through sensible heat and heating through out-going long-wave radiation) as well as domain-wide heating through an imposed subsidence velocity and radiative cooling in the profile top. The final domain-wide influence affecting the convective cloud development is the presence of horizontal wind-field, imposed to represent large-scale geostrophic balance. This wind-field causes to translate the clouds horizontally and affects cloud-growth through increasing mixture from the shearing of the vertical gradient in wind-speed (as will be discussed in section 6.3). The initial condition in terms of temperature and moisture (water vapour) profile can be seen in the left-most panel of Figure 6.1 whereas the forcing profile is plotted in Figure 6.2. The imposed surface fluxes are given by

$$\begin{aligned}
\overline{w'\theta_l'} &= -C_h|U|(\theta_l - \theta|_{z=0}), \\
\overline{w'q_t'} &= -C_q|U|(q_t - q_{sat}|_{z=0}), \\
\overline{u'w'} &= -C_m|U|u, \\
\overline{v'w'} &= -C_m|U|v,
\end{aligned}$$

where u and v the are velocity, q_t the total moisture specific mass and θ_l liquid potential temperature in the lowest model cell, the velocity magnitude is given as $|U| = \sqrt{u^2 + v^2}$ and the flux-transfer constants are given as $C_m = 0.001229$, $C_h = 0.001094$ and $C_q = 0.001133$. To compute the surface liquid potential temperature ($\theta|_{z=0}$) and surface saturation specific water vapour ($q_{sat}|_{z=0}$) the sea-surface temperature ($T_{SST} = 299.8K$) and reference pressure ($p_0 = 101540Pa$) is used.

The simulations were performed in the UCLA-LES model at $\Delta x = 25m$ isotropic resolution in a domain of $50km \times 50km \times 6km$ with doubly-periodic boundaries in the horizontal direction. The total simulation time was $t_{tot} = 216000s = 2.5days$. Owing to the large number of datapoints in the simulations, the full 3D simulation output available for analysis has the limited time-resolution of $\Delta t = 2hrs$; however these are complemented with 2D projected fields (integrated column water, maximum and minimum height of cloud-condensate, and column mean variables) as well as domain cross-sections at $z = [100, 700, 1000]$m which are available with $\Delta t = 2min$ temporal resolution.

In figure 6.3 the evolution of the mean state in the RICO simulation can be seen. After

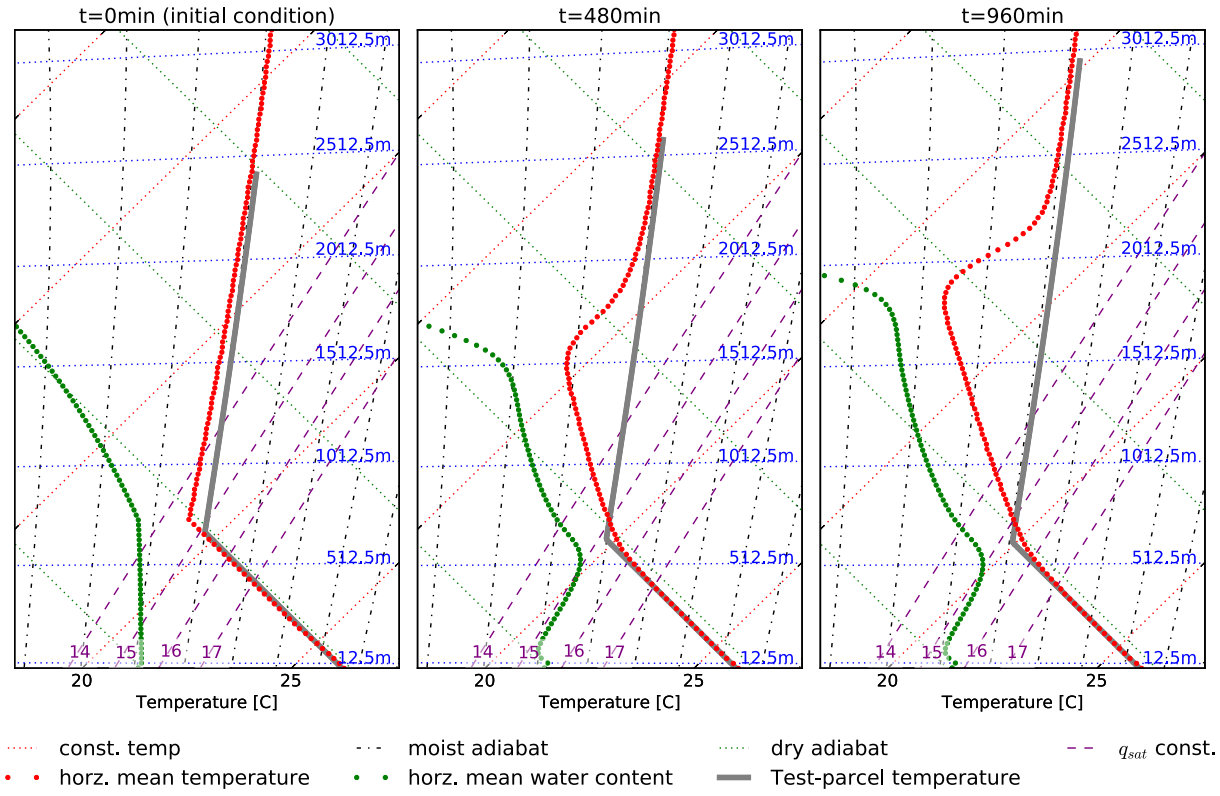

Figure 6.1: Tephigrams of the evolution of the ambient state in RICO simulations, from the inital condition and later in the two analysis intervals defined. Note how the production of convective clouds pushes the inversion layer higher (from $1.5km$ at $480min$ to $1.8km$ at $960min$) giving rise to deeper clouds as the simulation progresses. Plotted in grey is the temperature profile of an adiabatically lifted test-parcel, based on this the condensation level is predicted to be respectively $z_{LCL} = [680, 640, 625]m$ and the level of free convection $z_{LFC} = [680, 680, 660]m$. This suggests that there is no convective inhibition in the initial condition (explaining the initial vigorous convection), but also indicates that there is very little CIN later too.

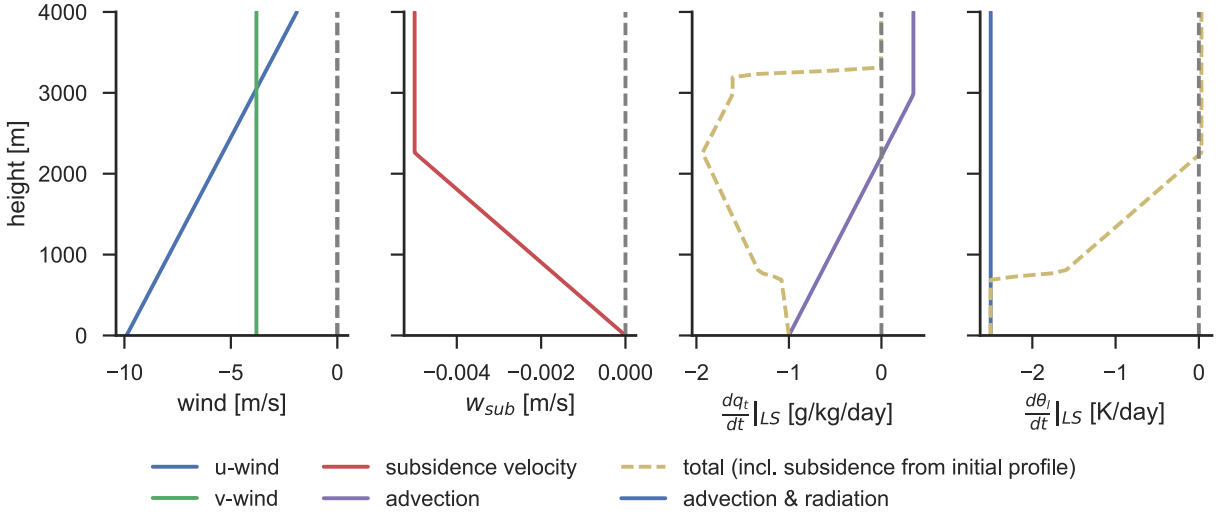

Figure 6.2: Large-scale forcing imposed on RICO simulations in terms of (u, v)-wind profile (representing large-scale geostropic balance), temperature changes through large-scale advection and radiation and moisture transport through large-scale advection. Note that the effect of subsidence is enforced through a subsidence velocity which is integrated in time. As the subsidence affect the temperature and and total moisture depending on the vertical gradient in both it instructive to consider the effect of subsidence given the profiles of both. Using the initial profiles of temperature and moisture the effect of subsidence has been included to compute the total effect on both. This will change over time as the mean profiles change, but the characteristic behaviour will be heating in the upper atmoshere and loss of moisture through the column which are enforced to balance the surface fluxes.

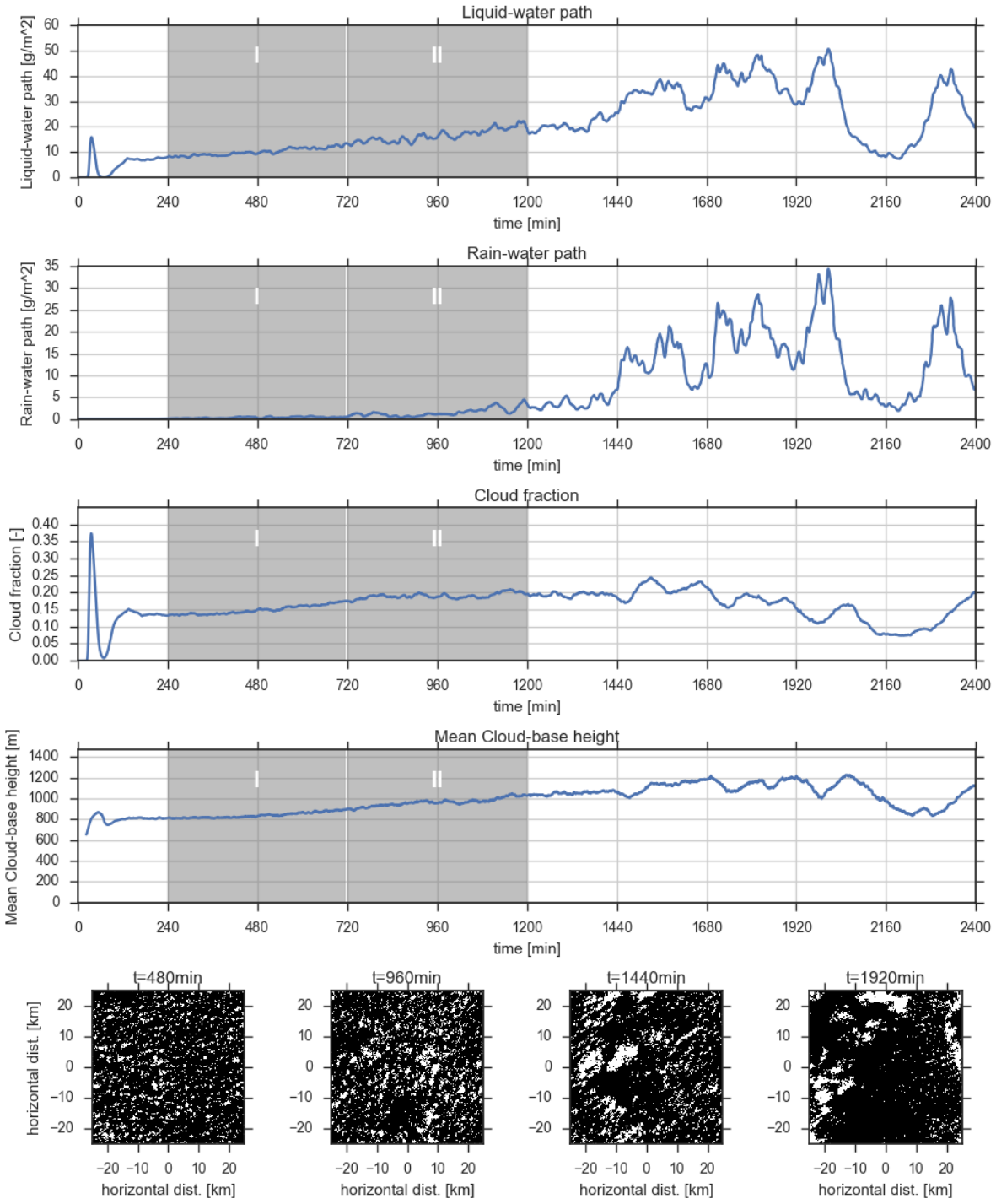

Figure 6.3: Top the evolution of domain-wide mean liquid-water and rain-water path, cloud fraction and mean cloud-base height. Below are horizontal plots of non-zero column liquid water path in white, thereby indicating where clouds are present in the domain. Note the initial rapid adjustment to the initial condition, after which all variables slowly increase with time until aggregation of convection becomes significant which can be seen from the clustering of convection and from the marked increase in rain. To facilitate analysis and comparison two analysis time-periods have been defined, indicated by grey shading and labelled by I ($t = 240\text{min} - 720\text{min}$) and II ($t = 720\text{min} - 1200\text{min}$).

an initial period of rapid adjustment to the initial condition and forcing (within which the cloud-fraction and liquid-water path varies widely) the simulation and domain-wide characteristics settle to a quasi steady-state around $t = 120min$ after which the ambient profile in the RICO simulation is characterised by a well-mixed boundary layer to $650m$ with characteristic moisture content $q_v \approx 15.4g/kg$ and potential temperature $\theta_0 \approx 297.8K$ (taken at $z = 700m$). Note a relative shallow layer ($\approx 50m$) near the surface with increased water vapour concentration ($\Delta q_v \approx 0.5g/kg$). Above this exists a relatively shallow layer with conditional instability which is capped by in an inversion maintained by the prescribed large-scale subsidence.

After the initial adjustment, the quasi steady-state evolves over the next ~20hrs (1200min) with a gradual near-monotonic increase in both liquid-water path, rain-water path and cloud-fraction as moist convection pushes against the inversion above. This slow evolution stops around $t = 1440min$ where there is a sudden marked change in the rain-water path which coincides with the transition to a largely aggregated state after which these bulk variables start to show large variations. The onset of large-scale aggregation also coincides with a marked increase in precipitation owing to the increased cloud-depth. The extent of convective aggregation can also be seen in the bottom of figure 6.3 (where areas of non-zero column-integrated liquid water is shown in white) with large patches of cloud-free regions emerging: these are of colder air which inhibit convection, commonly denoted as so-called *cold-pools*.

As CCFM does not represent the effect of aggregation, the study in this chapter will focus on the state evolution before aggregation begins playing an effect on the cloud-population and behaviour. Therefore two 8-hourly time-periods have been defined and labelled in figure 6.3 as $t_I \in [240, 480]min$ and $t_{II} \in [480, 1200]min$ over which analysis will be carried out.

In Figure 6.3 the vertical profile of the initial condition is plotted together with the horizontal mean profile at the mid-point of the analysis periods. For each profile the thermodynamic evolution of a parcel lifted pseudo-adiabatically is also plotted. The absence of CIN in the initial condition explains the vigorous initial creation of convection as any non-zero buoyancy causes convection in the absence of CIN. At later times a CIN player has appeared and the profile above the boundary-layer (which remains well-mixed) is noticably warmer and moister due to mixing through convection. Note however that the inversion above is maintained although the clouds layer grows deeper over time.

6.2 Cloud-tracking

To facilitate the identification of individual clouds and to be able to track these through time, the cloud tracking code by Thijs Heus (*Heus and Seifert* [2013]) was used. The algorithm operates on the 2D "projected" datasets output by UCLALES (i.e. comprising $25m \times 25m$ horizontal grid cells), and thus must infer the vertical connectivity of cloud cells using other variables as will be detailed below. The algorithm proceeds through the following steps:

1. Any cell with a column-integrated liquid-water path above $q_v^{lim} = 10g/m^2$ is deemed to be cloudy (i.e. contain at least one cloud). Horizontally neighbouring cells are then clustered by requiring that the minimum and maximum cloud-height of neighbouring cells implies vertical connectivity.

2. Within cloudy clusters, buoyant cores are identified by requiring that the buoyancy (calculated from the vertical potential temperature) be above a defined cut-off value of $\theta_v^{lim} = 0.5K$. If a given cloudy cluster contains multiple buoyant cores, that cluster is split into multiple clouds.

3. Cloud clusters are then tracked in time by requiring spatial overlap in successive timesteps.

Based on the presence of buoyant cores in a cloudy region, the identified individual clouds are then classified as: 1) single-plume (a cloudy region with only *one* buoyant core), 2) a split cloud from a multi-plume region (having multiple buoyant cores), 3) passive (cloudy region without a buoyant core) and finally 4) "outflow" (which will not be used in this work).

Using this framework it is possible to characterise the evolution of the RICO simulation through the number and type of convective elements present. In figure 6.4 the distribution of cloud life-span (defined as the time between when the cloud-tracking algorithm identifies the formation of a new cloud and until this cloud completely evaporates) over the duration of the simulation is plotted for single-core clouds. After an initial rapid response to the initial condition, the cloud-population relaxes to a near steady-state with a mean cloud life-span of $t_{life} \approx 23min$. Through the simulation this life-span decreases over time to $t_{life} \approx 19min$ at $t \approx 960min$, whereas the multi-core clouds show an initial increase in life-span duration settling to an average of $t_{life} = 18min$.

The principal limitation in the cloud-tracking software lies in the use of the 2D "projected" fields as this makes it impossible to vertically separate regions of cloudy air, and so the possible presence of mid-level convection cannot be studied. In addition there may be some sensitivity to the internal limit values used in identifying cloudy regions and to the discrete resolution in terms of temperature, moisture, that can be represented as these are scaled internally to integers for optimisation. This will be studied further in future work.

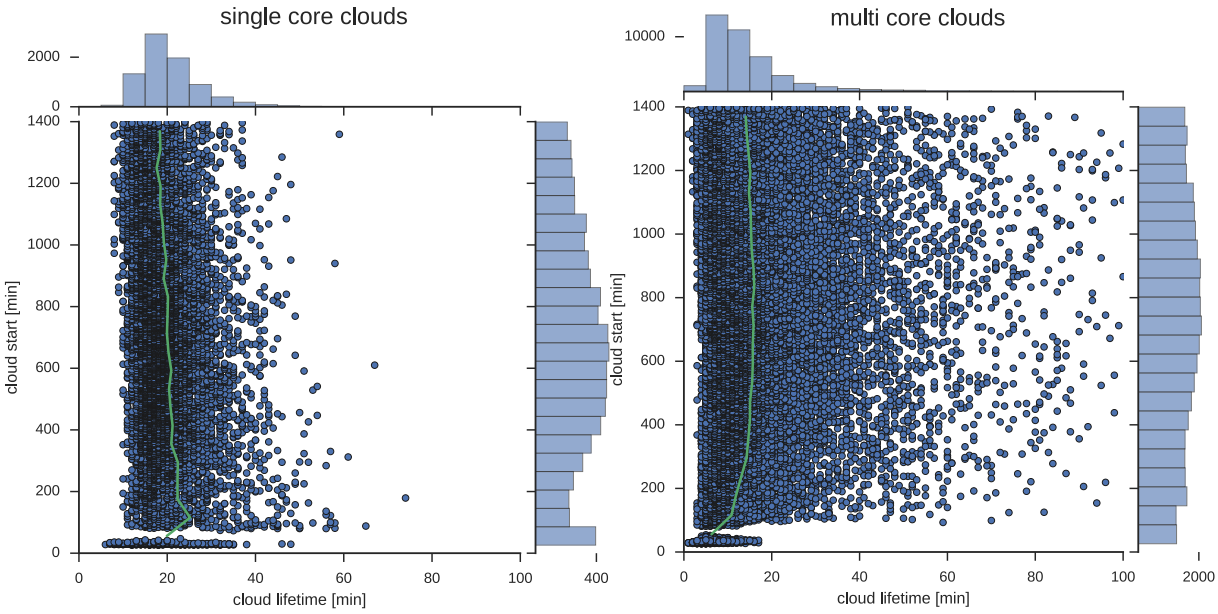

Figure 6.4: Scatter-plot of cloud lifespan vs cloud appearance time for single-core clouds (left) and multi-core clouds (right) before strong aggregation has started ($t < 1400\text{min}$). Above and right of each scatter plot are the distributions of cloud life-time and cloud appearance-time respectively. In green is the lifetime mean binned over 60min of cloud-appearance time. After an initial adjustment the mean lifetime becomes $t_{life} \approx 23min$ and slowly decreases over time to become $t_{life} \approx 19min$ for single-core clouds, whereas multi-core clouds have an average life-time of $t_{life} \approx 18min$ throughout most of the simulation. In addition the life-time appears to follow a long-tailed Poisson distribution. The number of single-core clouds peak at $t \approx 600min$, while multi-core clouds peak in number at $t \approx 800min$. It is clear that the multi-core clouds show much larger variation in their life-span, the specific reason for this will be investigated in future work by disseminating the cloud-tracking software.

6.3 Extracted cloud-properties

This section presents the analysis of cloud-properties in the RICO shallow convection simulation, discusses the impact of these findings on the formulation of the cloud-model in CCFM and the relevance of these findings to the setup and analysis when performing single-cloud simulations in ATHAM.

In all analyses performed in this section the cloudy region is defined to contain any point where cloud condensate is present ($q_l > 0g/kg$). A special distinction is made with respect to the definition of "cloud-base" as defined in the formulation of the UCLA-LES model output. In this work cloud-base will be defined as the lower-most region of the cloud from which the convective cloud could be supposed to "grow" (the height of initial condensation) in contrast to the definition in UCLA-LES where "cloud-base" pertains to the entire "underside" of the cloud; this is important as we are interested in defining what characteristic properties are necessary for the production of a convective cloud. The existence of a well-defined cloud-base will be investigated in Section 6.3.1. The choice of method for defining the base of a cloud significantly affects the mean cloud-base height, so that estimates that use the entire underside of the cloud show an increase in mean cloud-base height (averaged over all clouds) over time due to the upper (spreading) part of the clouds being included, whereas mean cloud-base height across all clouds, as estimated

using only the lower-most flat "base" of the cloud, stays largely unchanged over the simulation's evolution. As mentioned previously the time in a cloud's evolution may affect the properties extracted, and to make a meaningful choice of the time it is necessary to constrain the lifecycle of the cloud in time, as will be discussed in Section 6.3.2.

6.3.1 Cloud-base flatness

The extent to which an individual cloud may be viewed as growing from a single height (as would be predicted by the lifted-parcel approach in Section 2.1) can be investigated by examining the height distribution of cells making up a cloud's underside. By assuming each cloud to be axisymmetric and furthermore assuming that the lowest height of each cloud to be on this axis of symmetry, the heights of the underside of each cloud may be used to synthesize a vertical profile of the cloud's radius at a given height. This is done by forming concentric rings at constant altitude from the cloud-underside heights, the area of each ring being equal to the total area of all cells in the cloud's underside that have a given height. Although this is not an accurate representation of the actual cloud profile it does give an indication of the extent to which each cloud has a base, so that if there is little change in altitude as the cloud radius increases, the cloud has a flat base. At higher altitudes the ambient wind-field was observed (from 3D output) to cause clouds to bend over, which in turn causes the cloud radius estimated here to be exaggerated at higher altitudes, and so this measure of cloud-radius should only be taken as a proxy for the change of cloud-radius with height. Another limitation of this approach is that lowest heights of the cloud-base are not guaranteed to be contiguous and so the assumption of an axisymmetric cloud becomes a quite poor approximation. However despite the crudeness of this model it will be seen below to give a very clear suggestion of flatness of the analysed convective clouds.

By first applying this concept to all clouds present at a specific time in the simulation (here $t = 240min$) it is seen (Figure 6.5 left) that a large majority of clouds do in fact have a base region over which the height ($z \approx 650m$) is near-constant as the radius increases. This is especially true early in a cloud's lifespan. There are however a noticeable number of cloud profiles which appear not to be flat, which may either be due to a cloud being late in its evolution (and starting to detach from the condensation height), or may indicate that some clouds form without a well-defined cloud-base, or may in fact indicate an issue with the cloud-tracking algorithm by which only a part of a larger convective cloud has been identified as a single cloud.

To examine the extent to which this was due to a cloud simply being in the decay phase of its evolution, the same procedure of synthesizing a radius vs height profile was repeated for individual clouds through their *entire* evolution. In the right of Figure 6.5 the profile evolution for a single cloud clearly shows that this cloud *does* have a well-defined flat base earlier in its evolution, but was simply largely decayed at $t = 240$ (this cloud and

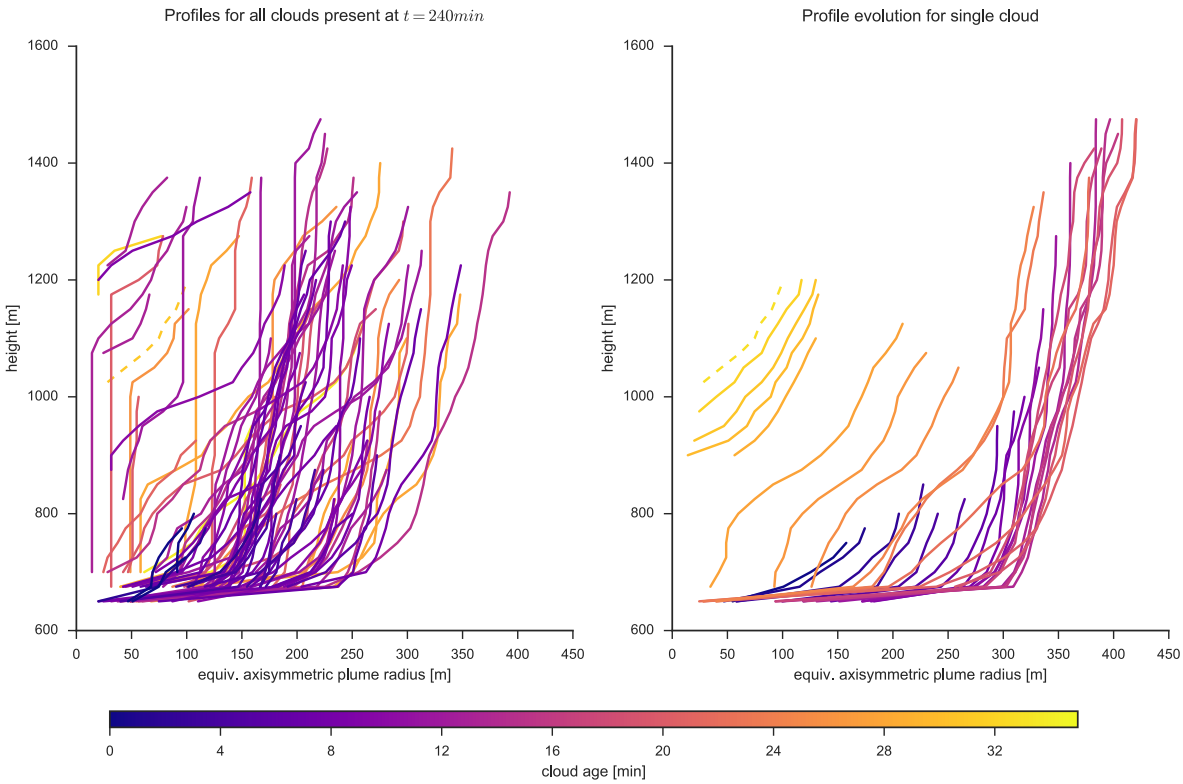

Figure 6.5: Synthesized radius vs height profiles assuming an axisymmetric cloud profile. On the left this concept has been applied to all clouds present at a specific timestep and on the right for a single cloud during that cloud's evolution. Note the dotted line represents the same cloud at the same simulation time in both plots.

timestep is indicated by the dotted line in each plot). These results indicate that at least for the shallow convective clouds in the RICO setup it *is* possible to speak of a well-defined cloud-base.

6.3.1.1 Defining the cloud-base region

To perform analysis of properties in and around the cloud-base, it is necessary to be able to systematically define a horizontal region constraining the base of the cloud. If instead the entire vertically projected region of condensate was used as the cloud-base region when computing e.g. the cloud-base area or any scalar average over the cloud-base, the part of the cloud in the expanding anvil will contribute to these calculations obscuring the estimates of what is actually the state at cloud-base. This can be seen in Figure 6.7 where the cloud underside heights have been plotted and visualised by wireframe in 3D. The expanding top of the clouds can clearly be seen around (in 2D) and above (in 3D) the cloudbase.

Plotting a histogram of the 2D field of cloud-underside heights for individual clouds (Figure 6.7) it is clear that for most clouds there is a cluster of cells which have a very similar height (as would be expected based on the analysis in the previous section); these cells make up the cloud-base and so their spatial location defines the cloud-base region. The

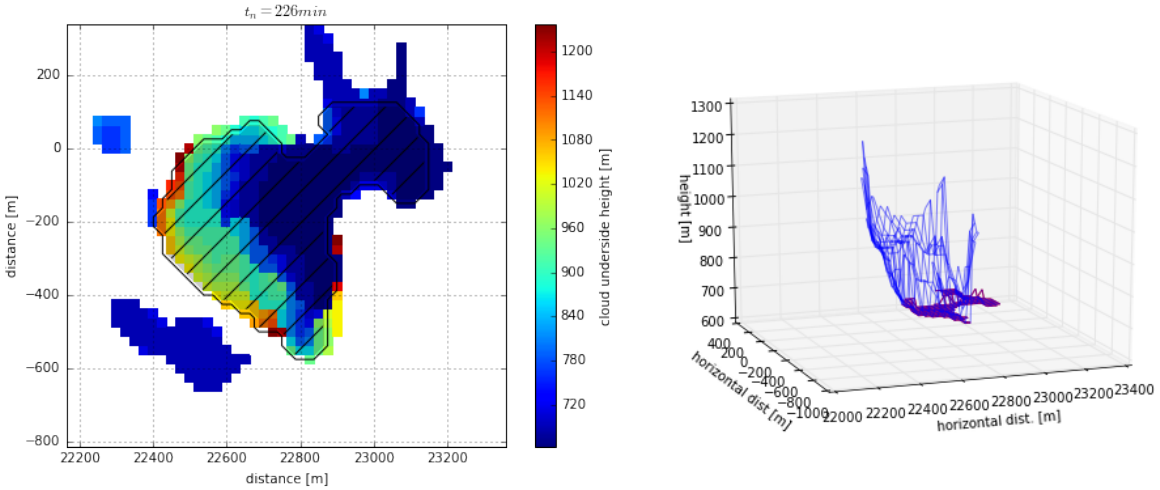

Figure 6.6: Visualisation of the "underside" of a single convective cloud calculated as the lowest height in each vertical column at which the liquid water concentration is above $0\mathrm{g/kg}$. On the left is plotted the "cloud-base" variable and on the right a wireframe visualisation of the same data. In the wireframe plot the cells which are within $100m$ of the lowest height of the cloud are coloured red. Note the flatness of the well-defined cloud-base.

cells to include as part of the cloud-base for each cloud were selected by first finding the peak of this distribution and the width of the distribution was defined as the distance between the minimum cloud-underside height and the peak's height. In Figure 6.7 the cut-off height for each cloud is indicated in red (for the majority of clouds this cut-off height was 1 cell above the histogram peak).

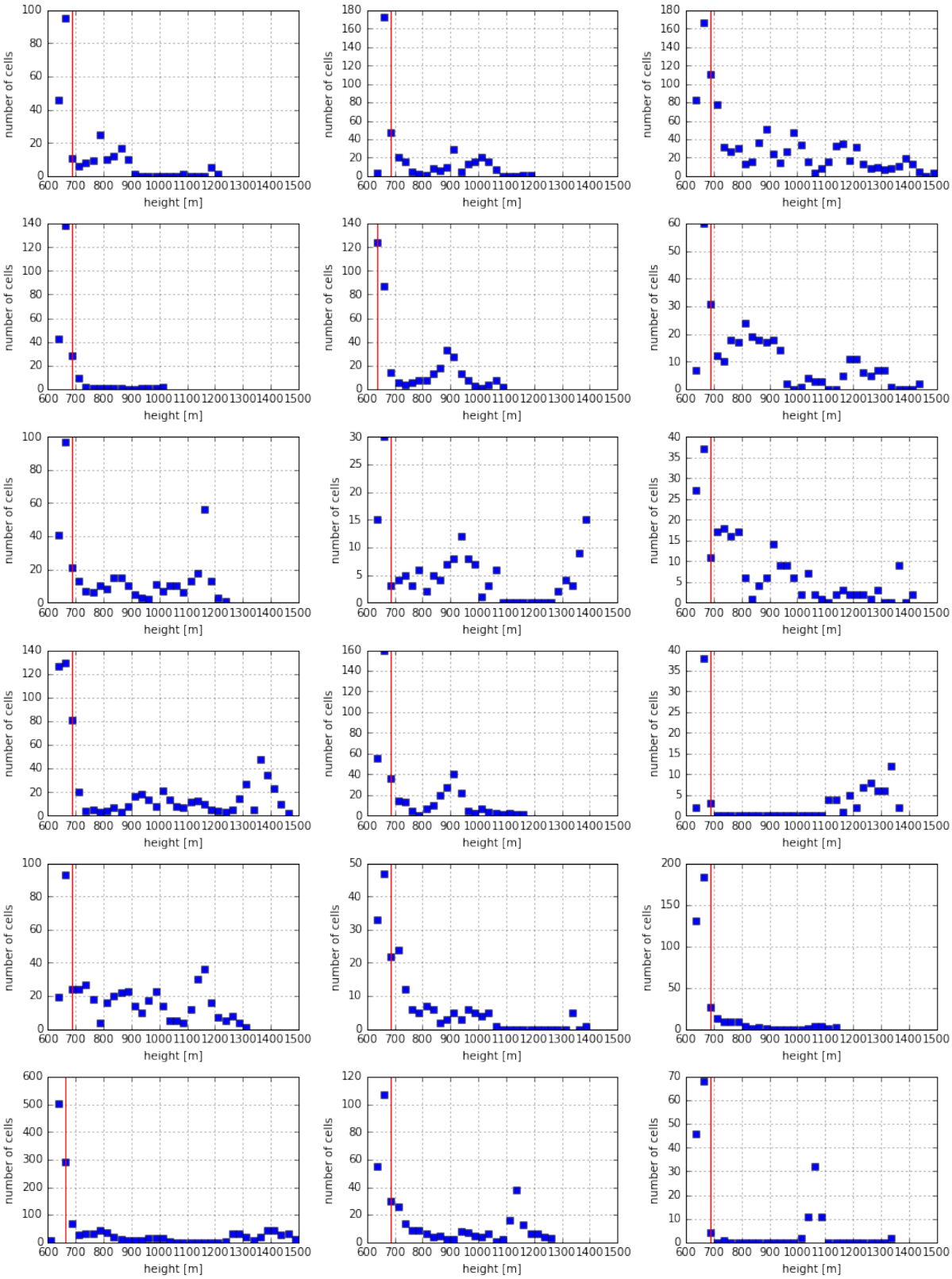

Figure 6.7: Histograms of heights of cells making up the cloud-underside for 18 randomly selected clouds present at $t = 240min$. For all clouds the histogram shows a peak below $z = 700m$, the cutoff height for cells deemed part of the cloudbase is indicated in red, for the majority of clouds this cutoff height was one grid-cells above the histogram peak.

6.3.2 Time-dependency of cloud-properties

In this section the time-dependency of cloud properties is studied. This is an important test of the fundamental assumption in CCFM that the convective clouds are in a steady-state, as this implies that a fully developed cloud exists with same vertical structure for a period of time longer than the time it takes the cloud to grow to this state. As will be discussed later it may not be necessary to make this assumption in CCFM, but this will require further work to investigate.

If the steady-state assumption is correct a number of variables (for example cloud-base radius, cloud-top height, cloud-base vertical velocity) could be used to find the time that the steady-state is reached given that all should tend to a steady-state value, and so the presence (or absence) of such a limit value may be used as a test for this assumption. In addition the steady-state plume picture employed in CCFM implies that a cloud is fully developed, i.e. the cloud has attained its maximum height, and is continually transporting moisture and heat from the boundary layer to the upper troposphere. This steady-state assumption therefore in detail requires that:

1. The cloudbase from which the cloud grows is still present when the maximum height is attained (otherwise the is no connection to the boundary-layer from which the vertical mass-flux causes transport). This may not be necessary when deep convection is studied in future work.

2. The cloudtop height reaches an altitude which is maintained over a period of time during which the cloudbase radius is unchanged too.

3. The vertical profiles of cloud radius and vertical momentum stay unchanged over a period of time.

To assertain to what extent these requirements are satisfied it is necessary to to be able to:

- identify the cloudbase region so that the radius can be estimated (the method for which was detailed in the previous section)
- identify the time at which the maximum cloud-top height is attained (here called the “mature state”); this is necessary because at any given time in the simulation there will be clouds present which are in different stages of their development

The unsteady nature of the convective clouds and thus the importance of the choice of timestep when testing predictions of the CCFM cloud-model is exemplified by the plots of cloudbase radius, cloudtop height, cloudbase height and near-cloudbase ($z = 700m$) vertical velocity as plotted for a number of single-core clouds in figure 6.8. The methods for defining cloudbase radius, height and cloudtop height will be detailed in Sections 6.3.4, 6.3.3 and 6.3.5 respectively, but in essence consist of defining the cloud-base region and

identifying the maximum height of cloud condensate. The vertical velocity was defined by averaging the domain cross-sections at $z = 700m$ (w_{700m}) over the cloud-base region, defining therefore not exactly the velocity at cloud-base, but the plotted changes in vertical velocity will be characteristic of the vertical velocity at cloud-base (the mean difference in height is $\approx 50m$ so that the vertical velocity plotted here is likely lagging the actual cloudbase velocity by a few minutes).

A general characteristic is that the cloud-base radius typically peaks before the cloud-top reaches its maximum altitude, a feature which was observed for both single-core and multi-core clouds. There is a large degree of variability in how long this lead-time is (and how long it takes an individual cloud to reach its maximum altitude), but typically the cloud-base radius peaks before the thermal has reached half-way to its maximum altitude.

Another characteristic is that the cloud-base radius for the majority of clouds drops to zero as the maximum cloud-top altitude is approached, suggesting that many clouds "detach" from the condensation height where they are originally formed. This is significant for the steady-state description of the individual clouds as this indicates that this description maybe only to a quite limited degree be an acceptable representation of the convective clouds.

In addition, a large number of the plumes with a single buoyant core have multiple peaks in mean in-cloud vertical velocity, suggesting multiple successive thermals rising from the same base and mostly rising successively higher. This multi-thermal behaviour is currently absent in the current CCFM parameterisation as the transient behaviour of convective plumes is not considered. To aid the comparison with CCFM only the development of the first thermal will be considered here, and so the mature state will be of the first plume in the succession. Although it could be argued that the comparison with CCFM should be made at the point in time at which the plume has reached its highest point, the possible effect (e.g. moistening of the environment) of previous thermals is not captured in CCFM directly (but indirectly through the moistening by convective during successive host-model timesteps) and so the agreement is likely to be poor if these were included. The impact on a cloud's vertical profile on whether a single multiple successive plume caused a cloud to reach a given height will be studied in future work (to assess the importance of including representation of these clouds) by utilizing 3D analysis at higher time resolution.

Given the lag-correlation in time of maximum cloud-base radius and cloud-top height, and the decay of cloud-base by the time the maximum cloud-top altitude is reached, it is clear that the steady-state picture does not generally hold. A characteristic analysis time per cloud must instead be defined, and as a matter of definition the time at which a cloud reaches its maximum altitude will be called the "mature state" from hereon. However since the cloud-base radius and vertical velocity rapidly decrease and become largely zero when the maximum altitude is reached, the extreme values over time of these variables will also be considered when examining other assumptions in CCFM besides the steady-state

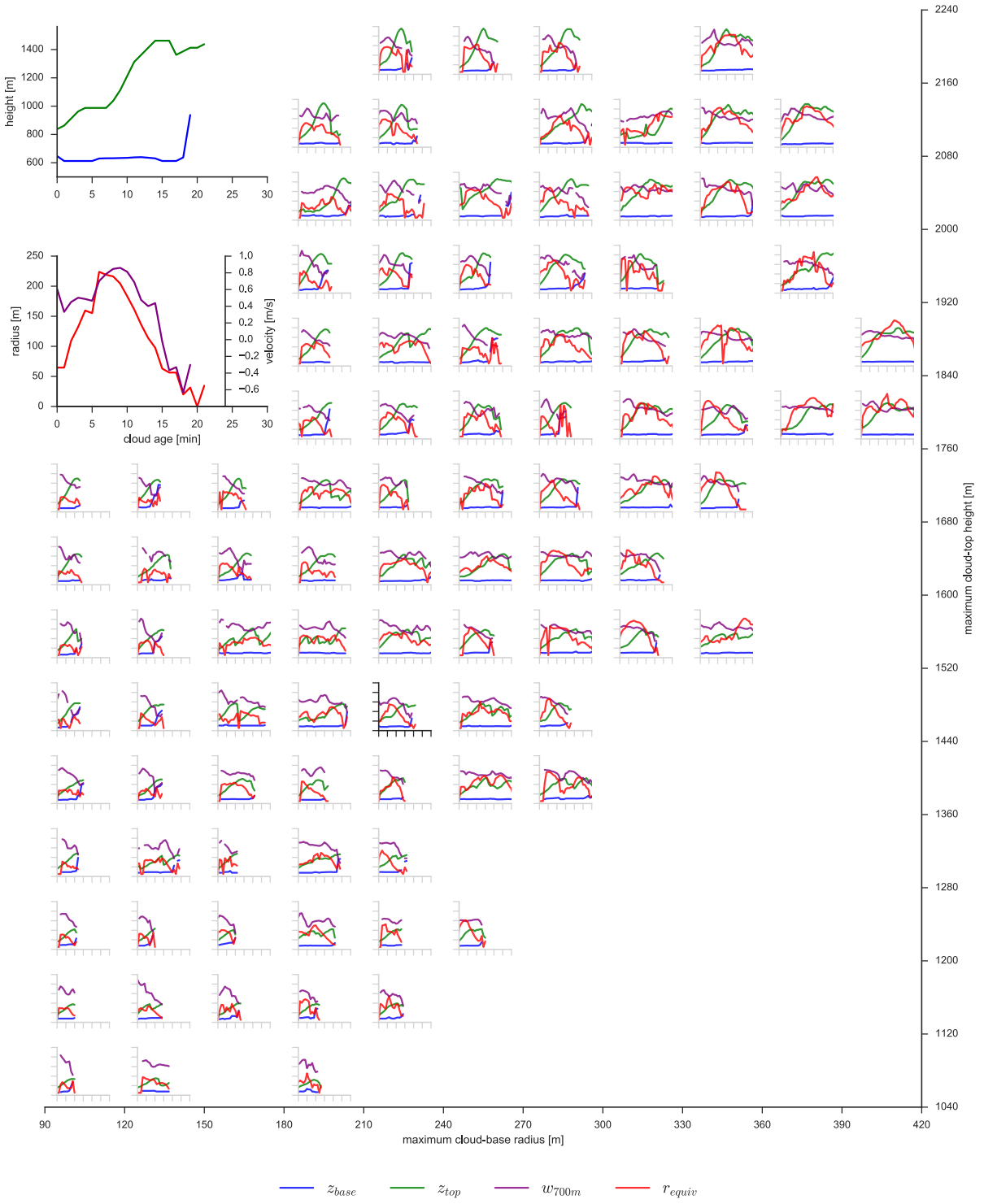

Figure 6.8: Profiles of evolution of individual clouds picked from intervals of maximum cloud-base radius and maximum cloud-top height. As either is increased the total lifetime is notably longer. Note that the cloud-base radius (in red) typically peaks before the maximum of cloud-top height (in green) is reached. The near cloud-base vertical velocity (purple) typically correlates closely with the cloud-base radius. Finally note that the cloud-base height (in blue) often has risen high above the condensation level before maximum cloud-top height is reached. In the top-left the profile indicated with solid-black axis is shown with labelled axis for reference

assumption.

6.3.3 Cloud-base height distribution

Using the method described in section 6.3.1.1 to estimate the cloud-base region, the per cloud mean cloud-base height was calculated at the time of maximum cloud-base radius for each cloud (Figure 6.9) during the two analysis intervals ($t_I \in [240; 720]$min and $t_{II} \in [720; 1200]$min). By fitting a Gaussian distribution to the histograms of mean cloud-base height (at the time of maximum cloud-base radius per-cloud) across all clouds present in each analysis interval the standard error in the mean can be estimated so that the mean cloud-base heights are 636 ± 20m and 624 ± 18m respectively. Given that this error is smaller than the grid-resolution ($\Delta x = 25$m) it is reasonable to assert that all clouds rise from the same cloud-base height.

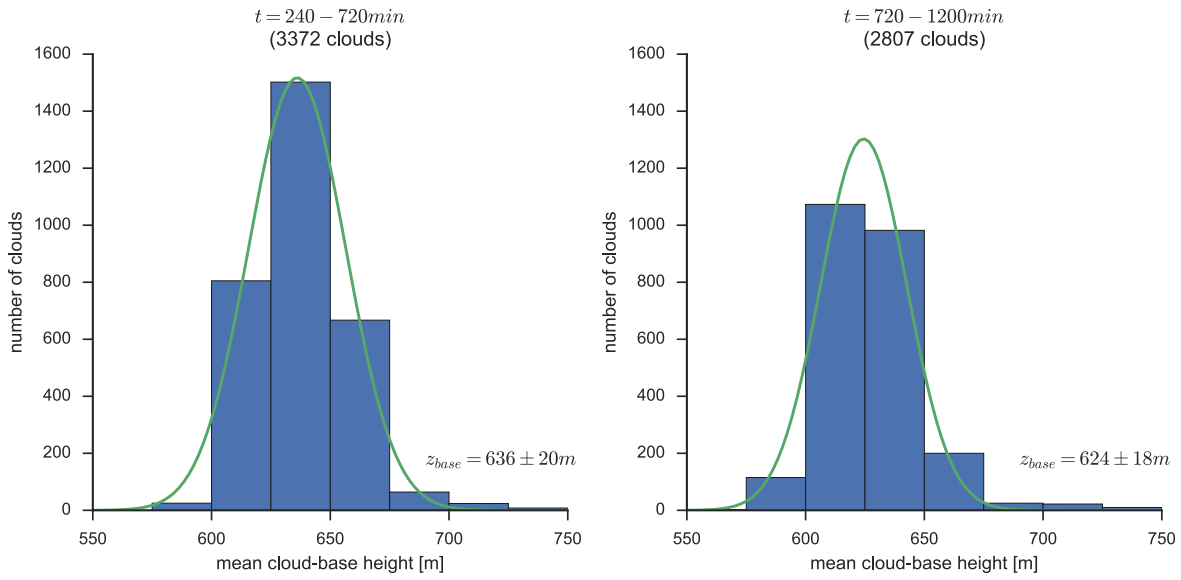

Figure 6.9: Distribution of mean cloud-base height over two 8-hourly intervals after simulation has reached steady-state. Note the rather small variation in the cloud-base height mean (as compared to the $\Delta x = 25m$ grid-resolution). Interestingly the there is a small decrease in cloud-base height over time even though the boundary layer deepens over time.

These estimates agree with the lifting condensation level (LCL) of a parcel lifted adiabatically from the surface (see Figure 6.1) which using the ambient profile halfway through each of the two analysis intervals is $z_{LCL} = 640$m and $z_{LCL} = 625$m at $t = 480$min and $t = 960min$ respectively. Both the LCL height and the LES-estimates predict a slight decrease in cloud-base height over time, however this change is smaller than the LES grid-resolution and will be investigated in further work at higher resolution.

The small variation in mean cloud-base height across all clouds present at a given time suggests that within the trigger of CCFM it is only necessary to consider a single cloud-base height (at least to $25m$ resolution). This conclusion may not hold for cases of deep convection and will not be true if mid-level convection takes place. Both of these questions

will be considered in future work with simulation setups which cause the formation of deep convection and mid-level convection.

6.3.4 Cloud-base radius

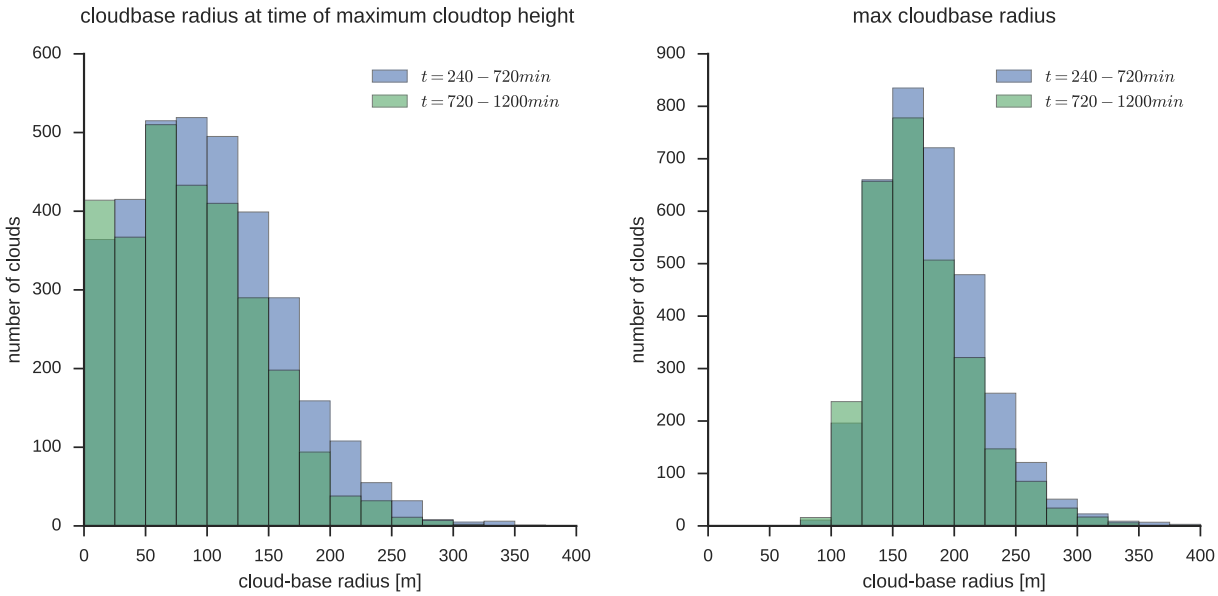

Figure 6.10: Cloudbase radius for all single-core clouds at the time of maximum radius (left) and maximum cloudtop over whole cloud lifetime.

Using the method described in the previous section for defining the cloud-base region, the radius of the cloud-base for a given cloud is calculated as the radius of a circle with the same area as the total area of a cloud's cloud-base region. To highlight the importance in choosing an analysis timestep when calculating the cloud-base and to emphasise the temporal variation of the cloud-base radius, Figure 6.10 plots both the cloud-base radius at the time of a cloud's maximum height (left) and the maximum cloud-base radius during each cloud's entire lifetime (right). It is clear that a large number of clouds have "disconnected" from the condensation height at the time where the maximum altitude is attained, so that ≈ 1400 clouds ($\approx 50\%$) have a cloudbase radius $r_{base} < 100m$ (only four grid cells, $\Delta x = 25$m). If we instead consider the maximum radius throughout a cloud's lifetime, the distribution is centered at $r \approx 160$m and almost no clouds (< 10) have a maximum cloudbase radius $r_{base} < 100$m.

In CCFM the discrete cloud-base radii used for profile integration are chosen to be maximally as large as the depth of the boundary layer (z_{BL}), which in the RICO simulations is $z_{BL,RICO} \approx 550m$. This limit value was also indicated in Chapter 5 where simulations of individual convective clouds were carried out, with the limit value reasoned through a geometrical argument of necessary mass-flux to support the production of a convective cloud. Given the analysis above however, it appears that the limit radius observed for *actual* clouds produced (at least in the RICO setup) is significantly smaller ($r_{lim} \approx 350$m) than the boundary-layer depth. This would suggest that at least for the case of shallow convection the limit radius in CCFM could be reduced, and CCFM's spectrum calculation should produce no clouds with a cloud-base radius larger than $r_{lim} \approx 350$m. The limit radius used is important because reducing it will allow for a more fine-grained representation of

the convective clouds that are *actually* formed, resulting in more accurate predictions of cloud-profiles and thus vertical transport by CCFM.

The analysis of cloud-base radius should be extended in future work to take into account the non-axisymmetric geometry of the cloud-base of most convective clouds, so that the estimates of entrainment will be based instead on distance along a cloud's edge (the surface through which entrainment takes place) which will be larger the more asymmetric a cloud is. In addition inclusion in this analysis of the multi-core clouds will likely skew the distribution of cloud-base radius to higher values.

6.3.5 Cloud-top height

In this section the distribution of cloud-top height is examined with the aim to both identify characteristics of these distributions and to highlight the implications of the choice of timestep when estimating cloud-top height. The cloud-top height was defined by finding the maximum height for each cloud where cloud condensate was present.

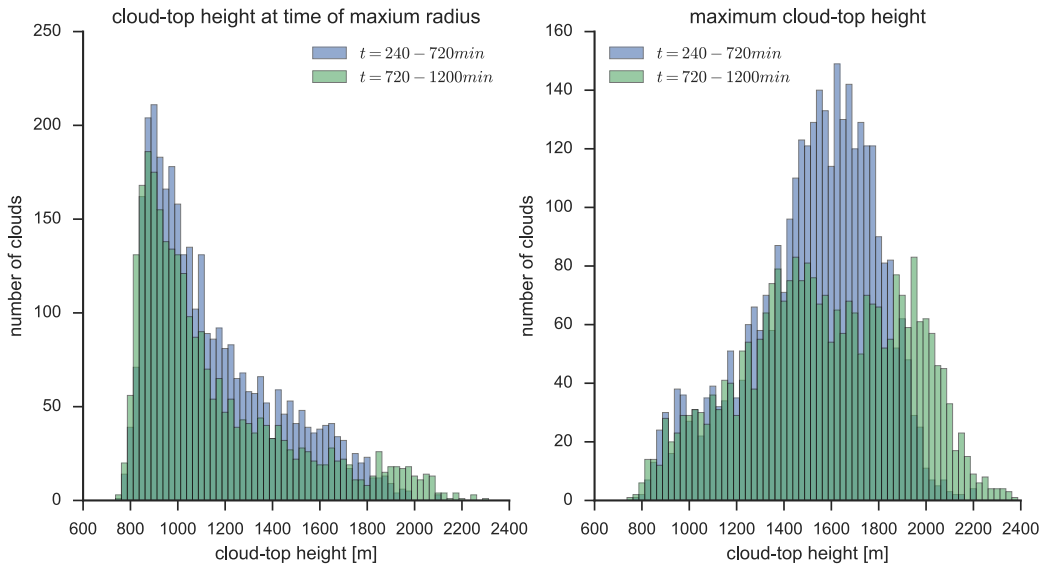

Figure 6.11: Cloudtop height for all single-core clouds at the time of maximum radius (left) and maximum cloudtop over whole cloud lifetime (right). Comparing the shape of the two distributions it is clear that the majority of clouds have not attained their maximum height when the maximum cloudbase radius is attained as the shape of the two distributions would otherwise be similar.

In Figure 6.11 the distribution of cloud-top height across all clouds that are present during the two analysis time periods is plotted, both at the time of maximum cloud-base radius (left) and at the time of maximum cloud-top height (right). For each single-core cloud the maximum cloud-top height (i.e. max height where $q_l > 0g/kg$) over each cloud's lifetime was identified. By comparing the shapes of the two histograms, it is clear from their difference in shape that the majority of clouds have not attained their maximum altitude at the time of maximum cloud-base radius.

Concerning the maximum cloud-top height (figure 6.11 right) most of the single-core clouds present in the first 8hrs of simulation time rise to $z \approx 1600m$. Over time this distribution widens so that the mean cloud-top height increases and the maximum grows from $z \approx 2200m$ to $z \approx 2400m$, agreeing with the increasing height of the capping inversion seen in figure 6.1. Interestingly the distribution appears unchanged below $z \approx 1400m$ suggesting that the convective clouds in this region are largely dominated by dilution through entrainment and lacking kinetic energy to overcome the convective inhibition. Although the level of free convection as predicted using an adiabatically lifted parcel would suggest a quite well-defined level of free convection, the effective convective inhibition (as mentioned in Section 3.8 when integrating the 1D cloud-model) that is felt by a particular cloud will be dependent on its radius as clouds of different radii entrain differently. This would lead to a continuum of heights at which free convection is attained. Above $z \approx 1400m$ a significant number of clouds previously stopped by the inversion attain a higher cloud-top height.

Given the considerable difference in shape of the cloud-top height histograms at time of maximum radius and maximum height it is clear that very few clouds have attained their maximum height at the time that the cloud-base radius is at its maximum. As mentioned in Section 6.3.2 frequently the cloud-base radius rapidly decreases as the cloud grows and in many cases the cloud-base completely disappears before the cloud's maximum height was attained. This suggests that these clouds behave more like a thermal than a plume, and so cannot be considered as being in a steady state. This has implications for both the type-classification in CCFM (which is based on cloud-base radius and so assumes that all clouds with the same cloud-base radius behave identically and reach the same height) and for the applicability of the steady-state cloud-model. The former, studying the extent to which the cloud-base radius may be taken as a good predictor of the eventual cloud-top height will be examined in Section 6.3.6. The latter will briefly be discussed here.

Although the steady-state assumption clearly cannot be applied to individual clouds (at least not to the shallow convection clouds present in the current setup) it may be that through considering together a number of clouds in different stages of their development, but going through nearly the same development (in terms of time-dependent vertical structure of radius, velocity, etc) that these clouds together could form an overall steady-state massflux, and so together cloud be represented by a steady-state plume. This grouping of individual convective thermals into an effective convective plume could thereby form a foundation for unifying the thermal/plume description of convective clouds which currently is unresolved in the literature. Studying the applicability of this idea will require detailed analysis of time-dependent 3D profiles of individual clouds, so that time-dependent cloud-profiles may be grouped by similar structure. This description of the steady-state may also alleviate some of the hostmodel timestep sensitivity of the CCFM's spectrum calculation (an issue which will be discussed in Section 6.5.2). This idea will be applied in future work through analysing 3D output with higher temporal resolution.

The principal limitations of this analysis lie in the study of only one case of shallow convection. It is clear from nature that deep convective clouds persist for longer durations, and so for these clouds the steady-state picture may be more applicable to a single convective cloud. It should be noted though deep convective clouds have been frequently observed to be composed of multiple rising thermals, giving the further evidence for the applicability of the above description of convection in a steady-state balance with the large-scale forcing. This will also be investigated in future work.

6.3.6 Cloud-base radius and cloud-top height

This section examines the extent to which cloud-base radius correlates with cloud-top height (the assumption of which forms the basis of CCFM's classification of cloud types by cloud-base radius). We look first at the relationship between the instantaneous cloud-base radius at the time of maximum cloud-top height for each cloud (Figure 6.12). It is clear that there is little correlation between the two with many clouds at their maximum altitude having little or no cloud-base (and so very small cloud-base equivalent radius), and a given instantaneous cloud-base radius being found for clouds with varying maximum cloud-top height. Two discernible features however are the two clusters of cloud-top height where clouds below $z \approx 1200m$ decaying before having disconnected from the condensation height. These two clusters are visible for both time periods analysed with the freely convecting clouds spreading to higher altitudes as the inversion in pushed up.

If we instead consider the maximum cloud-base radius during the entire life-time of a cloud against its maximum cloud-top height (Figure 6.13) some degree of correlation emerges, so that as maximum cloud-top increases these taller clouds are more likely to have had a larger cloud-base radius during their life time. The difference in the presence of correlation is particularly clear by comparing the mean cloud-base radius for clouds that reach a particular cloud–top height.

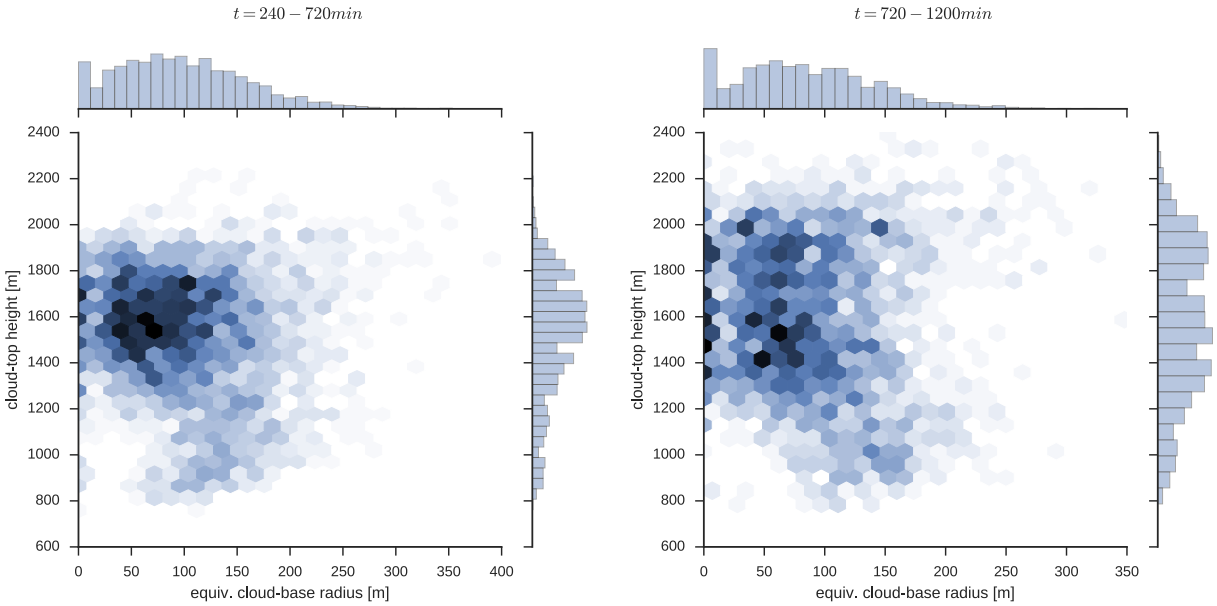

Figure 6.12: Joint histogram of insteanous cloudbase radius vs cloudtop height at time of maximum cloudtop height. Note the very small (near zero) cloudbase radius for many clouds above $z = 1200m$ indicating that by the time a cloud has reached its maximum height the cloudbase has eroded.

As seen in Section 2.1 the same cloud-top height can be achieved by varying Δq_v and $\Delta\theta$ to overcome CIN and put the parcel on the same moist adiabat while compensating for the extra entrainment for a smaller cloud. This means that clouds with different cloud-base radii can reach the same cloud-top height as long as Δq_v and $\Delta\theta$ are changed to compensate. However given that the maximum cloud-base radius does appear to be

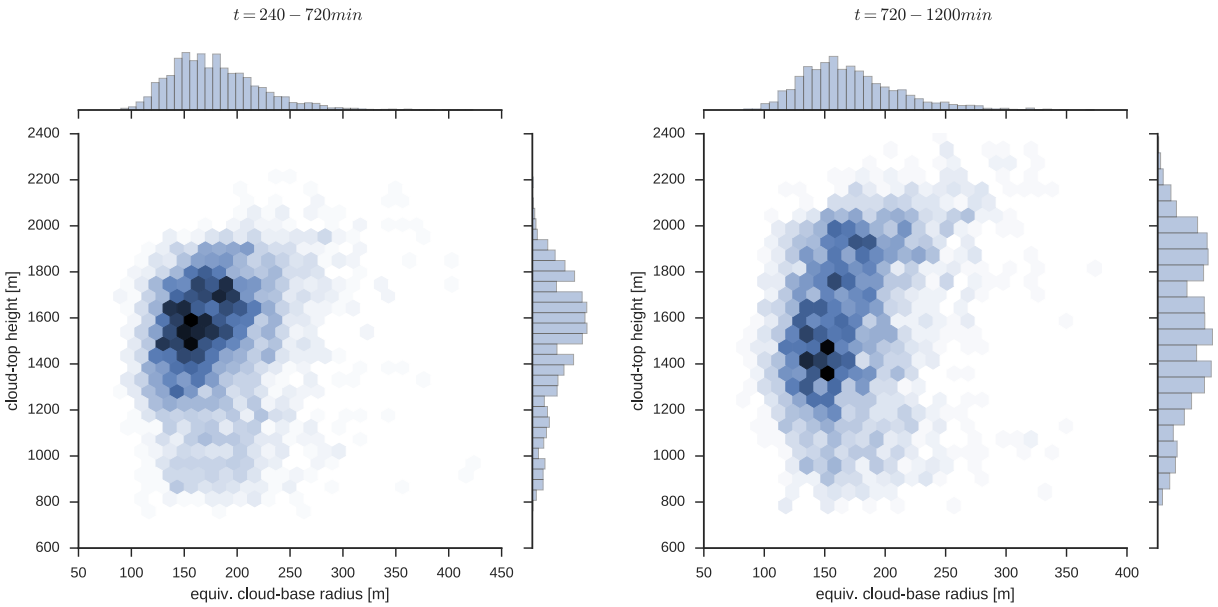

Figure 6.13: Maxiumum cloudbase radius vs maxium cloudtop height shows some degree of correlation (with larger radius leading to higher cloudtop height) when the maximum during each cloud's lifetime is considered. There is still a large spread in cloudtop height for a given cloudbase radius, which may partly be due to variations in cloudbase perturbation and partly due variations in the moisture and heat content of entrained ambient air

an indicator for the cloud-top height changes in perturbation magnitude (Δq_v and $\Delta\theta$) may merely act as to cause a spread around this trend of increasing cloud-top height with increasing cloud-base radius. The competing effect with perturbation magnitude is that larger clouds have a smaller circumference to volume ratio so that larger clouds fractionally entrain less and so can achieve higher altitude. Another cause for the spread of max cloud-base radius vs max cloud-top height may be due to the fact that the clouds were morphologically to varying degree different from axisymmetric clouds so that they entrain differently. This would not be captured in the axisymmetric estimate of cloud-radius and instead the circumference (as a function of height) would have to be estimated. This will be investigated in future work.

6.3.7 Characteristic cloud-base conditions

In this section the buoyant perturbations originating in the the boundary layer which lead to development of convective clouds will be estimated. This analysis is performed using the 3D 2-hourly simulation output to extract properties of the atmosphere at relevant heights in the boundary-layer and at the cloud-base. Owing to the coarse temporal resolution of the simulation output, the analysis is only performed as an instantaneous measure of the perturbation size and magnitudes; the variation of these perturbations in time will be considered in future work when 3D output with higher temporal resolution can be used for analysis.

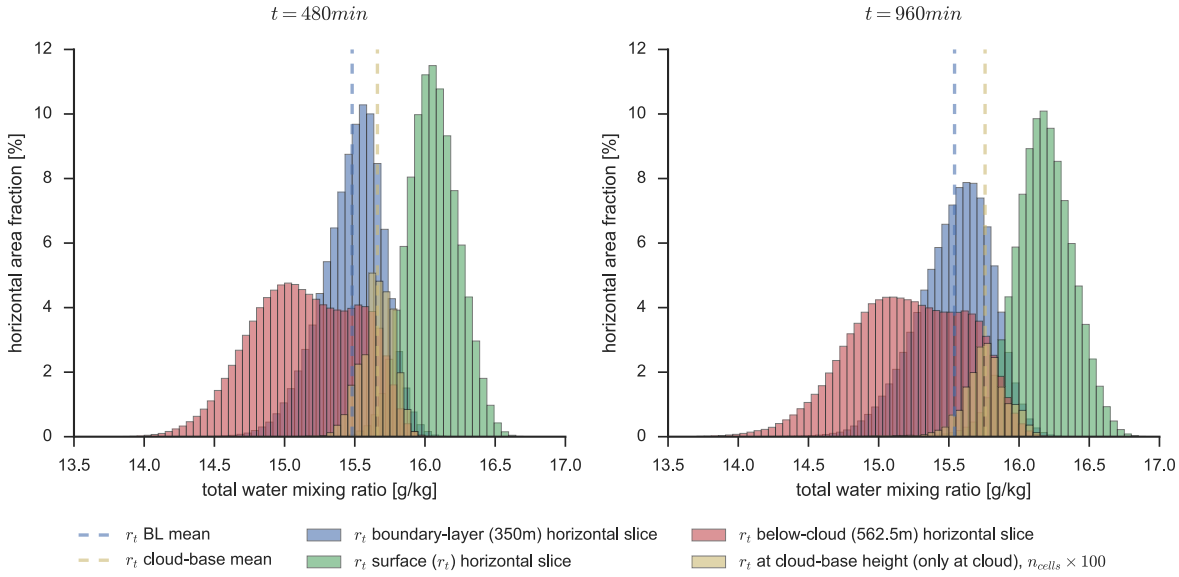

Figure 6.14: Histogram of moisture distribution at and in horizontal slices below cloud-base.

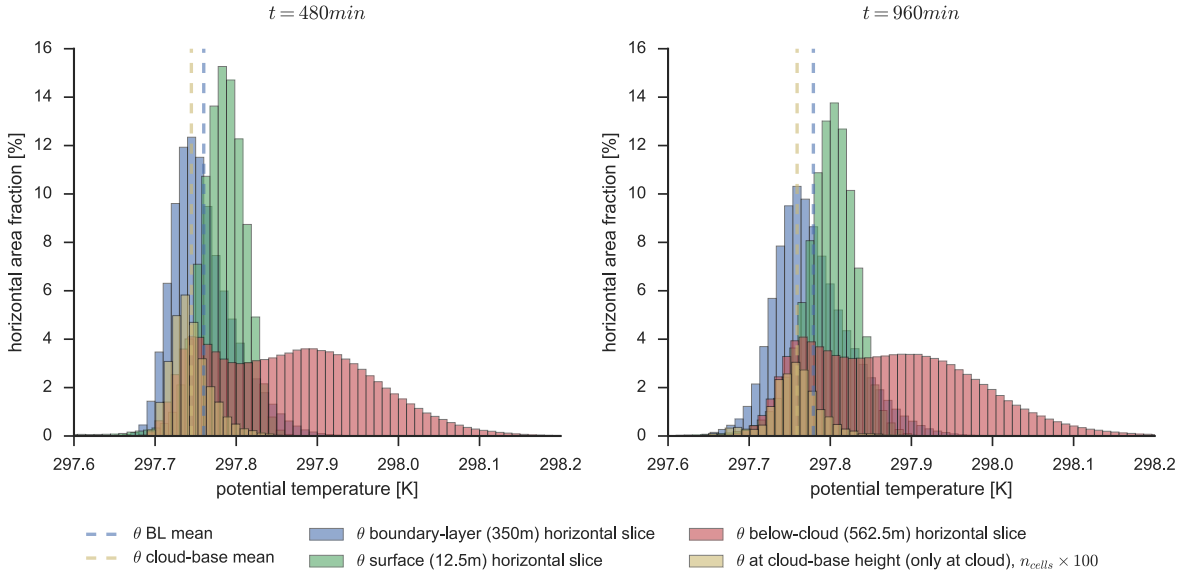

Figure 6.15: Histogram of temperature distribution at and in horizontal slices below cloud-base.

The below-cloud region is characterised by a well-mixed boundary-layer below and above

which exists a region of drier and warmer air which forms the potential barrier inhibiting convection. Only buoyant perturbations in the boundary layer with sufficient kinetic and thermal energy to overcome this convective inhibition will lead to free convection. The principal source of moisture and heat perturbations lies in surface fluxes. To examine the origin and magnitude of perturbations in the boundary, three characteristic heights are of interest: 1) characteristic moisture (total water mixing ratio) and heat-content (potential temperature) values for the well-mixed boundary layer as a whole (taken here at $z_{BL} \approx 350m$ as estimated from the plateau in moist static energy) as the reference state for perturbations, 2) the magnitude of perturbations produced by the surface fluxes (taken at $z \approx 12.5m$) and 3) below-cloud (taken $25m$ below the lowest cloud present) ambient conditions, indicating the characteristic conditions of the convective inhibition barrier. Finally the distribution of moisture and heat-content *at* cloud-base is extracted, so that the actual perturbations that lead to convective cloud production may be estimated. In figure 6.14 and figure 6.15 the distributions of moisture and heat-content in these regions have been plotted at $t = 480min$ and $t = 960min$, with the distribution mean at cloud-base and at the characteristic boundary layer height indicated (note that the number of cells at cloud-base has been exaggerated as these make up a small fraction of the domain's horizontal area). The at cloud-base values were only extracted for clouds which have their cloud-base height below $750m$ ($\approx 90\%$ of clouds) as these are mostly likely to have been produced by thermals originating in the boundary-layer (as mentioned previously, the other 10% clouds present are likely the decaying remnants of clouds that previously had a well-defined base).

Both the distribution of potential temperature and moisture in the vertical slice just below the cloud-base show a bi-modal distribution, the drier and warmer air coming from above this region being both drier and more stable than the air of the boundary layer. By comparing with the distribution of potential temperature and moisture sampled only where in the domain clouds are present, it is clear that these moister and colder parts of the distributions originate from thermals rising from the boundary layer, containing more moisture than the air above and cooling adiabatically as they rise from the boundary layer, thereby having potential temperature that follows that of the boundary layer.

When comparing the difference between the mean value at cloud-base and in the boundary layer, the moisture content shows a comparatively large difference as compared to potential temperature, the relative perturbations being $\Delta q_t \approx 0.20g/kg$, $\Delta\theta \approx 0.02K$ at $t = 480min$ and $\Delta q_t \approx 0.30g/kg$, $\Delta\theta \approx 0.01K$ at $t = 960min$. Based on the analysis in Section 2.1 $1.8g/kg$ of water vapour is equivalent to $1K$ in terms of producing buoyancy, which suggests that the buoyant thermals which lead to convective cloud development are not buoyant because they are hot but rather because of their higher moisture content (and so lower density).

In addition, the potential temperature at cloud-base is almost exactly the same as the mean potential temperature at $z = 100m$ suggesting that thermals that cause the perturbations

that lead to cloud-formation originate from near the surface

Finally the mean moisture content at cloud-base is larger than the mean moisture content near the surface ($z = 12.5m$), which on the one hand may suggest that the rising parcels which lead to cloud development are those with the highest moisture content (which cause these to have the lowest density) or may suggest that some degree of horizontal moisture convergence takes place in the boundary layer feeding into the boundary layer thermals, increasing the moisture content relative to what is present at the surface.

To properly identify the connection between thermals originating from the surface and the production of individual clouds, it will be necessary to produce 3D simulation output with higher temporal resolution. This will also make it possible to study how these perturbations vary over time, through this it may be possible to correlate perturbations at cloud-base with cloud-top height and cloud-base vertical velocity. In addition it will be possible to test the extent to which cloud-base vertical velocity agrees with estimates based on the CIN of adiabatically lifted parcels, which could provide the formulation of a more physically-based cloud-trigger.

Finally higher time-resolved simulation output would allow investigation into the exact mechanisms that lead to multiple thermals rising within the same cloud and to what extent neighbouring clouds effect each other's development.

In terms of vertical velocity (Figure 6.16) the mean vertical velocity at cloudbase is $w_{cldb} \approx 0.5$m/s which is within the range of values predicted in Section 2.1. The mean of the distribution over the whole cross-section of $\bar{w}_{BL} = 0$m/s is expected from flux-conservation.

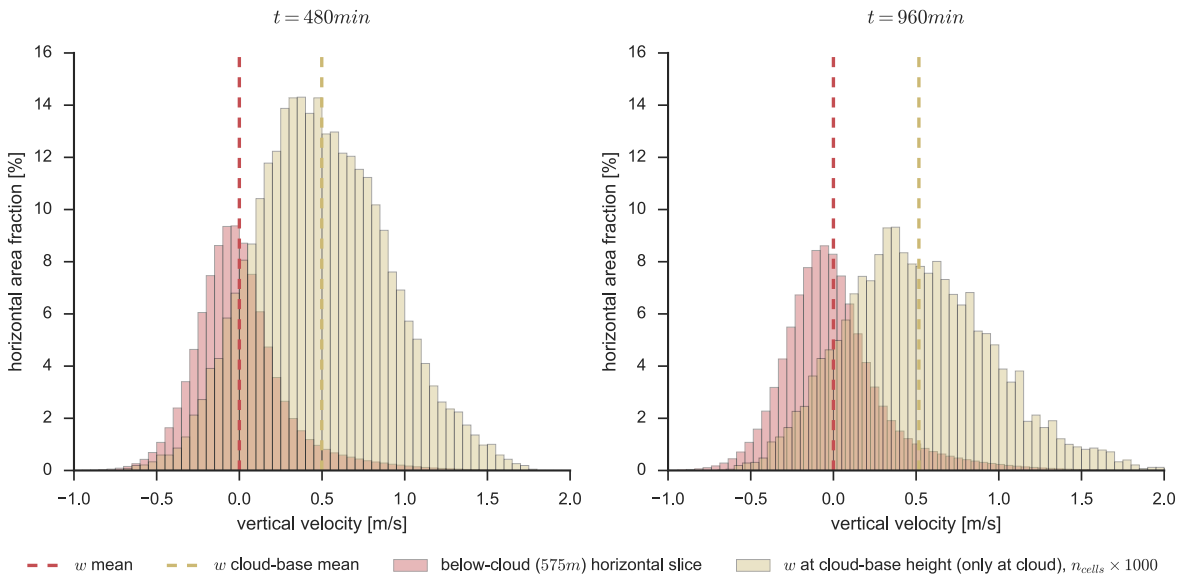

Figure 6.16: Histogram of vertical velocity distribution at and in horizontal slice below cloud-base.

6.4 Near-cloud environment and horizontal mean state

The purpose of the analysis in this section is to investigate the extent to which the horizontal mean atmospheric state represents the immediate environment, and so to what extent the mean state is adequate in predicting the environment in which a convective cloud grows. The existing assumption in CCFM is that the horizontal mean state is representative of the cloud's immediate environment, so that the mean horizontal state may be used to calculate the density of the environment (and thus the cloud's buoyancy) at a given height. In addition the previous version of CCFM (*Wagner and Graf* [2010]) assumed that the environment contained only dry air when calculating the entrainment which (if the environment *actually* contains a significant amount of moisture) would excessively try out the cloud. The importance of representing the moisture of air entrained into the cloud will be investigated below. It is important to bear in mind here that when used within a climate-scale hostmodel, the environmental profile provided to the convection scheme (e.g. CCFM) will be exactly the horizontal mean profile, and so any variations about this state would have to be represented internally by the convection scheme.

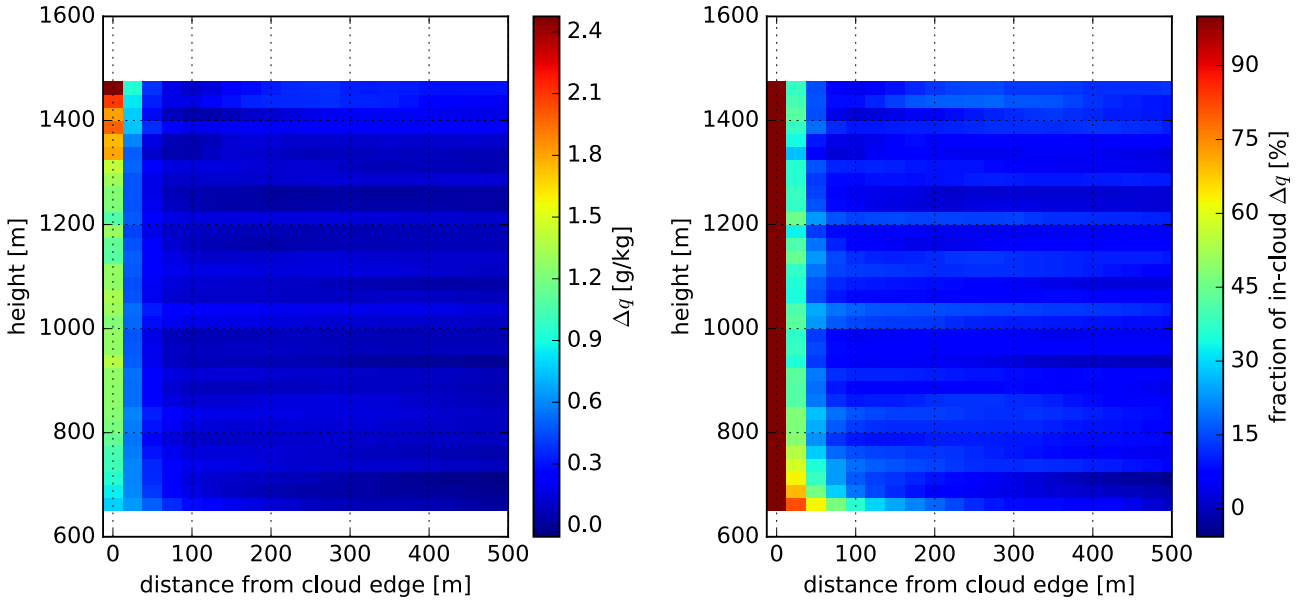

Figure 6.17: Deviation from horizontal mean total water specific mass at increasing distance from cloud edge. The absolute amount of water vapour is significantly larger in the near environment of the clouds, $\approx 0.4g/kg$ at $25\mathrm{m}$ and $\approx 0.1g/kg$ at $25\mathrm{m}$, and much larger as a fraction of in-cloud total water at the heighest altutide and hardly at all near cloud base.

Figure 6.17 and **??** show at a given height and distance from the cloud edge the deviation of total water specific mass and liquid potential temperature from the horizontal mean state for all single-core clouds present at $t = 240min$. The deviation was calculated by defining the cloudy region as anywhere where condensed water was present ($q_l > 0.0g/kg$) and extraction "shells" around the cloudy region from the 2-hourly 3D output data at increasing

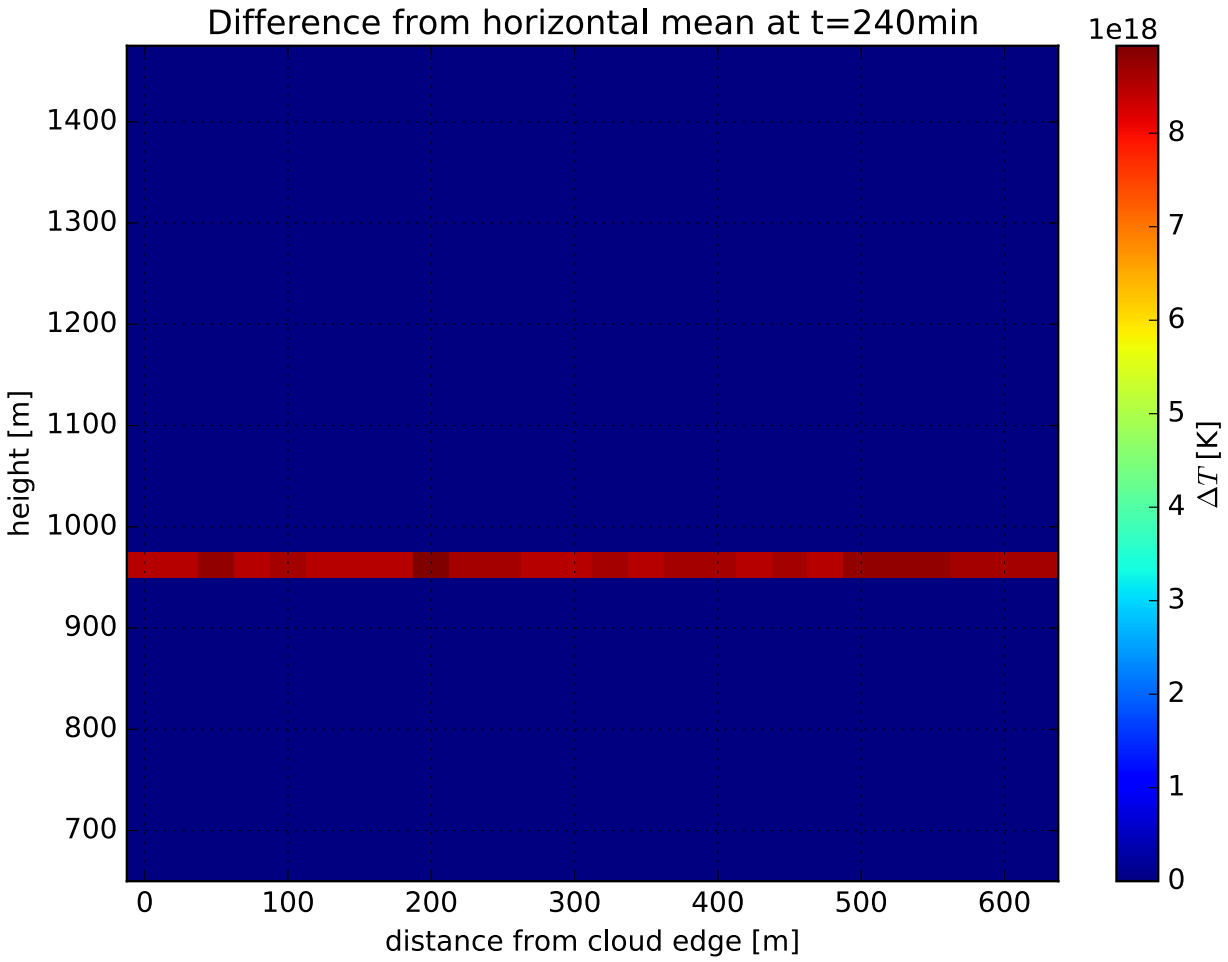

Figure 6.18: Deviation from horizontal mean absolute temperature at increasing distance from cloud edge. A clear cold downdraft shell can be seen around the cloud. When comparing the in-cloud temperature with the mean environment there is interestingly little difference compared with what is in the down-draft shell.

distance from the cloudy region. The single-core clouds were identified by identifying overlap with the 2D cloud-tracking information, and only the immediate environment of these clouds was extracted. For each cloud the environment was only sampled to the height of the cloud-top, which given that that only few clouds reach $1600m$ implies that the extracted environmental conditions are based progressively fewer clouds as altitude is increased. The steps in increased distance are at the grid resolution of $\Delta x = 25m$. At the origin ($0m$ distance) the deviation of the in-cloud mean to the horizontal mean is plotted for reference.

In terms of total moisture content, it is clear that in the immediate environment of the cloud (up to $\approx 50m$) there is significantly more moisture present than in the horizontal mean, so that at $50m$ the total moisture deviation is as a vertical average $\approx 20\%$ of the in-cloud deviation. This is significant as using simply the mean ambient state would thus predict more drying through entrainment than necessary, since the entrained air (assuming the immediate environment will be entrained into the cloud) would be represented by the horizontal mean state, and so entrainment will cause an excessive retardation of the cloud's growth than.

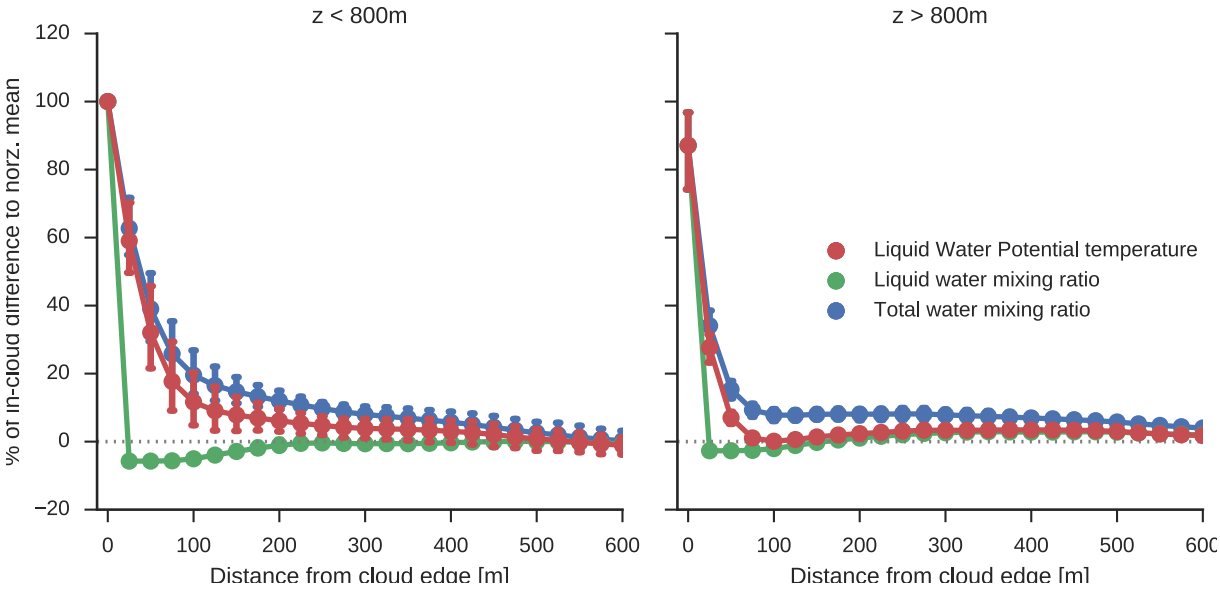

Figure 6.19: Deviation from horizontal mean at given distance from cloud edge as fraction of the mean in-cloud deviation from the horizontal mean for total moisture, averaged over heights below $z < 800\text{m}$ (left) and above $z > 800m$ (right) to highlight the stronger deviation near cloud-base. The deviation is plotted for liquid water and liquid potential temperature. In vertical averaging

Similarly the immediate environment of the cloud is significantly colder than the mean state, likely indicating the presence of "downdrafts" frequently observed in simulations in the literature (*Heus and Jonker* [2008]). Here simply using the mean horizontal state to represent the cloud's immediate environment would lead to an under-estimation of the cloud's buoyancy. This can be more clearly seen by examining the difference in density of the air surrounding the cloud (figure 6.20), where the air immediately around a given cloud is heavier than the horizontal mean density. It is also interesting to note that on

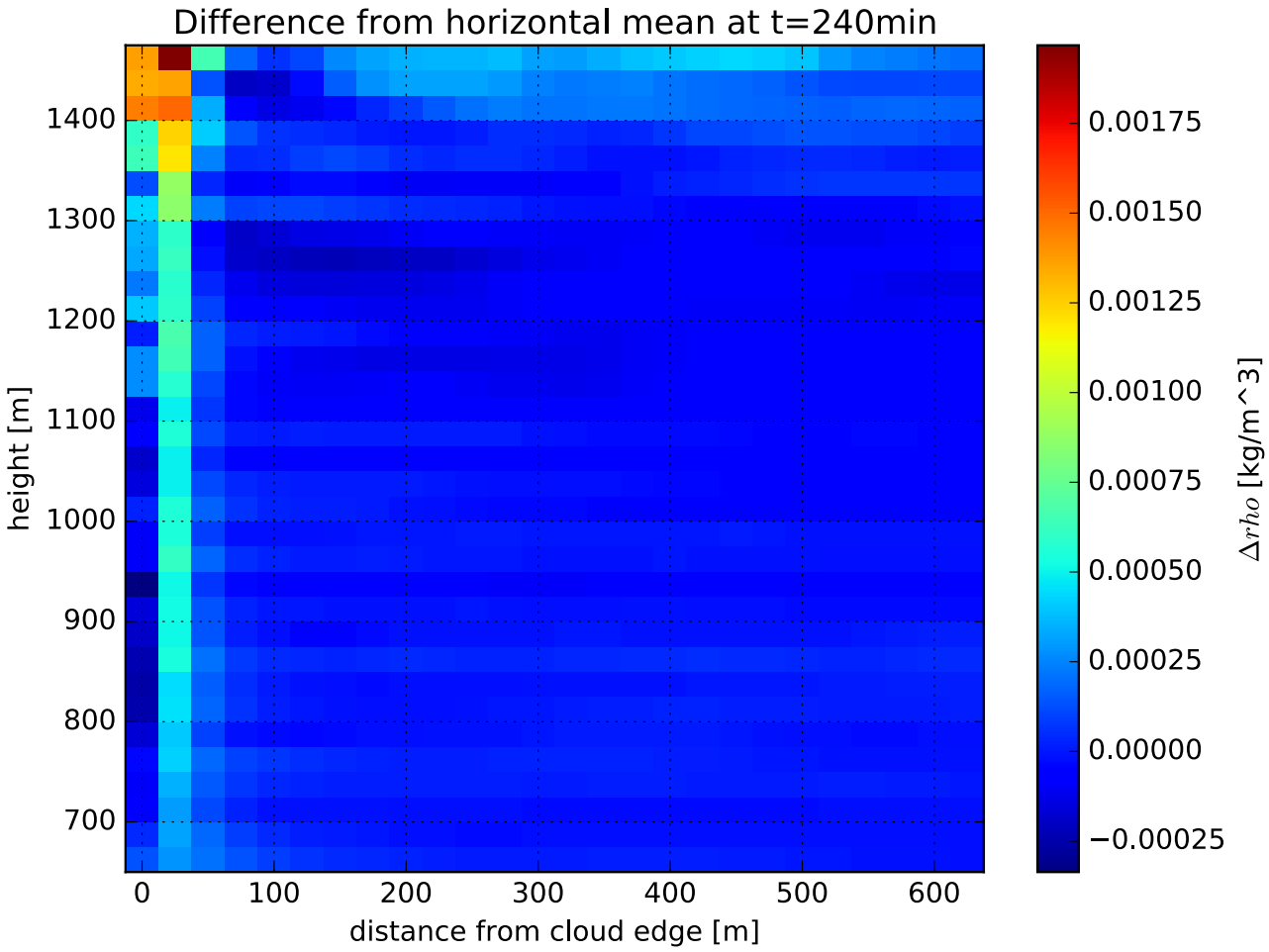

Figure 6.20: Deviation from horizontal mean density at increasing distance from cloud edge. Note the heavier air immediately surrounding ($\approx 25\mathrm{m} - 50\mathrm{m}$) the clouds indicating the presence of downdraft "shells". The mean in-cloud density also indicates that the clouds are on average buoyant up to $z \approx 1100\mathrm{m}$.

average the in-cloud air becomes heavier than the mean environment at $z \approx 1150$m which is very close to the split in distribution of maximum cloud top height seen in Section 6.3.6. It is possible that this height is determined by the entrainment, but the exact nature of this should be studied in further work with simulations in varying ambient profiles.

Finally the plot of cloud liquid water is significantly below the horizontal mean value immediately outside the cloud envelope and until a distance of $\approx 200m$. And so, until $\approx 200m$ there are on average less cloudy regions compared to the horizontal mean distribution, which suggests that on average individual clouds are separated by at least $200m$. This measure should be quantified in future work by calculating the distribution of cloud-distances between different cloud types (both passive and active, single and multi-core). Looking at the mean cloud-separation may help to clarify what affects the near-environment of individual clouds, and so to what extent the growth/presence of one cloud affects the growth of another.

The above deviations of the near-cloud state from the horizontally averaged averaged state across the entire simulation domain indicates that the cloud-model in CCFM should be extended to take these variations into account instead of using simply the horizontally averaged profile as provided from the host-model. This could take the form of formulating a "downdraft"-model which would also aid in the prediction of cold-pools in the boundary layer, as these are theorised to be driven by downdrafts (*Hohenegger and Bretherton* [2011]). The exact length-scale of variation in the near-cloud environment and the size of these variations should be looked at in future work by analysing simulation output at higher temporal resolution and establishing what physical parameters drive these variations.

The statistics of this analysis would be greatly improved by having 3D data output at higher temporal resolution, so that over a period where there is little change in the mean horizontal state (e.g. order of $10min$) a greater number of clouds could be included in the analysis. In addition, the environment of multi-core plumes has not been included here as there the individual cores of a single cloud would likely affect each other, further complicating the analysis. Finally, the extent to which the proximity of other clouds affects the immediate environment that a single cloud experiences will be studied in further work.

6.5 Comparison with CCFM

In this section the predictions of CCFM will be compared to results of the analysis in the previous sections. This comparison will by done primarily in terms of comparing the properties of individual clouds as predicted by CCFM's cloud-model (Chapter 3) to properties extracted from the RICO simulations, and secondarily by comparing the *spectrum* of clouds predicted by CCFM (number of clouds with a given cloud-base radius) to the spectrum extracted from RICO and examining the sensitivities of CCFM's spectrum calculation and how this affects the predictions of feedback on the large scales.

6.5.1 Predictions of CCFM's cloud-model

As was discussed in Chapter 3 the cloud-model integrations are most sensitive to the environmental air being entrained, so that even slight variations (on the order of a few percent) can drastically change the developed cloud profiles. In Figure 6.21 this is indicated by plotting the maximum cloud-top height as a function of cloud-base radius for individual integrations of the cloud-model in three ambient profiles where only the relative humidity was changed. In the extremes of low and high ambient humidity, the cloud-top height is seen to be largely unchanged as cloud-base radius changes, the clouds in the driest environment not reaching the level of free convection, and the clouds in the most moist environment all reaching up to the inversion height (and so are largely unaffected by the radius-dependent entrainment, as the air entrained is too moist to have any effect on the cloud-top height). By varying the ambient relative humidity it is possible to reproduce the general shape of the relationship between cloud-base radius and cloud-top height which was extracted from the RICO simulation in Figure 6.13.

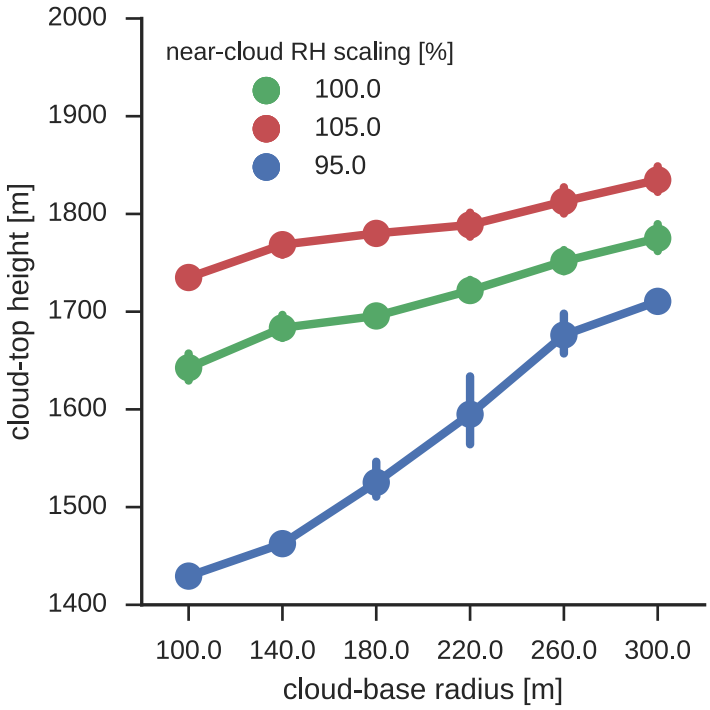

Figure 6.21: Plot of maximum cloudtop height vs cloud-base radius for integrations of the cloud-model using the RICO horizontal mean profile at $t = 480\text{min}$, each point representing one integration of the cloud-model. To show the impact of environmental moisture content the relative humidity has been varied by $\pm 5\%$ relative to the horizontal mean which creates a drastic change in maximum cloudtop height, the difference in $\Delta T = 0.2K\text{K}$ observed in the near-cloud analysis has been included too

Having achieved the general shape of the distribution through varying the ambient profile, Figure 6.22 plots again the cloud-top height as a function of cloud-base radius, now varying the cloud-producing perturbation to include the variations in cloud-producing perturbation in moisture content, temperature perturbation and vertical velocity extracted from the RICO simulation in Section 6.3.7. It is seen that the general shape of the relationship is

unchanged and the changes in cloud-base conditions instead are able to explain the spread around the general trend in the relationship between cloud-base radius and cloud-top height.

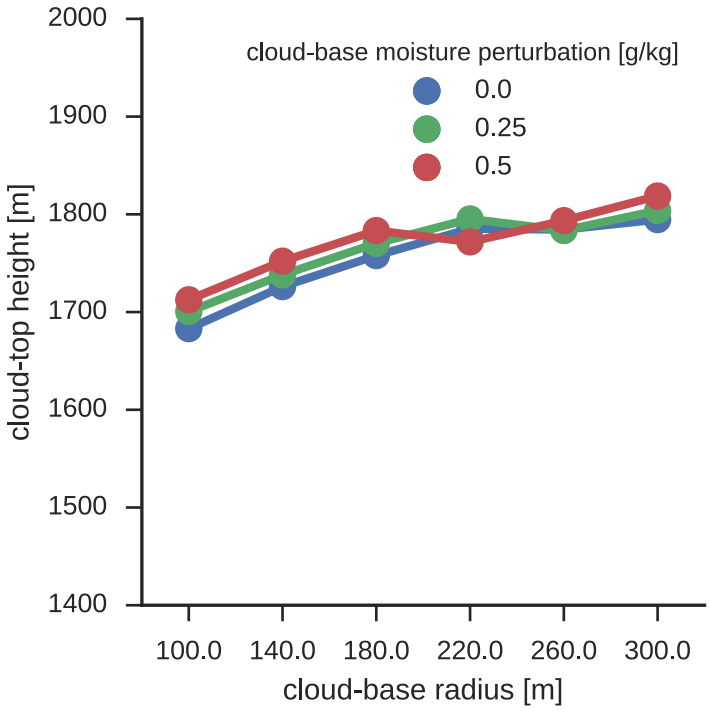

Figure 6.22: Plot of maximum cloudtop height vs cloud-base radius for integrations of the cloud-model using the RICO horizontal mean profile at $t = 480\text{min}$, each point representing one integration of the cloud-model. To show the effect of the change in cloud-base perturbation this has been been varied with the characteristic values found in the previous sections. Note that changing the perturbation has little impact on the cloud-top height compared to the effect of changing the near-cloud environment.

In future work it is the intention to extract from LES the variations in the cloud-producing perturbation and cloud-base vertical velocity, and correlate these with cloud top height to further constrain the relationship between these variables. With this information more integrations with the cloud-model will be performed and the presence of these direct relationships in the cloud-model investigated.

6.5.2 Predictions of the CCFM spectrum calculation

In Figure 6.23 is plotted the cloud spectrum as extracted from the RICO simulations where the cloud-type is classified by cloud-base radius. Due to the transient nature of the cloud-base radius (as discussed previously) the radius used is the maximum radius during each cloud's lifetime as this showed the strongest correlation with maximum cloud-top height (as apposed to the instantaneous cloud-base radius at a particular time during the simulation).

Note that the cloud-tracking algorithm requires at minimum 4 horizontally joining cells to denote a region of condensate as an individual cloud, and so at the simulation resolution ($\Delta x = 25m$) this limits the smallest cloud-radius to $r \approx \sqrt{2 \times 25m} \approx 36m$.

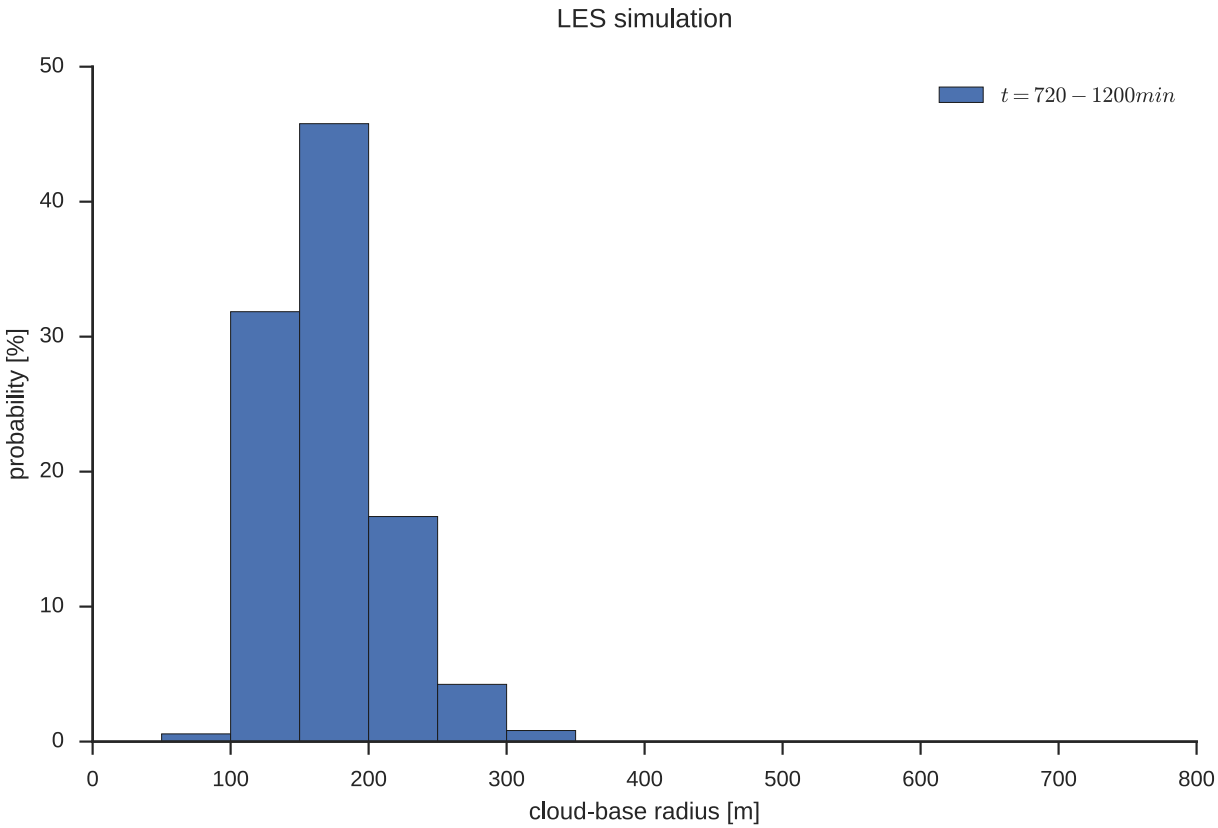

Figure 6.23: Probability-density distribution of maximum cloud-base radius in RICO simulations, and thereby the cloud "spectrum" as defined in CCFM.

In addition the smallest clouds are also likely to have a very small buoyancy and column integrated moisture, which would also exclude them for being captured by the cloud-tracking algorithm. This means that even **if** clouds as small as the grid-resolution do form in the simulation, these clouds will be absent in the spectrum extracted from RICO.

To calculate the cloud-spectrum in CCFM, a number of inputs are needed: the vertical profile of the environment, the large-scale forcing of moisture and temperature (formulated as time-derivatives of these variables in the vertical column) and finally the vertical forcing provided by the boundary-layer (as CCFM currently does not include a boundary-layer scheme and relies on predictions from the host-model). The vertical profile was extracted for each analysis interval from the RICO simulations as the horizontally averaged value of total moisture and temperature at $t = 480min$ and $t = 960min$ for each interval respectively (and thereby centered in each interval). The large-scale forcings were taken from the RICO setup and are constant in time. Finally, forcing from the boundary-layer processes were estimated from the RICO simulations from the Reynold's averaged vertical fluxes of moisture ($\overline{q_v' w'}$) and temperature ($\overline{\theta' w'}$), as simply using the fluxes as calculated from for example the horizontal mean vertical velocity and horizontal mean temperature would imply zero vertical transport (the mean vertical velocity being zero), whereas the net transport is driven by where vertical velocity and temperature vary together (the co-variance), which is exactly what is captured in Reynold's averaging.

When performing the CCFM spectrum calculation there are in addition a number of

variables which define how the integration takes place. Firstly the cloud-base conditions must be defined, which with the current cloud-trigger concerns defining the perturbation relative to the surface conditions of the parcel that is lifted adiabatically to condensation. The importance of these variables will be briefly discussed below. Secondly the number of cloud-types must be defined, both in terms of the maximum cloud-base radius represented r_{max} and in terms of the total number of cloud-types represented (and so in effect the "resolution" of the cloud spectrum). Using insight gained from analysis in Section 6.3 the importance and sensitivity of these aspect will be discussed in Section 6.5.2.1. Through the above analysis it was noted that the current spectrum calculation in CCFM has a number imperfections, the extent to which these are manifestation of issues with the numerical integration, formulation of the Lotka-Volterra solver or point to a larger issue will be briefly discussed in Section 6.5.2.1.

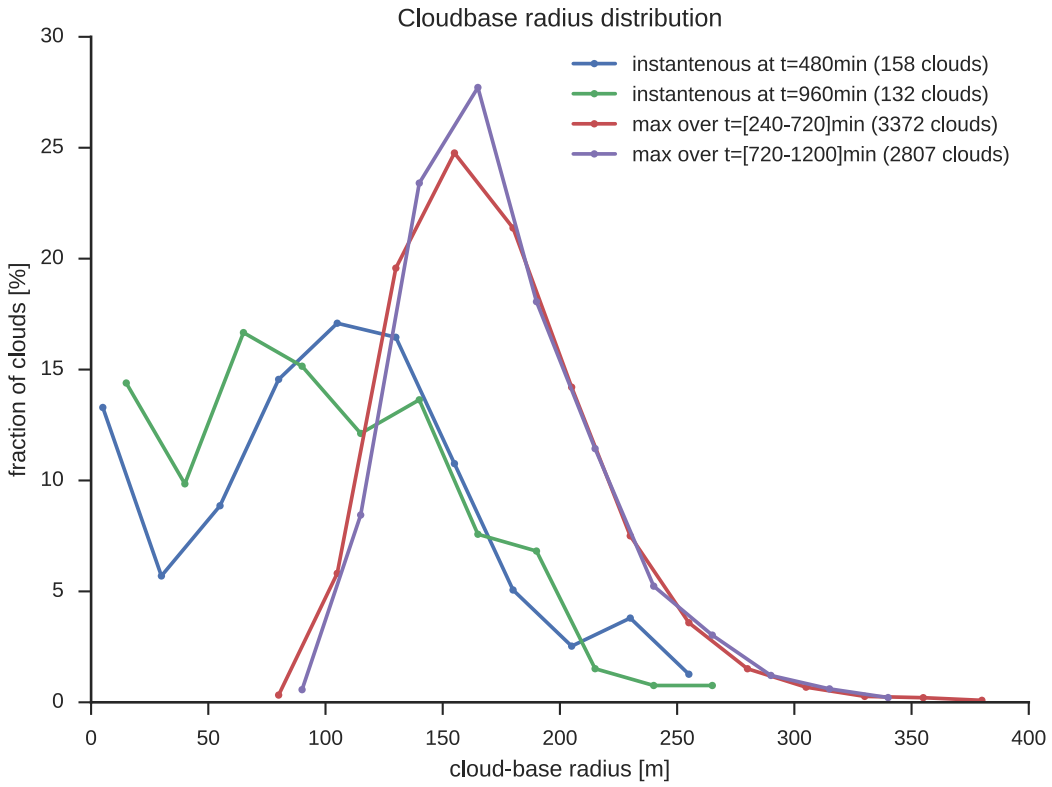

Figure 6.24: Probability distribution over different cloud-types (by cloud-base radius) using either insteaneous radius (at $t = 480\text{min}$ and $t = 960\text{min}$), a maximum radius over each cloud's lifetime of single-core convective clouds.

To aid the comparison with CCFM the spectrum analysis has been performed both as an instantaneous snapshot of a cloud-distribution at a given time in the LES simulations and also across clouds in their fully developed state. The former spectrum will contain clouds at different stages in their development, however as CCFM predicts only the dynamics of "steady-state" clouds, it is likely the agreement with CCFM will be poor. By instead analysing the cloud-properties in the mature state (time at which maximum cloud top height is attained) for each cloud that has appeared in a given time-window, the comparison

with CCFM is hoped to be more direct. This necessity to restrict the comparison does however highlight a possible shortcoming of the current cloud description in CCFM as it is clear the atmosphere adjusts to atmospheric changes in a temporally continuous manner and so the cloud spectrum *should* contain clouds at different stages of the their development.

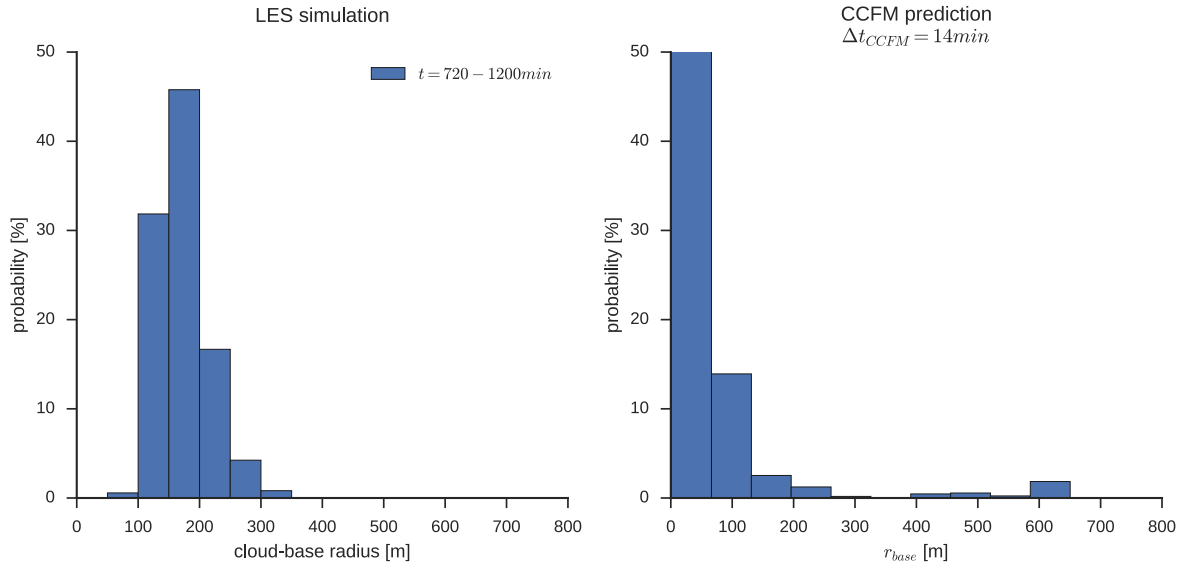

Figure 6.25: Histogram of cloud-types as predicted in CCFM's spectrum calculation. Note that due to the spectrum extracted from the RICO simulation contains no clouds smaller than $r \approx 100\text{m}$ which may be due to limitations in the cloud-tracking algorithm.

As mentioned previously the present analysis does not consider clouds with multiple buoyant cores (because CCFM cannot currently represent these clouds), but as clouds consisting of multiple buoyant cores are likely to have a larger cloud-base area these would likely shift the spectrum towards larger clouds. These multi-core should be included in future work by examining the contribution of these clouds to the cloud-spectrum and examining the extent to which CCFM is able to predict the presence of these clouds.

6.5.2.1 Noted sensitivities in the spectrum calculation

This section briefly summarises unexpected aspects of CCFM's spectrum calculation which were noticed while performing the above predictions of the cloud-spectrum and comparing to the spectrum found in the RICO simulation.

Firstly, by varying the time-step over which CCFM is used to calculate the cloud-spectrum, and thereby varying the duration over which the large-scale and estimated boundary-layer forcings alter the initial ambient state, the sensitivity of CCFM to the host-model integration timestep was studied. This analysis may also be seen as a means to consider the extent to which there exists an inherent time-scale that is significant in the interaction between the large-scale flow and the convective activity an isolated region. In the limit of decreasingly small timestep, the ambient state is nearly unchanged and so little convective

activity would occur. And in the limit of increasingly large time-step, the ambient environment may be forced into non-physical unstable state which would never occur in nature as convection would respond by consuming instability created. In between these two extremes exists a characteristic time-scale that would suggest what an appropriate integration timestep would be. In its existing formulation CCFM performs the integration of the 1D cloud-model (to produce a vertical cloud-profile for each cloud-type) in ambient conditions where the large-scale forcing has been integrated for the *entire* duration of the host-model timestep. By varying this timestep (and assuming large-scale forcing unchanged) it was noted that it might be beneficial to within CCFM introduce a form of sub-stepping in time, so that the ambient profile is not made too unstable. Currently the calculated spectrum shows some sensitivity to the host-model timestep because of how the large-scale forcings are used.

The second undesirable property of the spectrum calculation that was observed is a sensitivity of the calculated spectrum to the resolution in cloudbase radius (i.e. the number of cloud-types resolved). As both the ambient profile and the predicted vertical cloud-profiles are smooth and continuous in structure, and the vertical cloud-profiles vary smoothly as the cloud-base radius is changed, it is expected that the cloud spectrum predicted by CCFM be continuous so that there are no "gaps" in the spectrum where the number for some cloud-types (cloud-base radius sizes) is predicted to be zero. By examining the iterative solver used in finding the solution of the Lotka-Volterra system, it was noted that these gaps appear in the spectrum after very few (< 10) iterations, pointing to an issue with the numerical implementation of the current calculation of the weights in the linear system of equations. This should be investigated in future work by finding initial conditions which have analytical solutions and verifying the convergence under increase in resolution.

A third unexpected property of the cloud-spectra predicted by CCFM was a relative large number of clouds at the maximum cloud-base radius used in the definition of cloud-types. Drawing on analysis of the RICO simulation it appears the maximum cloud-base radius should be limited to $r_{base} = 300$m (at least for single buoyant core clouds). However, if the cloud-types used in the spectrum calculation we allowed to be larger, CCFM would consistently predict $\approx 20\%$ of clouds to have the radius of the maximum radius picked. Whether this points to an issue with the formulation of the CCFM spectrum calculation, or in fact indicates that CCFM (correctly) predicts that larger clouds (e.g. aggregated clouds) may also balance the large-scale forcing imposed, should be investigated in further work.

A fourth sensitivity which was observed was the change in fractional distribution of cloud-types as the total domain was changed. As the domain-size changes, the distribution of cloud-types should be unchanged so that the cloud-fraction covered by each cloud-type should be unchanged. Currently this is not the case and this should be addressed in future work.

The final shortcoming of the current implementation of CCFM is related to the vertical resolution used internally in CCFM. The issue is that currently the cloud-profiles integrated using the cloud-model (which is done with an adaptive step-size and therefore a higher resolution than the host-model) are coarsened down to the host-model vertical resolution before the spectrum calculation and net transport effect of the cloud ensemble is calculated. By coarsening the vertical resolution to the host-model resolution the cloud-base height is for example restricted to only a few discrete heights, strongly modifying the predicted CAPE consumed by each individual cloud. In addition the vertical transport by each cloud-type will be worsened too, strongly modifying the net vertical transport predicted by CCFM. This limitation should be removed in future work by keeping the full vertical resolution of the predicted cloud-profiles and instead interpolating into the ambient profile where higher resolution (than the host-model) is necessary.

Chapter 7

Conclusion and future work

In this work the development of moist atmospheric convection was studied through: 1) deriving from first principles a 1D cloud-model for predicting the vertical structure of a convective plume (Chapter 3, 2) developing a microphysics framework with adaptive time/space-integration of microphysical processes relevant to moist convection and, finally, 3) through studying the properties and time-dependent behaviour of convective clouds, using high-resolution numerical simulation of individual (Chapter 5) and multiple, interacting (Chapter 6) convective clouds. The findings in each of these topics will be briefly summarised below, and an outline for future work in each area detailed.

7.1 1D cloud-model

The 1D cloud-model of Chapter 3 was developed to replace the existing cloud-model used within CCFM with the following achieved aims: 1) formulate an energetically consistent, fully conservative set of model-equations based on first-principles, 2) allow for clear separation between cloud-dynamics and cloud-microphysics (so that the latter may be generalised into a separate software module), 3) allow for integration of all terms of the model-equations in a single numerically adapted timestep, removing the process priority of the previously-used split integration.

Through simulation of multiple initial conditions (in terms of cloud-trigger and ambient atmosphere), the relative importance of the physical processes captured by the governing equations of the cloud-model were asserted. In detail it appears that the principal influence on a convective cloud's eventual cloud-top height is the process of drying through entrainment of dry air, and the process of cooling through entrainment of cooler ambient air. This means that correctly representing the near-cloud environment (the air *actually* entrained) has a crucial impact on correctly capturing a cloud's development, so that if the near-cloud environment is at $> 90\%$ of saturation, the entrainment of ambient air has little effect on a cloud's vertical development, and the factors discussed below have

negligible impact.

The second-most important influence appears to be the cloud-base radius, a larger cloud-base radius generally leading to a larger cloud; this effect can be explained in terms of increased entrainment at smaller cloud radii, causing the influences of entrainment discussed above to come into effect.

The third-most important impact on cloud-top height variations is the magnitude of the perturbations at cloud-base leading to convection, as the exact temperature and moisture content at cloud-base defines the moist adiabat along which a convective cloud develops (correcting for the increased lapse rate due to entrainment): a larger perturbation in moisture and temperature generally leading to a higher cloud-top height. The size of cloud-base perturbation also plays a key role in whether a cloud will reach an altitude to be freely convecting; however the level of free convection was often markedly higher than predicted from an adiabatically lifted parcel, which is likely to be due to the radius-dependent amount of entrainment causing the effective convective inhibition to increase, making the level of free convection radius-dependent. The extent to which this concept generalises to *actual* convective clouds (and not just a 1D-model of these) should be studied in further work using high-resolution simulations.

Finally the effect of drag (and as was discussed, equivalently entrainment) did not have an impact on a cloud's cloud-top height, but its impact is to slow a cloud's vertical growth rate, causing the cloud-radius to increase with height. This can be explained by the rapid timescale of microphysical processes in adjusting to supersaturation, so that even at small values of drag the cloud is in near thermal equilibrium, (in fact supersaturation was observed to peak below $1-2\%$ near the base of a cloud $\lessapprox 150m$). Similarly, the effect of precipitation rain-out (currently included through a simplistic rain-out length-scale model) showed little impact on the final cloud-top height, unless the conditions were reached where there was a balance between buoyancy loss through cooling/drying from entrainment, and buoyancy gain from rain-out of precipitation, in which case a cloud would develop long thin tops of condensate. The extent to which this feature is physical or an issue with the precipitation model (possibly a sign of a non-physical fall-speed estimate at low condensate concentrations) should be investigated in future work.

The model-equations may be improved in further work by using the full conservation equations as a foundation to formulate a reduced set which represent the most important physical processes. This reduces the computational cost of using the cloud-model. Secondly, regarding the formation of precipitation, a more physically-based formulation of the rain-out rate should be developed and the fall of precipitation through the cloud taken into account. The latter may be considered as part of a "downdraft" model which captures the formation of cool downdraft "shells" (and thus the entrainment of these) and their impact on the formation of cold-pools, and impact of this on locally promoting convection; (the effect of cool-pools will likely require a modification of the formulation of the CCFM

as a whole to consider the coldpool formation during the spectrum calculation). Finally, once studied through the use of for example high-resolution of simulations, the effect of neighbouring clouds on a cloud's development should be included (likely by modifying the ambient profile). From the above finding it appears that the most pressing issue is to represent the effect of down-draft on the entrained air.

7.2 Cloud microphysics

In Chapter 4 a new microphysics module was implemented with the following achieved goals: 1) allow the representation of the finite formation time of cloud-water droplets, 2) to develop a microphysics framework which can be utilised identically in any host-model capturing the dynamics of fluid flow, and 3) to conceive and implement an adaptive time-step integration method suitable for integrating moist processes (by ensuring positive definiteness of the state variables).

The principal findings of this chapter were firstly that assuming always the presence of a fixed number of "droplets" (acting as activated CCNs) of a minimum radius appears to lead to a physically reasonable model of cloud-water droplet formation, giving condensation time-scales on the order of seconds. Together with a simple Kessler-type rain-droplet formation, this was seen to produce rain-droplets at physically reasonable rate and amount ($\approx 0.1 g/kg$).

In future work the microphysics framework can be improved upon both in terms of the numerical implementation, and the physical processes represented. With regards to the former, it would be beneficial to quantify the influences on and limit values of the maximum tolerated absolute error of different state variables, so that correct evolution of the physical state can be guaranteed, and stability of the overall scheme ensured. In addition a number of simpler (less computationally costly) adaptive Runge-Kutta-type schemes exist, which may suffice and would make the overall integration of the cloud-profiles require less computation time. In regards to future work on the processes represented in the microphysics framework, the ice-phase processes should be included so that the formation and evolution of deep convective clouds can be studied. In addition, it would be possible to include aerosol-concentration information from the host-model to better represent the process of aerosol activation, making the number of nucleation sites (and thus the likelihood of convective cloud formation) dependent on the host-model state.

7.3 Single-cloud simulations

In Chapter 5 individual convective clouds were triggered and evolution simulated using LES simulations. The first conclusion of this chapter is that to properly capture the full dynamic

evolution of a convective cloud it is necessary to use 3D simulation (2D axisymmetric simulations being inadequate) and a resolution at least at $\Delta x = 12m$. These findings suggest that the dynamic behaviour of entrainment has characteristic flow properties that are neither radial or azimuthal and that these motions are important for capturing the turbulent mixing. And secondly the requirement on length-scale indicates that there are turbulent eddies on the length-scale of $\approx$ 12m that non-trivially (i.e. non-isotropic turbulence) contribute to the mixing.

In terms of the necessary boundary-layer perturbations for formation of convective clouds (the so-called *cloud trigger*), the estimates of single-cloud simulations confirm the predictions of convective inhibition (CIN) calculated from an adiabatically lifted parcel, asserting that buoyancy may be produced by increasing the amount of water vapour and/or increasing a parcel's temperature, a characteristic trade-off between the two being $\frac{\Delta q_v}{\Delta T}\Big|_{w_{CIN}=const.} \approx 1.4g/kg/K$. Due to the temperature dependent adiabatic expansion, perturbations in temperature tend to lead to larger cloud-base radii, so that if a control of the cloud-base radius through the perturbation length-scale is desired, it is advantageous to perturb the moisture amount instead of temperature.

Using the CIN-based analysis mentioned above, characteristic values of vertical velocity necessary at the condensation height were also estimated. A general agreement with the predictions based on an adiabatically lifted parcel was found with characteristic perturbations and cloud-base velocities in the range of Δ0.5g/kg, $\Delta\theta = 0.1$K and $w = 1$m/s. These observations suggest that the perturbations used in published literature (often on the order of $\Delta T = 1 - 4K$) are not necessarily perturbing the correct variable (temperature instead of moisture) and are often too large.

This chapter also showed that there is a qualitative agreement between the cloud-profiles predicted integrating the 1D cloud-model and vertical profiles extracted from these single-cloud simulations. However these estimates are very sensitive to the definition of the plume envelope, whether the analysis is done considering the cloud-model as predicting the time-dependent rise of a cloud-thermal (and so averaging over a single cloud over multiple timesteps) or whether the analysis is carried out at a single timestep representing the "steady-state" (although such a state was infrequently observed to exist). Using this analysis this chapter also produced evidence that the classical Morton-Turner model of entrainment could be modified by including a linear correction using the in-cloud vertical velocity, although this should be studied in further work.

7.4 Simulation of multiple interacting clouds

From analysis of the large-domain LES simulation of shallow convection in the RICO setup in Chapter 6, a number of assumptions used in the CCFM convection scheme were investigated. Firstly, it was shown that it is reasonable to assume that all clouds

develop from the same cloud-base height, and that this height is well predicted by the lifting condensation level of an adiabatically lifted parcel. This has implications for the cloud-trigger in CCFM as it is only necessary to consider a single height when integrating each cloud-profile with the 1D cloud-model. This conclusion is likely to also apply to deep convection but will not be true for cases where midlevel convection occurs; these should both be studied in future work.

Secondly, it was shown that the maximum cloud-base radius observed in the RICO setup is significantly less than the boundary-layer depth ($max(r_{base} \approx 350\text{m}$ whereas $z_{BL} \approx 550\text{m})$). This is important for the choice of initial radii used (the CCFM *cloud-types*) when integrating the 1D cloud-model (to produce the vertical profile of each cloud type), as correctly constraining the cloud-base radius allows for better use of computational resources by having more cloud-types in the range of cloud-base radius where clouds do actually form.

The third important outcome of Chapter 6 was the significance of accurately representing the near-cloud environment when integrating the cloud-model. By analysing the 3D output from the RICO simulation and comparing the near-cloud environment to the horizontal mean across the whole model domain, it was noted that the near-cloud environment is significantly colder and moister than the horizontal mean. As discussed above in the context of the 1D cloud-model, the near-cloud environment has a direct impact on the properties of the air that is entrained, and as entrainment of moisture and heat are the only processes by which a convective cloud will lose buoyancy and die before the equilibrium level predicted by moist adiabatic ascent, then incorrectly representing the near-cloud environment can drastically affect the predicted cloud-top height. As an example a change in ambient relative humidity of 5% can affect a 500m change in cloud-top height.

The fourth outcome concerns the extent to which cloud-base radius is a good predictor of cloud-top height (and thus qualifies as a method by which to quantise the cloud ensemble into different cloud types), which indicates that in itself cloud-base radius is in adequate to predict cloud-top height. Although there is a general trend of increase in cloud-top height with increasing cloud-base radius (when the maxima in both over a cloud's lifetime is considered) there is a significant spread ($z_{top} \in [1300; 1800]\text{m}$) in cloud-top height for e.g. clouds with a maximum radius of $r_{base} \approx 150\text{m}$. From experimenting with integrating the 1D cloud-model (with values extracted from LES) it does not appear that this spread can be solely explained by variations in cloud-base conditions (i.e. the variations in moisture content, temperature and vertical velocity), but instead variations in the near-cloud environment (which is entrained) appears necessary to represent the full range of cloud-top height measured. This may mean that the "cloud-type" classification in CCFM should change, but it is unclear at this stage what a better classification would be. In further work classification by cloud-base massflux (as used in the Plant-Craig convection scheme *Plant and Craig* [2008]) should be considered.

The fifth outcome of the analysis in Chapter 6 was a realisation that the assumption that individual clouds are in a steady-state (as assumed in CCFM) with a well-defined cloud-base once the cloud is fully developed in vertical extent, does generally *not* apply to individual clouds in shallow convection. Instead the majority of clouds are observed to "disconnect" from the condensation height, the cloud-base disappearing before the maximum cloud-top height is reached. Although the steady-state assumption may not apply to individual clouds directly, it is suggested that it may however apply if a number of clouds in different stages of their development are considered together, each of these clouds going through the same evolution (having e.g. same cloud-base radius at a given time in their lifespan). This would imply that the cloud-model, instead of representing the profile of a single cloud, instead represents the vertical transport of a number of cloud thermals together, thereby changing what is considered to be in steady-state. This description is supported to some degree by the conclusions above where larger cloud-base radius generally leads to higher cloud-top height, however the spread here suggested that the discrete cloud evolutions to capture (which would be the measure of cloud types) must be revised.

This description is supported by the fourth outcome of the analysis of this chapter, which showed that although there is no correlation between the instantaneous cloud-base radius and cloud-top height, if instead the maximum in cloud-base radius and cloud-top height during a cloud's entire evolution is considered, a correlation does appear.

The correlation when maximum radius is used indicates that cloud-base radius is a predictor of how high an individual cloud will reach, and so is still likely acceptable as a method of defining a cloud-type; however the steady-state assumption must be modified. These conclusions may not apply equally well to deep convection as these cloud have been observed to persist for longer than their formation time, giving credit to the steady-state assumption; however deep convective clouds have also been observed to comprise of multiple rising thermals. Again this lends support to considering the convective transport as the steady-state integral effect of multiple transient thermals.

In future work it would be instructive to study the extent to which the cloud-base area of clouds formed in the RICO simulation are circular and the extent to which the clouds are axisymmetric. As the entrainment rate is dependent on the surface area over which entrainment takes place, it is likely that clouds which have a larger surface error with the same internal volume will entrain more, and so the entrainment rate should be higher than predicted from using the inverse equivalent area radius. It would also challenge the assumption of a top-hat distribution of in-cloud variables in the 1D cloud-model, which is implied by representing in-cloud state with a single horizontal mean value. This could be done by extracting cross-sections through convective cloud in simulation. Preliminary studies into this have indicated that the radial distribution is more Gaussian than constant, a modification which can likely be incorporated into the cloud-model formulation and may alter the mixing (entrainment) characteristics.

Bibliography

Angell, C. A., W. J. Sichina, M. Oguni, and W. J. Sichina (1982), Heat capacity of water at extremes of supercooling and superheating, *The Journal of Physical Chemistry*, *86*(6), 998–1002, doi:10.1021/j100395a032.

Arakawa, A. (2004), The Cumulus Parameterization Problem: Past, Present, and Future, *Journal of Climate*, *17*(13), 2493–2525, doi:10.1175/1520-0442(2004)017<2493:RATCPP>2.0.CO;2.

Arakawa, A., and W. H. Schubert (1974), Interaction of a Cumulus Cloud Ensemble with the Large-Scale Environment, Part I, *Journal of the Atmospheric Sciences*, *31*(3), 674–701, doi:10.1175/1520-0469(1974)031<0674:IOACCE>2.0.CO;2.

Arnold, H. (2010), Improving the Representation of Convective Clouds in Climate Models,

Bechtold, P. (2014), Atmospheric moist convection, *ECMWF Training Material*, (February).

Bechtold, P., M. Köhler, T. Jung, F. Doblas-Reyes, M. Leutbecher, M. J. Rodwell, F. Vitart, and G. Balsamo (2008), Advances in simulating atmospheric variability with the ECMWF model: From synoptic to decadal time-scales, *Quarterly Journal of the Royal Meteorological Society*, *134*(634), 1337–1351, doi:10.1002/qj.289.

Bony, S. et al. (2015), Clouds, circulation and climate sensitivity, *Nature Geoscience*, *8*(4), 261–268, doi:10.1038/ngeo2398.

Bryan, G. H., and J. M. Fritsch (2002), A Benchmark Simulation for Moist Nonhydrostatic Numerical Models, *Monthly Weather Review*, *130*(12), 2917–2928, doi:10.1175/1520-0493(2002)130<2917:ABSFMN>2.0.CO;2.

Cao, Z. (2015), Convection and its representation in global climate models, PhD thesis.

Costa, A. et al. (2016), Results of the eruptive column model inter-comparison study, *Journal of Volcanology and Geothermal Research*, doi:10.1016/j.jvolgeores.2016.01.017.

Dai, A. (2006), Precipitation characteristics in eighteen coupled climate models, *Journal of Climate*, *19*(18), 4605–4630, doi:10.1175/JCLI3884.1.

Dirmeyer, P. A. et al. (2012), Simulating the diurnal cycle of rainfall in global climate models: Resolution versus parameterization, *Climate Dynamics*, *39*(1-2), 399–418, doi:10.1007/s00382-011-1127-9.

Donner, L. J. (1993), A Cumulus Parameterization Including Mass Fluxes, Vertical

Momentum Dynamics, and Mesoscale Effects, *Journal of the Atmospheric Sciences*, *50*(6), 889–906, doi:10.1175/1520-0469(1993)050<0889:ACPIMF>2.0.CO;2.

ECMWF (2013), ECMWF Newsletter, (135).

Faber, T. E. (1995), *Fluid Dynamics for Physicists:* Cambridge University Press, Cambridge.

Falkovich, G. (2011), *Fluid mechanics: a short course for physicists*, Cambridge University Press, Cambridge.

Fehlberg, E. (1970), Klassische Runge-Kutta-Formeln vierter und niedrigerer Ordnung mit Schrittweiten-Kontrolle und ihre Anwendung auf W??rmeleitungsprobleme, *Computing*, *6*(1-2), 61–71, doi:10.1007/BF02241732.

Gregory, D. (2001), Estimation of entrainment rate in simple models of convective clouds, *Quarterly Journal of the Royal Meteorological Society*, *127*(571), 53–72, doi:10.1002/qj.49712757104.

Herzog, M., H.-F. Graf, C. Textor, and J. M. Oberhuber (1998), The effect of phase changes of water on the development of volcanic plumes, *Journal of Volcanology and Geothermal Research*, *87*, 55–74, doi:10.1016/S0377-0273(98)00100-0.

Heus, T., and H. J. J. Jonker (2008), Subsiding Shells around Shallow Cumulus Clouds, *J. Atmos. Sci.*, *65*(3), 1003?1018, doi:10.1175/2007JAS2322.1.

Heus, T., and a. Seifert (2013), Automated tracking of shallow cumulus clouds in large domain, long duration large eddy simulations, *Geoscientific Model Development*, *6*(4), 1261–1273, doi:10.5194/gmd-6-1261-2013.

Hoerner, S. F. (1965), *Fluid-dynamic drag: practical information on aerodynamic drag and hydrodynamic resistance*, Hoerner Fluid Dynamics.

Hohenegger, C., and C. S. Bretherton (2011), and Physics Simulating deep convection with a shallow convection scheme, (1991), 10389–10406, doi:10.5194/acp-11-10389-2011.

Kain, J. S., and J. M. Fritsch (1990), A One-Dimensional Entraining/Detraining Plume Model and Its Application in Convective Parameterization, *Journal of the Atmospheric Sciences*, *47*(23), 2784–2802, doi:10.1175/1520-0469(1990)047<2784:AODEPM>2.0.CO;2.

Kessler, E. (1969), On the Distribution and Continuity of Water Substance in Atmospheric Circulations, *Meteor. Monogr.*

Kim, J., K. M. Grise, and S. W. Son (2013), Thermal characteristics of the cold-point tropopause region in CMIP5 models, *Journal of Geophysical Research Atmospheres*, *118*(16), 8827–8841, doi:10.1002/jgrd.50649.

Klingaman, N. P. et al. (2015), Vertical structure and physical processes of the Madden-Julian oscillation: Linking hindcast fidelity to simulated diabatic heating

and moistening, *Journal of Geophysical Research: Atmospheres*, *120*(10), 4690–4717, doi:10.1002/2014JD022374.

Knight, C. G. et al. (2007), Association of parameter, software, and hardware variation with large-scale behavior across 57,000 climate models., *Proceedings of the National Academy of Sciences of the United States of America*, *104*(30), 12259–64, doi:10.1073/pnas.0608144104.

Kuo, H. L. (1965), On Formation and Intensification of Tropical Cyclones Through Latent Heat Release by Cumulus Convection, *Journal of the Atmospheric Sciences*, *22*(1), 40–63, doi:10.1175/1520-0469(1965)022<0040:OFAIOT>2.0.CO;2.

Levine, J. (1959), SPHERICAL VORTEX THEORY OF BUBBLE-LIKE MOTION IN CUMULUS CLOUDS, *Journal of Meteorology*, *16*(6), 653–662, doi:10.1175/1520-0469(1959)016<0653:SVTOBL>2.0.CO;2.

Levine, J. (1965), The dynamics of cumulus convection in the trades - a combined observational and theoretical study., PhD thesis, Massachusetts Institute of Technology.

Manabe, S., and R. F. Strickler (1964), Thermal Equilibrium of the Atmosphere with a Convective Adjustment, *Journal of the Atmospheric Sciences*, *21*(4), 361–385, doi:10.1175/1520-0469(1964)021<0361:TEOTAW>2.0.CO;2.

Marshall, J. S., and W. M. Palmer (1948), The Distribution of Raindrops With Size, *5*, 165–166, doi:10.1175/1520-0469(1948)005<0165:TDORWS>2.0.CO;2.

Matsuno, T. (1966), Quasi-Geostrophic Motions in the Equatorial Area, *Journal of the Meteorological Society of Japan. Ser. II*, *44*(1), 25–43.

MetOffice (2014), Met Office Numerical Weather Prediction models,

Morrison, H., and J. A. Milbrandt (2015), Parameterization of Cloud Microphysics Based on the Prediction of Bulk Ice Particle Properties. Part I: Scheme Description and Idealized Tests, *Journal of the Atmospheric Sciences*, *72*(1), 287–311, doi:10.1175/JAS-D-14-0065.1.

Morton, B. R., G. Taylor, J. S. Turner, L. Series, and P. Sciences (1956), Turbulent gravitational convection from maintained and instantaneous sources, *Proceedings of the Royal Society of London. Series A, Mathematical and Physical Sciences*, *234*(1196), 1–23.

Naveau, P., and M. W. Moncrieff (2003), A probabilistic description of convective mass fluxes and its relationship to extreme-value theory, *Quarterly Journal of the Royal Meteorological Society*, *129*(592), 2217–2232, doi:10.1256/qj.01.124.

Oberhuber, J. M., M. Herzog, H.-F. Graf, and K. Schwanke (1998), Volcanic plume simulation on large scales, *Journal of Volcanology and Geothermal Research*, *87*(1-4), 29–53, doi:10.1016/S0377-0273(98)00099-7.

Oort, A. H., and J. J. Yienger (1996), Observed Interannual Variability in the Hadley Circulation and Its Connection to ENSO, *Journal of Climate*, *9*(11), 2751–2767, doi:10.1175/1520-0442(1996)009<2751:OIVITH>2.0.CO;2.

Plant, R. S., and G. C. Craig (2008), A Stochastic Parameterization for Deep Convection

Based on Equilibrium Statistics, *Journal of the Atmospheric Sciences*, *65*(1), 87–105, doi:10.1175/2007JAS2263.1.

Rast, S. et al. (2013), User manual for ECHAM6,

Rauber, R. M. et al. (2007), Rain in Shallow Cumulus Over the Ocean: The RICO Campaign, *Bulletin of the American Meteorological Society*, *88*(12), 1912–1928, doi:10.1175/BAMS-88-12-1912.

Rogers, R., and M. K. Yau (1989), *A short course in cloud physics*, International series in natural philosophy, Pergamon Press.

Rooy, W. C. de, P. Bechtold, K. Fröhlich, C. Hohenegger, H. Jonker, D. Mironov, a. Pier Siebesma, J. Teixeira, and J.-I. Yano (2013), Entrainment and detrainment in cumulus convection: an overview, *Quarterly Journal of the Royal Meteorological Society*, *139*(670), 1–19, doi:10.1002/qj.1959.

Schumacher, C., and R. A. Houze (2006), Stratiform precipitation production over sub-Saharan Africa and the tropical East Atlantic as observed by TRMM, *Quarterly Journal of the Royal Meteorological Society*, *132*, 2235–2255, doi:10.1256/qj.05.121.

Seifert, A., and K. D. Beheng (2006), A two-moment cloud microphysics parameterization for mixed-phase clouds. Part 1: Model description, *Meteorology and Atmospheric Physics*, *92*(1-2), 45–66, doi:10.1007/s00703-005-0112-4.

Senior, C. A., and J. F. B. Mitchell (1993), Carbon Dioxide and Climate. The Impact of Cloud Parameterization, *Journal of Climate*, *6*(3), 393–418, doi:10.1175/1520-0442(1993)006<0393:CDACTI>2.0.CO;2.

Simpson, J., and V. Wiggert (1969), Models of precipitating cumulus towers, *Monthly Weather Review*, *97*(7).

Slawinska, J., W. W. Grabowski, H. Pawlowska, and H. Morrison (2012), Droplet Activation and Mixing in Large-Eddy Simulation of a Shallow Cumulus Field, *Journal of the Atmospheric Sciences*, *69*(2), 444–462, doi:10.1175/JAS-D-11-054.1.

Stevens, B. et al. (2005), Evaluation of Large-Eddy Simulations via Observations of Nocturnal Marine Stratocumulus, *Monthly Weather Review*, *133*(6), 1443–1462, doi:10.1175/MWR2930.1.

Stocker, T. F., Q. Dahe, G.-K. Plattner, T. Physical, and S. Basis (2013), Climate Change 2013: The Physical Science Basis, *Working Group I Contribution to the Fifth Assessment Report of the Intergovernmental Panel on Climate Change. Summary for Policymakers (IPCC, 2013)*.

Stommel, H. (1947), Entrainment Of Air Into a Cumulus Cloud, *Journal of Meteorology*, *4*(3), 91–94, doi:10.1175/1520-0469(1947)004<0091:EOAIAC>2.0.CO;2.

Suzuki, Y. J., A. Costa, M. Cerminara, T. Esposti Ongaro, M. Herzog, A. R. Van Eaton,

and L. Denby (2016), Inter-comparison of three-dimensional models of volcanic plumes, *Journal of Volcanology and Geothermal Research*, doi:10.1016/j.jvolgeores.2016.06.011.

Tiedtke, M. (1989), A Comprehensive Mass Flux Scheme for Cumulus Parameterization in Large-Scale Models, *Monthly Weather Review*, *117*(8), 1779–1800, doi:10.1175/1520-0493(1989)117<1779:ACMFSF>2.0.CO;2.

Toro, E. F. (2009), *Riemann solvers and numerical methods for fluid dynamics: a practical introduction (Google eBook)*, Springer.

Turner, J. S. (1962), The 'starting plume' in neutral surroundings, *Journal of Fluid Mechanics*, *13*(03), 356, doi:10.1017/S0022112062000762.

Turner, J. S. (1963), The motion of buoyant elements in turbulent surroundings, *Journal of Fluid Mechanics*, *16*(01), 1, doi:10.1017/S0022112063000549.

Wagner, T. M. (2009), A dynamical convective cloud field model and the effects of aerosols, PhD thesis.

Wagner, T. M., and H.-F. Graf (2010), An Ensemble Cumulus Convection Parameterization with Explicit Cloud Treatment, *Journal of the Atmospheric Sciences*, *67*(12), 3854–3869, doi:10.1175/2010JAS3485.1.

Wheeler, M., and G. N. Kiladis (1999), Convectively Coupled Equatorial Waves: Analysis of Clouds and Temperature in the Wavenumber–Frequency Domain, *Journal of the Atmospheric Sciences*, *56*(3), 374–399, doi:10.1175/1520-0469(1999)056<0374:CCEWAO>2.0.CO;2.

Yano, J.-I. (2014), Basic convective element: bubble or plume? A historical review, *Atmospheric Chemistry and Physics*, *14*(13), 7019–7030, doi:10.5194/acp-14-7019-2014.

7.5 Appendix

.1 On the ability of mass and momentum entrainment to halt cloud development

)

To cause a developing convective cloud to halt its vertical development and stop well below any inversion at high altitude the vertical velocity must decrease at some altitude. By considering the point at which this transition from acceleration to deceleration takes places it is possible to show analytically that in the formulation of the 1d cloud-model equations it is not possible through the entrainment of mass and momentum alone to effect the halting of a convective cloud's vertical development.

There must exist a point where $\frac{dw}{dz} = 0$ and at this same point we require that $\frac{d^2w}{dz^2} < 0$ so that the parcel is decelerating.

— *type up the derivation here*

It is not possible to to satisfy this inequality, suggesting that entrainment of mass and momentum alone is not enough. ## Rain-droplet size distribution

Write up derivation of:

- total number of droplets (through integrating total mass)
- length-scale λ_r
- accretion integral
- condensation/evaporation integral ## Saturation adjustment

Definition of the entrainment rate

When deriving the plume model equations two different approaches are taken: first is to consider the plume continuum (from which the mass conservation is developed) and the second is to consider a discrete parcel of the plume air (used for the momentum and energy conservation equations). These two approaches lead to different definitions of the entrainment rate μ, one in terms of the total mass flux (M) at a given height

$$\mu = \frac{1}{M}\frac{dM}{dz}$$

and the second in terms of the mass (m_c) of the parcel of cloudy air under consideration:

$$\mu = \frac{1}{m_c}\frac{dm_c}{dz}.$$

At first glance it this may seem as problem, as will be shown below however the two definitions are equivalent. This happens because the parcel of air under consideration spans the entire cross-section of the plume at a given height, and so in effect the mass of the parcel (m_c) is directly related to the total mass flux. This can be shown by writing out the momentum (p) of a parcel of plume air of thickness δz:

$$p = m_c w = \pi r^2 \rho_c w \delta z = M \delta z,$$

where ρ_c is the cloud density, w the vertical velocity and r the cloud plume radius.

We now expand the entrainment rate as defined by cloud parcel mass (m_c)

$$\begin{aligned}
\frac{1}{m_c}\frac{dm_c}{dz} &= \frac{1}{M\frac{\delta z}{w}}\frac{d}{dz}\left(M\frac{\delta z}{w}\right) \\
&= \frac{1}{M\cancel{\frac{\delta z}{w}}}\cancel{\frac{\delta z}{w}}\frac{dM}{dz} + \frac{1}{\cancel{M}\frac{\delta z}{w}}\cancel{M}\frac{d}{dz}\left(\frac{\delta z}{w}\right) \\
&= \frac{1}{M}\frac{dM}{dz} + \frac{w}{\delta z}\left[\frac{1}{w}\frac{d(\delta z)}{dz} - \frac{\delta z}{w^2}\frac{dw}{dz}\right] \\
&= \frac{1}{M}\frac{dM}{dz} + \frac{1}{\delta z}\left[\frac{d(\delta z)}{dz} - \frac{\delta z}{w}\frac{dw}{dz}\right]. \qquad (1)
\end{aligned}$$

We now consider how the vertical thickness of the cloud parcel varies with height. As there may be vertical variation in the vertical velocity inside the plume, the top of the cloud parcel may have a relative vertical velocity (w_{rel}) to the cloud parcel base:

$$w_{rel} = \frac{dw}{dz}\delta z$$

With this definition the change in parcel thinkness in a time interval dt is

$$d(\delta z) = w_{rel} dt$$

Expanding a rearranging the above expression we have that

$$\begin{aligned}
\frac{d(\delta z)}{dt} &= w_{rel} \\
\frac{dz}{dt}\frac{d(\delta z)}{z} &= \frac{dw}{dz}\delta z \\
w\frac{d(\delta z)}{z} &= \frac{dw}{dz}\delta z \\
\Rightarrow \quad \frac{d(\delta z)}{dz} &= \frac{\delta z}{w}\frac{dw}{dz}. \qquad (2)
\end{aligned}$$

And so we see that the last two terms in eqn. 1 cancel, showing that two different definitions of entrainment rate are equivalent

$$\begin{aligned}\frac{1}{m_c}\frac{dm_c}{dz} &= \frac{1}{M}\frac{dM}{dz} + \frac{1}{\delta z}\left[\frac{\cancel{d(\delta z)}}{\cancel{dz}} - \frac{\delta z\, \cancel{dw}}{\cancel{w}\ dz}\right], \\ &= \frac{1}{M}\frac{dM}{dz}. \end{aligned} \tag{3}$$